UNIVERSITÀ DELLA CALABRIA

UNIVERSITY OF CALABRIA

Department of Civil Engineering

Doctoral School "Pitagora" in Engineering Sciences

Doctoral Program in Materials and Structural Engineering

Cycle

XXVIII

Scientific Disciplinary Sector

ICAR/08

Modeling of Edge Debonding in Beams Strengthened with Composite Materials

Tutor:
Prof. Domenico Bruno

Co–Tutors:
Prof. Fabrizio Greco

Ing. Paolo Nevone Blasi

Ph.D. Candidate:
Stefania Lo Feudo

Ph.D. Program Director:
Prof. Renato Sante Olivito

Academic Year 2014/2015

Alla mia famiglia

A piccoli passi

Abstract

The main purpose of this study is the analysis of edge debonding in beams strengthened with externally bonded fiber–reinforced polymers (FRP) composite plates. At first, the topic is introduced in general terms by a literature review focused on composite materials main properties and modeling approaches. Then, an innovative multi–layer formulation is considered and adapted to the present case study, and a coupled failure criterion is extended to the case of delamination in mixed mode loading condition.

The considered structural system is modeled as an assembly of three physical components, namely the beam, the adhesive layer and the bonded plate, each one being modeled by one or several first–order shear deformable layers. Firstly, the problem is considered from an analytic point of view by obtaining the governing equations when each physical layer is represented by a single mathematical layer. Secondly, the proposed multi–layer formulation is implemented numerically by using a multivariable $1D$ finite element (FE) technique. In particular, strong and weak interface constitutive relations are introduced to model the physical and the mathematical interfaces between layers inside each physical components. As a result, interfacial stresses and fracture energies are evaluated, obtaining reasonable agreement with results achieved by using a continuum FE model, and greatly reducing computational costs. Then, debonding initiation is predicted by means of the novel mixed mode coupled criterion, which takes into account both fracture energies

and interfacial stresses and enables to consider different damage locations across the adhesive thickness. Debonding propagation is then studied by using a classic mixed mode fracture criterion. In addition, a parametric numerical analysis is conducted by varying interface critical parameters, such as fracture toughness and strength, in order to investigate the influence of these properties on interfacial debonding. The studies here carried out show that the present formulation is able to model strengthened systems and to predict edge debonding. Indeed, the solution accuracy can be improved by using more layers within each physical components and by adopting the coupled strong/weak interface formulation, however it is proved that edge debonding initiation and propagation may be also accurately predicted by using few layers to model each physical components.

KEY WORDS: *FRP, edge debonding, strong/weak interface, FE, crack initiation, crack propagation.*

Sommario

L'oggetto principale della presente tesi di dottorato, è costituito dallo studio dei fenomeni di scollamento d'interfaccia in sistemi di rinforzo composti da elementi strutturali rinforzati da piastre in materiale composito fibrorinforzato (FRP). L'argomento è inizialmente introdotto in termini generali attraverso un'attenta ricerca bibliografica, concentrata sulla definizione delle principali proprietà dei materiali compositi e sulla loro modellazione. Un'innovativa formulazione multistrato è poi presentata e adattata al caso oggetto di studio, e un criterio di frattura accoppiato è esteso al caso di delaminazione in presenza di condizioni di carico di modo misto.

Il sistema strutturale considerato è quindi costituito da tre componenti fisici, ossia la trave, lo strato di adesivo e la piastra incollata esternamente, ciascuno dei quali è modellato attraverso uno o più strati deformabili a taglio. Il problema è considerato in primo luogo da un punto di vista analitico, attraverso la formulazione delle equazioni governanti il problema nel caso in cui ad ogni componente fisico corrisponde un solo strato matematico. La formulazione multistrato è poi implementata numericamente, utilizzando degli elementi finiti (FE) multivariabili monodimensionali. In particolare, per modellare le interfacce tra gli strati fisici e matematici sono considerate sia delle equazioni costitutive di interfaccia forte che debole. Le tensioni interfacciali e le energie di frattura sono quindi calcolate, ottenendo un'accettabile corrispondenza con i risultati di un modello continuo FE e riducendo di molto gli

oneri computazionali. L'innesco dello scollamento è poi valutato grazie all'innovativo criterio di frattura di modo misto, il quale permette di prendere in considerazione sia le tensioni interfacciali che l'energia di frattura, consentendo allo stesso tempo di studiare differenti posizioni dello scollamento lungo lo spessore dell'adesivo. La propagazione del danno è quindi studiata utilizzando un criterio classico di frattura in modo misto. Uno studio parametrico, condotto al variare dei parametri critici dell'interfaccia quali la tenacità e la resistenza, ha infine permesso di valutare l'influenza di tali proprietà sul fenomeno dello scollamento. Gli studi condotti hanno evidenziato che la tecnica di modellazione proposta permette sia di modellare tali sistemi di rinforzo, sia di predire lo scollamento d'estremità. Inoltre, nonostante emerga che l'accuratezza della soluzione può essere migliorata aumentando il numero di strati matematici e adottando delle interfacce miste forti/deboli, è possibile concludere che l'utilizzo di pochi strati nella modellazione di ogni componente fisico permette di predire lo scollamento con ragionevole precisione.

PAROLE CHIAVE: *FRP, scollamento, interfacce forti/deboli, FE, multistrato, innesco della fessura.*

Preface

Fiber–reinforced plastic (FRP) strips, plates, and sheets are usually adopted in many kinds of engineering applications such as structural strengthening, seismic retrofitting, and repair of existing concrete or steel structures. Usually, FRP plates are externally bonded to the tension face of a concrete or steel beam by means of an adhesive layer, leading to a flexural reinforcement for structural elements. When this innovative technique is used to strengthen existing structures, a considerable number of advantages in the structural performance may be obtained in terms of strength and durability, despite the small changes in weight and dimension of the structural system. The possibility to apply external composite plates in the context of existing structures by using adhesive joint, gives flexibility to the method, which can be adopted for a large variety of structural elements such as beams, columns, frames, masonry structures, and others.

In spite of the above mentioned advantages, the use of adhesively bonded external FRP reinforcements exposes the strengthened structure to additional catastrophic failure modes, mainly related to a decrease of ductility. The obtained reinforced structural system, in fact, becomes vulnerable to debonding failure modes involving the FRP layer, usually associated with the initiation and growth of interfacial cracks at the interface between the adhesive layer and the lower face of the beam.

Interfacial debonding, one of the critical failure modes for structural elements reinforced by means of composite plates, is often caused by

high concentrations of normal and shear stresses at the end of the bonded plate, or by bonding defects in the application of the FRP reinforcement. Debonding of the reinforcement may thus start either from the edge of the composite plate or from an intermediate flexural crack, and adhesive substrate or adhesive/FRP interface debonding, can be experienced in both steel and concrete strengthened systems.

The initiation and propagation of interfacial debonding mechanisms critically affect the structural functionality of the structural element, leading in many cases to the global failure of the layered element. As a consequence, the capability of the adhesive layers and their interfaces to join the components together and to transfer interfacial shear and normal stresses is fundamental for an optimal structural performance of such kinds of strengthened systems.

Within this framework, the present research work investigates the onset and propagation of edge debonding for beams strengthened with externally bonded FRP composite plates. The thesis may be divided into two parts as follows. In Chapters 1 and 2, the topic is introduced in general terms by presenting several aspects related to the problem. At first, the composite material composition, the mechanics of composites at micro– and macro– level, and the most common modeling theories adopted are illustrated. Then, attention is focused on the application of composite materials in the form of FRP plates in order to reinforce structural elements. Typical failure modes encountered in these applications are presented and two main aspects necessary to analyze FRP debonding are studied. The former is the prediction of the stress distribution at the interfaces between the different structural components. The latter is the evaluation of the fracture energies in mixed mode loading condition related to the delamination growth. The complexity of the subject arises from the fact that materials with different properties are bonded together. In fact, as a consequence, continuum elasticity predicts a stress field with oscillatory singularities near discontinuities, as the plate ends and the crack tips, and classical decomposition of the En-

ergy Release Rate (ERR) into its modal components is not allowed. In order to overcome these problems, a multi–layer formulation combined with interface elements is here presented and developed. In particular, by using a variational approach, through the stationarity of the total potential energy functional of the strengthened system, the equations governing the problem are formulated. Therefore, by adopting a first–order theory, which takes into account shear deformability, equilibrium equations and boundary conditions are obtained in case of a three layer assembly, composed by a base beam, an adhesive layer, and a bonded plate. This analytical development is an original contribution of the present study. The formulation is then generalized to the case of subdivision of the physical elements into several mathematical layers, allowing to directly decompose the ERR by virtue of concentrated forces, which arise from the discontinuities in forces resultants at the crack tip.

In Chapters 3 and 4 a numerical investigation is carried out, by adopting the proposed multi–layer formulation in order to model reinforced concrete beams strengthened by FRP plates. Two main aspects of novelty with respect to the existing literature are introduced. The former one is represented by the analysis of edge debonding onset, performed by using an innovative mixed mode coupled criterion accounting for both fracture energies (Mode I and Mode II) and interfacial stresses (normal and shear). In particular, both pointwise and integral stress criteria are accounted, and the compressive normal stresses are appropriately penalized. The proposed crack onset coupled criterion thus represents an original extension of those introduced in the literature. As far as the latter aspect of novelty is concerned, the advanced multi–layer formulation is adapted to the case of strengthened systems and implemented by using one–dimensional elements. An assembly of first–order shear deformable mathematical layers connected by appropriate interface layers (with zero thickness) is considered, and one or several mathematical layers inside each one of the three physical components (the beam, the adhesive layer and the bonded plate) are used. Then, in order to model the two phys-

ical interfaces (i.e. beam/adhesive and adhesive/plate) both strong and weak interface constitutive relations are adopted, whereas for the mathematical interfaces between layers inside each physical components, a strong interface formulation is employed. As a result, an effective determination of both fracture and stress quantities, which are useful to predict edge debonding onset and subsequent propagation at the relevant location across the adhesive layer, is achieved. Meanwhile, compared to two–dimensional models, shortcomings due to the presence of bi–material interfaces are addressed, and computational cost are greatly reduced.

Premessa

I materiali fibro rinforzati a matrice polimerica (FRP) sono oggigiorno comunemente utilizzati sotto forma di strisce, piastre o pannelli, in diverse applicazioni ingegneristiche, quali il rinforzo strutturale, l'adeguamento sismico e la riabilitazione di strutture esistenti in calcestruzzo armato o acciaio. Ad esempio, una piastra in FRP può essere applicata, tramite uno strato di adesivo, sulla superficie esterna di una trave, in acciaio o in calcestruzzo, al fine di rinforzarla strutturalmente. Utilizzando quest'innovativo sistema di rinforzo, è possibile ottenere numerosi vantaggi in termini di resistenza e durabilità, a fronte di lievi modifiche di peso e dimensioni del sistema di partenza. La possibilità di applicare gli FRP esternamente, rende inoltre questa tecnica estramamente versatile, consentendone l'uso su una grande varietà di elementi strutturali, quali ad esempio travi, colonne, telai e strutture in muratura.

A fronte di tali vantaggi, il rinforzo tramite FRP espone la struttura a nuovi modi di collasso, legati principalmente alla diminuzione della duttilità del sistema. Il sistema rinforzato infatti, risulta soggetto a fenomeni di rottura dovuti al *debonding* tra la piastra in FRP e l'elemento strutturale stesso, il quale è generalmente associato con l'innesco e la crescita di fessure all'interfaccia tra lo strato di adesivo e la superficie della trave.

Lo frattura all'interfaccia, che rappresenta quindi uno dei modi critici di rottura degli elementi rinforzati da piastre in composito, è spesso causato dalle alte concentrazioni di tensioni normali e tangenziali che insorgono all'estremità della piastra incollata, o da problemi di incol-

laggio derivanti dalla fase di messa in opera. Il debonding può quindi innescarsi sia alle estremità della piastra in composito, sia in posizione intermedia, traendo origine da fessure flessionali nel calcestruzzo, e sia a livello dell'adesivo che delle interfacce tra l'adesivo e gli altri componenti, in entrambi i casi di rinforzo di strutture in acciaio o in calcestruzzo.

L'innesco e la propagazione di questi meccanismi di frattura all'interfaccia, influenzano in maniera altamente negativa la funzionalità dell'elemento strutturale, portando in molti casi alla sua completa rottura. Per questo motivo, la capacità dell'adesivo di connettere i diversi componenti, e quella delle interfacce di trasferire le tensioni normali e tangenziali, è di fondamentale importanza per ottenere delle elevate performance strutturali.

All'interno di questo contesto, si inserisce il presente lavoro di ricerca, il quale si occupa di analizzare l'innesco di estremità e la propagazione del debonding di FRP applicati su elementi strutturali di tipo trave. Il lavoro di tesi può quindi essere suddiviso in due parti, secondo quanto segue. I Capitoli 1 e 2 si occupano di introdurre l'argomento da un punto di vista generale, presentando diversi aspetti legati al problema. In primo luogo, vengono quindi presentate la definizione e la composizione dei materiali compositi, la meccanica dei compositi alla micro ed alla macro scala, e le più comuni teorie di modellazione utilizzate. L'attenzione è poi posta sull'impiego dei compositi, sotto forma di piastre in FRP, per il rinforzo strutturale. Sono quindi riportati i principali modi di rottura generalmente riscontrati, e sono presentati due aspetti di fondamentale importanza nello studio del debonding degli FRP. Il primo, riguarda la valutazione della distribuzione delle tensioni alle interfacce tra i diversi elementi strutturali; il secondo, si riferisce invece alla valutazione dell'energia di frattura di modo misto associata alla crescita della delaminazione. In particolare, la complessità dell'argomento risiede nel fatto che materiali con differenti proprietà meccaniche sono collegati tra loro. Infatti, come conseguenza, la teoria dell'elasticità fornisce un campo delle tensioni caratterizzato da una singolarità oscillatoria in

prossimità delle discontinuità, quali le estremità della piastra e l'apice delle fessure, non consentendo inoltre di scomporre direttamente il tasso di rilascio dell'energia (ERR) nelle sue componenti modali. Al fine di superare queste difficoltà, nella presente tesi sarà presentato e sviluppato un modello multistrato, ad interfacce forti e deboli, capace di studiare il fenomeno del debonding. In particolare, attraverso un approccio di tipo variazionale, ossia grazie alla stazionarietà del funzionale energia potenziale totale generalizzato del sistema rinforzato, è possibile ottenere le equazioni che governano il problema. Quindi, tramite l'adozione di una teoria del primo ordine, la quale tiene in conto della deformabilità a taglio dei vari strati strati, le equazioni di equilibrio e le rispettive condizioni al contorno sono ottenute nel caso di un assemblaggio composto da tre layer matematici corrispondenti a quelli fisici, ossia la trave di base, lo strato di adesivo e la piastra incollata. Questo sviluppo di tipo analitico rappresenta uno dei contributi originali ivi introdotti. La formulazione è poi generalizzata al caso di una suddivisione dei componenti in più strati matematici, e verrà confermato che l'adozione dei modelli multistrato consente, sia analiticamente che numericamente, di decomporre direttamente l'ERR grazie alla presenza di forze concentrate derivanti dalle discontinuità nelle forze risultanti all'apice della fessura.

Nei Capitoli 3 e 4 è invece condotta un'analisi di tipo numerico, applicando la formulazione multistrato al caso di una trave in calcestruzzo armato, modellata come un solido omogeneo, rinforzata da piastre in FRP. In particolare, due sono gli aspetti di novità introdotti rispetto a ciò che si ritrova nella letteratura esistente. Il primo aspetto è rappresentato dallo studio dell'innesco dei fenomeni di frattura all'interfaccia, attuata utilizzando un innovativo criterio accoppiato di modo misto, che tiene in conto sia delle energia di frattura (Modo I e Modo II), sia delle tensioni interfacciali (normali e tangenziali), in cui il criterio tensionale è utilizzato in entrambe le forme, puntuale e integrale, e le tensioni normali di compressione sono opportunamente penalizzate. Tale criterio accoppiato, capace di predire l'innesco della fessura, rappresenta un'estensione

originale dei criteri di frattura presenti nella letteratura. Il secondo aspetto di novità, riguarda invece l'applicazione dei modelli multistrato al caso di sistemi rinforzati e per mezzo di elementi monodimensionali. Un assemblaggio di layer matematici, modellati con la teoria di deformabilità a taglio del primo ordine, sono quindi connessi da strati di interfaccia, a spessore nullo, e più layer matematici sono considerati all'interno dei tre componenti di tipo fisico (la trave, l'adesivo e la piastra incollata). Inoltre, al fine di modellare le due interfacce fisiche, ossia trave/adesivo e adesivo/piastra, sono adottate delle equazioni costitutive di tipo forte e debole, prendendo invece in considerazione delle sole interfacce forti per strati matematici. Attraverso tale formulazione e modellazione, si dimostrerà la possibilità di ottenere un'accurata previsione dei fenomeni di innesco e successiva propagazione della delaminazione all'interno dello spessore dello strato di adesivo. Allo stesso, l'utilizzo di tale strategia consentirà di superare i limiti dei modelli bidimensionali, derivanti dalla presenza di interfacce tra materiali differenti e riducendo considerevolmente i costi computazionali.

Contents

Chapter 1

Structural application of composite materials

This chapter essentially deals with the composite material properties and behavior characterization. In Section 1.1, the principal composite features are introduced in terms of classifications, materials and manufacturing. In Section 1.2, the micro–mechanics of composites is analyzed, by passing from the microscopic to the the macroscopic models through homogenization models and multiscale methods. Then, in Section 1.3 the mechanics of composite material is presented. In particular, the classical, the first–order shear deformation and the layerwise theories are explained in detail, together with some interface model and a coupled interface/multi–layer model. Finally, in Section 1.4 some example of composite materials applications in the civil engineering field is illustrated.

1.1 Introduction

Composite materials are nowadays currently used in many engineering fields and adopted in several structural applications owing to their key properties, as the high strength-to-weight and stiffness-to-weight ratios.

Generally speaking, as composite material is identified a material made by combining two or more components of different type. In particular, the composites are constituted by a matrix and a filler, where the matrix holds the fillers together to form the bulk of the material. The matrix consists in general of various epoxy type polymers, but also metal matrix composites and thermoplastic matrix composites can be adopted. The filler is therefore embedded in the matrix, and it can be made by various types of materials, such as carbon fibers, glass bead, sand, or ceramic. This combination can be realized either in a macroscopic scale or in a microscopic one. In the former case, the components can be easily identified, in the latter the resulting material is macroscopically homogeneous. Moreover, a composite types called hybrid can be realized when more than one type of reinforcement component is used. A well designed composite exhibits a better behavior with respect to that of the individual constituents. For instance, it is possible to improve various properties such as strength, stiffness, corrosion and wear resistance, weight, fatigue life, thermal and acoustical insulation, temperature-dependent behavior and thermal conductivity.

1.1.1 Composite materials classification

A composite material classification adopted by Barbero [1] is below reported. Depending on the main features of the composite itself, these materials may be classified depending on:

1. *Reinforcement*
    - Continuous long fibers
        (a) Unidirectional fiber orientation
        (b) Bidirectional fiber orientation
        (c) Random orientation
    - Discontinuous fibers
        (a) Random orientation

(b) Preferential orientation

- Particles and whiskers
  (a) Random orientation
  (b) Preferential orientation

2. *Laminate configuration*

   - Unidirectional, including several layers with same material and orientation
   - Laminate, where some layers have different orientation or are made by different material

3. *Hybrid structure*

   - Different materials in various layers
   - Different reinforcement in a layer

By just looking to the filler component, [2], it is possible to distinguish therefore fiber, laminated and particulate composites. The *Fibrous composite materials* are made by fibers embedded in a matrix. In particular, the filler material has a length to diameter ratio, $1/d$, greater than one, and depending on the diameter ratio value they are subdivided in short or long fiber composites. The *Laminated composite materials* are realized by superposition of layer of different materials, which means that the filler material is used in form of sheet. Formica countertop is an example, where the matrix material is usually phenolic type thermoset polymer, whereas the filler may be any material such as craft paper (Formica), canvas (canvas phenolic) and (glass filled phenolic). *Particulate composite materials* are finally those in which particles are inserted and roughly rounded in a matrix. A classical example is the concrete, where the cement is the matrix and the sand is the filler.

The resulting properties are then represented by the combination of the properties of each constituent, and highly depend on the type of loading which acts on the composite itself.

1.1.1.1 Fiber reinforced polymer composite materials, materials and manufacturing process

The major object of this thesis is the study of the reinforcement of structural elements by adopting the fiber reinforced polymer, or plastic, composite materials, (FRP). These composites are made by high strength fibers, which cannot be used alone since they are not capable to sustain compression or transverse load, embedded in or bonded to a matrix. The matrix has the aim to keep the fibers in the required orientation, to protect them from environmental damage and to transfer the load in the medium, whereas the fibers are basically the load-carrying members. The most common type of fiber-reinforced composite used in structural applications is a laminate, in which multiples thin layers of fibers and matrix are superimposed to rich the desired thickness, and the fiber orientation in each layer can be changed according to the design requirements, [3].

The main components of the fiber reinforced composite materials are the fibers and the matrix, but also coupling agents, coating and fillers can be adopted. Coupling agents and coating are used in order to favorite bonding across the fiber-matrix interface and to lead a better loads' transfer, whereas fillers can be inserted in a polymeric matrix in order to reduce costs and to improve dimensional stability. The manufacture consists in the insertion of fibers in a thin layer of matrix to form a lamina, or a ply, which thickness is generally in the range of $0.1 - 1\ mm$. Since fibers occupy the largest volume fraction, the fiber type, length, volume fraction and orientation influences several characteristics of the laminate, such as density, tensile and compressive strength and modulus, fatigue strength, fatigue failure mechanism, electrical and thermal conductivity and cost. However, the fiber reinforced composite properties depend on the direction of measurement, so that it is not an isotropic material. For example, in case of unidirectional fiber reinforced polymer many properties, such as the tensile strength and modulus, the impact strength, the coefficient of thermal expansion and the thermal conductivity, are maximum when measured in the longitudinal direction of the

fibers, whereas are minimums when measured in the transverse direction. A way to obtain a more balanced set of properties is to use bi- or multi–directional reinforcements. Moreover, by using short fibers set randomly, it is possible to obtain equal mechanical and physical properties in all direction in the plane of the lamina.

Materials

Glass, carbon and aramid are the principal fibers in commercial use, but also boron, silicon carbide, and aluminum oxide fibers can be adopted. The matrix may be a polymer, a metal, or a ceramic material, [4]. All materials are produced at high temperatures and require a specialized industrialization process. In fact, after that the fiber filaments are produced, they require a post process in order to realize strands, sheets, fabrics and mats. Similarly, the polymer is generally blended with other resins and mixed with some additives.

Glass Fibers: this fibers are used to made FRP reinforcing bars, strengthening fabrics and structural profiles. The diameter of a single fiber goes from 3 to 24 μm, it has a white color and is generally considered as an isotropic material. Glass fibers are very sensitive to moisture, especially in presence of salt and elevated alkalinity, so that they must be well protected by the resin. Anyway, glass fiber are very well thermal and electrical insulating materials, and are the most inexpensive among the others high performance fibers.

Carbon Fibers: they are used in FRP strengthening sheets, fabrics, strips and in prestressing tendons. A single fiber has a diameter from 5 to 10 μm with a charcoal black color. They are considered to be transversely isotropic, since they show different properties in longitudinal and transverse direction. Carbon fibers own high durability and perform well at high temperature, in presence of moisture and when subjected to fatigue. They have a low coefficient of thermal expansion in the longitudinal direction but they are thermal and electrical conductors.

Aramid Fibers: these fibers, used to produce the first prestressing tendons, are sometimes also adopted to wrap columns or to be inserted

as sparse filler in unidirectional glass or carbon FRP. Aramid fibers have very high tenacity and toughness, a negative coefficient of thermal expansion in the longitudinal direction, and they are lighter with respect to the others fibers. However, due to the elevate production cost, the difficult manufacture, the high moisture absorption and the low strength to compression, they are less used then the other fibers.

Unsaturated polyester resins: they are used to realize pultruded FRP profiles and rebars. Although these resins are recommended when high corrosion resistance is required, epoxy resins are preferred owing to their adhesive properties, low shrinkage and environmental durability.

Epoxy resins: they are used in many applications, especially in carbon FRP strips. Epoxy resins ares also used to bond precured FRP strips to concrete and to dry fibers sheets in order to attach them to a surface. They are very resistant to corrosion and experience less shrinkage than the others resins. For this reason, they are less affected by thermals loads and can be used at high temperatures.

Vinylester resins: they are characterized by good corrosion resistance and easy manufacture, in particular they are use especially to make FRP rebars and profiles. A vinylester resin is a hybrid of an epoxy and an unsaturated polyester resin, which leads to various advantages in terms of properties and production process. On the other end, these resins are more expensive then the others.

Phenolic resins: they are the oldest used thermosetting resins. However, the phenolic resins have only recently started to be used for FRP products for structural engineering, owing to the difficulty of reinforcing them and curing them by condensation polymerization.

Polyurethane resins: they have recently been produced in high-density forms to be used in resin molding and pultrusion operations. Polyurethane resins have high toughness and lead to composites with high transverse tensile and impact strengths but, like the vynilester resins, they are very expensive.

Manufacturing process

The main manufacturing techniques used to produce the FRP composite materials adopted in structural engineering are the pultrusion and the hand layup or wet layup method, [4]. The pultrusion is an industrialized process, in which the FRP composites are produced in a factory and then installed in situ. Conversely, the hand layup is a manual method, where the FRP are manufactured in situ at the same time of the installation. The pultrusion is used especially in case of FRP reinforcing bars, strengthening strips and profiles, whereas the hand-layup method is used to manufacture and install dry fiber strengthening sheets and fabrics.

1.2 Micromechanics of composite materials

1.2.1 Microscopic models

With the aim to well characterize the composite materials behavior, it is essential to analyze the composite itself at a microscopic level. By means of a micromechanics approach it is possible to evaluate the interaction between the various composite components, and to represent an heterogeneous material as an homogeneous when a macro–scale is considered, [5]. In particular, the micromechanics formulation that will be here presented is valid under the following basic assumptions, [6]:

- the fibers and the matrix are perfectly bonded;
- the fibers are parallels and uniformly distributed across the composite layer;
- the matrix does not contain voids or microcracks and is initially in a stress–free state;
- fibers and matrix behave as isotropic elastic materials;
- the external loads are applied perpendicularly or in parallel to the longitudinal fiber direction.

1.2.1.1 Fiber and matrix fractions

By looking at the composite material constituents, it is possible to define the *fiber volume fraction* and the *matrix volume fraction*, which represent the ratio of the fiber and the matrix volume, V_f and V_m, respectively, to the total volume, V_T:

$$\begin{aligned} &\bar{V}_f = \frac{V_f}{V_T}, \quad \bar{V}_m = \frac{V_m}{V_T}, \\ &\bar{V}_f + \bar{V}_m = 1 \end{aligned} \tag{1.2.1}$$

In a similar manner, it is possible to define the *fiber weight fraction* and the *matrix weight fraction* as the ratio of the fiber and the matrix weight, W_f and W_m, respectively, to the total weight, W_T:

$$\begin{aligned} &\bar{W}_f = \frac{W_f}{W_T}, \quad \bar{W}_m = \frac{W_m}{W_T}, \\ &\bar{W}_f + \bar{W}_m = 1 \end{aligned} \tag{1.2.2}$$

The density of the composite may be evaluated from the fibers and mass density, ρ_f and ρ_m, respectively, and either the correspondent volume or weight, as follows:

$$\begin{aligned} &\rho_c = \rho_f \bar{V}_f + \rho_m \bar{V}_m \\ &\frac{1}{\rho_c} = \frac{\bar{W}_f}{\rho_f} + \frac{\bar{W}_m}{\rho_m} \end{aligned} \tag{1.2.3}$$

From a practical point of view, the weight fraction is easier to compute than the volume fraction during the manufacturing process. However, it is possible to pass from one to another by applying the following simple relationship:

$$\bar{W}_i = \frac{\rho_i}{\rho_c} \bar{V}_i \tag{1.2.4}$$

where i can be referred either to the fiber or the matrix constituent, or whatever else component constituting the composite.

Owing to the presence of voids in the composite, the total density

can be different from the actual evaluated experimentally, $\rho_{c,exp}$. The void volume fraction can be therefore expressed as [5]:

$$V_v = \frac{\rho_c - \rho_{c,exp}}{\rho_c} \tag{1.2.5}$$

1.2.1.2 Representative volume element

The evaluation of the composite properties starts from the analysis of the micro–constituents properties. In order to reduce the computational efforts, the concept of *Representative volume element*, RVE, was introduced. The RVE is defined as a material volume that represents statistically the infinitesimal material neighborhood of a material point of a continuum mass. The continuum material point is called a *macro–element*, whereas the micro–constituents of the RVE are called *micro–elements*.

A macro–element is characterized by a complex microstructure, with grains, inclusions, voids, cracks and other defects. For this reason, to be the RVE statistically representative of the local continuum properties, it must be include a lot of micro–elements. As a consequence, it is necessary to define two length scales, one is the *macro–length scale*, which measures the infinitesimal material neighborhood, the other one is the *micro–length scale*, which corresponds to the size of the smallest micro–constituent who effects the global properties of the macro–element. The dimensions of the macro–element, D, and of the micro–element, d, differ by orders of magnitude, with $D/d >> 1$. In general, as reference dimensions can be chosen the layer thickness and the fiber spacing, [1]. In Fig. 1.1, the typical RVE which may be adopted for a composite with a rectangular or a hexagonal packing array is shown. Others details in terms of RVE characteristics and scales were deeply examined by Nemat–Nasser & Hori [7].

Since the RVE components are heterogeneous, stresses and strains within the RVE are nonuniform. However, if a scale larger than those of the RVE is considered, it is possible to replace the volume occupied

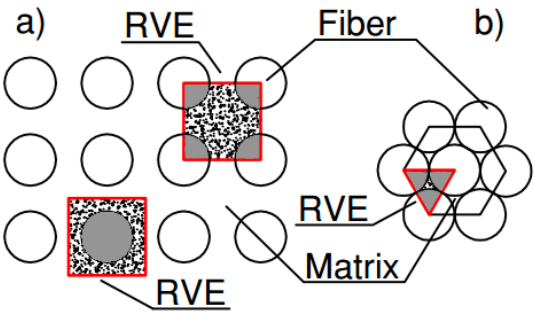

Figure 1.1: RVE for a) rectangular and b) hexagonal packing arrays

by the RVE, or vice versa, with another one made by homogeneous material without affect the stress state around the RVE, [1], as it is shown in Fig. 1.2.

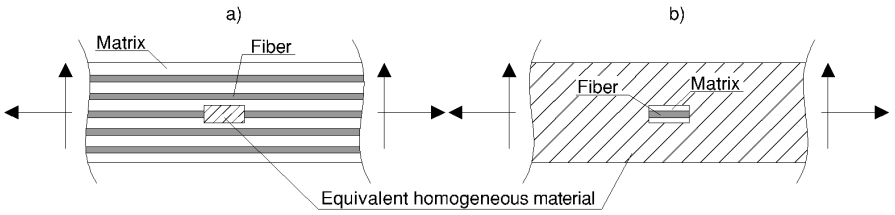

Figure 1.2: Homogeneous material replacing a) the RVE and b) all structure but the RVE

1.2.1.3 Components' stiffness

A material is *homogeneous* when its properties are independent by position, on the contrary, if the properties are function of the position, it is said to be *heterogeneous*. Moreover, a material is *isotropic* when all properties in a point are independent of the directions, otherwise it is said to be *anisotropic*. In particular, the analysis of the composites materials is within the framework of anisotropic elasticity.

Generally speaking, depending on the material planes of elastic sym-

metry, a material can be anistropic, orthotropic, transversely isotropic or isotropic. An anisotropic material has no plane of elastic symmetry, an orthotropic material three mutually orthogonal, a transversely isotropic has one axes of symmetry and for an isotropic material all planes are plane of symmetry. The way in which this subdivision influences the elastic properties of the material will be presented in Section 1.2.4 .

In the analysis of composite materials properties, the microscopic components, such as the fibers and the matrix, are assumed to be isotropic. In particular, an isotropic material is characterized by equals properties in all directions and, in order to fully describe its elastic properties, is necessary to consider only two elastic constants, i.e. the Young modulus and the Poisson's ratio, E and ν, respectively. E and ν are also related to the shear modulus by the following well–known relation:

$$G = \frac{E}{2(1+\nu)} \tag{1.2.6}$$

The combination of these two isotropic materials leads to an equivalent homogeneous anisotropic material, whose properties vary with the direction considered. In particular, since the composite laminate is assumed to be orthotropic, the stiffness of the material is described by five elastic constants, [1]:

- E_1 Young modulus in the longitudinal fiber direction
- E_2 Young modulus in the transverse fiber direction
- ν_{12} in–plane Poisson's ratio
- G_{12} in–plane shear modulus
- G_{23} out–of–plane shear modulus

Young modulus in the longitudinal fiber direction

In general, fiber and matrix are assumed to be perfectly bonded, so that they experience the same strains in the fiber longitudinal direction. Under this assumption, the Young modulus in the fiber direction, E_1, can be evaluated by adopting the rule of mixtures formula, [1]. In particular, the strain under axial load is defined as:

$$\epsilon_1 = \frac{\Delta L}{L} \tag{1.2.7}$$

in which ΔL is the fiber and matrix elongation and L the length of the considered RVE. By using the stress–strain relation in case of isotropic elastic material, such are supposed to be the fiber and the matrix, the stresses are given by:

$$\sigma_f = E_f \epsilon_1, \quad \sigma_m = E_m \epsilon_1 \tag{1.2.8}$$

The total load applied on the RVE is:

$$P = \sigma_1 A = \sigma_f A_f + \sigma_m A_m \tag{1.2.9}$$

where σ_1 is the average stress acting on the whole cross section of the RVE, with $A = A_f + A_m$. By substituting Eq. (1.2.8) into Eq. (1.2.9) and dividing by A, σ_1 can be expressed as:

$$\sigma_1 = \epsilon_1 \left(E_f \frac{A_f}{A} + E_m \frac{A_m}{A} \right) = \epsilon_1 (E_f V_f + E_m V_m) \tag{1.2.10}$$

where V_f and V_m are the fiber and the matrix volume fraction, respectively. Since for an homogeneous material the Hook's law leads to $\sigma_1 = E_1 \epsilon_1$, it follows that the elasticity modulus can be expressed as:

$$E_1 = E_f V_f + E_m V_m \tag{1.2.11}$$

which, by applying the second of Eq. (1.2.1), becomes:

$$E_1 = E_f V_f + E_m(1 - V_f) \tag{1.2.12}$$

The elastic modulus E_1 varies hence linearly with V_f and is dominated by the fiber contribute.

Young modulus in the transverse fiber direction

The equilibrium in the transverse is guaranteed by the assumption of uniform stress in the fiber and in the matrix. In addition, this condition allows to determine the Young modulus in the transverse fiber direction. The components' strains under the hypothesis of linear elastic material are:

$$\epsilon_f = \frac{\sigma_f}{E_f}, \quad \epsilon_m = \frac{\sigma_m}{E_m} \tag{1.2.13}$$

The average strain ϵ_2 act on the width the W of the RVE, the strains ϵ_f and ϵ_m on the portions $V_f W$ and $V_m W$, respectively. The total elongation in the transverse direction is therefore given by:

$$\epsilon_2 W = \epsilon_f V_f W + \epsilon_m V_m W \tag{1.2.14}$$

By substituting Eq. (1.2.13) into Eq. (1.2.14) and considering $\sigma = \sigma_2 = \sigma_f = \sigma_m$, the average strain can be expressed as:

$$\epsilon_2 = \frac{\sigma_2}{E_f} V_f + \frac{\sigma_2}{E_m} V_m \tag{1.2.15}$$

which, by virtue of the Hook's law, leads to:

$$\frac{1}{E_2} = \frac{V_m}{E_m} + \frac{V_f}{E_f} \tag{1.2.16}$$

From Eq. (1.2.16), it appears that E_2 is dominated by the matrix elastic modulus. However, Eq. (1.2.16) it is proved to underestimate the Young modulus and Barbero [1] suggests to use it only for qualitative estimations. He reports then a semi–empirical formula to be choose in a

design process:

$$E_2 = E_m \left[\frac{1 + \zeta \eta V_f}{1 - \eta V_f} \right], \quad \eta = \frac{(E_f/E_m) - 1}{(E_f/E_m) + \zeta} \tag{1.2.17}$$

where ζ is an empirical parameter which, for circular fiber, can be taken equal to 2.

In–plane Poisson's ratio The Poisson's ratio ν_{ij} is defined as the ratio of the strain in the j–th direction when stressed in the i–th direction, namely

$$\nu_{ij} = -\frac{\epsilon_j}{\epsilon_i} \tag{1.2.18}$$

With reference to a composite material, the Poisson's ratio can be therefore rewritten as:

$$\nu_{12} = \nu_f V_f + \nu_m V_m \tag{1.2.19}$$

In–plane shear modulus In a similar way, it is possible to express the in–plane shear modulus as:

$$\frac{1}{G_{12}} = \frac{V_m}{G_m} + \frac{V_f}{G_f} \tag{1.2.20}$$

According to Eq. (1.2.20), also G_{12} in presence of stiff fibers depends mostly on the matrix. Eq. (1.2.20) can be also rearranged in:

$$G_{12} = \frac{G_m}{V_m + V_f G_m / G_f} \tag{1.2.21}$$

where the shear modulus can be evaluated from Eq. (1.2.6). However, Barbero, [1], reports another more accurate formula for the G_{12} estimation, that is:

$$G_{12} = G_m \left[\frac{(1 + V_f) + (1 - V_f) G_m / G_f}{(1 - V_f) + (1 + V_f) G_m / G_f} \right] \tag{1.2.22}$$

Out–of–plane shear modulus The out–of–plane or interlaminar shear modulus G_{23} can be evaluated in the following manner:

$$\begin{aligned} G_{23} &= G_m \frac{V_f + \eta_{23}(1 - V_f)}{\eta_{23}(1 - V_f) + V_f G_m / G_f} \\ \eta_{23} &= \frac{3 - \nu_m + G_m/G_f}{4(1 - nu_m)} \end{aligned} \tag{1.2.23}$$

Finally, it is assumed $G_{13} = G_1$, which is an exact solution for transverse isotropic material whose axis of symmetry coincide with the longitudinal fiber direction.

A method able to correct not accurate formula by using experimental evidences can be found in [1], as well as the evaluations of thermal and strength properties.

1.2.2 Homogenized models

The heterogeneity of the composite materials leads to the challenging need of establish a rigorous methodology able to predict the composite effective properties. As a matter of fact, the composite properties differ by the properties of the individual constituents and, although the individual constituents of the composite material may have a linear elastic behavior, the response of the macro–element is in general inelastic and history–dependent, [7]. This issue arises from the presence of defects such as flaws, microcracks, damage at matrix–inclusion interfaces and cavities. In fact, when the defects develop during deformation within the RVE, the RVE microstructure changes, leading to the nonlinear behavior of the macro–elements. A direct evaluation of the composite global properties can be carried out by experimental investigations, which however are often expensive and impractical. A valid alternative to the experimental tests is constituted by the adoption of the so called *homogenization* techniques, which are aimed to replace the heterogeneous constituents of the composite with an equivalent material.

The homogenized models proposed in the literature can be basically

classified into analytic and numerical methods. In particular, most of the analytic approximate solutions are based on the *self–consistend methods*, where the material is treated as an initially homogeneous material with inclusions of different materials. However, these methods, which are reviewed by Hollister and Kikuchi in [8], may be laborious to apply. On the other hand, the numerical methods are based on the finite element method (FEM), and they may be classified into two categories, the *average–field theory* and the *homogenization theory*, for a complete treatise please see Hori and Nemat–Nasser [9] and Nevone Blasi [10].

The *Average–field theory* represents a physics approach to the homogenization problem. According to this theory, the macro–fields are defined as the volume averages of the micro–fields, so that the effective properties of the composite are evaluated from relations between the averaged micro–fields. This approach arises from the experimental evidence on the behavior of microscopically heterogeneous samples. In fact, it appears that the effective mechanical properties of such a samples derive from relations between the strain and the stress volume averages.

On the contrary, the *homogenization theory* is mathematical approach based on mathematical relations beetween the micro– and the macro–fields by means of a multiscale perturbation method.

In the homogenization theory, the differential equations governing the problem, which coefficients vary rapidly, are replaced by differential equations with constant or slowly varying coefficients. This limit theory is therefore based on asymptotic expansion and on the assumption of periodicity, [11].

The homogenization method consists of two step. First, the problem is solved at a local level within a unit cell, and the effective material properties are obtained. Then, the homogenized material is considered and the boundary value problem is solved.

1.2.2.1 Problem setting

Let's define a relative length scalar parameter ε as:

$$\varepsilon = \frac{D}{d} >> 1 \tag{1.2.24}$$

where D and d are the dimensions of the macro– and micro–element, respectively, as shown in Fig. 1.3.

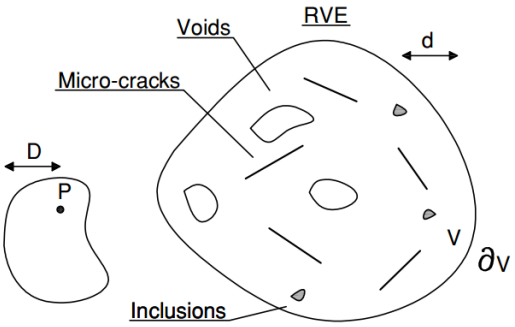

Figure 1.3: Schematic representation of a heterogeneous material

Let $\mathbf{X}$ be a point within a volume B. The elasticity tensor $\mathbf{C}^\varepsilon = \mathbf{C}^\varepsilon(\mathbf{X})$ varies highly with the point location, and the superscript ε denotes a variability at the ε scale. Also the displacement, the strain and the stress fields vary with $\mathbf{X}$:

$$\begin{cases} \mathbf{u}^\varepsilon = \mathbf{u}^\varepsilon(\mathbf{X}), \\ \epsilon^\varepsilon = \epsilon^\varepsilon(\mathbf{X}), \\ \sigma^\varepsilon = \sigma^\varepsilon(\mathbf{X}) \end{cases} \tag{1.2.25}$$

Owing to the different scale of micro– and macro–elements, it is possible to neglect the body forces, and the equilibrium of the body B can

be expressed as:

$$\begin{cases} \nabla(\sigma^{\varepsilon}) & = 0, \\ \epsilon^{\varepsilon}(\mathbf{X}) & = sym(\nabla \otimes \mathbf{u}^{\varepsilon}(\mathbf{X})), \\ \sigma^{\varepsilon}(\mathbf{X}) & = \mathbf{C}^{\varepsilon}(\mathbf{X}) : \epsilon^{\varepsilon}(\mathbf{X}) \end{cases} \tag{1.2.26}$$

where $\otimes$ is the tensor product, and $sym(\nabla \otimes \mathbf{u}^{\varepsilon}(\mathbf{X}))$ denotes the symmetric part of the displacement field gradient. If surface displacements are assigned on the boundary, namely $\mathbf{u} = \mathbf{u}^0$ on ∂B, the following boundary–value problem is obtained:

$$\begin{aligned} \nabla(\mathbf{C}^{\varepsilon}(\mathbf{X}) : (\nabla \mathbf{u}^{\varepsilon}(\mathbf{X}))) = 0 \quad & in\ B, \\ \mathbf{u}^{\varepsilon}(\mathbf{X}) = \mathbf{u}^0(\mathbf{X}) \quad & on\ \partial B \end{aligned} \tag{1.2.27}$$

However, the above presented boundary–value problem cannot be easily solved since $\mathbf{C}^{\varepsilon}(\mathbf{X})$ varies rapidly within the micro–scale d. A micromechanics theory, which introduces stress and strain fields varying at the macro–scale D, may be therefore adopted. In particular, the considered fields will be denoted as *macrofields* and *microfields* depending on the scale of variation, namely D and d.

1.2.2.2 Average–field theory

The average-field theory is based upon the representative volume element concept, which was presented in Section 1.2.1.2. The material effective properties are obtained as relations between the strains and stresses fields evaluated from the RVE surface displacements and traction, respectively. In particular, these strains and stresses correspond to the volume average of those obtained within the RVE. Therefore, for a compatible strain and a self–equilibrating stress, ϵ and σ, respectively,

the averaging theorem leads to, [9]:

$$\begin{aligned} < \epsilon >_V &= \frac{1}{V} \int_{\partial V} sym(\mathbf{n} \otimes \mathbf{u}) \; dS, \\ < \sigma >_V &= \frac{1}{V} \int_{\partial V} \mathbf{t} \otimes \mathbf{x} \; dS \end{aligned} \tag{1.2.28}$$

where $< >_V$ is the volume average taken over the volume V of the RVE, $\mathbf{n}$ is the unit outward normal on the boundary ∂B, $\mathbf{u}$ and $\mathbf{t}$ are the surface displacement and traction.

Macrofields of average–field theory

The macrofields variables are therefore defined as the weighted averages of the correspondents microfields evaluated on the RVE. It is now introduced a weight function, $\phi_V = \phi_V(\mathbf{x})$, which has the following properties:

$$\begin{aligned} \int \phi_V \; dV &= 1, \\ \phi_V &= \begin{cases} \frac{1}{V} & in \; V, \\ 0 & on \; \partial V \end{cases} \end{aligned} \tag{1.2.29}$$

The macrodisplacement, macrostrain, and macrostress fields can be thus expressed as:

$$\begin{Bmatrix} \mathbf{U}^{\varepsilon}(\mathbf{X}) \\ \mathbf{E}^{\varepsilon}(\mathbf{X}) \\ \mathbf{\Sigma}^{\varepsilon}(\mathbf{X}) \end{Bmatrix} = \int_B \phi_V(\mathbf{X} - \mathbf{Y}) \begin{Bmatrix} \mathbf{u}^{\varepsilon}(\mathbf{Y}) \\ \epsilon^{\varepsilon}(\mathbf{Y}) \\ \sigma^{\varepsilon}(\mathbf{Y}) \end{Bmatrix} dV_Y \tag{1.2.30}$$

where the weight function ϕ_V prevents the oscillations of the field variables that may be appear at the micro–scale. Moreover, the macrostrain and macrostress have to satisfy the compatibility and the equilibrium equations within the volume B, so that:

$$\begin{aligned} \mathbf{E}^{\varepsilon}(\mathbf{X}) &= sym(\nabla \otimes \mathbf{U}^{\varepsilon}(\mathbf{X})) \\ \nabla \cdot \mathbf{\Sigma}^{\varepsilon}(\mathbf{X}) &= 0 \end{aligned} \tag{1.2.31}$$

Once that an *effective elasticity tensor* of the homogeneous material, namely $\bar{\mathbf{C}}$, is found, a constitutive relation between macrostress and macrostrain fields may be stated as follows:

$$\mathbf{\Sigma}^{\varepsilon}(\mathbf{X}) = \bar{\mathbf{C}} : \mathbf{E}^{\varepsilon}(\mathbf{X}) \tag{1.2.32}$$

As a consequence, the following boundary–value problem is obtained:

$$\begin{cases} \nabla \cdot (\bar{\mathbf{C}} : (\mathbf{\Delta} \otimes \mathbf{U}^{\varepsilon}(\mathbf{X})) = 0 \quad in\ B \\ \mathbf{U}^{\varepsilon} = \mathbf{u}^{0} \quad on\ \partial B \end{cases} \tag{1.2.33}$$

The effective elasticity tensor, which relates the volume average of the microstrains and the microstresses, can be in turn expressed in terms of a *strain concentration tensor*, $\mathbf{A}$. The strain concentration tensor relates the average strain of the inclusion and of the RVE, $< \epsilon >_I$ and $< \epsilon >_V$, respectively, according to:

$$< \epsilon >_I = \mathbf{A} < \epsilon >_V \tag{1.2.34}$$

The effective elasticity tensor may be therefore expressed as:

$$\bar{\mathbf{C}} = \mathbf{C}^M + f(\mathbf{C}^I - \mathbf{C}^M) : \mathbf{A} \tag{1.2.35}$$

where f is the inclusion phase volume fracion, and $\mathbf{C}^M$ and $\mathbf{C}^I$ are the elasticity tensor of the matrix and of the inclusion phase, respectively.

Statistical homogeneous material

Let's define as a *statistical homogeneous* material, a material in which the probability of finding a phase at a point does not depend on the point itself, [9]. If an heterogeneous material is statistical homogeneous, then Eq. (1.2.32) holds, that is it exists an effective elasticity tensor which relates the weighted average stress and strain within the body.

Therefore, also the average strain energy and the average strain are

linked together by this elasticity tensor in the following manner:

$$\begin{aligned}&\frac{1}{2}\mathbf{E}^{\varepsilon}(\mathbf{X}) : \bar{\mathbf{C}} : \mathbf{E}^{\varepsilon}(\mathbf{X}) = \\ &\int_B \phi_V(\mathbf{X}-\mathbf{Y})(\frac{1}{2}\epsilon^{\varepsilon}(\mathbf{Y}) : \mathbf{C}^{\varepsilon} : \epsilon^{\varepsilon}(\mathbf{Y})\ dV_Y\end{aligned} \tag{1.2.36}$$

By defining the strain energy as:

$$< \epsilon : \sigma >_V = \frac{1}{V}\int_{\partial V} \mathbf{t}\cdot\mathbf{u}\ dS \tag{1.2.37}$$

the averaging theorem for the strain energy proves the validity of Eq. (1.2.36), in fact:

$$\begin{aligned}&< \epsilon : \sigma >_V - < \epsilon >_V : < \epsilon >_V \\ =&\frac{1}{V}\int_{\partial V}(\mathbf{u}-\mathbf{x}\cdot < \epsilon >)\cdot(\mathbf{t}-\mathbf{n}\cdot < \sigma >)\ dS\end{aligned} \tag{1.2.38}$$

where the right side of Eq. (1.2.38) vanishes as the size of the RVE volume, V, increases within a statistically homogeneous material. For this reason, when the RVE is sufficiently large in such a material, it is possible to assume that Eq. (1.2.36) is valid since the average weighted by ψ_V and the unweighted volume average are almost the same.

However, in case of homogeneous strain or stress boundary conditions:

$$\begin{cases}\mathbf{u} = \mathbf{x}\cdot\epsilon^0 & \textbf{homogeneous strain} \\ \mathbf{t} = \mathbf{n}\cdot\sigma^0 & \textbf{homogeneous stress}\end{cases} \quad on\ \partial V \tag{1.2.39}$$

the right side of Eq. (1.2.38) vanishes also when the material is not statistically homogeneous, but the obtained strain and the stress fields within the RVE are different. This issue implies that the effective elasticity tensor depends on the boundary conditions, and the so–called *universal*

inequalities, [7], hold:

$$< \epsilon^{\Sigma} : \mathbf{C} : \epsilon^{\Sigma} >_V \leq < \epsilon^{G} : \mathbf{C} : \epsilon^{G} >_V \leq < \epsilon^{E} : \mathbf{C} : \epsilon^{E} >_V \qquad (1.2.40)$$

where $(\epsilon^{\Sigma}, \epsilon^{G}, \epsilon^{E})$ are the average strain fields when the RVE boundary is subjected to homogeneous strain, mixed and homogeneous stress boundary conditions, respectively.

To explain this expression it may be considered that, since the strain and stress fields within the RVE depend on the boundary conditions adopted to solve the boundary value problem, the assumed boundary conditions may be not representative of all the possible boundary conditions to which the RVE is subjected. In particular, the more the boundary conditions represent the all possible boundary conditions, the more the achieved results are accurate. Consider the case where the in–situ boundary conditions are different from the applied but lead to the same average RVE strains (displacement prescribed on the boundary). Due to the principle of minimum strain energy, the average stiffness predicted by the average–field analysis is greater than the actual stiffness. In fact, whereas the in–situ boundary conditions minimize the energy, the assumed boundary conditions are admissible but give higher energy. Since the strain is the same, a higher energy is produced by higher average stress within the RVE. In the same manner, it can be considered the case in which the applied boundary conditions lead to the same average RVE stresses (traction prescribed on the boundary). According to the principle of minimum complementary energy, in this situation the homogeneous traction boundary conditions will produce a higher complementary energy than an in–situ traction condition, which leads to a lower stiffness. Therefore, the analyses under given displacements and traction on the boundary gives an upper bound and a lower bound, respectively, of the actual stiffness, [8].

As a consequence, in order to well define the effective elasticity tensor,

the chosen RVE must leads to:

$$< \epsilon^{\Sigma} : \mathbf{C} : \epsilon^{\Sigma} >_V - < \epsilon^{E} : \mathbf{C} : \epsilon^{E} >_V \rightarrow 0 \tag{1.2.41}$$

1.2.2.3 Homogenization theory

A heterogeneous material has a regular periodicity when some physical characteristic is represented by a function that repeats its values in regular intervals:

$$F(\mathbf{X} + \mathbf{NY}) = F(\mathbf{X}) \tag{1.2.42}$$

where $\mathbf{X} = (X_1, X_2, X_3)$, is the position vector of a point, $\mathbf{N} = sym(n_1, n_2, n_3)$ is a 3×3 diagonal matrix which components are integer numbers, $\mathbf{Y} = (Y_1, Y_2, Y_3)^T$ is a constant vector representing the period, and F can be a scalar, a vectorial or a tensioral function of the position vector $\mathbf{X}$.

For a composite material with periodic structure, the constitutive relation can be therefore expressed as:

$$\sigma_{ij} = c_{ijhk}(\mathbf{X} + \mathbf{NY})\epsilon_{hk} \tag{1.2.43}$$

Since in the homogenization theory the period $\mathbf{Y}$ is very small with respect to the whole domain dimension, the characteristics of the body vary rapidly in a neighborhood of the point $\mathbf{X}$. The dependence of the parameters on the two scales, the macro– and the micro–scale, leads therefore to rapid oscillations. In particular, by denoting as g a generic function, according to Eq. (1.2.24), we may say that $g = g(D, D/\varepsilon) = g(D, d)$.

Let's consider a function $\Phi(x)$ of a physical quantity of a heterogeneous material. It is possible to consider its oscillations at a double scale, and the parameter ε gives us information about the proportion between them, [11]. By adopting this double-scale technique, the coefficients of the partial governing equations governing the problem may be expressed as $a(D/\varepsilon)$ or $a(d)$, and the obtained boundary problem may be solved

by expanding asymptotically the solution in powers of the parameter ε. The function $\Phi(x)$ can be therefore written as:

$$\Phi^{\varepsilon}(\mathbf{X}) = \Phi^{0}(\mathbf{X},\mathbf{x}) + \varepsilon\Phi^{1}(\mathbf{X},\mathbf{x}) + \varepsilon^{2}\Phi^{2}(\mathbf{X},\mathbf{x}) + ... \tag{1.2.44}$$

where $\mathbf{X} = (X_1, X_2, X_3)$ and $\mathbf{x} = (x_1, x_2, x_3)$ are the macroscopic and the microscopic coordinate system, respectively, of a composite with periodic structure. The domain of such a body, it may be also seen as composed by a sequence of periodic cell of dimension $\varepsilon Y_1, \varepsilon Y_2, \varepsilon Y_3$, where Y_1, Y_2, Y_3 are the base cell side in the local coordinate system. Moreover, the functions $(\Phi^0(\mathbf{X},\mathbf{x}), \Phi^1(\mathbf{X},\mathbf{x}), ...)$ are smooths with respect to $\mathbf{X}$ and Y–periodic in $\mathbf{x}$, so that they take the same value at the opposite sides of the parallelepiped base cell.

Homogenization theory basic equations

Let's consider the problem presented in Section 1.2.2.1, the displacement field may be therefore expanded asymptotically with respect to the parameter ε in the following manner:

$$\mathbf{u}^{\varepsilon}(\mathbf{X}) \approx \sum_{n=0} \varepsilon^{n}\mathbf{u}^{n}(\mathbf{X},\mathbf{x}) \tag{1.2.45}$$

By applying the following chain rule to a field variable which depends on the two scales,

$$\begin{aligned}\frac{\partial\Phi(\mathbf{X},\mathbf{x}=\mathbf{X}/\varepsilon)}{\partial X_i} &= \frac{\partial\Phi(\mathbf{X},\mathbf{x})}{\partial X_i} + \frac{\partial\Phi(\mathbf{X},\mathbf{x})}{\partial x_k}\frac{\partial x_k}{X_i} = \\ &= \frac{\partial\Phi(\mathbf{X},\mathbf{x})}{\partial X_i} + \frac{1}{\varepsilon}\frac{\partial\Phi(\mathbf{X},\mathbf{x})}{\partial x_i}\end{aligned} \tag{1.2.46}$$

the ∇ operator can be expressed as:

$$\nabla(\circ) = \nabla_X(\circ) + \varepsilon^{-1}\nabla_x(\circ) \tag{1.2.47}$$

By substituting then Eq. (1.2.47) into the governing equations Eq.

(1.2.27) and after some manipulation, [9], one obtains:

$$\begin{aligned}
&\varepsilon^{-2}[\nabla_{\mathbf{x}} \cdot (\mathbf{C}(\mathbf{x}) : (\nabla_{\mathbf{x}} \otimes \mathbf{u}^0(\mathbf{X}, \mathbf{x})))]+ \\
&\quad + \varepsilon^{-1}[\nabla_{\mathbf{X}} \cdot (\mathbf{C}(\mathbf{x}) : (\nabla_{\mathbf{x}} \otimes \mathbf{u}^0(\mathbf{X}, \mathbf{x})))+ \\
&\quad + \nabla_{\mathbf{x}} \cdot \mathbf{C}(\mathbf{x}) : (\nabla_{\mathbf{x}} \otimes \mathbf{u}^0(\mathbf{X}, \mathbf{x}) + \nabla_{\mathbf{x}} \otimes \mathbf{u}^1(\mathbf{X}, \mathbf{x}))]+ \\
&\quad + \sum_{n=0} \varepsilon^n [\nabla_{\mathbf{X}} \cdot (\mathbf{C}(\mathbf{x}) : (\nabla_{\mathbf{X}} \otimes \mathbf{u}^n(\mathbf{X}, \mathbf{x}) + \nabla_{\mathbf{x}} \otimes \mathbf{u}^{n+1}(\mathbf{X}, \mathbf{x}))+ \\
&\quad + \nabla_{\mathbf{x}} \cdot (\mathbf{C}(\mathbf{x}) : (\nabla_{\mathbf{X}} \otimes \mathbf{u}^{n+1}(\mathbf{X}, \mathbf{x}) + \nabla_{\mathbf{x}} \otimes \mathbf{u}_{n+2}(\mathbf{X}, \mathbf{x}))] = 0
\end{aligned} \tag{1.2.48}$$

To solve Eq. (1.2.48), it is assumed that $\mathbf{u}^0$ is function only of the macro–scale length $\mathbf{X}$, and for $\mathbf{u}^1$ is assumed a periodic behavior at the micro–scale $\mathbf{x}$, that is:

$$\begin{cases} \mathbf{u}^0 = \mathbf{u}^0(\mathbf{X}) \\ \mathbf{u}^0(\mathbf{X}, \mathbf{x}) = \chi^1(\mathbf{x})(\nabla_{\mathbf{X}} \otimes \mathbf{u}^0(\mathbf{X})) \end{cases} \tag{1.2.49}$$

where χ^1 is a third–order symmetric tensor periodic with respect to $\mathbf{x}$. The terms $O(\varepsilon^{-2})$ vanish, and the $O(\varepsilon^{-1})$ take the following form:

$$[\nabla_{\mathbf{x}} \cdot (\mathbf{C}(\mathbf{x}) : (\nabla_{\mathbf{x}} \otimes \chi^1(\mathbf{x}) + \mathbf{1}^{(4s)}))] : (\nabla_{\mathbf{X}} \otimes \mathbf{u}^0(\mathbf{X})) \tag{1.2.50}$$

where $\mathbf{1}^{(4s)}$ is the fourth–order symmetric identity tensor. Since the terms in Eq. (1.2.50) must vanish in the same manner for $\mathbf{X}$ and $\mathbf{x}$, the tensor χ^1 must satisfy the following condition with periodic boundary conditions:

$$\nabla_{\mathbf{x}} \cdot (\mathbf{C}(\mathbf{x}) : (\nabla_{\mathbf{x}} \otimes \chi^1(\mathbf{x}) + \mathbf{1}^{(4s)})) = 0 \tag{1.2.51}$$

$\chi^1(\mathbf{x})(\nabla_{\mathbf{X}} \otimes \mathbf{u}^0(\mathbf{X}))$ represents therefore a microscopic displacement field correspondent to the not equilibrate stress field $\mathbf{C} : (\nabla_{\mathbf{X}} \otimes \mathbf{u}^0(\mathbf{X}))$, for further details please see Hori et al. [9]. Once that the tensor χ^1 is evaluated, in Eq. (1.2.48) only the $O(\varepsilon^0)$ terms left. By rearranging the equation, and by taking the volume average over the unit cell, the

governing equations can be expressed in terms of $\mathbf{u}^0$:

$$\nabla_{\mathbf{X}} \cdot (\bar{\mathbf{C}}^0 : (\nabla_{\mathbf{X}} \otimes \mathbf{u}^0(\mathbf{X}) = 0 \quad on\ B \tag{1.2.52}$$

where

$$\bar{\mathbf{C}}^0 = \frac{1}{U} \int_U \mathbf{C}(\mathbf{x}) : (\nabla \otimes \chi^1(\mathbf{x}) + \mathbf{1}^{(4s)}))\ dV \tag{1.2.53}$$

In this way, if it is assumed that $\mathbf{u}^0 \approx \mathbf{u}^\varepsilon$, a boundary–value problem for $\mathbf{u}^0$ is obtained, where $\mathbf{u}^0$ is prescribed on ∂B.

Macrofields of homogenization theory

The $\mathbf{u}^0(\mathbf{X})$ term represents the macro–displacement in the average–field theory, whereas the $\varepsilon\mathbf{u}^1$ term gives a small contribute since it vanishes over the unit cell due to the χ^1 periodicity.

The strain and the stress field can be also asymptotically expanded and, by relating the leading terms of the expansion to $\mathbf{u}^0$ and χ^1, they can be expressed as:

$$\begin{aligned} \epsilon^0(\mathbf{X},\mathbf{x}) &= sym\{\nabla_{\mathbf{X}} \otimes \mathbf{u}^0(\mathbf{X})\} + \\ &\quad + sym\{\nabla_{\mathbf{x}} \otimes \chi^1(\mathbf{x})\} : (\nabla_{\mathbf{X}} \otimes \mathbf{u}^0(\mathbf{X})), \\ \sigma^0(\mathbf{X},\mathbf{x}) &= \mathbf{C}(\mathbf{x}) : (\nabla_{\mathbf{x}} \otimes \chi^1(\mathbf{x}) + \mathbf{1}^{(4s)}) : (\nabla_{\mathbf{X}} \otimes \mathbf{u}^0(\mathbf{X})) \end{aligned} \tag{1.2.54}$$

Owing to the periodicity of χ^1, the volume average of the strain and the stress field taken over the unit cell U can be expressed as:

$$\begin{aligned} &< \epsilon^0 >_U (\mathbf{X}) = sym\{\nabla_{\mathbf{X}} \otimes \mathbf{u}^0(\mathbf{X})\} \\ &< \sigma^0 >_U (\mathbf{X}) = \bar{\mathbf{C}}^0 :< \epsilon^0 >_U (\mathbf{X}) \end{aligned} \tag{1.2.55}$$

It is possible to remark that the above fields correspond to the macrofields of the the average–field theory. The homogenization theory defines therefore the macrofields as the volume averages of the microfields, which are represented by the $O(\epsilon^0)$ terms.

In conclusion, there are two significant differences between he homogenization and the average–field theory. First of all, the homogenization

theory deals with a unit cell within a periodic structure, whereas the average–field theory with a RVE of a statistically homogeneous material. Moreover, the homogenization theory is able to account higher–order terms in the asymptotic expansion, leading to more accurate solutions. However, an hybrid theory was proposed by Hori et al. [9], proving that the homogenization theory may be adopted also in case of materials with a non-periodic microstructure, and that average–field theory allows to account higher order terms by considering appropriate micro–structural models. Equivalent results obtained starting from the virtual displacement equation are obtained by Wang et al. [12], togheter with a new solution proposed to solve the homogenization problem.

In this framework, Brighenti [13] proposed an homogenization model for a fiber reinforced composite material. The material is composed by two phases, namely an elasto–plastic matrix and a fiber phase. The fibers have same length and cross section, and their orientation is randomly distributed within the body. Imperfect bonds are also taken into account, so that even thought the single components may be linear elastics, the composite acts in a non–linear way. The problem is then solved by formulating incremental equilibrium equations. In particular, by equating the work rate made by the composite and the equivalent homogenized material, the equivalent elastic tensor is found. For further details also see Nevone Blasi [10] and Leonetti [14].

1.2.3 Multiscale methods

The composite materials may frequently show a high non linear behavior due to the presence of damage and contact mechanisms. However, a fully micro–mechanic analysis of the composite damaging process would require a very high computational effort. The multiscale methods allow therefore to analyze the composite behavior by using simplified models. In particular, the macroscopic and microscopic models are coupled taking advantage of both peculiarity, which means the possibility to acquire the required information without solve the full microscopic problem.

Several engineering problems are multiscale in nature and, according to Weinan et al. [15], these kind of problems may be classified according to their own features into:

- **Type A**: these problems are characterized by the presence of local and isolated defects or singularities, namely cracks, dislocations, contact surfaces and shocks. In these kind of problems, a microscopic model is required only near such singularities, elsewhere the macroscopic model is sufficient.

- **Type B**: in these problems a microscopic model is need in the all domain as support to the macroscopic model. An example is constituted by the homogenization problem where, due to the material heterogeneity, the macroscopic model defines only the required macroscopic variables and, the microscopic model allows their evaluation, as discussed in Section 1.2.2.3.

- **Type C**: these problems have characteristics of both Type A and Type B problems.

- **Type D**: these problems have the special feature of be self–similar in scales, this is the case of critical phenomena in fractal, turbulent transport and statistical physics, which are of not interest in this thesis work.

The approach generally adopted to solve Type A problems is the so–called *domain decomposition method* (DDM), which consists in divide the domain in two sub–domains to be solved at different scales. The scale coupling is then localized at the sub–domains interface, [14]. Conversely, for the Type B problems, the most suitable approach is to couple everywhere within the considered domain the macro– and the micro– models. The *heterogeneous multiscale method* (HMM) constitutes an example of such an approach. In particular, the macro–model provides the environment, that is the constraints, for the micro–model, which gives the information needed by the macroscale solver, [15].

The microscale methods able to resolve these multiscale problems can be classified, as summarized by Leonetti [14], in:

- **Hierarchical methods**: in these methods the problem with prescribed boundary condition is solved within a RVE for a range expected macro–strains and, from the achieved results, a constitutive law is obtained. A periodic RVE is assumed, together with uniformity of the macroscopic field variables, [16]. However, the hierarchical methods, which are very efficient for linear problems, are no longer suitable in presence of non linear phenomena.

- **Concurrent methods**: in these methods the fine–scale model is embedded into the coarse–scale model and the continuity is assured by imposing compatibility conditions and momentum balance at the interface. The micro– and the macro– scale models are solved simultaneously, so that the models are linked together *on the fly*, [15]. However, such an approach is suitable for subdomains with a refined scale small with respect to the whole domain.

- **Semi–concurrent methods**: these methods may be collocated between the hierarchical and the concurrent methods. The response of a fine–scale model is first evaluated for an input needed by the coarse–model, and then the obtained data are transferred to the coarse–scale and used during the analysis of the coarse–model.

1.2.4 Macroscopic constitutive laws

1.2.4.1 Costitutive relations

In a three-dimensional Cartesian coordinate system it is possible to represent the state of deformation of a solid by six components of stresses and strains, where three are the normal and three the shear components. The generalized Hook's law, which is a linear relation between stresses

and strains, can be expressed as:

$$\sigma_k = C_{kj}\epsilon_j, \quad k = 1, 2, ..., 6 \tag{1.2.56}$$

where C_{kj} are the coefficients, called *elastic coefficients*, of a 6×6 matrix. When the material is heterogeneous C_{kj} are functions of the position, otherwise the C_{kj} coefficients are constant through the material. σ_k and ϵ_j are the components of the stress and the strain tensor, respectively, written in contracted notation according to:

$$\begin{aligned} \sigma_\alpha &= \sigma_{mn} = \sigma_{nm} \\ \epsilon_\alpha &= \epsilon_{mn} = \epsilon_{nm} \end{aligned} \tag{1.2.57}$$

where the subscript m corresponds to the direction of the normal to the plane of interest and n to the direction of the stress, while the contraction rule is, [5]

$$\begin{aligned} &\alpha = m, \quad if \quad m = n \\ &\alpha = 9 - m - n, \quad if \quad m \neq n \end{aligned} \tag{1.2.58}$$

The 36 C_{ij} coefficients are not all independent of each other. First of all they are symmetric, that is $C_{kj} = C_{jk}$, if the strain energy density function U_0 fulfills the following condition:

$$\frac{\partial U_0}{\partial \epsilon_k} = \sigma_k \tag{1.2.59}$$

In fact, by expressing U_0 as

$$U_0 = \int_0^{\epsilon_k} \sigma_k d\epsilon_k \tag{1.2.60}$$

by substituting Eq. (1.2.56) into Eq. (1.2.60) and by integrating, it is obtained

$$U_0 = \frac{1}{2} C_{ij}\epsilon_i\epsilon_j \tag{1.2.61}$$

and the substitution of Eq. (1.2.61) into Eq. (1.2.59) leads to

$$\sigma_k = \frac{1}{2}(C_{kj} + C_{jk})\epsilon_j \tag{1.2.62}$$

By comparing Eq. (1.2.62) with Eq. (1.2.56), it is possible to verify that $C_{kj} = C_{jk}$. Hence, for anisotropic materials, there are 21 independent elastic constants and Eq. (1.2.56) can be expressed in a matrix form as:

$$\begin{pmatrix} \sigma_1 \\ \sigma_2 \\ \sigma_3 \\ \sigma_4 \\ \sigma_5 \\ \sigma_6 \end{pmatrix} = \begin{bmatrix} C_{11} & C_{12} & C_{13} & C_{14} & C_{15} & C_{16} \\ & C_{22} & C_{23} & C_{24} & C_{25} & C_{26} \\ & & C_{33} & C_{34} & C_{35} & C_{36} \\ & & & C_{44} & C_{45} & C_{46} \\ & & Sym. & & C_{55} & C_{56} \\ & & & & & C_{66} \end{bmatrix} \begin{pmatrix} \epsilon_1 \\ \epsilon_2 \\ \epsilon_3 \\ \epsilon_4 \\ \epsilon_5 \\ \epsilon_6 \end{pmatrix} \tag{1.2.63}$$

However, when a plane of elastic symmetry exists, the coefficients at a point have the same value for every pair of mirror–symmetrical points in this plane. The material is therefore called *monoclinic* and the elastic coefficients are 13. Moreover, if $x_3 = 0$ is the plane of symmetry, it is possible to show that the out–of–plane stresses, σ_4 and σ_5, are independent of normal and in–plane shear strains.

If a material system has three perpendicular planes of elastic symmetry, the number of independent elastic coefficients becomes 9, and the material is said to be *orthotropic*. In this case, there is no interaction between extensional and shear components when the material is loaded along the material coordinates, and the stress–strain relations are:

$$\begin{pmatrix} \sigma_1 \\ \sigma_2 \\ \sigma_3 \\ \sigma_4 \\ \sigma_5 \\ \sigma_6 \end{pmatrix} = \begin{bmatrix} C_{11} & C_{12} & C_{13} & 0 & 0 & 0 \\ & C_{22} & C_{23} & 0 & 0 & 0 \\ & & C_{33} & 0 & 0 & 0 \\ & & & C_{44} & 0 & 0 \\ & & Sym. & & C_{55} & 0 \\ & & & & & C_{66} \end{bmatrix} \begin{pmatrix} \epsilon_1 \\ \epsilon_2 \\ \epsilon_3 \\ \epsilon_4 \\ \epsilon_5 \\ \epsilon_6 \end{pmatrix} \tag{1.2.64}$$

If the three material directions (x_1, x_2, x_3) are perpendicular to the planes of elastic symmetry, then the stiffness coefficients for an orthotropic material can be expressed as:

$$\begin{aligned}
C_{11} &= \frac{1-\nu_{23}\nu_{32}}{\Delta E_2 E_3},\ C_{12} = \frac{\nu_{21}+\nu_{31}\nu_{23}}{\Delta E_2 E_3} = \frac{\nu_{12}+\nu_{32}\nu_{13}}{\Delta E_1 E_2} \\
C_{13} &= \frac{\nu_{31}+\nu_{21}\nu_{32}}{\Delta E_2 E_3} = \frac{\nu_{13}+\nu_{12}\nu_{23}}{\Delta E_1 E_2},\ C_{22} = \frac{1-\nu_{13}\nu_{31}}{\Delta E_1 E_3} \\
C_{23} &= \frac{\nu_{32}+\nu_{12}\nu_{31}}{\Delta E_1 E_3} = \frac{\nu_{23}+\nu_{21}\nu_{13}}{\Delta E_1 E_2},\ C_{33} = \frac{1-\nu_{12}\nu_{21}}{\Delta E_1 E_2} \\
C_{44} &= G_{23}, \quad C_{44} = G_{23}, \quad C_{55} = G_{13}, \quad C_{66} = G_{12} \\
\Delta &= \frac{1-\nu_{12}\nu_{21}-\nu_{23}\nu_{32}-\nu_{31}\nu_{13}-2\nu_{21}\nu_{32}\nu_{13}}{E_1 E_2 E_3}
\end{aligned} \tag{1.2.65}$$

where E_i is the Young modulus in the i direction, ν_{ij} is the Poisson ratio for transverse strain in the j–th direction when stressed in the i–th direction, namely

$$\nu_{ij} = -\frac{\epsilon_j}{\epsilon_i} \tag{1.2.66}$$

and G_{23}, G_{31}, G_{12} are the shear moduli in the $2-3$, $3-1$ and $1-2$ planes, respectively.

If in one of the planes of elastic symmetry of an orthotropic material, the material is isotropic, it is said to be *transversely isotropic*, and there are only 5 independent elastic coefficients. In particular, if x_1 is the coordinate normal to the isotropic plane, the strain–stress relationships are:

$$\begin{pmatrix} \sigma_1 \\ \sigma_2 \\ \sigma_3 \\ \sigma_4 \\ \sigma_5 \\ \sigma_6 \end{pmatrix} = \begin{bmatrix} C_{11} & C_{12} & C_{23} & 0 & 0 & 0 \\ & C_{22} & C_{23} & 0 & 0 & 0 \\ & & C_{22} & 0 & 0 & 0 \\ & & & \hat{C} & 0 & 0 \\ & & Sym. & & C_{66} & 0 \\ & & & & & C_{66} \end{bmatrix} \begin{pmatrix} \epsilon_1 \\ \epsilon_2 \\ \epsilon_3 \\ \epsilon_4 \\ \epsilon_5 \\ \epsilon_6 \end{pmatrix} \tag{1.2.67}$$

where

$$\hat{C} = \frac{1}{2}(C_{11} - C_{12}) \tag{1.2.68}$$

Finally, when a material owns infinite planes of elastic symmetry, it is called *isotropic*, and there are only 2 independent elastic constants:

$$\begin{pmatrix} \sigma_1 \\ \sigma_2 \\ \sigma_3 \\ \sigma_4 \\ \sigma_5 \\ \sigma_6 \end{pmatrix} = \begin{bmatrix} C_{11} & C_{12} & C_{12} & 0 & 0 & 0 \\ & C_{11} & C_{12} & 0 & 0 & 0 \\ & & C_{11} & 0 & 0 & 0 \\ & & & \hat{C} & 0 & 0 \\ & & Sym. & & \hat{C} & 0 \\ & & & & & \hat{C} \end{bmatrix} \begin{pmatrix} \epsilon_1 \\ \epsilon_2 \\ \epsilon_3 \\ \epsilon_4 \\ \epsilon_5 \\ \epsilon_6 \end{pmatrix} \tag{1.2.69}$$

where the two coefficients can be expressed in terms of Young Modulus E and Poisson ration ν as

$$\begin{aligned} C_{11} &= \frac{E(1-\nu)}{(1+\nu)(1-2\nu)} \\ C_{12} &= \frac{\nu E}{(1+\nu)(1-2\nu)} \end{aligned} \tag{1.2.70}$$

A fiber–reinforced composite material, if it is assumed that all fibers in a lamina are parallel, can be considered as an homogeneous orthotropic material, where the x_1 axis is parallel to the fiber directions.

1.2.4.2 Orthotropic lamina

For an orthotropic lamina which material coordinates are $(\bar{x}_1, \bar{x}_2, \bar{x}_3)$, the stress–strain relations are reduced to:

$$\begin{pmatrix} \bar{\sigma}_1 \\ \bar{\sigma}_2 \\ \bar{\sigma}_6 \end{pmatrix} = \begin{bmatrix} \bar{Q}_{11} & \bar{Q}_{12} & 0 \\ \bar{Q}_{12} & \bar{Q}_{22} & 0 \\ 0 & 0 & \bar{Q}_{66} \end{bmatrix} \begin{pmatrix} \bar{\epsilon}_1 \\ \bar{\epsilon}_2 \\ \bar{\epsilon}_6 \end{pmatrix} \tag{1.2.71}$$

and

$$\begin{pmatrix} \bar{\sigma}_4 \\ \bar{\sigma}_5 \end{pmatrix} = \begin{bmatrix} \bar{C}_{44} & 0 \\ 0 & \bar{C}_{55} \end{bmatrix} \begin{pmatrix} \bar{\epsilon}_4 \\ \bar{\epsilon}_5 \end{pmatrix} \tag{1.2.72}$$

In particular, the $\bar{Q}_{ij}$ coefficients are called *plane stress-reduced stiffnesses* since they are obtained from C_{ij} in case of plane stress state, $\sigma_{33} = 0$, and can be expressed as:

$$\begin{aligned} \bar{Q}_{11} &= \frac{E_1}{1-\nu_{12}\nu_{21}}, \ \bar{Q}_{22} = \frac{E_2}{1-\nu_{12}\nu_{21}} \\ \bar{Q}_{12} &= \frac{\nu_{12}E_2}{1-\nu_{12}\nu_{21}}, \ \bar{Q}_{66} = G_{12} \end{aligned} \tag{1.2.73}$$

moreover

$$\begin{aligned} \bar{C}_{44} &= G_{23} \\ \bar{C}_{55} &= G_{13} \end{aligned} \tag{1.2.74}$$

However, if the material directions $(\bar{x}_1, \bar{x}_2, \bar{x}_3)$ are not aligned with the material coordinate system used to formulate the governing equations of the structural problem, (x_1, x_2, x_3), a coordinate transformation can be employed to obtain the $\bar{\sigma}_1, \bar{\sigma}_2, \bar{\sigma}_3$ stresses in terms of the stresses $\sigma_1, \sigma_2, \sigma_3$ in the global coordinates, [17].

1.3 Mechanics of composite materials

Composite laminates are made by superposition of various composite layers of different materials and with different fibers orientation. Since the composite laminates are elements with on dimension smaller then the others two, they are commonly treated as plate elements. In this context, it is possible to adopt one among these approaches to analyze composite plates, [6]:

1. Equivalent single–layer theories (2D)
   (a) Classical laminated plate theory
   (b) Shear deformation laminated plate theories
2. Three-dimensional elasticity theories (3D)

(a) Traditional 3D elasticity formulation

(b) Layerwise theories

In the three-dimensional elasticity theory, each layer is modeled as a three–dimensional solid. By making certain assumptions on the kinematics of deformation or on the stress state through the laminate thickness, it is possible to reduce the problem from a three– to a two–dimensional one.

In the equivalent single layer laminated plate theories, where the composite laminate is modeled as an equivalent single layer, the displacement and the stress field are assumed to be a linear combination of unknown functions and thickness coordinates, ϕ_j^i and z, respectively, in the following manner:

$$\phi_i(x, y, z, t) = \sum_{j=0}^{N} (z)^j \phi_j^i(x, y, t) \tag{1.3.1}$$

where (x, y) are the in–plane coordinates and t represents the time. When ϕ_i are displacements, the principle of virtual displacement allows to determine the unknown functions. By taking into account the temporal variable the principle of virtual displacement can be stated as:

$$\int_0^T (\delta U + \delta V - \delta K) dt = 0 \tag{1.3.2}$$

where δU, δV and δK are the virtual strain energy, the virtual work done by externals loads and the virtual kinetic energy, respectively, evaluated in terms of actual stress and virtual strains. Conversely, when ϕ_i represent the stress components, the governing equations are evaluated by applying the principle of virtual forces.

The simplest among the equivalent single layer plate theories is the *Classical laminated plate theory* ($CLPT$), which is derived directly from the Kirchhoff plate theory and basically neglects transverse shear and normal effects. In this way, the deformation is considered to be due only

to bending and in–plane stretching. On the other hand, an extended theory is the *First order shear deformation theory* ($FSDT$). The transverse shear deformation is accounted in the kinematics assumptions, and the transverse shear strain is assumed to be constant along the plate thickness. However, both theories, $CLPT$ and $FSDT$, are developed in a plane stress state.

When the hypothesis of inexstensibility and strainghtness of transverse normals are removed, the second– and high–order plate theories are obtained. However, the $FSDT$ appears to be the best in terms of accuracy of the solution and required computational costs.

1.3.1 The classical laminated plate theory

The $CLPT$ is an extension of the Kirchhoff classical plate theory to laminated plates, which are composed by several composite laminae bonded together to reach the required thickness. Basically, the in–plane displacements are assumed to be linear across the thickness, whereas the transverse to be constant. This theory leads to reliable results when the thickness of the laminate is about two order of magnitude smaller than the others two dimensions.

The Kirchhoff–Love assumptions adopted to develop the model hold also in case of laminated plates. These hypothesis essentially concern the straight lines perpendicular to the mid–plane before deformations, i.e. the transverse normals. In particular, the assumptions can be stated, according to [6, 17], as:

- the transverse normals remain straight after deformation;
- the transverse normals are inextensible;
- the transverse normals stay perpendicular to the mid–surface after deformation.

As a consequence, the transverse shear ϵ_{xz}, ϵ_{yz} and normal strain ϵ_{zz} are neglected. This implies also the omission of σ_{zz}, since the product of

ϵ_{zz} and σ_{zz} vanishes in the total potential energy functional of the plate. Moreover, also σ_{xz} and σ_{yz} are neglected. Therefore, in the $CLPT$ the transverse deformation and stress state are not accounted, and the plate is considered to be infinitely rigid in the transverse dimension. This issue may not be truly representative of the real behavior of composites, for this reason these assumptions are considered to be valid only for thin plates.

1.3.1.1 Displacements and strains

The composite plate here considered is composed by N orthotropic layers and its thickness is h. The principal material coordinates (x_1^k, x_2^k, x_3^k) of each k–th lamina are rotated of an angle θ_k with respect to the laminate coordinate x, and the (x, y) plane corresponds to the undeformed mid–plane of the laminate, Ω_0. The total domain $\bar{\Omega}_0$ is obtained by doing the following tensor product $\Omega_0 \otimes (-h/2, h/2)$, the boundaries are the top surface $S_t(z = -h/2)$ and the bottom surface $S_b(z = h/2)$, and the edge $\bar{\Gamma}$ is the $\Gamma \otimes (-h/2, h/2)$ tensor product. In general, Γ is a curved surface with outward normal $\hat{\boldsymbol{n}} = n_x \hat{\boldsymbol{e}}_x + n_y \hat{\boldsymbol{e}}_y$ and is subjected to both generalized forces and displacement. It is then assumed that:

- the layer are perfectly bonded;
- each layer is made by a linear elastic orthotropic material;
- each layer is of uniform thickness;
- the strain and displacement are small;
- the transverse shear stresses on the boundaries surfaces are zero.

A point P of coordinates (x, y, z) in the undeformed state, moves to the position $(x + u_1, y + u_2, z + u_3)$ after deformation, where (u_1, u_2, u_3) are the component of the total displacement vector $\boldsymbol{u}$

$$\boldsymbol{u} = u_1 \hat{\boldsymbol{e}}_{\boldsymbol{x}} + u_2 \hat{\boldsymbol{e}}_{\boldsymbol{y}} + u_3 \hat{\boldsymbol{e}}_{\boldsymbol{z}} \tag{1.3.3}$$

and $(\hat{\boldsymbol{e}}_{\boldsymbol{x}}, \hat{\boldsymbol{e}}_{\boldsymbol{y}}, \hat{\boldsymbol{e}}_{\boldsymbol{z}})$ are the unit vector along the (x, y, z) coordinates. According to the Kirchhoff assumptions the displacements (u_1, u_2, u_3) are:

$$\begin{aligned} u_1(x, y, z, t) &= u(x, y, t) + z\psi_1(x, y, t) \\ u_2(x, y, z, t) &= v(x, y, t) + z\psi_2(x, y, t) \\ u_3(x, y, z, t) &= w(x, y, t) \end{aligned} \tag{1.3.4}$$

where (u, v, w) are the displacements of a material point on the laminate mid–plane, ψ_1 and ψ_2 are the rotation of a transverse normal about the y– and x–axis, respectively, and t represents the time. From the third of the Kirchhoff assumptions is also obtained that:

$$\begin{aligned} \psi_1 &= -\frac{\partial w}{\partial x} \\ \psi_2 &= -\frac{\partial w}{\partial y} \end{aligned} \tag{1.3.5}$$

The displacement field of the classical plate theory then becomes, see Fig. 1.4:

$$\begin{aligned} u_1(x, y, z, t) &= u(x, y, t) - z\frac{\partial w}{\partial x} \\ u_2(x, y, z, t) &= v(x, y, t) - z\frac{\partial w}{\partial y} \\ u_3(x, y, z, t) &= w(x, y, t) \end{aligned} \tag{1.3.6}$$

By adopting the equivalent single–layer theory, it is worth noting that strains are assumed to be continuous along the laminate thickness, also through interfaces between layers of different material, and this assumption does not allow to represent adequately the interlaminar stresses. The strains associated to the displacement field expressed by Eq. (1.3.6), can be evaluated accounting also the nonlinear strains and with the aid of

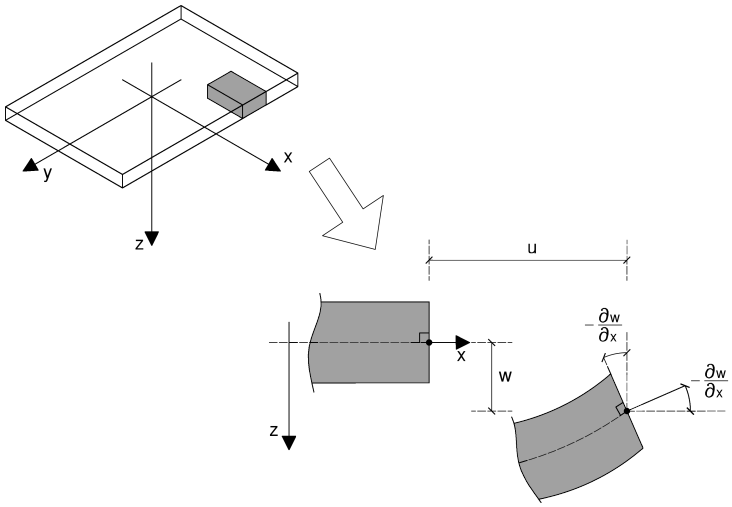

Figure 1.4: Assumed deformation according to the CLPT

the following strain–displacement relations:

$$\begin{aligned}
\epsilon_{xx} &= \frac{\partial u_1}{\partial x} + \frac{1}{2}\left[\left(\frac{\partial u_1}{\partial x}\right)^2 + \left(\frac{\partial u_2}{\partial x}\right)^2 + \left(\frac{\partial u_3}{\partial x}\right)^2\right] \\
\epsilon_{yy} &= \frac{\partial u_2}{\partial y} + \frac{1}{2}\left[\left(\frac{\partial u_1}{\partial y}\right)^2 + \left(\frac{\partial u_2}{\partial y}\right)^2 + \left(\frac{\partial u_3}{\partial y}\right)^2\right] \\
\epsilon_{zz} &= \frac{\partial u_3}{\partial z} + \frac{1}{2}\left[\left(\frac{\partial u_1}{\partial z}\right)^2 + \left(\frac{\partial u_2}{\partial z}\right)^2 + \left(\frac{\partial u_3}{\partial z}\right)^2\right]
\end{aligned} \tag{1.3.7}$$

$$\begin{aligned}
\epsilon_{xy} &= \frac{1}{2}\left(\frac{\partial u_1}{\partial y} + \frac{\partial u_2}{\partial x} + \frac{\partial u_1}{\partial x}\frac{\partial u_1}{\partial y} + \frac{\partial u_2}{\partial x}\frac{\partial u_2}{\partial y} + \frac{\partial u_3}{\partial x}\frac{\partial u_3}{\partial y}\right) \\
\epsilon_{xz} &= \frac{1}{2}\left(\frac{\partial u_1}{\partial z} + \frac{\partial u_3}{\partial x} + \frac{\partial u_1}{\partial x}\frac{\partial u_1}{\partial z} + \frac{\partial u_2}{\partial x}\frac{\partial u_2}{\partial z} + \frac{\partial u_3}{\partial x}\frac{\partial u_3}{\partial z}\right) \\
\epsilon_{yz} &= \frac{1}{2}\left(\frac{\partial u_2}{\partial z} + \frac{\partial u_3}{\partial y} + \frac{\partial u_1}{\partial y}\frac{\partial u_1}{\partial z} + \frac{\partial u_2}{\partial y}\frac{\partial u_2}{\partial z} + \frac{\partial u_3}{\partial y}\frac{\partial u_3}{\partial z}\right)
\end{aligned} \tag{1.3.8}$$

In the hypothesis of small strains, the terms of second order can be neglected, except those associated with the rotations of transverse

normals, $\partial u_3/\partial x$ and $\partial u_3/\partial y$, if they are around $10° - 15°$. Therefore, Eqs. (1.3.7) and (1.3.8), reduce to:

$$\begin{aligned}
\epsilon_{xx} &= \frac{\partial u_1}{\partial x} + \frac{1}{2}\left(\frac{\partial u_3}{\partial x}\right)^2, \quad \epsilon_{xy} = \frac{1}{2}\left(\frac{\partial u_1}{\partial y} + \frac{\partial u_2}{\partial x} + \frac{\partial u_3}{\partial x}\frac{\partial u_3}{\partial y}\right), \\
\epsilon_{yy} &= \frac{\partial u_2}{\partial y} + \frac{1}{2}\left(\frac{\partial u_3}{\partial y}\right)^2, \quad \epsilon_{xz} = \frac{1}{2}\left(\frac{\partial u_1}{\partial z} + \frac{\partial u_3}{\partial x} + \frac{\partial u_3}{\partial x}\frac{\partial u_3}{\partial z}\right), \\
\epsilon_{zz} &= \frac{\partial u_3}{\partial z}, \qquad \epsilon_{yz} = \frac{1}{2}\left(\frac{\partial u_2}{\partial z} + \frac{\partial u_3}{\partial y} + \frac{\partial u_3}{\partial y}\frac{\partial u_3}{\partial z}\right)
\end{aligned} \tag{1.3.9}$$

the latter are called the *von Kármán strains*. By substituting Eq. (1.3.6) into Eq. (1.3.9), we get:

$$\begin{aligned}
\epsilon_1 \equiv \epsilon_{xx} &= \frac{\partial u}{\partial x} + \frac{1}{2}\left(\frac{\partial w}{\partial x}\right)^2 - z\frac{\partial^2 w}{\partial x^2} \\
\epsilon_2 \equiv \epsilon_{yy} &= \frac{\partial v}{\partial y} + \frac{1}{2}\left(\frac{\partial w}{\partial y}\right)^2 - z\frac{\partial^2 w}{\partial y^2} \\
\epsilon_6 \equiv 2\epsilon_{xy} &= \left(\frac{\partial u}{\partial y} + \frac{\partial v}{\partial x} + \frac{\partial w}{\partial x}\frac{\partial w}{\partial y}\right) - 2z\frac{\partial^2 w}{\partial x \partial y} \\
\epsilon_4 \equiv 2\epsilon_{yz} &= -\frac{\partial w}{\partial y} + \frac{\partial w}{\partial y} = 0 \\
\epsilon_5 \equiv 2\epsilon_{xz} &= -\frac{\partial w}{\partial x} + \frac{\partial w}{\partial x} = 0 \\
\epsilon_3 \equiv \epsilon_{zz} &= \frac{\partial w}{\partial z} = 0
\end{aligned} \tag{1.3.10}$$

In addition, the achieved strains can be set in the following form:

$$\epsilon_i = \epsilon_i^0 + z\epsilon_i^1, \quad i = 1, 2, 6 \tag{1.3.11}$$

In particular, ϵ_i^0 are the *membrane strains* associated with the stretching and in–plane shearing of the mid–plane, whereas ϵ_i^1 are the *curvatures* related to the flexural strains, [6, 17]. How it could be seen, strains vary linearly along the laminate thickness, not depending by each lamina material. Moreover, for a fixed z, the strain components are nonlinear functions of x and y, together with the time t in the dynamical problems.

1.3.1.2 Governing equations

The equations governing the problem may be evaluated either by using variational principles or by applying the Newton's law. The former allows to derive the equation of equilibrium, or the equation of motion in dynamics analysis, with the proper boundary conditions by either minimizing the total potential energy or by maximizing the total complementary energy. The latter leads to the equilibrium equations through equilibrium considerations on a representative volume element subjected to external forces and couples.

In the framework of the energy principles, the principle of virtual displacement states that for a body in equilibrium, the total virtual work done by all externals and reacting forces through their compatibles virtual displacement is equal to zero. The total virtual work is the sum of the internal and the external virtual work. Therefore, by evaluating the virtual strain energy δU and the virtual work done by externals loads δV for no time–dependent problem, by applying the fundamental lemma of variational calculus, and after some manipulations, [6], the following equations are obtained:

$$\begin{aligned} &\frac{\partial N_1}{\partial x} + \frac{\partial N_6}{\partial y} = 0 \\ &\frac{\partial N_6}{\partial x} + \frac{\partial N_2}{\partial y} = 0 \\ &\frac{\partial^2 M_1}{\partial x^2} + 2\frac{\partial^2 M_6}{\partial y \partial x} + \frac{\partial^2 M_2}{\partial y^2} + N(w) + q = 0 \end{aligned} \tag{1.3.12}$$

where

$$N(w) = \frac{\partial}{\partial x}\left(N_1 \frac{\partial w}{\partial x} + N_6 \frac{\partial w}{\partial y}\right) + \frac{\partial}{\partial y}\left(N_6 \frac{\partial w}{\partial x} + N_2 \frac{\partial w}{\partial y}\right) \tag{1.3.13}$$

and q are the distributed transverse loads, N_i the *force resultants* and M_i the *moments resultants*, Fig. 1.5

$$\begin{Bmatrix} N_1 \\ N_2 \\ N_6 \end{Bmatrix} = \int_{-h/2}^{h/2} \begin{Bmatrix} \sigma_1 \\ \sigma_2 \\ \sigma_6 \end{Bmatrix} dz$$
$$\begin{Bmatrix} M_1 \\ M_2 \\ M_6 \end{Bmatrix} = \int_{-h/2}^{h/2} z \begin{Bmatrix} \sigma_1 \\ \sigma_2 \\ \sigma_6 \end{Bmatrix} dz \tag{1.3.14}$$

Below, essential and natural boundary conditions for the $CLPT$ are reported:

$$\begin{aligned} u_n, \quad u_{ns}, \quad w, \quad \frac{\partial w}{\partial n} \quad & \textbf{(essential)} \\ N_n, \quad N_{ns}, \quad \hat{Q}_n, \quad M_n \quad & \textbf{(natural)} \end{aligned} \tag{1.3.15}$$

where

$$\begin{aligned} u_n &= un_x + vn_y \\ u_{ns} &= -un_y + vn_x \\ \frac{\partial w}{\partial n} &= \frac{\partial w}{\partial x} n_x + \frac{\partial w}{\partial y} n_y \end{aligned} \tag{1.3.16}$$

and

$$\begin{aligned} N_n &= N_1 n_x^2 + N_2 n_y^2 + 2N_6 n_x n_y \\ N_{ns} &= (N_2 - N_1) n_x n_y + N_6 (n_x^2 - n_y^2) \\ M_n &= M_1 n_x^2 + M_2 n_y^2 + 2M_6 n_x n_y \\ M_{ns} &= (M_2 - M_1) n_x n_y + M_6 (n_x^2 - n_y^2) \\ \hat{Q}_n &= Q_1 n_x + Q_2 n_y - \frac{\partial M_{ns}}{\partial s} \end{aligned} \tag{1.3.17}$$

wherein n_x and n_y are the direction cosines of the unit normal to the plate boundaries, and Q_1 and Q_2 are the transverse shear forces.

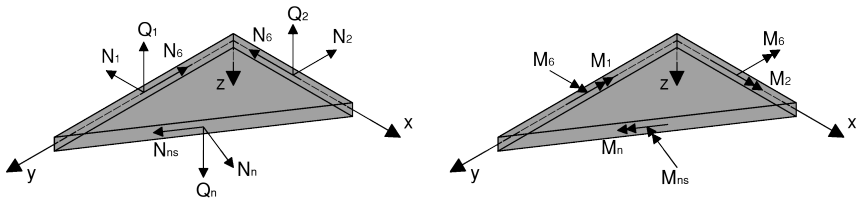

Figure 1.5: Forces and moments resultants on a laminate edge

1.3.1.3 Laminate constitutive relations

The laminate constitutive relations aim to relate resultant forces and moments with laminate's strains. Each layer is assumed to be orthotropic with respect to its material symmetry axis, and obeys to Eq. (1.2.16). Although one of the principal assumption of the *CLPT* concerns the continuity of strains along the whole plate thickness, this issue is not true for stresses. Therefore, by expressing stresses into Eq. (1.3.14) in terms of strains and with respect to the laminate coordinates, after integration along the z–axis, the forces and moments resultants can be expressed as:

$$\begin{Bmatrix} N_1 \\ N_2 \\ N_6 \end{Bmatrix} = \begin{bmatrix} A_{11} & A_{12} & A_{16} \\ A_{12} & A_{22} & A_{26} \\ A_{16} & A_{26} & A_{66} \end{bmatrix} \begin{Bmatrix} \epsilon_1^0 \\ \epsilon_2^0 \\ \epsilon_6^0 \end{Bmatrix} + \begin{bmatrix} B_{11} & B_{12} & B_{16} \\ B_{12} & B_{22} & B_{26} \\ B_{16} & B_{26} & B_{66} \end{bmatrix} \begin{Bmatrix} \epsilon_1^1 \\ \epsilon_2^1 \\ \epsilon_6^1 \end{Bmatrix} \tag{1.3.18}$$

$$\begin{Bmatrix} M_1 \\ M_2 \\ M_6 \end{Bmatrix} = \begin{bmatrix} B_{11} & B_{12} & B_{16} \\ B_{12} & B_{22} & B_{26} \\ B_{16} & B_{26} & B_{66} \end{bmatrix} \begin{Bmatrix} \epsilon_1^0 \\ \epsilon_2^0 \\ \epsilon_6^0 \end{Bmatrix} + \begin{bmatrix} D_{11} & D_{12} & D_{16} \\ D_{12} & D_{22} & D_{26} \\ D_{16} & D_{26} & D_{66} \end{bmatrix} \begin{Bmatrix} \epsilon_1^1 \\ \epsilon_2^1 \\ \epsilon_6^1 \end{Bmatrix} \tag{1.3.19}$$

where A_{ij} are the *extensional stiffnesses*, D_{ij} the *bending stiffnesses* and B_{ij} the *bending–extensional coupling stiffnesses* of the laminate, [6, 17]. The stiffness coefficients may be also defined in terms of the material stiffness of each k–th lamina in the following manner:

$$(A_{ij}, B_{ij}, D_{ij}) = \sum_{k=1}^{N} \int_{z_k}^{z_{k+1}} Q_{ij}^k (1, z, z^2) dz \tag{1.3.20}$$

where Q_{ij}^k are referred to the laminate coordinates, N is the layers' number and (z_k, z_{k+1}) are the bottom and the top k–th lamina coordinate, respectively. Being the latter constant through each layer, Eq. (1.3.20) can be easily integrated, which gives:

$$\begin{aligned} A_{ij} &= \sum_{k=1}^{N} Q_{ij}^k (z_{k+1} - z_k) \\ B_{ij} &= \frac{1}{2} \sum_{k=1}^{N} Q_{ij}^k (z_{k+1}^2 - z_k^2) \\ D_{ij} &= \frac{1}{3} \sum_{k=1}^{N} Q_{ij}^k (z_{k+1}^3 - z_k^3) \end{aligned} \tag{1.3.21}$$

In order to express the equilibrium equations (1.3.12) in terms of displacements, the first step is the substitution of Eqs. (1.3.10) and (1.3.11) into Eqs. (1.3.18) and (1.3.19), the second one, the introduction of the resulting force and moments resultants into the equilibrium equations (1.3.12). The full set of equations is reported by Reddy, [6].

1.3.2 First–order shear deformation theory

The *FSDT* is a displacement based theory in which the displacement components are expanded as a linear combination of the thickness coordinate and unknowns functions of position in the reference surface, [17]. The equations of equilibrium can be then derived by employing either the principle of virtual work or the free body diagram. In addition, being the *FSDT* part of the equivalent single–layer plate theories group, the displacements and the strains are still supposed to be continuous along thickness, whereas the interlaminar stress field is discontinuous due to the difference of the elastic coefficients at the interface between layers.

The *FSDT*, known as Mindlin plate theory, is therefore one among the theories who accounts the transverse shear deformation, and gives a constant transverse shear strain along the plate thickness. This issue contrasts with the actual distribution, which is of quadratic or higher–

order and, for this reason, it is necessary to adopt a shear correction factor, which depends on the laminate geometry and on the boundary conditions, [6].

1.3.2.1 Displacements and strains

In the $FSDT$ the third assumptions considered in the $CLPT$ is removed, that is the transverses lines normal to the mid–plane laminate does not remain perpendicular after deformation, Fig. 1.6. This issue imply the accounting of the shear strains and that the rotations ψ_1 and ψ_2 of a transverse normal do not depend by $\partial w/\partial x$ and $\partial w/\partial y$.

According to the same Kirchhoff assumptions adopted in the $CLPT$, the displacements field can be expressed as:

$$\begin{aligned} u_1(x,y,z,t) &= u(x,y,t) + z\psi_1(x,y,t) \\ u_2(x,y,z,t) &= v(x,y,t) + z\psi_2(x,y,t) \\ u_3(x,y,z,t) &= w(x,y,t) \end{aligned} \tag{1.3.22}$$

where the symbols notation is the same adopted in Eq. (1.3.4).

Taking into account the nonlinear strains, the strain–displacement

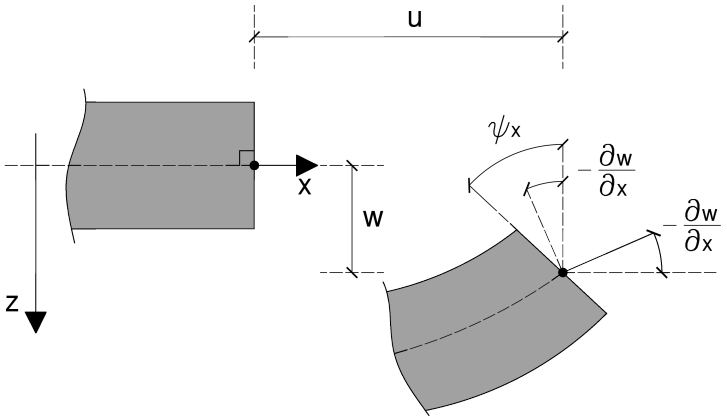

Figure 1.6: Assumed deformation according to the FSDT

relations are given by:

$$\epsilon_i = \epsilon_i^0 + z\epsilon_i^1, \quad i = 1, 2, 6, 4, 5 \tag{1.3.23}$$

where

$$\begin{aligned}
\epsilon_1 &= \frac{\partial u}{\partial x} + \frac{1}{2}\left(\frac{\partial w}{\partial x}\right)^2 - z\frac{\partial \psi_1}{\partial x} \\
\epsilon_2 &= \frac{\partial v}{\partial y} + \frac{1}{2}\left(\frac{\partial w}{\partial y}\right)^2 - z\frac{\partial \psi_2}{\partial y} \\
\epsilon_6 &= \left(\frac{\partial u}{\partial y} + \frac{\partial v}{\partial x} + \frac{\partial w}{\partial x}\frac{\partial w}{\partial y}\right) - z\left(\frac{\partial \psi_1}{\partial y} + \frac{\partial \psi_2}{\partial x}\right) \\
\epsilon_4 &= \frac{\partial w}{\partial y} + \psi_2 \\
\epsilon_5 &= \frac{\partial w}{\partial x} + \psi_1 \\
\epsilon_3 &= 0
\end{aligned} \tag{1.3.24}$$

From Eq. (1.3.24) it is possible to see that the strains $(\epsilon_1, \epsilon_2, \epsilon_6)$ are linear along the thickness, whereas the strains (ϵ_4, ϵ_5) are constants.

1.3.2.2 Governing equations

The equilibrium equations of the $FSDT$, derived from the principle of virtual displacements are, [17]:

$$\begin{aligned}
&\frac{\partial N_1}{\partial x} + \frac{\partial N_6}{\partial y} = 0 \\
&\frac{\partial N_6}{\partial x} + \frac{\partial N_2}{\partial y} = 0 \\
&\frac{\partial Q_1}{\partial x} + \frac{\partial Q_2}{\partial y} + N(w) + q = 0 \\
&\frac{\partial M_1}{\partial x} + \frac{\partial M_6}{\partial y} - Q_1 = 0 \\
&\frac{\partial M_6}{\partial x} + \frac{\partial M_2}{\partial y} - Q_2 = 0
\end{aligned} \tag{1.3.25}$$

where

$$Q_1 = \int_{-h/2}^{h/2} \sigma_5 dz$$
$$Q_2 = \int_{-h/2}^{h/2} \sigma_4 dz \tag{1.3.26}$$

and $N(w)$,N_i and M_i are defined in Eqs. (1.3.13) and (1.3.14). The boundary conditions are in the same form as Eqs. (1.3.16) and (1.3.17), in which the primary and secondary variables are:

$$\begin{aligned} &u_n, \quad u_{ns}, \quad w, \quad \psi_n, \quad \psi_{ns} \quad \textbf{(essential)} \\ &N_n, \quad N_{ns}, \quad Q_n, \quad M_n \quad M_{ns} \quad \textbf{(natural)} \end{aligned} \tag{1.3.27}$$

1.3.2.3 Laminate constitutive equations

The laminate constitutive relations in the *FSDT* are composed by Eqs. (1.3.18) and by

$$\begin{Bmatrix} Q_1 \\ Q_2 \end{Bmatrix} = \begin{bmatrix} A_{55} & A_{45} \\ A_{45} & A_{44} \end{bmatrix} \begin{Bmatrix} \epsilon_5^0 \\ \epsilon_4^0 \end{Bmatrix} \tag{1.3.28}$$

where

$$A_{ij} = K_{ij} \int_{-h/2}^{h/2} Q_{ij}^k dz = K_{ij} \sum_{k=1}^{N} Q_{ij}^k (z_{k+1} - z_k), \quad (i,j = 4,5) \tag{1.3.29}$$

and K_{ij} are the *shear correction coefficients*.

The equilibrium equations can be therefore expressed in terms of displacements by substituting into Eq. (1.3.25) the forces and moments resultants (1.3.18),(1.3.19) and (1.3.28). For the complete set of the achieved equilibrium equations please see [6, 17].

1.3.3 Layerwise theory

The layerwise theory, proposed by Reddy [17], owns to the category of three–dimension elasticity theories. A 3D analysis may be necessary in case of composite materials characterized by embedded delamination, free edges or regions where the plane stress state assumption is no longer valid.

In particular, the layerwise theory is based on the displacement expansion across the thickness of the laminate. Each layers can be either mathematical or physicals, being therefore possible to couple more layers into a sublaminate.

1.3.3.1 Displacements and strains

In the layerwise theory, displacements are expanded through the thickness of the composite laminate in the following way:

$$u_i(x,y,z) = \sum_{j=1}^{N} U_i^J(x,y)\Phi^J(z) = U_i^J(x,y)\Phi^J(z), \quad i = 1,2,3 \quad (1.3.30)$$

where J and N denote the interface and the finite elements node number considered along the laminate thickness, respectively. (U^J, V^J, Z^J) are the nodal values of (u, v, w). $\Phi^J(z)$ are known functions, namely the *global interpolation functions*, defined in terms of the Lagrange interpolation functions linked to the layers separated by the J–th interface. As a consequence of the local definition of the $\Psi^J(z)$ functions, the displacements are continuous across the thickness, as is not for their derivative with respect to z, thus the transverse strains, which are discontinuous at the interface. For this reason, the interlaminar transverse stresses obtained by applying the layer constitutive relations can be continuous. On the contrary, the in–plane strains $(\epsilon_x, \epsilon_y, \epsilon_{xy})$ are continuous, whereas the in–plane stresses $(\sigma_x, \sigma_y, \sigma_{xy})$ are discontinuous at the interface owing to the different properties of the layers in contact. The layerwise theory is therefore characterized by $3N$ variables and $3N$ two–dimensional dif-

ferential equations. However, the obtained model can be represented by using just $2D$ finite elements. The number of elements in which the laminate is subdivided, N, influences the accuracy of the solution in terms of stress distribution. If for each physical layer at least one element is used, an accurate solution is achieved, [17]. In addition, it can be easily demonstrate as the single layer plate theories are a special case of the layerwise theory.

Considering a laminate of thickness h, the strain–displacement relations accounting non–linearity can be obtained by substituting Eq. (1.3.30) into Eq. (1.3.9), which leads to:

$$\begin{aligned}
\epsilon_1 \equiv \epsilon_{xx} &= \frac{\partial U^J}{\partial x}\Phi^J + \frac{1}{2}\left(\frac{\partial W^J}{\partial x}\Phi^J\right)\left(\frac{\partial W^J}{\partial x}\Phi^J\right) \\
\epsilon_2 \equiv \epsilon_{yy} &= \frac{\partial V^J}{\partial y}\Phi^J + \frac{1}{2}\left(\frac{\partial W^J}{\partial y}\Phi^J\right)\left(\frac{\partial W^J}{\partial y}\Phi^J\right) \\
\epsilon_3 \equiv \epsilon_{zz} &= W^J\frac{d\Phi^J}{dz} \\
\epsilon_4 \equiv 2\epsilon_{yz} &= V^J\frac{d\Phi^J}{dz} + \frac{\partial W^J}{\partial y}\Phi^J \\
\epsilon_5 \equiv 2\epsilon_{xz} &= U^J\frac{d\Phi^J}{dz} + \frac{\partial W^J}{\partial x}\Phi^J \\
\epsilon_6 \equiv 2\epsilon_{xy} &= \left(\frac{\partial U^J}{\partial y} + \frac{\partial V^J}{\partial x}\right)\Phi^J + \left(\frac{\partial W^J}{\partial x}\Phi^J\right)\left(\frac{\partial W^J}{\partial y}\Phi^J\right)
\end{aligned} \tag{1.3.31}$$

1.3.3.2 Governing equations

The principle of virtual displacement allows to obtain the equilibrium equations, which can be expressed as follows, [17]:

$$\begin{aligned}
&\frac{\partial M_1^I}{\partial x} + \frac{\partial M_6^I}{\partial y} - Q_1^I = 0, \quad I = 1, 2, ..., N \\
&\frac{\partial M_6^I}{\partial x} + \frac{\partial M_2^I}{\partial y} - Q_2^I = 0, \\
&\frac{\partial K_1^I}{\partial x} + \frac{\partial K_2^I}{\partial y} - Q_3^I + N^I(W^J) = 0
\end{aligned} \tag{1.3.32}$$

where

$$N^I(W^J) = \frac{\partial}{\partial x}\left(S_1^{IJ}\frac{\partial W^J}{\partial x} + S_6^{IJ}\frac{\partial W^J}{\partial y}\right) + \\ + \frac{\partial}{\partial y}\left(S_6^{IJ}\frac{\partial W^J}{\partial x} + S_2^{IJ}\frac{\partial W^J}{\partial y}\right) \tag{1.3.33}$$

and the forces and moments resultants are

$$\begin{aligned} M_i^I &= \int_{-h/2}^{h/2} \sigma_i \Phi^J(z) dz, \\ S_i^{IJ} &= \int_{-h/2}^{h/2} \sigma_i \Phi^I(z)\Phi^J(z) dz, \quad i = 1, 2, 6 \\ Q_1^I &= \int_{-h/2}^{h/2} \sigma_5 \frac{d\Phi^J}{dz} dz, \quad Q_2^I = \int_{-h/2}^{h/2} \sigma_4 \frac{d\Phi^J}{dz} dz, \\ Q_3^I &= \int_{-h/2}^{h/2} \sigma_3 \frac{d\Phi^J}{dz} dz, \\ K_1^I &= \int_{-h/2}^{h/2} \sigma_5 \Phi^J dz, \quad K_2^I = \int_{-h/2}^{h/2} \sigma_4 \Phi^J dz \end{aligned} \tag{1.3.34}$$

By using the layer constitutive equations and the strain–displacements relations (1.3.31), the resultants $(M_i^I, S_i^{IJ}, Q_i^I, K_i^I)$ can be expressed also in terms of interface displacements functions U_i^J.

1.3.4 Linear and nonlinear interface models

Several interface models aimed to describe the zone existing between two adjacent layers were proposed in the literature. In particular, the interface can be represented as a layer of zero thickness placed between two adjacent plies, Fig. 1.7. By properly defining a constitutive law, it is possible to relate the interlaminar stresses $\sigma = \{\sigma_{zx}, \sigma_{zy}, \sigma_{zz}\}^T$ with the displacements discontinuities between the two layers, $\mathbf{\Delta} = \{\Delta u, \Delta v, \Delta z\}^T$, in the x, y and z direction, respectively. This displacements' jump may be expressed as $\Delta u = u^+ - u^-$, $\Delta v = v^+ - v^-$, $\Delta w = w^+ - w^-$, where $+$ and $-$ denote the lower and the upper layer, respectively.

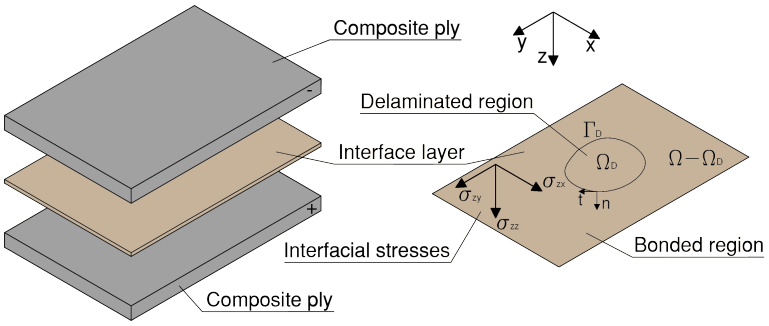

Figure 1.7: Interface layer between adjacent composite layers

Once that the critical strength of the interface is reached, an opening displacement $\mathbf{\Delta o}$ occurs. However, along a certain area, it may be still possible to transfer the interlaminar stresses, which decrease with the opening or the sliding relative displacement up to a critical value $\mathbf{\Delta c}$. When $\mathbf{\Delta c}$ is reached, delamination occurs and the layers are completely separated, [18]. Such a damaging interface falls into the category of the cohesive crack models, which are deeply examined by Bažant & Planas [19]. This damage process is also called *debonding* and will be further treated in Chapter 2.

According to Corigliano [20], through the definition of a linear or a non linear *interface constitutive law*, it is therefore possible to model the softening behavior of the interface strength until that complete debonding occurs. The anisotropy of the response, the presence of irreversible displacements, and the difference in tensile and compressive behavior in the direction normal to the crack face, can be also taken into account. In view of a finite element analysis, others advantages were reported by Bui et al. [21] when the interface is represented by a thin layer element with vanishing thickness. By using the interface elements, it is in fact possible to estimate the interlaminar stresses at the interface itself, which has zero thickness, avoiding to extract the stresses from extrapolation or averaging procedure through internal integration points. In addition, interlaminar stresses across the interface are always continuous and can

be evaluated from equilibrium equations. The traction–free condition on boundaries can also be recovered by applying appropriate constraints to the involved nodal displacements. Moreover, the interlaminar stresses can be evaluated at different stages of the delamination process. In fact, as stated also by Rabinovitch [22], the adoption of such a damage interface allows to cover the interface behavior from the perfect bonded state to the complete delamination. However, face the possibility to predict the crack initiation, these methods require very high computational costs.

In the below Figures 1.8, 1.9 and 1.10, some interface models proposed in the literature are illustrated. In particular, the dotted area denotes the specific elastic energy stored at the beginning of the damaging process, [23]

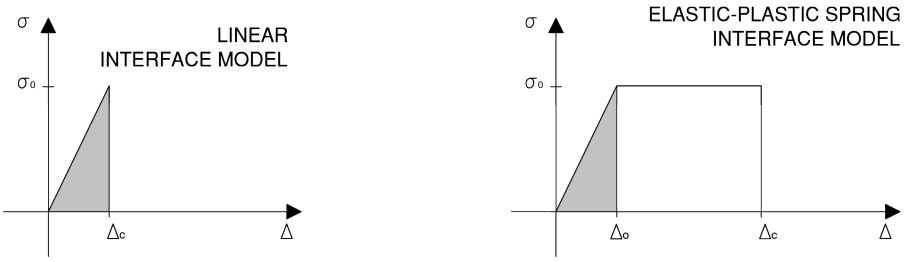

Figure 1.8: Linear elastic [24] and elastic plastic spring interface models [25]

The *linear elastic interface model* presented in Fig. 1.8, can be characterized, according to Bruno et al. [24], by the following simple constitutive law valid in the undelaminated region:

$$\sigma_{zx} = k_{zx}\Delta u, \quad \sigma_{zy} = k_{zy}\Delta v, \quad \sigma_{zz} = k_{zz}\Delta w \tag{1.3.35}$$

where (k_{zx}, k_{zy}, k_{zz}) represent the interface stiffness treated as penalty parameters. In addition, with the aim to avoid interpenetration between the two adjacent delaminated layers, Bruno et al. [24] adopted an unilateral frictional contact interface model. In particular, by the intro-

duction of a damage variable d, in case of opening relative displacement $\Delta w \geq 0$, a zero stiffness is considered, whereas in case of closing relative displacement $\Delta w < 0$, a positive stiffness is used. Therefore, the following constitutive law, valid in both, the bonded and the debonded region, is introduced, [24]:

$$\begin{aligned} \sigma_{zx} &= (1-d)k_{zx}\Delta u, \\ \sigma_{zy} &= (1-d)k_{zy}\Delta v, \\ \sigma_{zz} &= \left[1 - \frac{1}{2}d(1+sign(\Delta w))\right] k_{zz}\Delta w \end{aligned} \tag{1.3.36}$$

where $d = 0$ denotes perfect adhesion between layer, whereas $d = 1$ the complete delamination. σ_{zz} is the contact stress, k_{zz} the penalty parameter imposing the contact constraint and $sign$ is the signum function. When $d = 1$, σ_{zz} represents the contact stress of such a contact interface, and the contact constraint is guaranteed by a large k_{zz}.

On the right side of Fig. 1.8, the *elastic plastic spring interface model* proposed by Weicheng Cui and Winsnom, [25], is shown. This interface model is characterized by the adoption of non linear spring elements. In the finite element analysis, the interface layer has zero thickness and duplicate nodes are used across the interface itself. Each pair of nodes are then connected by two independent springs, one vertical and the other horizontal. The vertical spring force is evaluated as the integration of the normal stress acting through the thickness over the element length, whereas the horizontal spring force as the integration of the shear stress acting through the thickness over the element length. Once that a limit spring force value is reached, interlaminar displacement takes place at constant force until a critical displacement, which leads to the springs breakage.

In Fig. 1.9 two non linear interface models proposed by Corigliano in [20] are presented. In the *Elastic damage interface model*, there is a degradation of the elastic stiffness with the damaging growth, and the displacement discontinuities consist only of an elastic and reversible

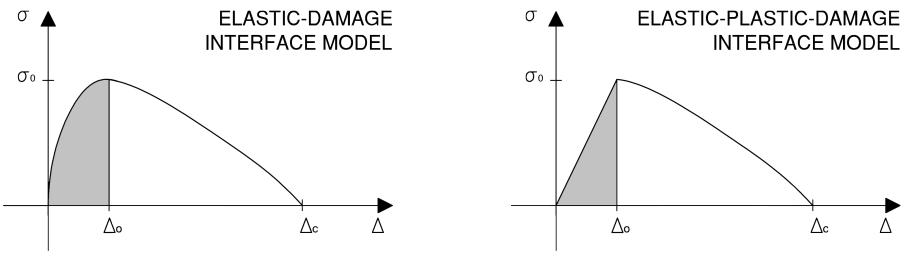

Figure 1.9: Elastic and elastic plastic damage interface models [20]

component. On the contrary, the *Elastic plastic damage interface model* is characterized by both reversible and irreversible plastic displacement discontinuities. However, in both models the behavior in case of compression at the interface is always elastic and with constant stiffness. Constitutive relations and damage evolution laws can be found in [20].

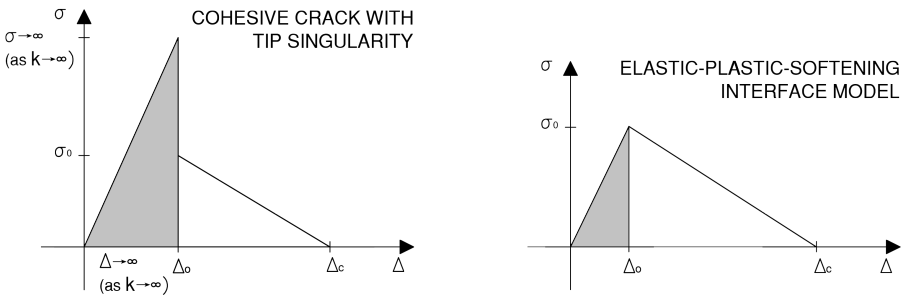

Figure 1.10: Cohesive interface model with stress singularity [19, 26] and elastic plastic softening interface model [20]

In the left side of Fig. 1.10, a *Cohesive interface model with stress singularity* is shown. This model essentially takes into account the presence of stress singularity at the crack tip, which is followed by a softening branch. For example, Greco et al. [26] adopted such a model to account bridging stresses acting at the crack faces. In particular, the fiber bridging consists in the exertion of a force across the width of a crack caused by the fibers pulling from one side of the delamination plane to the other, [27]. As a result, the achieved fracture toughness is higher than those obtained when delamination occurs only along the matrix of

the composite.

Therefore, in [26], the authors used a penalized linear interface model where perfect adhesion holds, with the strain energy of the linear interface acting as the penalty functional. Hence, as the penalty parameters go to infinity, the stresses become singulars. In the framework of a two–dimensional analysis, the bridging mechanism was therefore modeled by a non–linear interface in which the interlaminar stresses depend on the jump displacements in the following manner:

$$\sigma = f(\boldsymbol{\Delta}) \tag{1.3.37}$$

where the relation between a potential, function of the interfacial displacements, and the normal and the shear stresses is

$$\sigma = \frac{\partial U(\boldsymbol{\Delta})}{\partial \boldsymbol{\Delta}}, \quad U(\mathbf{0}) = 0 \tag{1.3.38}$$

In particular, the linear softening law adopted by Greco et al. can be expressed as:

$$\begin{cases} \sigma_{zx} & = \sigma^0_{zx} \frac{\Delta u}{|\Delta u|} - \frac{\sigma^0_{zx}}{\Delta u_c} \Delta u, \quad if \quad \mid \Delta u \mid \leq \Delta u_0, \\ \sigma_{zx} & = 0, \quad if \quad \Delta u > \Delta u_0, \end{cases}$$
$$\begin{cases} \sigma_{zz} & = \sigma^0_{zz} - \frac{\sigma^0_{zz}}{\Delta w_c} \Delta w, \quad if \quad \Delta w \leq \Delta w_0, \\ \sigma_{zz} & = 0, \quad if \quad \Delta w > \Delta w_0 \end{cases} \tag{1.3.39}$$

where σ_{zx} and σ_{zz} are the interfacial strengths in the x and z–direction, respectively.

In the right side of Fig. 1.10, the *Elastic plastic softening model* is presented.

As a matter of fact, the softening function depends on the material properties, and it can be derived experimentally by conducting stable tensile tests, [28]. However, these experimental tests shown some inherent difficulties, such as the possible presence of multiple cracks and the

not knowledge of the cohesive crack initial location. To overcome these and others issues, indirect methods based on inverse analysis or data reduction can be applied to determine the softening function, [28]. Anyway, for small cracked and undamaged specimens, the initial slope of the softening curve can be adopted, leading to the above mentioned elastic plastic softening model. It is important to remark, how it was pointed by Elices et al. [28], why it is not considered in this model the presence of a hardening branch after the reaching of the critical stress level. In fact, if the softening branch is preceded by a hardening part, at the point where σ_0 is reached, the stress must increases to allow the crack opening. As a consequence, also the stresses at points in the neighborhood increase, so that within a finite zone around the original crack, an infinite number of others cohesive cracks with infinitely small crack openings forms, leading to a perfectly plastic model.

In the framework of a single Mode delamination analysis, an analytic expression of such a model is reported by Alfano and Crisfield, [23]:

$$\sigma_i = \begin{cases} k_i \Delta_i, & \begin{array}{l} if \;\; (s_i[\Delta_i])_{max} \leq \Delta_{oi} \\ or \;\; (i = 1 \; and \; \Delta_i < 0), \end{array} \\ k_i \Delta_i \left[1 - \left(\dfrac{(s_i[\Delta_i])_{max} - \Delta_{oi}}{(s_i[\Delta_i])_{max}} \right) \left(\dfrac{\Delta_{ci}}{\Delta_{ci} - \Delta_{oi}} \right) \right], & \begin{array}{l} if \;\; \Delta_{oi} < (s_i[\Delta_i])_{max} < \Delta_{ci} \\ or \;\; (i \neq 1 \; or \; \Delta_i \geq 0), \end{array} \\ 0, & \begin{array}{l} if \;\; (s_i[\Delta_i])_{max} \geq \Delta_{ci} \\ and \; (i \neq 1 \; or \; \Delta_i \geq 0) \end{array} \end{cases} \tag{1.3.40}$$

where $(s_i[\Delta_i])_{max}$ is the maximum value assumed by $s_i[\Delta_i]$ in a particular instant $\tau \epsilon [0, T]$

$$(s_i[\Delta_i])_{max} = \max_{0 \leq \tau' \leq \tau} (s_i[\Delta_i(\tau')]) \tag{1.3.41}$$

and k_i are the penalty stiffness parameters. Moreover, when Mode I of fracture is considered, in order to take into account the different behavior in compression and in tension and to avoid layer interpenetration, the

following notation is adopted:

$$(s_i[x]) = \begin{cases} < x > & if\ i = 1, \\ |x| & if\ i = 2 \end{cases} \tag{1.3.42}$$

where $< >$ are the Mc Cauley brackets:

$$< x >= \begin{cases} x & if\ x \geq 0, \\ 0 & if\ x \leq 0 \end{cases} \tag{1.3.43}$$

For a pure Mode II delamination, a cohesive bilinear law was proposed by De Lorenzis et al. [29]. How it was pointed out by the authors, this model allows to estimate the linear elastic properties and the cohesive strength of the interface through the ascending and the softening branch, respectively, together whit the fracture energy, which is represented by the area beneath the curve. However, when the complete delamination occurs for one mode of fracture, complete damage is considered to take place also in the others two modes, [20].

In Fig. 1.11 a qualitative stress distribution in the process zone for the aforementioned model is shown. How it could be seen, the stresses drop linearly from the crack tip to the end of the process zone itself.

Interface models have been therefore widely used to simulate interfacial delamination, both for pure Mode [25, 20, 31] and Mixed Mode [18, 32, 23] delamination.

1.3.5 Coupled interface/multilayer models

Interlaminar delamination is a damage mechanism which frequently affects fiber reinforced composite laminates. This mechanism may be induced by several factors, as the mismatch in the plies properties or between the FRP and a strengthened structure, and as the transverse cracking. In particular, delamination is driven by interlaminar stresses, which may assume high values near the free edges. It is therefore nec-

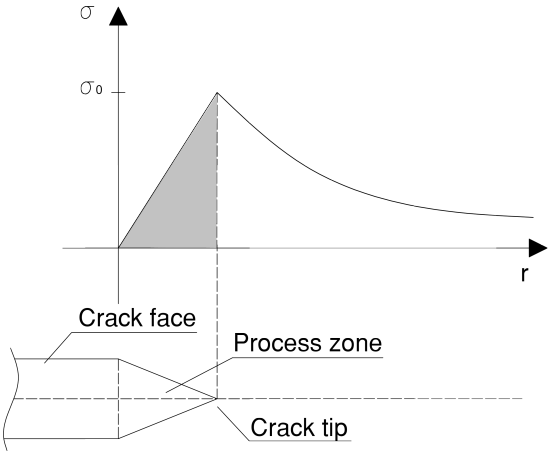

Figure 1.11: Stress distribution in the process zone, [30]

essary to implement a model able not only to describe the composite behavior, but also to represent these interfacial stresses.

In a classic group of models, the laminate composites are modeled as an assembly of two plates in the damaged region and of a single plate in the undamaged one. However, these kind of models do not allow the estimation of the stresses at the interface and consequently of the individual components of the energy release rate. In fact, since at the crack tip and in the undelaminated region there are interfacial forces and moments, both are involved in the total energy release rate expression and may contribute to all modes. For this reason, although the total energy release rate can be accurately estimated, the individual components may be not properly predicted. This represents the main limitation in the analysis of the mixed mode delamination problems, since the interface toughness shows a mixed mode dependency. Moreover, the mismatch of material properties at the interface generates a stress field with an oscillatory singularity at the tip, leading to inadmissible interpenetration of crack surfaces.

To overcome these difficulties, Zou et al. [33] proposed to divide also the undamaged region into sublaminates, which are governed by the

transverse shear deformable laminate theory. The laminate theory allows in fact to eliminate the oscillatory behavior and the stress singularity, which is replaced by a jump in the stress resultants at the crack tip. In addition, interfacial moments are proved to be zero, so that the total energy release rate can be partitioned into individual components. The modal convergence can be then obtained by refining the sublaminated division.

Then, with the aim to study mixed mode delamination problems, a coupled interface and multilayer approach was proposed and numerically applied by Bruno et al. [24], where a composite is modeled in the thickness direction as an assembly of first–order shear deformable laminated plates and coupled with interface elements. Therefore, across the interface two regions can be identified, one where perfect adhesion holds between layers, and the other one where delamination takes place. Such an approach is at an intermediate level between classic delamination and continuum models, which are computationally expensive.

The authors demonstrated also in [34] that an accurate mode partition can be performed in the context of a $3D$ analysis. According to this modeling technique, in the delaminated interface, displacement continuity and contact are modeled by means of a penalty method, whereas in the undelaminated interfaces continuity is enforced by adopting Lagrange's method. However, it is well known that the Lagrangian and the penalty method applied to impose adhesion are equivalents. Therefore, the delamination problem and the evaluation of the energy release rate components may be solved in a local or in a global sense, that is in terms of interlaminar stresses and relative displacements, or in terms of plate stresses and strains, respectively. In particular, the penalty method corresponds to the local approach, which consists in adopting a thin adhesive layer of vanishing thickness, and consequently an infinitely high interface stiffness. On the other hand, the Lagrange method represents a global approach, where the interface assures only the adhesion constraint between layers, and computation of interfacial stresses and

relative displacements is not allowed.

This multi–layer approach based on the $FSDT$, and coupled with the linear elastic interface model, will be deeply studied from theoretical and numerical points of view in the next Chapters. Results will be also shortly published in [35].

However, other strategies may be adopted in order to model laminate composites. For example, Kim et al. [36] joined the $FSDT$ with the *Higher–order ZigZag displacement theory*, accounting also multiples delamination at the interfaces. In particular, the $ZigZag$ theory, which consider 5 kinematic variables, ensures the transverse shear stresses continuity and the traction–free conditions on the top and on the bottom surface of the laminate. The authors considered therefore different stages of damage at the interface, which is modeled as a spring layer. Moreover, trough their model, which is called *Enhanced First Order Shear Deformation Theroy with Imperfections* ($EFSDTWI$), they are able to determine also the effective *Shear Correction Factor* (SCF). In particular, according to them, for an unidirectional FRP, as the shear deformation and the damage level rise, the SCF value drops.

In the framework of the laminate theories, Caron et al. proposed in [37] the *Multiparticle Model of Multilayered Materials*, then renamed *Layerwise Stress Model* ($LS1$) by Lerpiniere et al. [38]. This model is based on the Hellinger–Reissner variational principle wherein the membranal stresses in each ply are approximated by a first–order polynomial, therefore as linear across the thickness. The approximate displacements of each layer, which are consistent with the approximate stresses, are then represented by a 5 variables kinematic field. Moreover, the model allows not only to evaluate the displacement discontinuities at the interface existing when the delamination occurs, but also to account an inelastic strain field, due for example to the interface sliding. Therefore, the $LS1$ is a pure layerwise stress approach, since no hypothesis are made on the displacement field. In particular, when this formulation is adopted, finite values of the interfacial stresses are always obtained, also

at the free edges, allowing the adoption of a tensional criterion for the prediction of the delamination onset, (see Caron et al. [37, 39]). These stresses, as pointed out by Lerpiniere et al. [38], arise from an integration over a characteristic length, which is the thickness of the ply, and represent therefore a mean stress value concentrated at the edge. Then, a finite element suitable for this model was implemented by Nguyen and Caron in [40].

A number of studies, aimed to evaluate stress state and fracture energies in delaminated orthotropic composite plates have been also performed by Szekrényes, where the composite plates were modeled by using the $CPLT$, the $FSDT$, the second– and the three–order shear deformation theory [41, 42, 43]. The author found that when the third–order theory is used, the displacement field is better approximated then when second–order theory is adopted, which on the contrary gives better results in terms of stress field.

To sum up, Kant and Swaminathan reviewed in [44] several methods adopted to estimate interlaminar stresses in laminate composites. Beside the approximate analytic methods, which may be tedious to solve for complex situations, studies based on numerical analysis, such as the *finite elements* (FE) methods, were also presented. Finally several FE methods based on laminate plate theories have been examined by Zhang and Yang in [45].

1.4 Fiber Reinforced Polymers application in the Civil Engineering field

Fiber Reinforced Polymers (FRP) are nowadays largely used in several engineering fields. In fact, thanks to their low density, they own higher strength-weight and modulus-weight ratio than common metallic materials, together with an elevated fatigue strength and damage tolerance. Moreover, they own an high inherent damping, which not only improve the energy absorption capability of the material, but also leads

to a reduction of the transmission of noise and vibration. Another useful characteristic of fiber reinforced polymers is a noncorroding behavior. However, since the FRP's external surface can absorb moisture or chemicals from the environment, they must be properly protected. It is also important to remark that, contrary to the structural metals, these composites exhibit in general an elastic tensile stress - strain relationship to failure, so that the fibers are characterized by a brittle failure mode.

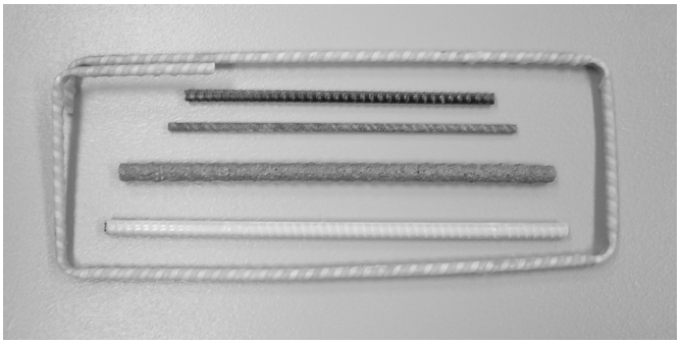

Figure 1.12: FRP glass and carbon bars. Reprinted from [4]

Among the various fields in which they are adopted, it is possible to find several applications of FRP in the aircraft, space, automotive, marine and medical industry. Anyway, the applications of major interest in this thesis are those related to the civil engineering.

The FRP used in structural engineering are generally made by glass, carbon or aramid fibers inserted in a matrix of epoxy, polyester, vinylester, or phenolic thermosetting resins. Concerning the form in which FRP are used, they can be realized in form of structural profiles, reinforcing bars, strips and sheets, see Figs. 1.12,1.13 and 1.14. In particular, in case of profiles or bars, FRP are manufactured in such a way as to be ready to be used, whereas in the other cases, the structural component may be realized in situ starting from dries fibers and liquid resins.

By focusing on the reinforcement of new concrete structural members, FRP can be categorized in, [4]:

- *FRP* bars or grid for reinforced concrete (*RC*) members. The bars are typically made by glass and carbon fibers, which can be connected to the steel bars in a common way. Several applications can be found in underground tunnels and bridges decks.
- *FRP* tendons for prestressed concrete (*PC*) members. For this application specially aramid and carbon fibers are used. However, due to the necessity to develop particular anchorage systems, this kind of application is not largely spread.
- stay-in place *FRP* formwork for RC members. They can be used as bridge deck panels, serving as tensile reinforcement for the concrete or in a tubular form to realize beam and column members.

Figure 1.13: FRP strip installation. Reprinted from [4]

On the contrary, the applications where *FRP* are used to strengthen and repair existing structural members are called retrofitting applications. They can be classified in two types:

Figure 1.14: FRP sheets installation. Reprinted from [4]

Figure 1.15: Columns confinement by means of FRP sheets. Reprinted from [4]

- *strengthening*: the original strength or ductility of the structure is increased with respect to the original in order to adequate it to the currents building codes, for example in terms of seismic response, or owing to a change in the use of the structure itself.

- *repair*: FRP are used to retrofit a damaged structure in order to reacquire the design characteristics.

The FRP are currently used to reinforce not only concrete members, but also timber, masonry and metal structures. Thery are adopted both for bridge and buildings, as well as for the flexural and shear strengthening of concrete beams, and for axial strengthening and confinement of concrete columns, Fig. 1.15. One of the adopted methods consists in the adhesive bond of a rigid FRP strip of about 100 mm of width and 1.6 mm of thickness to the external surface of the structural member. Alternatively, it is possible crate in situ the FRP by using flexible dry fiber fabrics or sheet and liquid polymers.

Bibliography

[1] E. J. Barbero. *Introduction to composite materials design.* Taylor & Francis, 1999.

[2] R. M. Jones. *Mechanics Of Composite Materials.* CRC press Taylor & Francis Group, 2nd edition, 1999.

[3] P. K. Mallick. *Fiber–reinforced composites. Materials, Manufacting and Desing.* CRC press Taylor & Francis Group, 3th edition, 2007.

[4] L. C. Bank. *Composites for construction: structural design with FRP materials.* John Wiley & Sons, Inc., 2006.

[5] E. J. Barbero. *Finite element analysis of composite materials.* CRC Press, Taylor & Francis, 2008.

[6] J. N. Reddy. *Mechanics of laminated composite plates and shells. Theory and Analysis.* CRC Press, 2nd edition, 2004.

[7] S. Nemat-Nasser and M. Hori. *Micromechanics: Overall Properties of Heterogeneous Materials.* Elsevier Science Publishers B. V., 1991.

[8] S. J. Hollister and N. Kikuchi. A comparison of homogenization and standard mechanics analyses for periodic porous composites. *Computational Mechanics*, 10:73–95, 1992.

[9] M. Hori and S. Nemat-Nasser. On two micromechanics theories for determining micro–macro relations in heterogeneous solids. *Mechanics of Materials*, 31:667–682, 1999.

[10] P. Nevone Blasi. *Risposta macroscopica di materiali compositi in presenza di fenomeni di microfrattura e contatto.* PhD thesis, Unversitá della Calabria, 2007.

[11] B. Hassani and E. Hinton. A review of homogenization and topology optimization I – homogenization theory for media with periodic structure. *Computers and Structures*, 69:707–717, 1998.

[12] W. Wang, D. Luo, Y. Takao, and K. Kakimoto. New solution method for homogenization analysis and its application to prediction of macroscopic elastic constant of materials with periodic microstructures. *Computers and Structures*, 84:991–1001, 2006.

[13] R. Brighenti. A mechanical model for fiber reinforced composite materials with elasto–plastic matrix and interface debonding. *Computational Material Science*, 29:475–493, 2004.

[14] L. Leonetti. *Multiscale approaches for failure anaylises of composite materials.* PhD thesis, Unversità della Calabria, 2014.

[15] E. Weinan, B. Engquist, X. Li annd W. Ren, and E. Vanden-Eijnden. The heterogeneous multiscale method: a review. *Commun. Comput. Phys.*, 2(3):367–450, 2007.

[16] S. Ghosh, J. Bai, and P. Raghavan. Concurrent multi–level model for damage evolution in mifrostructurally debonding composites. *Mechanics of Materials*, 29:241–266, 2007.

[17] O. O. Ochoa and J. N. Reddy. *Finite element analysis of composite laminates.* Kluwer Academic Publishers, 1992.

[18] O. Allix and A. Corigliano. Modeling and simulation of crack propagation in mixed–modes interlaminar fracture specimens. *International Journal of Fracture*, 77:111–140, 1996.

[19] Z. P. Bažant and J. Planas. *Fracture and Size Effect in Concrete and Other Quasibrittle Materials.* CRC Press, 1998.

[20] A. Corigliano. Formulation, identification and use of interface models in the numerical analysis of composite delamination. *International Journal of Solids and Structures*, 30(20):2779–2811, 1993.

[21] V. Q. Bui, E. Marechal, and H. Nguyen-Dang. Imperfect interlaminar interfaces in laminated composites: interlaminar stresses and strain–energy release rates. *Composites Science and Technology*, 60(1):131–143, 2000.

[22] O. Rabinovitch. Debonding analysis of fiber–reinforced–polymer strengthened beams: Cohesive zone modeling versus a linear elastic fracture mechanics approach. *Engineering Fracture Mechanics*, 75:2842–2859, 2008.

[23] G. Alfano and M. A. Crisfield. Finite element interface models for the delamination analysis of laminated composites: mechanical and computationl issues. *Int. J. Numer. Meth. Eng.*, 50:1701–1736, 2001.

[24] D. Bruno, F. Greco, and P. Lonetti. A coupled interface–multilayer approach for mixed mode delamination and contact analysis in laminated composites. *International Journal of Solids and Structures*, 40:7245–7268, 2003.

[25] Weicheng Cui and M. R. Winsnom. A combined stress–based and fracture–mechanics–based model for predicting delamination in composites. *Composites*, (6):467–474, 1993.

[26] F. Greco, P. Lonetti, and R. Zinno. An analytical delamination model for laminated plates including bridging effects. *Internationl Journal of Solids and Structures*, 39:2435–2463, 2002.

[27] W. S. Johnson and P. D. Mangalgiri. Investigation of fiber bridging in double cantilever beam specimens. *Journal of Composites, Technology and Research*, 9(1), 1987.

[28] M. Elices, G. V. Guinea, J. Gomez, and J. Planas. The cohesive zone model: advantages, limitations and challenges. *Engineering Fracture Mechanics*, 69:137–163, 2002.

[29] L. De Lorenzis and G. Zavarise. Cohesive zone modeling of interfacial stresses in plated beams. *Internationl Journal of Solids and Structures*, 46:4181–4191, 2009.

[30] Y. Mi, M. A. Crisfield, and G. A. O. Davies. Progressive delamination using interface elements. *Journal of Composite Materials*, 32(14):1246–1272, 1998.

[31] N. Point and E. Sacco. Delamination of beams: an application to the *dcb* specimen. *International Journal of Fracture*, 79:225–247, 1996.

[32] J. Chen, M. Crisfield, A. J. Kinloch, E. P. Busso, F. L. Matthews, and Y. Qiu. Predicting progressive delamination of composite material specimens via interface elements. *Mechanics of Composite Materials and Structures*, 6:301–317, 1999.

[33] Z. Zou, S. R. Reid, P. D. Soden, and S. Li. Mode separation of energy release rate for delamination in composite laminates using sublaminates. *International Journal of Solids and Structures*, 38:2597–2613, 2001.

[34] D. Bruno, F. Greco, and P. Lonetti. A 3D delamination modelling technique based on plate and interface theories for laminated structures. *European Journal of Mechanics A/Solids*, 24:127–149, 2005.

[35] D. Bruno, F. Greco, S. Lo Feudo, and P. Nevone Blasi. Multi–layer modeling of edge debonding in strengthened beams using interface stresses and fracture energies. *Engineering Structures*, Article in Press.

[36] J. Kim, J. Oh, and M. Cho. Efficient analysis of laminated composite and sandwich plates with interfacial imperfections. *Composites Part B: Engineering*, 42(5):1066–1075, 2011.

[37] J. F. Caron, A. Diaz Diaz, R. P. Carreira, A. Chabot, and A. Ehrlacher. Multi–particle modelling for the prediction of delamination in multi–layered materials. *Composites Science and Technology*, 66:755–765, 2006.

[38] A. Lerpiniere, J. F. Caron, A. Diaz Diaz, and K. Sab. The LS1 model for delamination propagation in multilayered materials at $0°/\theta°$ interfaces: A comparison between experimental and finite elements strain energy release rates. *International Journal of Solids and Structures*, 51:3973–3986, 2014.

[39] N. Saeedi, K. Sab, and J. F. Caron. Stress analysis of long multilayered plates subjected to invariant loading: Analytical solutions by a layerwise stress model. *Composite Structures*, 100:307–322, 2013.

[40] V. T. Nguyen and J. F. Caron. A new finite element for free edge effect analysis in laminated composites. *Computers and Structures*, 84:1538–1546, 2006.

[41] A. Szekrényes. Analysis of classical and first–order shear deformable cracked orthotropic plates. *Journal of Composite Materials*, 2013.

[42] A. Szekrényes. Interface fracture in orthotropic composite plates using second–order shear deformation theory. *International Journal of Damage Mechanics*, 22(8):1161–1185, 2013.

[43] A. Szekrényes. Stress and fracture analysis in delaminated orthotropic composite plates using third–order shear deformation theory. *Applied Mathematical Modeling*, 38(15–16):3897–3976, 2014.

[44] T. Kant and K. Swaminathan. Estimation of transverse/interlaminar stresses in laminated composites – a selective

review and survey of current developments. *Composite Structures*, 49:65–75, 2000.

[45] Y. X. Zhang and C. H. Yang. Recent developements in finite element analysis for laminated composite plates. *Composite Structures*, 88:147–157, 2009.

Chapter 2

FRP reinforced beams

In this Chapter the use of Fiber Reinforced Polymers (FRP) in strengthened systems will be analyzed in detail.

In Section 2.1 the most common failure mechanisms related to the application of FRP, and deriving from manufacturing process or loading conditions, is presented.

Then, by focusing on damage phenomena arising from debonding (or delamination) at interface of composite plies or between different structural components, the challenging task related to the interfacial stresses and fracture energies computation is faced. In particular, in Section 2.2 several works concerning the evaluation of interfacial stresses are reviewed, and governing equations for a three layer assembly (concrete beam, adhesive layer and FRP plate) are analytically obtained by means of a variational approach.

On the other hand, Section 2.3 deals with the evaluation of fracture energy characterizing strengthened systems, by introducing at first the classic concepts of the Linear Elastic Fracture Mechanics, and then by reporting different strategies and formulations adopted in mixed mode problems.

In Section 2.4 a general formulation based on multi–layers and interface elements is presented. This formulation not only is able to provide

the governing equations of the problem, but also gives interfacial stresses and individual components of the Energy Release Rate. In particular, by adopting different types of interface, the present model will be applied numerically in the next Chapters, where it will be confirmed as a powerful alternative to others existing models, in terms of computational costs and accuracy, for the evaluation of interfacial stresses and fracture energy.

Finally, Section 2.5 focuses on the available criteria able to evaluate damage initiation and propagation. In particular, in Section 2.5.2 a relatively recent criterion for crack initiation, which couples tension and energetic considerations, is extended at the present application of reinforced concrete beams under mixed mode loading condition.

2.1 Introduction

2.1.1 FRP failure mechanisms

The complexity of the composite material damage process arises from the mechanical composition of the composite itself. Indeed, the coexistence of multiples micro–constituents with different properties leads to manifold defects interaction and coupling. As a consequence, the FRP load carrying capacity and durability is affected by the presence of internal defects, which generally are originated by the manufacturing process and grow during the composite work life.

The nature and specificity of each defect depends on the adopted manufacturing process, and their interaction lead to several damage mechanisms. Both, principals defects and damage processes are listed in Tab. 2.1. In particular, a class of defects concerns the fiber misalignment, the not uniform distribution and the incorrect volume fraction. Also the presence of voids, inclusions in the matrix and local bound failure may be present. Moreover, the layer adjoin may cause some internal defects. In fact, for several structural applications, FRP are commercialized in *prepreg* sheets composed by single fibers layers embedded in

a resin matrix and flattered by paper carrier sheets. The various sheets are then joined together, leading sometimes to gaps and overlaps. Others defects, such as blisters and wrinkles, may arise from the moisture absorption into the voids which are located near the laminate surface, and from the sheets draping, respectively [1].

Initial defects	**Failure mechanisms**
voids	matrix microcracking
inclusions	fiber microbuckling
gaps	fiber/matrix debonding
overlaps	fiber breakage
fiber misalignment	fiber pull-out
blisters	splitting
wrinkles	kinking
ply drop-off	delamination

Table 2.1: FRP initial defects and damage mechanisms

The FRP failure mechanisms can be roughly classified into *intralaminar* and *interlaminar*. In particular, the intralaminar damage occurs inside each lamina and represents the early stage of damage wherein multiple micro–cracks and voids grow. On the contrary, the interlaminar damage refers to cracking of adjacent laminate plies. This failure mode, which generally occurs near free edges and holes, usually leads to the FRP collapse through a progressive loss of structural strength, Leonetti [2].

In Fig. 2.1, the most common failure mechanisms are shown. In particular, depending on the lamina stress state, different type of failure may appear. Indeed, tensile stress causes generally debonding at the fiber/matrix interface, fibers breakage and pull–out phenomena, whereas failure associated with compressive loads is related with fibers microbuckling, crushing and splitting, see for instance Fleck [3], Budianksy and Fleck [4, 5].

Matrix microcracking: the cracking of the matrix represents generally the early stage of the FRP damage process. Starting from defects

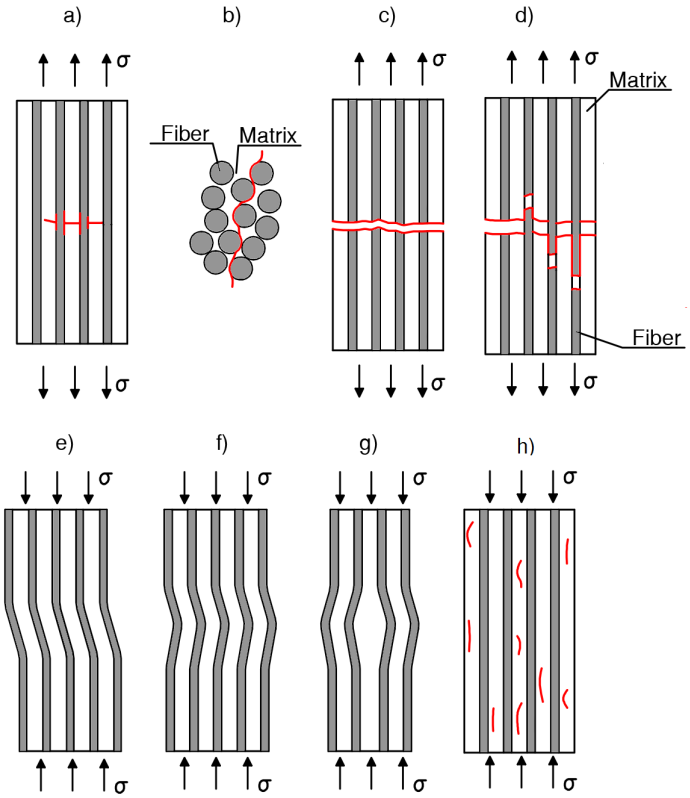

Figure 2.1: Schematic representation of principals FRP damage mechanisms: a) and b) fibers/matrix debonding, c) fibers breakage d) fibers pull–out, e) plastic microbuckling, f) elastic microbuckling, g) fibers crushing and h) fibers splitting.

such as voids, inclusions and debondend interfaces, the cracks may grow into a ply across the thickness and parallel to the fibers direction. However, although the matrix cracking does not cause the FRP failure, it affects largely the material stiffness, and facilitates the progression of the others damage mechanisms. These effects are produced in general by the voids growth, which may be originated during the manufacturing process or from others damage mechanisms.

Fiber microbuckling and kinking: in case of FRP subjected to compressive load, the microbuckling and the plastical kinking cause

the fiber failure. In particular, the kinking arises from a possible fibers misalignment and it is influenced by the shear stresses.

Fiber/matrix interfacial debonding: the debonding at the interface between the fiber and the matrix is one of the most common failure mechanisms for the FRP materials. In particular, since the fibers are stiffer than the matrix, the properties of the interface highly influences the failure behavior of the composite. In fact, in case of weak interface, debonding occurs at low levels of load and diffuse cracking in the transverse direction takes place before failure. On the contrary, in case of strong interface, the FRP failure occurs for higher load levels following up fibers breakage.

Fiber breakage: the FRP failure under tensile stress state occurs as a result of the fibers breakage. When a fiber breaks, the stresses redistribute at the neighborhood fibers, which may in turn break. However, this failure mechanism has a statistical character, since it is influenced by the nonuniform fibers' strength along the fiber itself and by the redistribution of the stresses. Moreover, the larger numbers of fibers breakage appears to occur near to the interface where the ply cracks end, [2].

Delamination: the term delamination refers to an interlaminar damage mechanism where the crack grows at the interface between two laminae. The interfacial delamination process was investigated by many researchers in the past decades, from analytic and numerical points of view. In particular, two major approaches may be adopted. One is the *Cohesive zone model* (CZM), which allows to simulate the FRP delamination by adopting interfacial cohesive laws and interfacial cohesive elements, as it was discussed in Section 1.3.4,. In this framework, the debonding at the interface between a reinforced concrete beam and a FRP laminate was studied by Achintha and Burgoyne [6], in case of damage starting either near the cut–off section of the FRP or at a high–moment zone. In particular, the authors assumed that debonding occurs within the concrete, between the FRP and the steel bars of the beam, so that the parameter governing the damage analysis is the fracture energy

of the concrete.

One of the main advantage of using the CZM is that it enables to study the delamination also in case of mixed–mode crack initiation and propagation, allowing the partition of the energy release rate and the modeling of multiple cracks. However, the CZM has some disadvantages, how it was also pointed out by Rabinovitch in [7]. Indeed, not only an high computation effort is required, but also the determination of the interface constitutive law needs a complicate calibration process, which have to take into account a large amount of parameters.

On the other hand, when the non linearity of the damaging process is negligible, the crack propagation may be predicted in the framework of the Linear Elastic Fracture Mechanics ($LEFM$). Therefore, through the definition of a linear analytic model, and with a small number of needed material parameters, namely related to the interfacial toughness and strength, the delamination problem may be simulated. However, it is well know that the principles of the classical fracture mechanics are suitable for the crack propagation only, that is when an initial defect is already present. To overcome this intrinsic problem, how it will be shown in Section 2.5, a coupled energetic and tensional criterion may be adopted to evaluate the crack onset. In fact, the primary purpose of Ph.D. study is the prediction of crack initiation within the framework of the $LEFM$, together with the analysis of the crack propagation through the Virtual Crack Closure Technique ($VCCT$), and by modeling the structural system, subjected to mixed mode loading condition, as a multi–layer assembly of shear deformable 2 and 1–dimensional elements. The study results will be also published in [8].

2.2 Interfacial stresses

A strengthened system composed by FRP composite plates bonded to structural elements may fails because of debonding [9], which usually occurs after initiation and growth of interfacial cracks at the interface

between the adhesive layer and the lower face of the beam, [7]. Interfacial debonding starts owing to high concentrations of stresses at the cut–off section of the plate or from intermediate flexural crack [10], and in many cases it leads to the global failure of the layered element [11].

Since debonding failure modes are strictly related to high interfacial shear or normal stresses, arising from the transfer of tensile stresses from the bonded plate to the strengthened beam at the edge of the reinforcement, an accurate prediction of these interfacial stresses is of fundamental importance [12]. Therefore, in the last decade several approximate closed–form analytic solutions have been developed, based on simplified assumptions for the adhesive layer behavior [13]. Most of the existing analytic solutions devoted to beams strengthened with externally bonded FRP plates, are based on the assumption of linear elastic behavior of the analyzed materials and on the use of classical beam theory to model the mechanical behavior of the structural system components. Moreover, it is often assumed that shear and normal stresses are constant across the thickness of the adhesive layer, since this assumption enables to obtain relatively simple closed–form solutions. This is the case of the *elastic foundation models*. In particular, the one parameter elastic foundation model accounts only the shear resistance of the adhesive, which is represented by a set of shear springs. Consequently, normal stress and bending effects within the adhesive are neglected and shear stresses are constants through the thickness. On the other hand, in the two parameter elastic foundation model, both vertical and shear springs are considered, so that normal and shear stresses within the adhesive are constants and vertical and longitudinal displacement linear. However, the elastic foundation models not only do not fulfill the point equilibrium within the thickness of the adhesive and do not provide interaction between normal and shear stresses, but also they do not satisfy the requirement of null shear stresses at the free edge of the FRP [14, 15].

In this context, another general and accurate closed–form solution including the contributions of all deformations from the three components

of the strengthened system, with only the effects of shear deformability, has been proposed in [13].

To overcome the foundation models lacks, a refined closed–form solution, referred to as *higher order analysis*, considering the adhesive layer as an orthotropic elastic continuum with a negligible longitudinal stiffness, was proposed in [14]. In spite of the simplified assumptions of a constant shear stress distribution across the adhesive layer and of zero shear stress at the adhesive layer free edges, the higher order solution is able to capture the variations of normal stresses across the adhesive layers and to show that near the plate end the normal stress at the adhesive/concrete interface is tensile and compressive at the adhesive/plate one. Consequently, Rabinovitch and Frostig [14] for the first time pointed out that this aspect is the reason why the adhesive/concrete interface is more vulnerable to debond than the other.

Beside the above mentioned closed–form solutions, also several numerical stress analyses based on finite element calculations have been carried out to estimate interfacial stresses in strengthened beam systems. In [12] a finite element investigation on the interfacial stresses in reinforced concrete beams strengthened with a bonded FRP plate is carried out, in order to evaluate the accuracy of the above mentioned simplified closed form solutions. In particular the authors point out the existence of the stress singularity at the plate end and the necessity to use a very fine mesh in order to obtain an accurate determination of the interfacial stresses. The work shows also that the closed–form solution proposed in [13], as well as others similar closed–form solutions, can be considered as a reasonable approximation of stresses along the middle–thickness section of the adhesive layer, and that interfacial stresses vary strongly across the adhesive, becoming uniform at a small distance from the end of the plate. Also Zhang and Teng [16] have implemented various finite element models based on different combination of $2D$ plane stress, classical beam and spring elements, in order to predict interfacial stresses, comparing numerical results with various analytical solutions

proposed in the literature. The authors evidenced the influence of the adopted model to describe the behavior of the components in terms of interfacial shear and normal stresses prediction, and the efficacy of the simple analytical beam–spring–beam model.

2.2.1 A variational approach to modeling FRP reinforced beams

In order to analyze the debonding problem for beams strengthened with externally bonded fiber–reinforced composite plates, a variational approach is here adopted. Indeed, as it will be shown, the principle of stationary total potential energy allows to obtain the problem governing equations.

The structural system considered in the present formulation is composed by three physical components, namely a concrete beam, an adhesive layer and a FRP plate, as shown in Fig. 2.2. Each physical layer is modeled by a first–order shear deformable mathematical layer and, in order to guarantee displacements continuity at the perfect interfaces (i.e. the undelaminated regions), a strong formulation is employed. The latter consists in the adoption of appropriate Lagrange multipliers representing interfacial stresses. This method was also adopted by Wu and Kuo in [17], who imposed the displacement continuity at the interface by introducing into the potential energy functional the Lagrange multipliers. Then, the variation of the potential energy with respect to the primary variables, which are the generalized displacement and the interlaminar stresses (i.e. the Lagrange multipliers) leads to the equilibrium equations.

The analysis of the composite system is carried out with reference to a unit width, and a two–dimensional formulation is considered (plane strain or plane stress conditions), assuming that all the generalized displacements are independent on the y–coordinate.

In the present variational formulation the following energy functional

Π is therefore introduced:

$$\Pi = U + \Lambda - W \tag{2.2.1}$$

where U is the system strain energy, Λ is the Lagrange functional which ensures the displacement continuity in the bonded region, and W is the work performed by applied external load. The problem governing equations may be therefore obtained through the stationarity of the Π functional due to a variation of the generalized displacements in the layers and of the Lagrange multipliers:

$$\delta U + \delta\Lambda - \delta W = 0 \tag{2.2.2}$$

where δ is the variational operator.

In the following, the structural system is modeled by considering three mathematical layer, which correspond to the different physical layers. Moreover, although different locations for the debonding across the adhesive layer can be considered, and will be analyzed in the numerical examples, for the sake of simplicity in the subsequent analytical developments it is assumed that delamination is located at the physical interface between the adhesive layer and the concrete beam.

Let's consider an elastic beam of length L and thickness t_b. The beam is reinforced by means of an elastic FRP plate of thickness t_p, which is

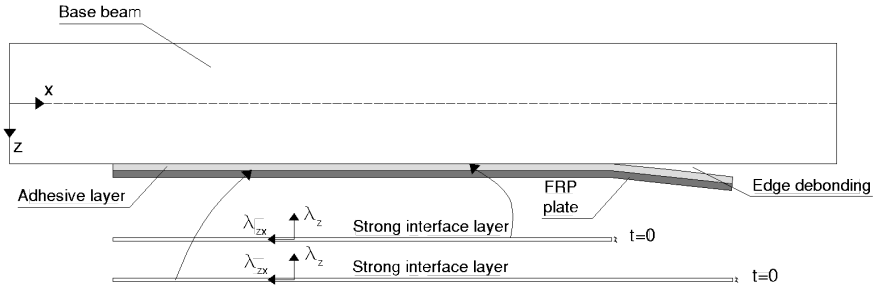

Figure 2.2: The analyzed strengthened structural system.

bonded over a region $L_u < x < L_u + L_s$ through an adhesive layer of thickness t_a. Assuming that the width of all the structural elements is equal to B, two different unstregthened regions are considered, that is $0 < x < L_u$ and $L_u + L_s < x < L$, whereas the delaminated region corresponds to $L_u + L_s - a < x < L_u + L_s$, in which contact is excluded by hypothesis.

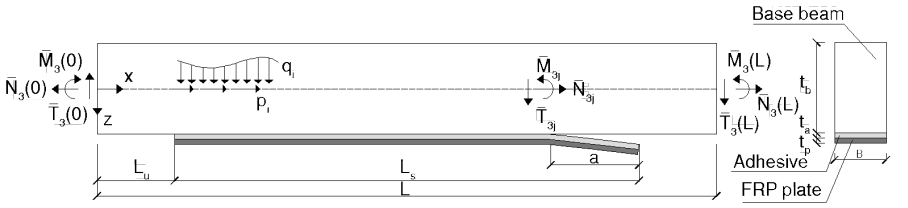

Figure 2.3: Mathematical notations and conventions for loads, stress resultants and displacements.

The mathematical notation and conventions for the local co–ordinate systems of each layer, stress resultants, external and end loads, and displacements, are shown in Fig. 2.3. In particular, in the present formulation the distributed or concentrated loads are assumed to act only on the beam. The upper mathematical layer is denoted with the subscript 3, and the lower one with the subscript 1, with each layer of thickness t_i and $i = 1, 2, 3$. The present formulation is an extension of that already proposed by Greco et al. in [18], where only two mathematical layers were considered, one representing the reinforced beam, and the other one the adhesive and the bonded plate coupled together.

For the generic layer, the kinematics expressions may be introduced for the membrane strain at the reference surface ϵ_i, the curvature κ_i and the transverse shear strain γ_i:

$$\epsilon_i = u_i', \quad \kappa_i = \psi_i', \quad \gamma_i = \psi_i + w_i' \tag{2.2.3}$$

where $u_i(x)$ and $w_i(x)$ are the mid–surface in–plane and transverse dis-

placements, respectively, $\psi_i(x)$ are the rotation of transverse normals, and prime denotes the derivative with respect to x. The first variation of the strain energy is:

$$\begin{aligned}\delta U = \int_{L_u}^{L_u+L_s} (N_1\delta\epsilon_1 + N_2\delta\epsilon_2 + T_1\delta\gamma_1 + T_2\delta\gamma_2 + M_1\delta\kappa_1 + \\ + M_2\delta\kappa_2)dx + \int_0^L (N_3\delta\epsilon_3 + T_3\delta\gamma_3 + M_3\delta\kappa_3)dx\end{aligned} \tag{2.2.4}$$

where N_i are the membrane force resultants, M_i the moment resultants and T_i the transverse shear force resultants.

The variation of the Lagrange functional related to the interface displacement continuity between adjacent layers can be expressed as:

$$\begin{aligned}\delta\Lambda = \int_{L_u}^{L_u+L_s} \sum_{j=1}^{2} (\lambda_{zxj}\delta\Delta u_j + \lambda_{zj}\delta\Delta w_j + \delta\lambda_{zxj}\Delta u_j + \\ + \delta\lambda_{zj}\Delta w_j)dx\end{aligned} \tag{2.2.5}$$

where Δu_j and Δw_j denote displacement jump across the j–interface between adjacent layers and are given by:

$$\begin{cases}\Delta u_j &= u_j - \dfrac{t_j}{2}\psi_j - u_{j+1} - \dfrac{t_{j+1}}{2}\psi_{j+1} \\ \Delta w_j &= w_j - w_{j+1}, \quad j = 1,2\end{cases} \tag{2.2.6}$$

and λ_{zxj} and λ_{zj} are the Lagrange multipliers, which physically represent interlaminar stresses at the interfaces, see Fig. 2.2.

The variation of the external load work is:

$$\delta W = \int_0^L (p_3\delta u_3 + q_3\delta w_3)dx + \delta\bar{W}^c + \delta\bar{W} \tag{2.2.7}$$

where p_3 and q_3 are the distributed axial and transverse external loads acting on the beam, respectively. $\delta\bar{W}^c$ is the variation of the work of concentrated external loads, $\bar{N}_{3i}$ and $\bar{T}_{3i}$, and bending moments, $\bar{M}_{3i}$,

exerted at $x = x_i$ on the base beam and is defined as:

$$\bar{W}^c = \sum_{i=1}^{n} \int_0^L (\bar{N}_{3i}\delta u_3 + \bar{T}_{3i}\delta w_3 + \bar{M}_{3i}\delta\psi_3) D(x - x_i) dx \tag{2.2.8}$$

where D is the Dirac delta function and n is the number of concentrated loads. On the other hand, the quantity $\delta\bar{W}$ appearing in Eq. (2.2.7) is the variation of the work of external concentrated loads and bending moments at the two ends of the upper layer:

$$\bar{W} = [\bar{N}_3\delta u_3 + \bar{T}_3\delta w_3 + \bar{M}_3\delta\psi_3]_0^L \tag{2.2.9}$$

where $[f(x)]_b^a$ denotes the difference between the values of the considered function at $x = a$ and $x = b$, namely $f(a) - f(b)$.

For the i–th mathematical homogeneous layer, the constitutive relations associated to an orthotropic behavior are defined by the classical extensional, bending–extensional coupling, bending and shear stiffnesses, A_i, D_i, B_i and H_i, respectively. Assuming plane stress or plane stress conditions, the constitutive relations take the following form (see Sections 1.3.1.3 and 1.3.2.1 for additional details):

$$\begin{Bmatrix} N_i \\ M_i \\ T_i \end{Bmatrix} = \begin{bmatrix} A_i & B_i & 0 \\ B_i & D_i & 0 \\ 0 & 0 & H_i \end{bmatrix} \begin{Bmatrix} \epsilon_i \\ \kappa_i \\ \gamma_i \end{Bmatrix} \tag{2.2.10}$$

where

$$\begin{aligned} (A_i, B_i, D_i) &= \int_{-t_i/2}^{t_i/2} \bar{E}_i(z_i)(1, z_i, z_i^2) dz_i, \\ H_i &= \int_{-t_i/2}^{t_i/2} f G_i(z_i) dz_i \end{aligned} \tag{2.2.11}$$

wherein $\bar{E}_i$ is an equivalent longitudinal modulus, G_i the transverse shear modulus, and f the shear correction factor chosen as 5/6 in this work. In particular, the longitudinal and transverse shear moduli may depend

on the constitutive properties of the plies which constitute the layers. In case of plane stress and plane strain assumptions in the y–direction, and for a specially orthotropic homogeneous layer, $\bar{E}_i$ is given by:

$$\bar{E}_i = \begin{cases} E_i & \textbf{plane stress} \\ \dfrac{E_i}{1-\nu_{xyi}\nu_{yxi}} & \textbf{plane strain} \end{cases} \tag{2.2.12}$$

where ν_{xyi} and ν_{yxi} are the Poisson ratios and E_i the Young moduli.

For the sake of simplicity, a symmetric layup about the mid–plane is assumed for the composite strengthening plate, and the base beam and the adhesive layer are considered made of homogeneous and isotropic materials. As a consequence, for the upper layer the stiffness coefficients may be expressed as:

$$A_3 = \bar{E}_3 t_3, \quad D_3 = \frac{\bar{E}_3 t_3^3}{12}, \quad B_3 = 0, \quad H_3 = f G_3 t_3 \tag{2.2.13}$$

In the general form, that is when a mathematical layer does not correspond to a physical layer, the stiffness terms can be evaluated as:

$$\begin{aligned} A_i &= \bar{E}_i t_i + \bar{E}_{i+1} t_{i+1}, \\ D_i &= \frac{\bar{E}_i t_i (3t_{i+1}^2 + t_i^2) + \bar{E}_{i+1} t_{i+1} (3t_i^2 + t_{i+1}^2)}{12}, \\ B_i &= \frac{(\bar{E}_i - \bar{E}_{i+1}) t_i t_{i+1}}{2}, \\ H_i &= f(G_i t_i + G_{i+1} t_{i+1}), \quad for\ i = 1, 2 \end{aligned} \tag{2.2.14}$$

However, since the adhesive and the FRP layers are not coupled in the case study, the stiffness coefficients are evaluated in the same manner as for Eq. (2.2.13).

2.2.2 Governing equations for a three mathematical layer system

The variation of Π with respect to the Lagrange multipliers leads to the constraint equations assuring displacement continuity at the interfaces:

$$\begin{cases} \Delta u_j = 0 \\ \Delta w_j = 0 \end{cases} \quad , \quad j = 1, 2 \tag{2.2.15}$$

which, by virtue of Eq. (2.2.6) leads to

$$\begin{cases} u_{j+1} = u_j - \dfrac{t_j}{2}\psi_j - \dfrac{t_{j+1}}{2}\psi_{j+1} \\ w_{j+1} = w_j \end{cases} \quad , \quad j = 1, 2 \tag{2.2.16}$$

On the other hand, by substituting Eq.(2.2.3) into Eq. (2.2.4), the first variation of the strain energy becomes:

$$\begin{aligned} \delta U = \int_{L_u}^{L_u+L_s} (N_1 u_1'' + N_2 u_2'' + T_1 \psi_1' + T_1 w_1'' + T_2 \psi_2' + T_2 w_2'' + \\ + M_1 \psi_1'' + M_2 \psi_2'')dx + \int_0^L (N_3 u_3'' + T_3 \psi_3' + T_3 w_3'' + M_3 \psi_3'')dx \end{aligned} \tag{2.2.17}$$

and the integration by part gives

$$\begin{aligned} \delta U = \int_{L_u}^{L_u+L_s} -(N_1' \delta u_1 + N_2' \delta u_2 - T_1 \delta \psi_1 + T_1' \delta w_1 - T_2 \delta \psi_2 + \\ + T_2' \delta w_2 + M_1' \delta \psi_1 + M_2' \delta \psi_2)dx + \int_0^L -(N_3' \delta u_3 - T_3 \delta \psi_3 + \\ + T_3' \delta w_3 + M_3' \delta \psi_3)dx + [N_1 \delta u_1 + N_2 \delta u_2 + T_1 \delta w_1 + T_2 \delta w_2 + \\ + M_1 \delta \psi_1 + M_2 \delta \psi_2]_{L_u}^{L_u+L_s} + [N_3 \delta u_3 + T_3 \delta w_3 + M_3 \delta \psi_3]_0^L \end{aligned} \tag{2.2.18}$$

The variation of the potential energy functional, $\delta\Pi$, by substituting Eqs. (2.2.5), (2.2.7), (2.2.18) into Eq. (2.2.2), and by virtue of the

displacement continuity conditions (2.2.16), can be therefore expressed as:

$$\begin{aligned}
\delta\Pi = &\int_{L_u}^{L_u+L_s-a}[(N_1'+N_2'+N_3')\delta u_1+(M_1'-\frac{t_1}{2}N_2'-\frac{t_1}{2}N_3'+\\
&-T_1)\delta\psi_1+(M_2'-\frac{t_2}{2}N_2'-t_2N_3'-T_2)\delta\psi_2+(M_3'-\frac{t_3}{2}N_3'-T_3)\delta\psi_3+\\
&+(T_1'+T_2'+T_3'+q_3)\delta w_1]dx-\int_0^{L_u}[N_3'\delta u_3+(M_3'-T_3)\delta\psi_3+\\
&+(T_3+q_3)\delta w_3]dx-\int_{L_u+L_s-a}^{L_u+L_s}[(N_1'+N_2')\delta u_1+(M_1'-\frac{t_1}{2}N_2'+\\
&-T_1)\delta\psi_1+(M_2'-\frac{t_2}{2}N_2'-T_2)\delta\psi_2+(T_1'+T_2')\delta w_1]dx+\\
&-\int_{L_u+L_s-a}^{L}[N_3'\delta u_3+(M_3'-T_3)\delta\psi_3+(T_3'+q_3)\delta w_3]dx+\\
&-\sum_{k=d,c}[\![(N_1+N_2+N_3)\delta u_1+(T_1+T_2+T_3)\delta w_1+\\
&+(M_1-\frac{t_1}{2}N_2-\frac{t_1}{2}N_3)\delta\psi_1+(M_2-\frac{t_2}{2}N_2-t_2N_3)\delta\psi_2+\\
&+(M_3-\frac{t_3}{2}N_3)\delta\psi_3]\!]_k-\delta\bar{W}^i-\delta\bar{W}=0
\end{aligned} \tag{2.2.19}$$

where only transverse distributed forces q_3 are considered, $\delta\bar{W}^i$ is the work of the internal forces at the ends of the layers,

$$\begin{aligned}
\delta\bar{W} = &-\left(\sum_{i=1,2}N_i\delta u_i+M_i\delta\psi_i+T_i\delta w_i\right)|_{x=L_u+L_s}+\\
&-[N_3\delta u_3+M_3\delta\psi_3+T_3\delta\psi_3]_0^L
\end{aligned} \tag{2.2.20}$$

and the double brackets $[\![f]\!]_k = f^+ - f^-$, when $k = d$ refer to the jump across the delamination tip ($x = L_u + L_s - a$), whereas when $k = c$ refer to the jump across the cut–off section of the strengthening plate ($x = L_u$). In particular, for any function f, the subscript $+$ denotes the function evaluated at x^+, whereas the subscript $-$ denotes the function

evaluated at x^-.

The stationarity of Eq. (2.2.19) leads therefore to a boundary value problem for the system considered, since the equilibrium equations, the matching and the boundary conditions, (MC) and (BC), respectively, may be obtained. In particular, the equilibrium equations are: one translational in the x–direction and one in the z–direction for the layer assemblies, and one rotational for each mathematical layer. The variational method allows also to determine the Lagrange multipliers, which represent the interfacial forces, both stresses and forces, mutually exerted by two adjacent mathematical layers in the undelaminated region.

Therefore, the equilibrium equations in the strengthened region, namely $x \in [L_u, L_u + L_s - a]$, are:

$$\begin{cases} N_1'(x) + N_2'(x) + N_3'(x) = 0 \\ T_1'(x) + T_2'(x) + T_3'(x) + q_3 = 0 \\ M_1'(x) + M_2'(x) + M_3'(x) - T_1(x) - T_2(x) - T_3(x) + \\ -\dfrac{N_2'(x)(t_1 + t_2)}{2} - \dfrac{N_3'(x)(t_1 + 2t_2 + t_3)}{2} = 0 \\ M_2'(x) - T_2(x) - \dfrac{N_2'(x)t_2}{2} - N_3'(x)t_2 = 0 \\ M_3'(x) - T_3(x) - \dfrac{N_3'(x)t_3}{2} = 0 \end{cases} \tag{2.2.21}$$

The equilibrium equations in the unstrengthened region, namely $x \in [0, L_u]$ and $x \in [L_u + L_s - a, L]$, are:

$$\begin{cases} N_3'(x) = 0 \\ T_3'(x) + q_3 = 0 \\ M_3'(x) - T_3(x) = 0 \end{cases} \tag{2.2.22}$$

and in the delaminated region, $x \in [L_u + L_s - a, L_u + L_s]$, for the composite laminate and the adhesive assemblies are

$$\begin{cases} N_1'(x) + N_2'(x) = 0 \\ T_1'(x) + T_2'(x) = 0 \\ M_1'(x) + M_2'(x) - T_1(x) - T_2(x) - \dfrac{N_2'(x)(t_1+t_2)}{2} = 0 \\ M_2'(x) - T_2(x) - \dfrac{N_2'(x)t_2}{2} = 0 \end{cases} \tag{2.2.23}$$

The correspondent matching force conditions at the crack tip, $k = d$, and at the cut–off section, $k = c$, are:

$$\begin{aligned} &[\![N_1(x) + N_2(x) + N_3(x)]\!]_k = 0 \\ &[\![T_1(x) + T_2(x) + T_3(x)]\!]_k = 0 \\ &[\![M_1(x) + M_2(x) + M_3(x) - \frac{N_2(x)(t_1+t_2)}{2} + \\ &- \frac{N_3(x)(t_1+2t_2+t_3)}{2}]\!]_k = 0 \\ &\left[\!\!\left[M_2(x) - \frac{N_2(x)t_2}{2} - N_3(x)t_2\right]\!\!\right]_k = 0 \\ &\left[\!\!\left[M_3(x) - \frac{N_3(x)t_3}{2}\right]\!\!\right]_k = 0 \end{aligned} \tag{2.2.24}$$

and the boundary conditions may be expressed as

$$\begin{aligned} N_i = \alpha\bar{N}_i \ or \ u_i = \bar{u}_i, \\ T_i = \alpha\bar{T}_i \ or \ w_i = \bar{w}_i, \\ M_i = \alpha\bar{M}_i \ or \ \psi_i = \bar{\psi}_i \end{aligned} \tag{2.2.25}$$

where, for $i = 3$, $\alpha = 1$ or $\alpha = -1$ for $x = L$ and $x = 0$, respectively, whereas for $i = 1, 2$, $\alpha = 0$ and Eq. (2.2.25) refers to the cut–off section ($x = L_u$) and to the end of the delaminated interface ($x = L_u + L_s$), while ($\bar{u}_i$, $\bar{w}_i$, $\bar{\psi}_i$) are prescribed displacements. Moreover, it must be evidenced that the boundary conditions at $x = L_u$ and at $x = L_u + L_s$ for the lower layer assembly are imposed in accordance with the requirement

of free edge conditions, which for example at $x = L_u$ implies that:

$$N_i^- = 0, \quad T_i^- = 0, \quad M_i^- = 0, \quad for\ i = 1, 2 \tag{2.2.26}$$

Also the Lagrange multipliers, i.e. the interlaminar stresses, can be obtained through this variational method. Indeed, by collecting like terms in Eqs. (2.2.5) and (2.2.18), and owing to the first two equations in (2.2.21), stresses at the interface are given by:

$$\begin{aligned} \lambda_{zx1} &= N_1' = -(N_2' + N_3') \\ \lambda_{zx2} &= N_1' + N_2' = -N_3' \\ \lambda_{z1} &= T_1' = -(T_2' + T_3') \\ \lambda_{zx2} &= T_1' + T_2' = -T_3' \end{aligned} \tag{2.2.27}$$

Moreover, it is possible to evidence that the matching conditions in Eq. (2.2.24) can be also evaluated by equilibrium considerations on an assembly of infinitesimal volume elements as shown in Fig. 2.4. These matching conditions are also compatibles with horizontal and vertical concentrated interfacial forces at the j–th strong interface at the delamination tip and cut–off sections, which may be expressed as:

$$\begin{aligned} \Sigma_{zx1} &= N_1^+ - N_1^- = \sum_{i=2,3} N_i^- - \sum_{i=2,3} N_i^+ \\ \Sigma_{zx2} &= N_3^- - N_3^+ = \sum_{i=1,2} N_i^+ - \sum_{i=1,2} N_i^- \\ \Sigma_{z1} &= T_1^+ - T_1^- = \sum_{i=2,3} T_i^- - \sum_{i=2,3} T_i^+ \\ \Sigma_{zx2} &= T_3^- - T_3^+ = \sum_{i=1,2} T_i^+ - \sum_{i=1,2} T_i^- \end{aligned} \tag{2.2.28}$$

where membrane and transverse shear forces are evaluated at the positive or negative sides of the delamination tip and of the cut–off sections. These concentrated forces arise from the discontinuities in membrane and shear stress resultants across the delamination tip. In fact, according

also to Zou et al. [19], in the laminate theory, since the dimension in the thickness direction is eliminated, the stress singularity disappears and it is converted into the jump in the stress resultants. The evaluation of concentrate interfacial forces is therefore a key element to determine energy release rate during delamination growth. In fact, the out–of–plane and the in–plane interfacial forces are directly related to the Mode I and Mode II of fracture, respectively, how it will be further investigated in Section 2.4.2.

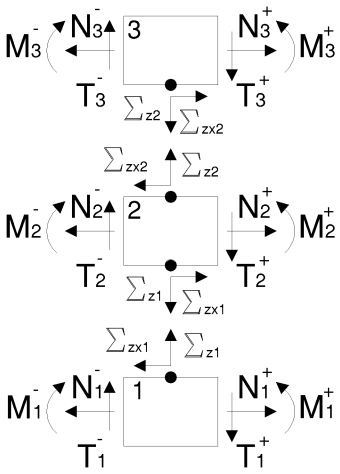

Figure 2.4: Interfacial concentrated forces

2.2.2.1 FRP reinforced cantilever beam subjected to an edge moment and an edge transverse force

Let's consider a cantilever beam of length L reinforced by a FRP plate over a length L_s, and delaminated at the concrete/adhesive interface along a distance a from the cut–off section. The beam is also subjected to an edge moment and an edge trasverse force, as shown in Fig. 2.5.

Tab. 2.2 and Fig. 2.6 summarize the different regions that may be identified for the present scheme.

region 1	unstrengthened region	$L_u + L_s - a < x \leq L$
region 2	delaminated region	$L_u + L_s - a < x \leq L_u + L_s$
region 3	strengthened region	$x \leq L_u + L_s - a$

Table 2.2: Structural system zoning

Therefore, the system of ordinary differential equations (ODEs) (2.2.21) describes the system equilibrium in the *region 3* and, from Eq. (2.2.25), it is possible to define the boundary conditions, which are given by:

$$\begin{cases} \bar{N}_i(x = L_s) = 0, \quad \bar{T}_i(x = L_s) = 0, \quad \bar{M}_i(x = L_s) = 0, \\ \quad for\ i = 1, 2 \\ \bar{N}_3(x = L) = 0, \quad \bar{T}_3(x = L) = -\bar{F}, \quad \bar{M}_3(x = L) = \bar{M}, \\ \bar{u}_i(0) = 0, \quad \bar{w}_i(0) = 0, \quad \bar{\psi}_i(0) = 0, \quad for\ i = 1, 2, 3 \end{cases} \tag{2.2.29}$$

The matching force condition at the delamination tip, which will be denote hereafter as $L_d = L_s - a$, are obtained from Eq. (2.2.24), and are

$$\begin{cases} N_1(x) + N_2(x) + N_3(x)|_{x=L_d} = 0 \\ T_1(x) + T_2(x) + T_3(x)|_{x=L_d} = -\bar{F} \\ M_1(x) + M_2(x) + M_3(x) - \dfrac{N_2(x)(t_1 + t_2)}{2} + \\ -\dfrac{N_3(x)(t_1 + 2t_2 + t_3)}{2}|_{x=L_d} = \bar{M} + \bar{F}(L - x)|_{x=L_d} \\ M_2(x) - \dfrac{N_2(x)t_2}{2} - N_3(x)t_2|_{x=L_d} = 0 \\ M_3(x) - \dfrac{N_3(x)t_3}{2}|_{x=L_d} = \bar{M} + \bar{F}(L - x)|_{x=L_d} \end{cases} \tag{2.2.30}$$

The first step, in order to analytically solve the problem, consists in defining the strain field through the displacement field, that is by using Eq. (2.2.3). Then, forces and moments resultants may be expressed through the displacement field, according to the constitutive relations, (2.2.10), where the bending–extensional coupling stiffness coefficients,

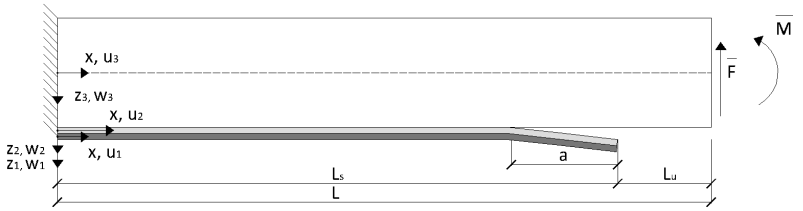

Figure 2.5: FRP reinforced cantilever beam subjected to an edge moment and an edge transverse force

B_i, are null since the laminate is symmetric with respect to the mid–plane.

By using the displacement continuity conditions in the bonded region, (2.2.16), the first two of Eq. (2.2.21) may be solved with the correspondents two MC, which gives:

$$\begin{aligned}(A_1+A_2+A_3)\left(\frac{d}{dx}u_1(x)\right)-\frac{1}{2}t_1(A_2+A_3)\left(\frac{d}{dx}\psi_1(x)\right)+\\-\frac{1}{2}t_2(A_2+A_3)\left(\frac{d}{dx}\psi_2(x)\right)-\frac{1}{2}A_3t_3\left(\frac{d}{dx}\psi_3(x)\right)=0\end{aligned} \tag{2.2.31}$$

$$(H_1+H_2+H_3)\left(\frac{d}{dx}w_1(x)\right)+H_1\psi_1(x)+H_2\psi_2(x)+H_2\psi_2(x)+\bar{F}=0 \tag{2.2.32}$$

The integration of Eqs. (2.2.31) and (2.2.32), with the correspondent BC at the fixed end in terms of prescribed displacement, Eq. (2.2.29),

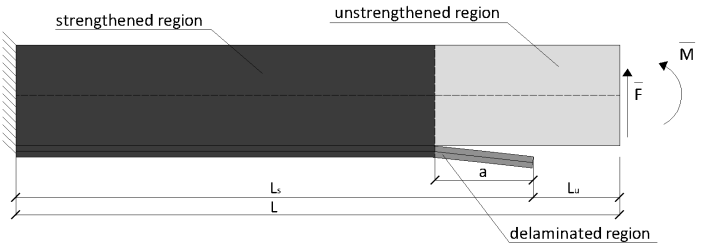

Figure 2.6: Double cantilever reinforced beam zoning

leads to:

$$\psi_3(x) = \frac{2(A_1+A_2+A_3)u_1(x)}{A_3 t_3} - \frac{t_1(A_2+A_3)\psi_1(x)}{A_3 t_3} - \frac{t_2(A_2+2A_3)\psi_2(x)}{A_3 t_3} \tag{2.2.33}$$

$$\frac{d}{dx}w_1(x) = -\frac{H_1\psi_1(x) + H_2\psi_2(x) + H_3\psi_3(x) + \bar{F}}{H_1+H_2+H_3} \tag{2.2.34}$$

By integrating the third of Eq. (2.2.21), taking into account the integration of (2.2.33), and integrating again, it is possible to express the axial displacement of the lower layer as a function of the rotation of the two lower layers:

$$u_1(x) = -\frac{b\psi_1(x) + c\psi_2(x) + gx + \dfrac{hx^2}{2}}{a} \tag{2.2.35}$$

where the coefficients (b, c, g, h) are given in Appendix 4.2.

Proceeding in a similar manner with the others ODE an MC, and after some manipulation, it is possible to express the system governing equations in term on only two second order ODE:

$$\begin{cases} \psi_1''(x) + \lambda_1\psi_1(x) + \lambda_2\psi_2''(x) + \lambda_3\psi_2(x) + c_1x^2 + c_2x + c_3 = 0 \\ \psi_1''(x) + \lambda_4\psi_1(x) + \lambda_5\psi_2''(x) + \lambda_6\psi_2(x) + c_4x^2 + c_5x + c_6 = 0 \end{cases} \tag{2.2.36}$$

which coefficient are reported in Appendix 4.2.

The associated boundary conditions are obtained from Eqs. (2.2.29) and (2.2.30) and, after some manipulation, they can be expressed as:

$$\begin{cases} \psi_1(0) = 0 \\ \psi_2(0) = 0 \\ \psi_1'(L_d) = -c_7\bar{M}_{tot} \\ \psi_2'(L_d) = c_8\bar{M}_{tot} \end{cases} \tag{2.2.37}$$

where also the coefficients (c_7, c_8) are given in Appendix 4.2 and

$$\bar{M}_{tot} = (L_d - L)\bar{F} + \bar{M} \tag{2.2.38}$$

In a similar manner, starting from Eqs. (2.2.22) and (2.2.23), and by using proper MC and BC, (2.2.24) and (2.2.25), respectively, it is possible to express the governing equations of *region 1* and *region 2* in term of displacement variables. In particular, although the delamination tip is a singular point where the generalized displacement derivatives are discontinuous, the displacement variables are continuous across the tip, leading to:

$$(u_i^-, w_i^-, \psi_i^-) = (u_i^+, w_i^+, \psi_i^+), \quad i = 1, 2, 3 \tag{2.2.39}$$

which can be taken into account when the BC at the tip for *region 2* are defined. Therefore, once that the elastic solution is found for all regions, forces and moments resultants can be evaluated. Then, by virtue of Eq. (2.2.27), the interfacial stresses in the bonded region, and in a similar manner at the adhesive/FRP interface, may be obtained.

2.3 Fracture energies in mixed mode problems

The initiation and propagation of the delamination at the interface between the FRP composite material and a structural element, or through the thickness of a reinforcement components, is generally a brittle phenomenon. For this reason, a review of the basic concept of the *Linear Elastic Fracture Mechanics* ($LEFM$) may be necessary to clearly understand the further developments. A vast literature exists in the field, and some reference works are those of Bažant [20], Broek [21], Knott [22] and Anderson [23]. Moreover, since in the delamination of strengthened system, the critical fracture energy for interface crack growth has a mixed mode dependence, it is necessary to extract the individual energy release rate components. Therefore, the following Section is organized as follows: at first, the Fracture Mechanics basic principles are briefly

reviewed; then, with the aim to analytically obtain the ERR modal partition, some analytic and numerical methods are presented; finally, some considerations about the experimental determination of the interfacial toughness are reported.

2.3.1 LEFM aspects

Defects deriving from the manufacturing process are commonly found into structural components but, up to a certain level, these inherent flows do not affect the element strength and performance. However, during the structural elements work life, several external factors may cause the flows growth, which can lead to various failure mechanisms, as shown in Section 2.1.1.

According to a classic definition, crack propagation arises from the superposition of three *Modes* of fracture, which depend on the acting load. These Modes are represented in Fig. 2.7 and are defined as follows:

- **Opening mode (Mode I)** - a tensile stress is applied orthogonally to the crack plane.
- **Sliding mode (Mode II)** - a shear stress is applied on the crack plane, in a perpendicular direction with respect to the crack front.
- **Tearing mode (Mode III)** - a shear stress acts in the direction of the crack front and parallel with respect to the crack plane

Let's consider a Mode I crack problem, where a plate of infinite length is subjected to a bi–axial stress. A polar coordinate system may be considered, with the origin fixed at the crack tip, Fig. 2.8. The stresses at the crack tip are known, and are given by:

$$\sigma_{ij} = \frac{K_I}{\sqrt{2\pi r}} f_{ij}(\theta) \tag{2.3.1}$$

where $f_{ij}(\theta)$ is a real function which fulfills the boundary conditions, and K_I is the *Stress Intensity Factor* (SIF), which gives a measure

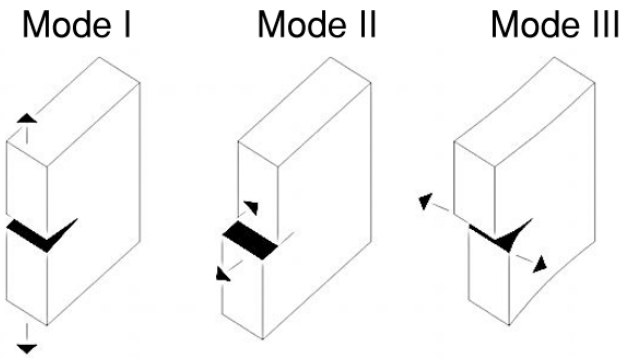

Figure 2.7: Fracture Modes

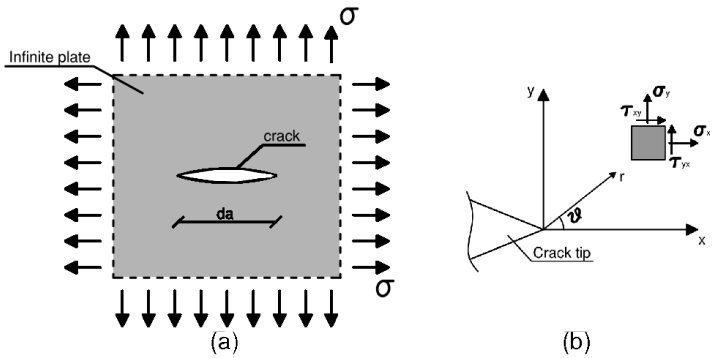

Figure 2.8: (a) Infinite plate under bi–axial stress, (b) polar coordinate system

of the stress singularity at the crack tip. Indeed, as $r \to 0$, i.e. the distance from the tip, stresses tend to be singulars, whereas as $r \to \infty$ stresses tend to those externally applied on the plate. It is also possible to demonstrate that:

$$K_I = \sigma\sqrt{\pi a} \tag{2.3.2}$$

Several SIF values for plates of finite dimension, and in case of circular and elliptical cracks are listed in [21].

The singularity at the crack tip leads to the presence of a plastic zone ahead the tip, Fig. 2.9. Firstly, the plastic zone shape is supposed to be

circular, then the effective plastic zone size may be evaluated considering a crack which length is greater then the actual and under the hypothesis of edges subjected to a yield stress tending to close the crack.

Therefore, once that the plastic zone size is known, it is possible to evaluate the exact SIF. In particular, by using a yield criterion, such as Von Mises or Tresca, it is possible to obtain also the actual boundary of the plastic zone, which is generally greater in a plane stress state. In fact, by considering a plate which thickness is at least equal to the plastic zone size, a plane stress state may be found on the plate surface, whereas a plane strain state inside the plate. Therefore, since the yield of the material within the thickness is contrasted by the neighboring material, the effective yield stress in plane strain state may be three times greater then the uni–axial yield stress.

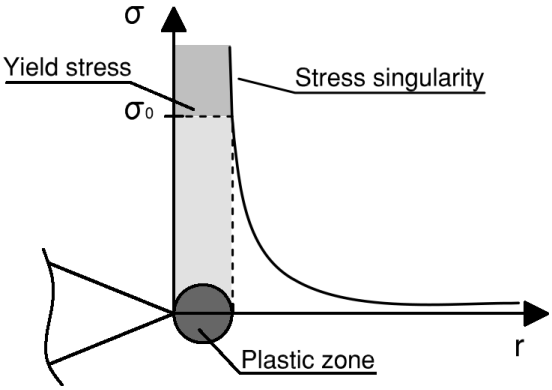

Figure 2.9: Crack tip plastic zone

As a result, the stress state at the crack tip and the failure mechanism depend on the plate thickness. Indeed, in case of thin plates, the fracture plane is inclined of 45° with respect to the external surface, *slant fracture*, whereas, above a certain thickness value, the fracture plane is orthogonal to the plate surface, *flat tensile fracture*. Moreover, it is possible to identify a critic value of the SIF, K_{IC}, which represents the material toughness. K_{IC} depends on the thickness and it can be evaluated experimentally.

The base equation of Fracture Mechanics was introduced by Griffith in 1921. According to Griffith, a crack propagates if the energy released during propagation corresponds to the energy required for the crack growth. For example, let's consider the force–displacement plot of a specimen loaded at the two ends and cracked at one edge shown in Fig. 2.10, where v denotes the relative displacement between the application points of the load P.

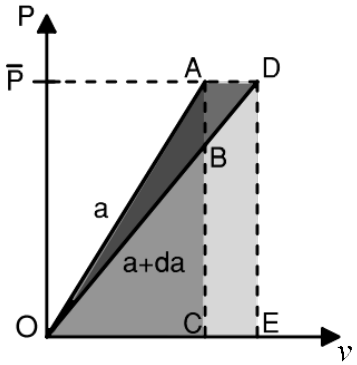

Figure 2.10: Load–displacement plot of a cracked specimen

The OAC triangle area represents the specimen elastic energy. When the crack propagates of a length da, the specimen stiffness is reduced. In particular, when the specimen ends are fixed, the load drop from A to B and the area OAB is the released elastic energy. On the contrary, if the crack propagates at constant load, from point A to D, the relative displacement increases of CE, and the elastic energy stored into the plate corresponds to the ODE area, whereas the area $ADEC$ denotes the load work. By neglecting the ADB area, it is possible to affirm that the energy available for the crack propagation is the same in case of *fixed grip* and *constant load*, i.e. the area OAB. In particular, in the fixed grip case, the available energy arises from the elastic energy, whereas in the constant load case from the load.

Therefore, crack growth occurs if:

$$\frac{dU}{da} = \frac{dW}{da} \tag{2.3.3}$$

where U is the elastic energy and W the energy required for the crack propagation. For a plate of unit thickness, the elastic energy may be expressed as:

$$\frac{dU}{da} = \frac{\pi\sigma^2 a}{E} \tag{2.3.4}$$

The quantity dU/da and the energy consumed during propagation may be also defined as:

$$\begin{aligned} G &= \frac{\pi\sigma^2 a}{E} \\ R &= \frac{dW}{da} \end{aligned} \tag{2.3.5}$$

where G is called *Energy Release Rate* (ERR) or *Crack Driving Force*, which dimensions are $[J/m^2]$ or $[N/m]$, and R is the *Crack Resistance*. In plane strain state, it is possible to assume that the energy necessary to the crack propagation keeps constant for each da increment, thus $R = cost.$, therefore, condition for the crack growth is that ERR reaches a critical value G_{IC}:

$$G_{IC} = \frac{\pi\sigma_c^2 a}{E} \tag{2.3.6}$$

which, by using Eq. (2.3.2), becomes:

$$G_{IC} = \frac{K_{IC}^2}{E} \tag{2.3.7}$$

Therefore, in Fig. 2.11 the criterion for crack propagation in an homogeneous material is shown when R is assumed to be constant. The ERR of a crack of length OF, subjected to a stress σ_2 is equal to A, which means that the crack does not propagates. However, the same crack under $\sigma_1 > \sigma_2$ reaches the critical value G_{IC} and the crack grows along BC. On the contrary, a crack which length is OE subjected to σ_2

propagates along BD, which is parallel to FA.

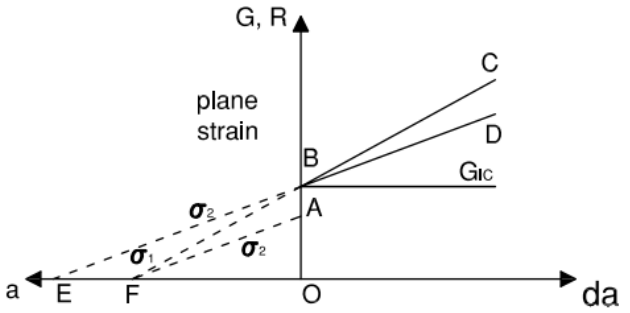

Figure 2.11: Energetic criterion in plane strain state

On the other hand, in a plane stress state, the Crack Resistance varies with da, Fig. 2.12. In particular, if $G < R$, the crack does not grow, point A, or the propagation stops at constant load, line BF. On the contrary, whereas if $G > R$ the crack grows in a unstable manner until fracture, point D.

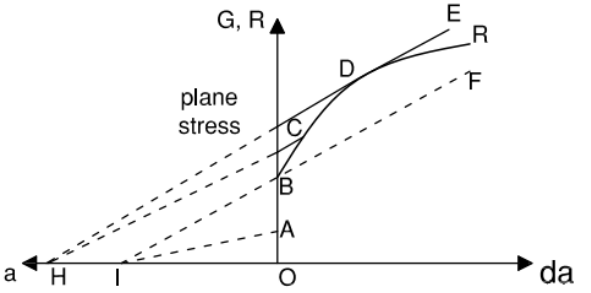

Figure 2.12: Energetic criterion in plane stress state

The energetic criterion in plane stress may be therefore set as:

$$\frac{\partial G}{\partial a} = \frac{\partial R}{\partial a} \tag{2.3.8}$$

If during crack propagation the plastic zone is not small, the ERR can not be longer evaluated from the elastic stress field. However, it is possible to use the so–called J *integral*, which is a contour path integral, independent of the path. By virtue of the conservation energy principle, in the $2D$ form, the J integral is given by:

$$J = \int_{\Gamma} \left(\mathbf{W} dy - \mathbf{T} \frac{\partial u}{\partial x} ds \right) \tag{2.3.9}$$

where Γ is a closed boundary oriented counterclockwise defined within a stressed solid, u is the displacement in the x–direction, ds is an element of Γ, and $\mathbf{W}$ and $\mathbf{T}$ are the strain energy per unit volume and the tension vector:

$$\begin{aligned} \mathbf{W} &= \mathbf{W}(x, y) = \mathbf{W}(\varepsilon) = \int_0^{\varepsilon} \sigma_{ij} d\epsilon_{ij} \\ \mathbf{T} &= \sigma \mathbf{n} \end{aligned} \tag{2.3.10}$$

where the tension vector $\mathbf{T}$ is perpendicular and outward to Γ. It is possible to demonstrate that $J = 0$ along a closed boundary.

In Fig. 2.13 the closed contour $ABCD$ around a crack tip is considered. The integral vanishes and it does not depend on the path. Indeed, since $T = 0$ and $dy = 0$ along the AB and CD lines, the contribution of AC is the same of that of BD but with opposite sign, [21, 23]. Moreover, since the J integral corresponds to the variation of potential energy for a virtual crack extension of da, it represents the elastic energy release rate, and it is an universal fracture criterion, which is valid in the linear elastic case, where $J = G$, as well as in the non–linear case.

2.3.2 Mixed mode Energy Release Rates

Crack propagation in orthotropic materials, or at the interface between components with different properties, may be a mixed mode dependent problem, in both cases of kinking or straight propagation. For this reason, it is extremely important to be able to extract the individual

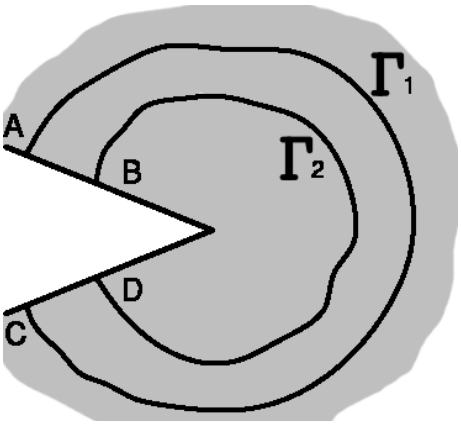

Figure 2.13: Closed contours around the crack tip

components of the total ERR, which can be expressed as their sum, $G = G_I + G_{II} + G_{III}$. In particular, G_I and G_{II} are generally defined as the work done by normal and shear traction at the interface through the correspondent jumps displacements, opening and sliding, respectively. However, this definition is somehow approximate in such cases where an oscillatory singularity exists.

In the first studies related to the evaluation of the ERR in laminates, the adjacent layers were considered as rigidly connected at the interface, so that the damaged zone were modeled by two arms, whereas the bonded region by a unique element. For example, Yin and Wang [24] evaluated the total ERR by starting from equilibrium of a portion of plate containing the crack tip, and then by using the J–integral concept. Another method, called *crack–tip force method*, was proposed by Park and Sankar in [25], where a delaminated plate is subdivided into 4 sublaminates, 2 behind and 2 ahead the crack tip, and the total ERR was evaluated through the jump in force and moment resultants arising across the crack tip.

Generally speaking, for the evaluation of the total ERR and its components, two different approaches may be adopted, the *global methods* and the *local methods*. According to the global methods, $ERRs$ are com-

puted from the generalized resultants and deformations obtained when the beam or plate theories are used. On the other hand, when the local methods are employed, *ERRs* depend on stresses and strains near the crack tip obtained from continuum models. Then, in the framework of a numerical analysis, the *virtual crack closure technique* can be used to evaluate the *ERR* modes.

Among the global and local methods, it is possible to adopt beam (plate) multi–layer models coupled with interface variables. As a matter of fact, how it will be shown theoretically in Section 2.4, and numerically in the next Chapter, these models have a certain number of advantages, such as a no vanishing *ERRs* for cracks tending to zero, and a well definition of the *ERR* modal components also in case of adjacent materials with elastic mismatch.

2.3.2.1 Global methods

The first studies on the modal partition of the *ERR* in laminated beams are those conducted by Williams in [26]. In the framework of a simplified global approach, namely by adopting the beam theory and by modeling the undelaminated region as a single element, the author proposed a partition rule based on the analysis of the forces acting on the cracked laminate. However, the Williams's assumptions were shown to be not generally fulfilled, for example in case of delaminated laminates with asymmetric arms. In fact, by considering for example a Double Cantilever Beam loaded at the two ends by opposite moments, the Williams approach predicts a pure Mode I loading also in case of asymmetric specimens, that is when arms have different thickness but, in this case, a sliding relative displacement exists at the interface, and the *ERR* has a modal dependence.

Bruno and Greco introduced then in [27] an interface model, which allows to obtain the *ERRs* by taking the limit of the strain energy per unit interface surface at the crack tip as the interfacial stiffness tends to infinity. Therefore, by modeling layers as Kirchhoff or Reissner–Mindlin

plates, the authors presented analytic solutions for energy release rates, also by taking into account the effect of shear deformability on the interlaminar fracture energies. In particular, when the Reissner–Mindlin plate theory is adopted, they shown that the undamaged region cannot be longer modeled as a single element, since section rotations are different in the upper and in the lower arm. Moreover, the $ERRs$ prediction, conducted through the J–integral, shows the presence of a coupling term between shear and normal stresses at the crack tip, which affects greatly the $ERRs$. The authors also concluded that the mode partition depends greatly on the hypothesis made for the stress distribution (see also [28, 29]).

A different approach was adopted by Diaz Diaz et al. [30], where $ERRs$ in delaminated plates are evaluated by using a layerwise stress model, referred as $LS1$. Indeed, since the $LS1$ model gives finite values of the interfacial stresses everywhere, also at the free edges, an analytic evaluation of the individual $ERRs$ is allowed. Also Qing et al. presented in [31] a semi–analytic solution for sublaminates, with either linear or curve delamination front, which interfaces are made by linear spring layers. A state space approach is adopted, and the major achieved advantage is that the obtained governing equations result independent from thickness and layer number. Then, Wang and Guan presented in [32] a numerical investigation for the evaluation of the individual component of the ERR in presence of mode mixity. A Double Cantilever Beam under tip bending moments is analyzed and an analytic modal partition method based on both, classic beam and Thimoshenko theories, is validated according to a FE analysis. The authors found that beam and Thimoshenko theory provide an upper or a lower bound for the strain energy rate partition. In particular, the analytic developments can be found in [33], where an average partition rules is also proposed.

Two layer symmetric scheme

A delaminated composite plate clamped at one end is now considered. In particular, the plate is subdivided into two homogeneous and isotropic

linear elastic sublaminates with equal properties, namely equal bending stiffness D, axial stiffness A, thickness h and width B. The two layers are connected by a linear elastic interface, which constitutive law is expressed by Eq. (1.3.36), (see Section 1.3.4 for further details).

The ERR components may be evaluated as the work done by the interlaminar stresses σ_{zz} and σ_{zx} through the correspondent displacement jump, Δw and Δu, respectively, as the interfacial stiffness parameters k_{zz} and k_{zx} tend to infinity for a virtual crack extension δa, further details will be given in Section 2.3.2.3. Consequently, ERR's components assume the following form:

$$\begin{aligned} G_I &= \frac{1}{2B} \lim_{k_{zz}\to\infty} k_{zz}\Delta w^2 \quad (if\ \Delta w > 0), \quad G_I = 0 \quad (if\ \Delta w < 0) \\ G_{II} &= \frac{1}{2B} \lim_{k_{zx}\to\infty} k_{zx}\Delta u^2 \end{aligned} \tag{2.3.11}$$

The $ERRs$ analytic expression for such a symmetric scheme will be below presented when both Kirchhoff or Reissner–Mindlin plate models are adopted, reporting the formulation and results achieved by Bruno and Greco in [27] and [28], respectively.

Kirchhoff plate theory

The Kirchhoff plate theory belongs to the category of $CLPT$, which governing equations can be found in Section 1.3.1, wherein transverse shear and normal effects are neglected. When the symmetric scheme represented in Fig. 2.14 is considered, as shown in [27], the problem may be solved through the stationarity of the system total potential energy.

In particular, when $T_1 = T_2$, the following expression for G_I is obtained:

$$G_I = \frac{(M_1 - M_2)^2}{4DB} \tag{2.3.12}$$

where no shear effect appears. On the other hand, when $T_1 = -T_2$, G_{II}

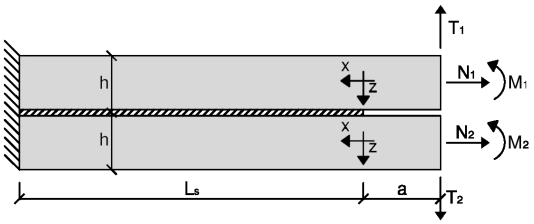

Figure 2.14: Two layer symmetric scheme

may be evaluated as:

$$G_{II} = \frac{A}{16B}\left[\frac{N_1 - N_2}{A} + \frac{h(M_1 - M_2)}{2D}\right]^2 \tag{2.3.13}$$

which depends on the mismatch between axial forces and moments of the same sign, and also in this case it does not include any contribution of the shear forces.

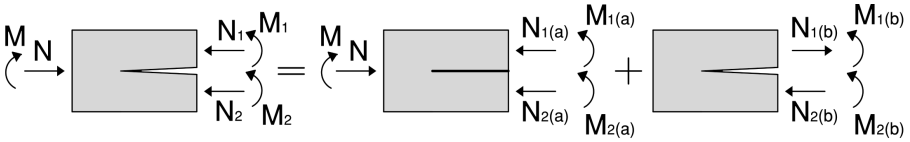

Figure 2.15: Decomposition of the stress resultants at the crack tip

In order to evaluate the influence of the loading conditions on the *ERRs*, according to Yin and Wang [24] and Bruno and Greco [27], two subsystems may be identified, Fig. 2.15:

$$\begin{aligned} N_1 &= N_{1(a)} - N_{1(b)} \\ N_2 &= N_{2(a)} + N_{2(b)} \\ M_1 &= M_{1(a)} + M_{1(b)} \\ M_2 &= M_{2(a)} + M_{2(b)} \end{aligned} \tag{2.3.14}$$

where $N_{1(b)} = N_{2(b)} = N_{(b)}$. The first subsystem does not contribute to the *ERRs*, and it can be solved by equilibrium considerations and by imposing equivalence of strain and curvature of the upper and lower

layer (complete solution is reported in [27]), which are denoted with the subscripts 1 and 2, respectively. On the other hand, the second subsystem produces a singular stress field and it may decomposed in turn, as shown in Fig. 2.16, as the sum of a Mode I and a Mode II stress resultant component:

$$\begin{aligned} N_{(b)} &= N_I + N_{II} \\ M_{1(b)} &= M_{1,I} + M_{1,II} \\ M_{2(b)} &= M_{2,I} + M_{2,II} = \eta_1 M_{1,I} + \eta_2 M_{1,II} \end{aligned} \tag{2.3.15}$$

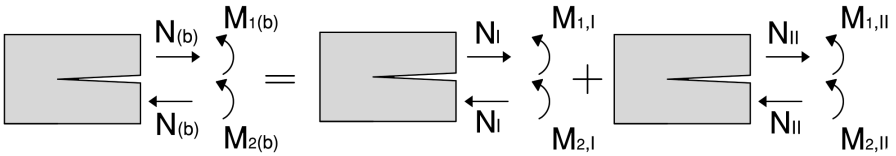

Figure 2.16: Effective loading system

The equilibrium of rotations at the crack tip gives:

$$\begin{cases} M_{1,I} + M_{2,I} - N_I \dfrac{h_1 + h_2}{2} = 0 \\ M_{1,II} + M_{2,II} - N_{II} \dfrac{h_1 + h_2}{2} = 0 \end{cases} \tag{2.3.16}$$

where h_1 and h_2 are the layer thicknesses. By substituting the third equation of (2.3.15) into Eq. (2.3.16), N_I and N_{II} can be expressed as:

$$\begin{aligned} N_I &= \frac{2(1+\eta_1)M_{1,I}}{h_1 + h_2} \\ N_{II} &= \frac{2(1+\eta_2)M_{1,II}}{h_1 + h_2} \end{aligned} \tag{2.3.17}$$

Since the ERR in case of layers made by different material may be

expressed as follows:

$$G = \frac{1}{2B}\left[\frac{N_{(b)}^2}{A_1} + \frac{N_{(b)}^2}{A_2} + \frac{M_{1(b)}^2}{D_1} + \frac{M_{2(b)}^2}{D_2}\right] \tag{2.3.18}$$

by substituting Eqs. (2.2.15) and (2.2.17) into Eq. (2.2.18), the ERR may be decomposed into the two components

$$\begin{aligned} G_I &= \frac{1}{2B}\left\{\frac{M_{1,I}^2}{D_1} + \frac{\eta_1^2 M_{1,I}^2}{D_2} + \left[\frac{2(1+\eta_1)M_{1,I}}{h_1+h_2}\right]^2\left(\frac{1}{A_1}+\frac{1}{A_2}\right)\right\} \\ G_{II} &= \frac{1}{2B}\left\{\frac{M_{1,II}^2}{D_1} + \frac{\eta_2^2 M_{1,II}^2}{D_2} + \left[\frac{2(1+\eta_2)M_{1,II}}{h_1+h_2}\right]^2\left(\frac{1}{A_1}+\frac{1}{A_2}\right)\right\} \end{aligned} \tag{2.3.19}$$

if the following quantity containing the mixed products vanishes:

$$\begin{aligned} G_{I,II} =& \frac{1}{2B}\left[\frac{2M_{1,I}M_{1,II}}{D_1} + \frac{2\eta_1\eta_2 M_{1,I}M_{1,II}}{D_2}\right] + \\ &+ \frac{1}{2B}\left[\frac{8(1+\eta_1)(1+\eta_2)M_{1,I}M_{1,II}}{(h_1+h_2)^2}\left(\frac{1}{A_1}+\frac{1}{A_2}\right)\right] \end{aligned} \tag{2.3.20}$$

The parameter η_1 can be evaluated by considering the condition of pure Mode I, namely when $N_1 = N_2 = N = 0$ and the two moments M_1 and M_2 produce the same strain at crack tip. In fact, in this case the bending moments are related by the parameter $\bar{\eta}_1$:

$$M_2 = \bar{\eta}_1 M_1 \tag{2.3.21}$$

where $\bar{\eta}_1 = -D_2 h_1/(D_1 h_2)$. Also the parameter η_1 can be expressed as the ratio of the moments resultants of the second subsystem, and Eq. (2.3.15) gives

$$\eta_1 = \frac{M_{2(b)}}{M_{1(b)}} = \frac{M_2 - M_{2(a)}}{M_1 - M_{1(a)}} = \frac{\bar{\eta}_1 M_1 - M_{2(a)}}{M_1 - M_{1(a)}} \tag{2.3.22}$$

which, as demonstrated in [27], leads to:

$$\eta_1 = -\frac{D_1 h_2^2 + D_2 h_1 (4h_1 + 3h_2)}{D_2 h_1^2 + D_1 h_2 (3h_1 + 4h_2)} \tag{2.3.23}$$

On the other hand, η_2 can be obtained by setting $G_{I,II} = 0$, and it is given by:

$$\eta_2 = \frac{h_2}{h_1} \tag{2.3.24}$$

Finally, the dual parameter of $\bar{\eta_1}$, $\bar{\eta_2} = M_2/M_1$, which gives only the Mode II ERR component, is

$$\bar{\eta_2} = \frac{D_2[D_2 h_1^2 + D_1 h_2 (3h_1 + 4h_2)]}{D_1[D_1 h_2^2 + D_2 h_1 (4h_1 + 3h_2)]} \tag{2.3.25}$$

Reissner–Mindlin plate theory

The Reissner–Mindlin plate theory, see the $FSDT$ in Section 1.3.2, allows to take into account the transverse shear deformations, and it is adopted in [28] in order to evaluate the influence of shear deformability on the $ERRs$. In particular, the total ERR is greater than when the $CLPT$ is adopted owing to the shear effect, and also to a coupling effect arising between normal and shear stresses and affecting the G_I component.

Moreover, it is worth noting that, in the perfectly bonded region, the condition of zero relative displacement at the interface, imposed through a penalty formulation, does not lead to null relative section rotations between adjacent layers owing to the shear deformation. For this reason, the undamaged region can not be modeled as a single plate.

The loading schemes represented in Fig. 2.17 will be now considered. In particular, the first scheme is referred as *Double Cantilever Beam* (DCB), the second as *End Loaded Split* (ELS), and the third as *Asymmetrically Loaded Double Cantilever Beam* if $N_1 = N_2 = 0$ ($ALDCB$), or as *Asymmetric End Loaded Split* ($AELS$) if $T_1 = N_1 = N_2 = 0$.

By considering the DCB configuration, the ERR, which involves only Mode I, can be obtained through the limit process of the stiffness

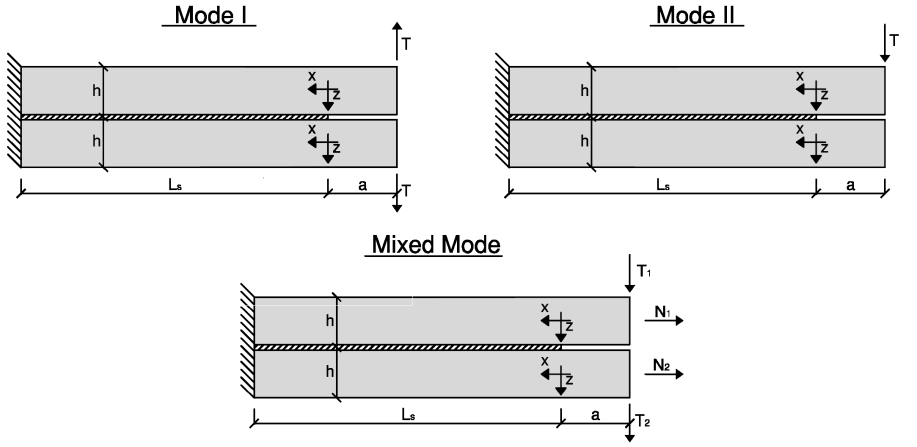

Figure 2.17: Two layer symmetric schemes loading condition

interfacial springs, or by employing the J–integral. However, the same results is achieved, which is:

$$G_I = \frac{M^2}{DB} + \frac{T^2}{HB} + \frac{2MT}{B\sqrt{HD}} \tag{2.3.26}$$

where H is the shear stiffness, Eq. (2.2.12), and $M = Ta$. In Eq. (2.3.26) two new terms appear with respect to the solution within the Kirchhoff theory, i.e. $M^2/(DB)$, which arise from the shear jump at the crack tip and from the coupling between bending and shear stresses, $T^2/(HB)$ and $2MT/(B\sqrt{HD})$, respectively.

The pure Mode II can be analyzed with reference to the ELS scheme, where the correspondent ERR, evaluated Bruno and Greco [28] by applying Eq. (2.3.11), is given by:

$$G_{II} = \frac{3M^2}{4DB} \tag{2.3.27}$$

which is the same value obtained from the $CLPT$ without any shear correction or coupling term, so that the undamaged region behaves like an unique plate.

For the mixed mode delamination, the third scheme of Fig. 2.17 can be considered and, depending on the loading condition, it reduces to the $AELS$ or $ALDCB$ configurations.

The $ERRs$ for the general configuration are:

$$\begin{aligned} G_I &= \frac{(M_1 - M_2)^2}{4DB} + \frac{(T_1 - T_2)^2}{4HB} + \frac{(M_1 - M_2)(T_1 - T_2)}{2B\sqrt{HD}} \\ G_{II} &= \frac{3}{16BD}\left[(M_1 + M_2) + 2D\left(\frac{N_1 - N_2}{Ah}\right)\right]^2 \end{aligned} \tag{2.3.28}$$

where $M_1 = T_1 a$ and $M_2 = T_2 a$, and the bending/shear interaction appears only in the Mode I ERR. In particular, this effect is greater for laminates with low shear to bending stiffness ratio.

2.3.2.2 Local methods

The mixed mode propagation of an interfacial crack between dissimilar materials may be treated also from a local point of view. However, since the ERR modal decomposition is obtained after evaluation of the stress field near the crack tip by means of a continuum analysis, some inherent difficulties related to stress singularity, interpenetration of the crack faces, and oscillatory behavior of the $ERRs$ may be encountered.

In this framework, an important work is that of Suo [34], who analyzed the problem of interfacial cracks and their interaction with pointwise stress singularities. Suo evaluated the SIF in case of crack within an infinite homogeneous medium in plane strain state and in bonded regions of different materials by using a complex potential, proposing also an universal relation able to extend the solution to the case of bi–material interfacial cracks. A comprehensive work treating the mixed mode cracking problem is that of Hutchinson and Suo [35], where the authors adopt the classical plate model to compute the total ERR, and a local continuum analysis to determine individual components. The continuum analysis refers to a simplified scheme, namely a semi–infinite crack subjected to remote edge load, and deals with the singular stress

field ahead a crack tip. However, although this method gives an accurate solution in term of stresses at the tip, it may be computationally expensive and it does not allow to taking into account shear deformability. Others important studies are those of He and Hutchinson, who analyzed in [36] the competition between the crack penetration and deflection into an interface, which was also treated by Buyukozturk [37], and of Eischen et al. [38], who compared three methods able to predict interfacial stresses in case of thermal loading. Then, by employing the J–integral concept and within the Kirchhoff plate theory, Sheinman and Kardomateas proposed in [39] an analytic formulation for the evaluation of the total ERR for a generic non–homogeneous material, and a modal partition rule valid under the assumption of orthotropic behavior. Recently, a mixed approach was adopted by Luo and Tong [40], who evaluated the $ERRs$ by employing a global method on a damaged laminate in case of pure bending moments, and then combined the obtained mode partition equations with a local method based on a crack–tip force model, proposing closed–form solutions in case of axial and bending moments.

The basic concepts related to the cracked bimaterial system represented in Fig. 2.18 in term of singular stress field and ERR partition will be now reported following Hutchinson and Suo [35].

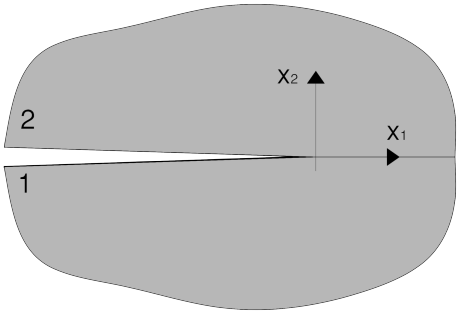

Figure 2.18: Bimaterial system with an interfacial crack

In the solution of the elasticity problem when two different materials, denoted hereafter with the subscripts 1 and 2, are bonded together, an

important role is recovered by the so–called *Dundurs* elastic mismatch parameters, which are defined as:

$$\begin{aligned} \alpha &= \frac{G_1(\kappa_2+1) - G_2(\kappa_1+1)}{G_1(\kappa_2+1) + G_2(\kappa_1+1)} \\ \beta &= \frac{G_1(\kappa_2-1) - G_2(\kappa_1-1)}{G_1(\kappa_2+1) + G_2(\kappa_1+1)} \end{aligned} \tag{2.3.29}$$

where

$$\begin{cases} \kappa_i = 3 - 4\nu_i & \textbf{plane strain} \\ \kappa_i = \dfrac{3-\nu_i}{1+\nu_i} & \textbf{plane stress} \end{cases} \qquad i = 1, 2 \tag{2.3.30}$$

The parameter α may be also expressed as:

$$\alpha = \frac{\bar{E}_1 - \bar{E}_2}{\bar{E}_1 + \bar{E}_2} \tag{2.3.31}$$

where the Young modulus take a different form in plane stress or plane strain state, according to Eq. (2.2.12). The admissible values of α and β are defined within a dominion of parallelogram shape, which is enclosed by $\alpha = \pm 1$ and $\alpha - 4\beta = \pm 1$. In particular, α measures the mismatch in the Young modulus across the interface ($\alpha \to 1$ denotes that the material 1 is stiffer then material 2), and β measures the mismatch in the in–plane bulk modulus ($\beta = 0$ for in–compressible materials with $\nu_1 = \nu_2 = 0.5$). Another parameter, called *oscillatory index*, can be defined as:

$$\bar{\epsilon} = \frac{1}{2\pi} \ln\left(\frac{1-\beta}{1+\beta}\right) \tag{2.3.32}$$

which is a very small quantity directly related to the oscillatory behavior of stresses and fracture energy (see Toya [41] for the influence of $\bar{\epsilon}$ on the *ERRs*). In particular, when the elastic mismatch disappears or $\beta = 0$, then $\bar{\epsilon} = 0$.

By introducing the *complex interface stress intensity factor*, defined as

$$K = K_1 + iK_2 \tag{2.3.33}$$

where $i = \sqrt{-1}$, the traction at the interface at a distance r from the crack tip may be expressed as

$$\sigma_{22} + i\sigma_{12} = \frac{(K_1 + iK_2)r^{i\bar{\epsilon}}}{2\pi r} \tag{2.3.34}$$

or as

$$\begin{aligned} \sigma_{22} &= \frac{Re(Kr^{i\bar{\epsilon}})}{2\pi r} \\ \sigma_{12} &= \frac{Im(Kr^{i\bar{\epsilon}})}{2\pi r} \end{aligned} \tag{2.3.35}$$

therefore the real and the imaginary part of K, K_1 and K_2, respectively, have the same meaning of the Mode I and Mode II SIF.

The relative displacement between the crack faces at a distance r along the negative x_1–axis are given by:

$$\delta_2 + i\delta_1 = \frac{8(K_1 + iK_2)r^{i\bar{\epsilon}}}{[1 + 2i\bar{\epsilon}\cosh(\pi\bar{\epsilon})]E^*} \left(\frac{r}{2\pi}\right)^{1/2} \tag{2.3.36}$$

where

$$\frac{1}{E^*} = \frac{1}{2}\left(\frac{1}{\bar{E}_1} + \frac{1}{\bar{E}_2}\right) \tag{2.3.37}$$

and the total ERR can be expressed as

$$G = \frac{1 - \beta^2}{E^*}(K_1^2 + K_2^2) \tag{2.3.38}$$

The normal and shear components of stresses and relative displacement are therefore not decoupled when $\beta \neq 0$. However, according to Hutchinson and Suo [35] an index of the *mode mixity* may be introduced and defined as:

$$\bar{\psi} = \tan^{-1}\left[\frac{Im(Kl^{i\bar{\epsilon}})}{Re(Kl^{i\bar{\epsilon}})}\right] = \tan^{-1}\left[\left(\frac{\sigma_{12}}{\sigma_{22}}\right)_{r=l}\right] \tag{2.3.39}$$

where l is a reference length which choice is somehow arbitrary. Indeed, l may be related to either the specimen geometry size (i.e. the crack

length) or to the material scale (i.e. process zone size), the influence of the l value on $\bar{\psi}$ is studied in [35].

2.3.2.3 Virtual crack closure technique

Starting from numerical results obtained by a FE analysis, the virtual crack closure technique ($VCCT$) allows to perform directly the ERR mode separation. In particular, two methods may be identified: the first one, which is referred as *finite crack extension method*, requires two numerical analyses, the other one, which is commonly referred as *modified virtual crack closure technique* or *virtual crack closure technique* requires only one numerical analysis. A comprehensive bibliographic overview regarding the virtual crack closure technique formulation and application can be found in the work of Krueger [42], which basic considerations will be below reported and summarized.

The *finite crack extension method* is based on the Irwin's crack closure integral method and on the assumption that the energy released during propagation of a crack from a length a to a length δa equals the energy necessary to close the crack. For this reason, it is necessary to carry out two FE analyses. At first, the crack is closed and forces are computed by summing those acting at common nodes located at the tip of the finite elements on the upper and lower side of the crack plane. Then, during a second analysis, the crack is extended of δa, and, at the same nodes of above, the relative displacement are evaluated. This method was employed for example by Toya in [41], where the Irwin crack closure method was adopted in order to evaluate ERR's components at a bimaterial interface. The author proved also the strong $ERRs$ oscillatory behavior as $\delta a \to 0$.

On the other hand, the *virtual crack closure technique* requires only one analysis since it is assumed that a crack extension of δa does not alter greatly the stress state at the tip. Therefore, nodal forces are evaluated at the crack tip, and relative displacements ahead a distance δa.

In a $2D$ FE analysis, where crack is represented by a $1D$ discon-

tinuity, i.e. a line, if a four–nodes finite element is used, the *ERRs* components may be evaluated as:

$$\begin{aligned} G_I &= -\frac{1}{2\delta a}\Sigma_v^i \Delta w^j \\ G_{II} &= -\frac{1}{2\delta a}\Sigma_h^i \Delta u^j \end{aligned} \tag{2.3.40}$$

where F_v^i and F_h^i are the vertical and horizontal forces, respectively, at the crack tip (i.e. node i), and Δw^j and Δu^j are the opening and sliding displacements, respectively, at a distance δa from the crack tip (i.e. node j). Since the ERR is evaluated as the ratio of the energy to the crack surface created, in this case the new crack surface is $\delta a \times 1$, where an unitary thickness is considered.

The $VCCT$, owing to its capability to directly furnish the modal decomposition, has been widely used in the analysis of composite delamination. Zou et al. [43] verify that, when sublaminates are used to model a delaminated composite, the $VCCT$ allows to decouple the modal components of the ERR, and that convergence is achieved by augmenting layer's number. Indeed, since in laminate theory each node represents the layer cross–section, the thickness dimension is eliminated and the oscillatory singularity is avoided. Therefore, stress singularity is transformed into a stress jump across the tip, namely into concentrated forces [19]. Also Bruno et al. [29] modeled a composite laminate by adopting multi–layer shear deformable plates and interface elements. In particular, the authors, in order to ensure continuity employed the Lagrange method in the undelaminated interfaces, whereas a penalty procedure in the undamaged region of the delaminated interface, as it will be show in Section 2.4. The total ERR is proved again to be not dependent on the sub–laminates division, whereas the relation between the individual $ERRs$ convergence and layers number is studied. It is found that the sublaminate subdivision must reflect the plate configuration, i.e. more layers for the thicker arm when the delamination is not sited at the mid–plane of the whole laminate. Then, Bruno et al. [44]

adopted this mathematical multi–layer representation of the debonding problem in case of strengthened beams, and proposed closed form solutions for specifics loading condition and geometric configurations in [18]. In case of a bimaterial system, also Yang et al. [45] evaluated the ERR components at the interface between concrete and FRP by using the $VCCT$, and analyzed influence of the parameters, such as Young modulus and layer thickness, on the ERR. The authors found that the bigger is the stiffness mismatch between the FRF and the concrete, the easier debonding takes place at the interface.

2.3.3 Interface toughness

The evaluation of *interface toughness*, or *critical energy release rate*, G_C is a crucial point in the composite material damage analysis since G_C is one of the parameters governing crack initiation and propagation. The interfacial toughness can be evaluated experimentally at the interfaces of *unidirectional* (UD) or *multidirectional* (MD) composite laminate, and in case of pure or mixed mode depending on the adopted specimen and loading condition. In particular, from the load–displacement curve obtained experimentally, it is possible to identify the crack initiation as the starting point of non–linearity. This critical point may be then used in the compliance method to evaluate the interface toughness. Moreover, it was proved by many researcher that, by passing from a pure Mode I condition to a pure Mode II, the load–displacement curve behavior changes. In fact, in Mode I load increases linearly up to crack initiation, and then reaches an approximately constant value denoting a stable propagation, whereas in pure Mode II load drops radically after crack initiation denoting an unstable crack propagation. Consequently, in mixed mode condition the load dropping, and instability, increases with the G_{II} percentage. These experimental evidences were obtained in studies conducted on UD glass/epoxy composites by Benzeggagh and Kenane [46], Kenane and Benzeggagh [47], Ducept et al. [48] and Mathews and Swanson [49]. In addition, analysis conducted by Prombut et.

al [50] proved that for UD laminates an analytic local method based on that of Hutchinson and Suo [35] matches well with numerical results, whereas in case of MD laminates analytic results appear to be no longer reliable. Hwang et al. and Andersons and König [51, 52] showed also that the critical ERR rises with the angle between plies at the interface, which however affects more G_{IIC} and, by considering cracked adhesive bondend joints, Dillard et al. [53] found that in some cases fracture toughness in presence of mixed mode is less than in pure Mode I. Interfacial fracture toughness, togheter with tensile and compressive strength, were also proved to be badly affected by the moisture content in case of concrete/epoxy bonded system by Lau and Büyüköztürk. [54].

Therefore, interface toughness in mixed mode condition is no longer a material parameter, but is function also of the modes percentage. As a consequence, crack initiation occurs when ERR reaches the interface toughness $\Gamma(\bar{\psi})$, which depends on the mode mixity $\bar{\psi}$ defined in Eq. (2.3.39). For example, a mixed mode toughness function reported by Hutchinson and Suo [35] is:

$$\Gamma(\bar{\psi}) = G_{IC}\{1 + \tan^2[(1-\alpha)\bar{\psi}]\} \tag{2.3.41}$$

wherein G_{IC} is the Mode I interface toughness and α is a sensitivity parameter accounting influence of Mode II. Indeed, for $\alpha = 1$ the material is ideally brittle and crack growth depends only on the fracture Mode I toughness for all mode combinations, whereas for $\alpha = 0$ crack propagation is driven only by the ERR Mode I component.

When $\beta \neq 0$, where β is one of the Dundurs parameters defined in Eq. (2.3.29), the interface toughness is also function of the reference length l and $\Gamma(\bar{\psi}, l)$ (see Section 2.3.2.2).

2.4 Multi–layer and interface models: a variational formulation

In the following Section an innovative multi–layer formulation is presented with the aim to analyze the onset and propagation of edge debonding for beams strengthened with externally bonded fiber–reinforced composite plates.

The three physical components of the system, namely the beam, the adhesive layer and the bonded plate, are modeled by means of one or several first–order shear deformable layers, assuming both strong and weak interface formulations for the two physical interfaces (i.e. beam/adhesive and adhesive/plate) and a strong formulation for the mathematical interfaces between layers. This multi–layer approach provides a refined methodology able to accurately predict the local quantities governing the debonding problem for reinforced beams, and thus overcomes the inaccuracies of the beam based models already proposed in the literature. Moreover, in Section 2.4.2 an analytic partition of the individual ERR components compatible with these models will be reported.

2.4.1 Theoretical formulation for a general multi–layer assembly

A damaged composite laminate composed by several unidirectional fiber reinforced plies is now considered, and formulation presented in Section 2.2.1, where each physical component is modeled by a single mathematical layer, will be here extended in case of multiple mathematical subdivision of components, namely the base beam, the adhesive layer and the FRP plate, Fig. 2.19.

Therefore, each physical layer is modeled by means of one or several mathematical first–order shear deformable layers, assuming both strong and weak interface formulations for the two physical interfaces (i.e. adhesive/concrete (AC) and adhesive/plate (AP)), in order to guarantee displacement continuity at the undelaminated interfaces, and a strong for-

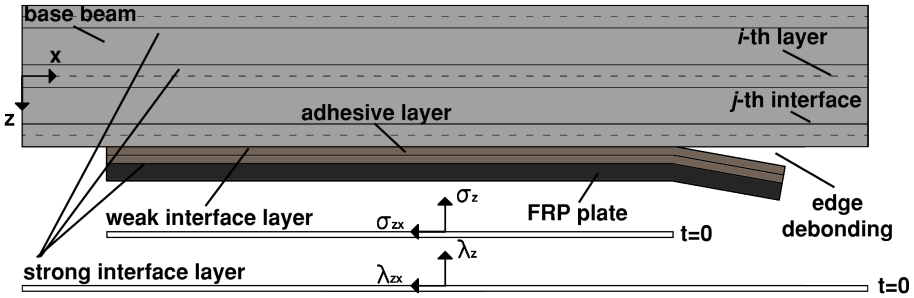

Figure 2.19: The analyzed strengthened structural system

mulation for the mathematical interfaces between layers, among which is of particular interest the one placed at the mid–adhesive location (MA).

In particular, for the strong interface formulation appropriate Lagrange multipliers, representing interfacial stresses, are introduced, whereas for the weak one a penalty-like method is adopted. It is worth noting that, when the stiffness parameters used within the weak interface formulation approach infinity, the penalty formulation becomes equivalent to the Lagrange multipliers method. On the other hand, as shown in the next Chapter, the weak interface formulation, assuming finite values for the stiffness parameters, allows to take into account for transverse deformability of the mathematical layers by means of an appropriate calibration of the stiffness parameters as a function of the geometrical and mechanical parameters of the physical system. As a consequence transverse deformability, neglected in the context of the adopted beam theory, can be simulated.

In the present variational formulation the following energy functional Π (for unit width) is introduced:

$$\Pi = U + \Lambda + I - W \tag{2.4.1}$$

in which U is the strain energy of the structural system, Λ is the Lagrange functional imposing displacement continuity for the strong interfaces, I the strain energy of the weak interface representing the penalty func-

tional, and W is the work done by the applied loads. In order to obtain the governing equations for the problem, the stationarity of Π, considering a variation of the generalized displacements in the layers and of the Lagrange multipliers, is considered:

$$\delta U + \delta \Lambda + \delta I - \delta W = 0 \tag{2.4.2}$$

where δ is the variational operator.

Although different locations for the debonding across the adhesive layer can be considered, and will be analyzed numerically in Chapter 3, for the sake of simplicity in the subsequent analytical developments it is assumed that the delamination is located at the physical interface between the adhesive layer and the concrete beam. Moreover, although strong or weak formulations can be adopted in the present model for each physical or mathematical interface, the weak interface formulation is here adopted only to model the interface containing the delamination, whereas all the remaining interfaces are modeled by means of a strong formulation. An elastic beam of length L and thickness H_b is considered. The beam is reinforced by means of an elastic FRP plate of thickness H_p bonded over the region $L_u \leq x \leq L_u + L_s$ through an adhesive layer of thickness H_a. Assuming that for the beam, the adhesive layer and the strengthening plate the width is equal to B, two different unstregthened regions are consided, the first one being defined for $0 \leq x \leq L_u$ and the second one for $L_u + L_s \leq x \leq L$, whereas it is assumed that debonding occurs in the region $L_u + L_s - a \leq x \leq L_u + L_s$. The horizontal axis x is oriented from left to right and the vertical axis z is oriented downwards. In the formulation distributed or concentrated loads are assumed acting only on the beam, and on the upper and lower side of the delamination n_b and $n_a + n_p$ mathematical layers are considered, respectively, assuming that the first layer is the lowest one and that the thickness of the i-th layer is t_i, Fig. 2.20. In particular, n_b, n_a and n_p are the number of layers considered for the base beam, the adhesive layer and the FRP

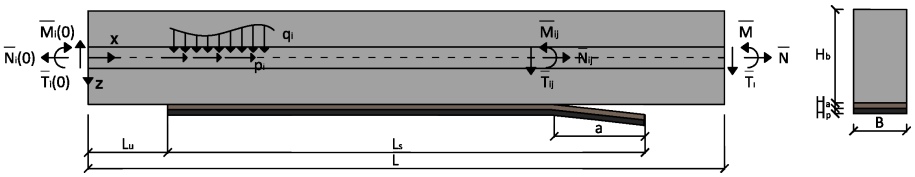

Figure 2.20: Mathematical notations and conventions for loads and stress resultants

plate, respectively.

Considering the mid-surface in-plane and transverse displacements, $u_i(x)$ and $w_i(x)$ respectively, and the rotations of transverse normals $\psi_i(x)$, for a generic layer the following kinematics expressions are respectively introduced for membrane strain at the reference surface, curvature and transverse shear strain:

$$\epsilon_i = u_i', \quad \kappa_i = \psi_i', \quad \gamma_i = \psi_i + w_i' \tag{2.4.3}$$

where prime denotes derivative with respect to x.

The first variation of strain energy is

$$\delta U = \int_{L_u}^{L_u+L_s} \sum_{i=1}^{n_p+n_a} [\sigma_i \cdot \delta\epsilon_i] \, dx + \int_0^{L} \sum_{i=n_p+n_a+1}^{n_p+n_a+n_b} [\sigma_i \cdot \delta\epsilon_i] \, dx \tag{2.4.4}$$

where $\sigma_i = \{N_i, M_i, T_i\}$ and $\epsilon_i = \{\epsilon, \kappa_i, \gamma_i\}$ are the vectors containing stress resultants and strains for the i–th layer, respectively, and dot denotes the scalar product. In particular, N_i is the membrane force resultant, M_i the moment resultant and T_i the transverse shear force resultant. With by considering the strong interface formulation, the variation of the Lagrange functional related to interface displacement continuity between adjacent layers can be expressed as:

$$\delta\Lambda = \int_{L_u}^{L_u+L_s} \sum_{j=1}^{n_p+n_a-1} [\lambda_j \cdot \delta\Delta\mathbf{u}_j] \, dx + \int_0^{L} \sum_{j=n_p+n_a+1}^{n_p+n_a+n_b-1} [\lambda_j \cdot \delta\Delta\mathbf{u}_j] \, dx \tag{2.4.5}$$

where $\Delta\mathbf{u}_j = \{\Delta u_j, \Delta w_j\}$ is the vector of the relative displacements at the j–th interface between the j–th and the $j+1$–th mathematical layer, defined as:

$$\begin{cases} \Delta u_j & = u_j - \dfrac{t_j}{2}\psi_j - u_{j+1} - \dfrac{t_{j+1}}{2}\psi_{j+1} \\ \Delta w_j & = w_j - w_{j+1} \end{cases} \tag{2.4.6}$$

and $\lambda_j = \{\lambda_{zxj}, \lambda_{zj}\}$ is the Lagrange multipliers vector, physically representing interlaminar stresses at the j–th interface, as shown in Fig. 2.19.

Assuming that debonding occurs at the physical interface between the adhesive layer and the concrete beam, a weak formulation is considered to assure displacements compatibility. In particular, for the $(n_p + n_a)$–th interface containing the crack, the variation of the strain energy assumes the form (see Section 1.3.4 and Eq. (1.3.36) for further details):

$$\delta I = \int_{L_u}^{L_u+L_s} \delta\Omega \; dx, \quad \Omega = \frac{1}{2}\mathbf{t}_{z\ n_p+n_a} \cdot \Delta\mathbf{u}_{n_p+n_a} \tag{2.4.7}$$

where $\Delta\mathbf{u}_{n_p+n_a} = \{\Delta u_{n_p+n_a}, \Delta w_{n_p+n_a}\}$ contains the relative displacements at the (n_p+n_a)–th interface and $\mathbf{t}_{z\ n_p+n_a} = \{\sigma_{zx\ n_p+n_a}, \sigma_{z\ n_p+n_a}\}$ contains the interlaminar normal ($\sigma_{zx\ n_p+n_a}$) and shear ($\sigma_{z\ n_p+n_a}$) stresses (see Fig. 2.19) that, in the weak interface formulation, assume the following expressions:

$$\sigma_{z\ n_p+n_a} = \bar{k}_z \Delta w_{n_p+n_a}, \quad \sigma_{zx\ n_p+n_a} = \bar{k}_{zx} \Delta u_{n_p+n_a} \tag{2.4.8}$$

with

$$\bar{k}_z = (1-d)k_z, \quad \bar{k}_{zx} = (1-d)k_{zx} \tag{2.4.9}$$

in which d is a variable taking the value 1 in the damaged zone and the value 0 in the bonded zone of the interface, and k_z and k_{zx} are the interface stiffness parameters (having dimensions FL^{-3}). In particular, when the stiffness parameters approach infinity, the penalty formulation

becomes equivalent to the Lagrange method.

Further, the variation of external load work is:

$$\delta W = \int_0^L \sum_{i=n_p+n_a-1}^{n_p+n_a+n_b} \left[p_i \delta u_i + q_i \delta w_i \right] \, dx + \delta \bar{W}^c + \delta \bar{W} \tag{2.4.10}$$

where p_i and q_i are respectively the distributed axial and transverse external loads applied to the i–th layer, $\delta \bar{W}^c$ is the variation of the work of concentrated external loads and bending moments, and $\delta \bar{W}$ is the variation of the work of external concentrated loads and bending moments at the two ends of each layer.

For the i–th mathematical homogeneous layer, the constitutive relations associated to an orthotropic behavior are defined by means of the classical extensional, bending-extensional coupling, bending stiffnesses and shear stiffnesses, assuming plane stress or plane stress conditions (see Section 1.3.2 for additional details):

$$\begin{Bmatrix} N_i \\ M_i \\ T_i \end{Bmatrix} = \begin{bmatrix} A_i & B_i & 0 \\ B_i & D_i & 0 \\ 0 & 0 & H_i \end{bmatrix} \begin{Bmatrix} \epsilon_i \\ \kappa_i \\ \gamma_i \end{Bmatrix} \tag{2.4.11}$$

Owing to the assumed strong formulation for the mathematical interfaces between layers, the constraint equations, expressing displacement continuity requirements, are obtained by means of the variation of Π with respect to Lagrange multipliers:

$$\begin{cases} \Delta u_j & = 0 \\ \Delta w_j & = 0 \end{cases}, \quad j = 1, ...n_p + n_a + n_b - 1, \; j \neq n_p + n_a \tag{2.4.12}$$

that, after considering Eqs. (2.4.6), become:

$$\begin{cases} w_i & = w_{n_p+n_a}, \quad i = 1, ..., n_p + n_a - 1 \\ w_i & = w_{n_p+n_a+1}, \quad i = n_p + n_a + 2, ..., n_p + n_a + n_b \end{cases} \tag{2.4.13}$$

$$\begin{cases} u_i = u_{n_p+n_a} + \dfrac{t_{n_p+n_a}}{2}\psi_{n_p+n_a} + \displaystyle\sum_{k=i+1}^{n_p+n_a-1} t_k\psi_k + \frac{t_i}{2}\psi_i, \\ \qquad i = 1, ..., n_p + n_a - 1, \\ u_i = u_{n_p+n_a+1} + \dfrac{t_{n_p+n_a+1}}{2}\psi_{n_p+n_a+1} + \displaystyle\sum_{k=n_p+n_a+2}^{i-1} t_k\psi_k - \frac{t_i}{2}\psi_i, \\ \qquad j = n_p + n_a + 2, ..., n_p + n_a + n_b \end{cases} \tag{2.4.14}$$

As a consequence, the independent displacement variables are reduced to only $n_p + n_a + n_b + 4$, which are:

$$\{w_{n_p+n_a}, w_{n_p+n_a+1}, u_{n_p+n_a}, u_{n_p+n_a+1}, \psi_i\} \qquad i = 1, ..., n_p + n_a + n_b \tag{2.4.15}$$

Using the above introduced expressions, and considering the fundamental lemma of variational calculus in conjunction with appropriate continuity conditions for the generalized displacement variables, is possible to obtain a boundary value problem characterized by two equations for the translational equilibrium in the x–direction and in the z–direction of the layer assemblies at the two sides of the interface crack, and by one equation for rotational equilibrium of each mathematical layer. Moreover, the variational procedure (see [18, 44] for additional details) gives the associated boundary (specified at $x = 0$ and at $x = L$ for the layers located on the upper side of the debonding interface; whereas specified at $x = L_u$ and $x = L_u + L_s$ for the layers located at the lower side of the debonding interface) and matching conditions (specified at $x = Lu$ and at $x = L_u + L_s$ for the layers located on the upper side of the debonding interface, and at $x = L_u + L_s - a$ for the two sets of layers at the two sides of the debonding interface).

The variational method leads also to determine the Lagrange multi-

pliers as follows:

$$\begin{aligned} \sigma_{zx\ i} &= \sum_{j=1}^{i} N'_j, \quad i = 1, ..., n_p + n_a - 1 \\ \sigma_{z\ i} &= \sum_{j=1}^{i} T'_j, \quad i = 1, ..., n_p + n_a - 1 \end{aligned} \tag{2.4.16}$$

or, alternatively, as

$$\begin{aligned} \sigma_{zx\ i} &= -\sum_{j=i+1}^{n_p+n_a+n_b} N'_j, \quad i = n_p + n_a + 1, ..., n_a + n_p + n_b - 1 \\ \sigma_{z\ i} &= -\sum_{j=i+1}^{n_p+n_a+n_b} T'_j, \quad i = n_p + n_a + 1, ..., n_a + n_p + n_b - 1 \end{aligned} \tag{2.4.17}$$

Moreover, it is possible to observe how the matching conditions are compatible with concentrated interfacial forces (with dimension force/length) arising as reactions to constraint equations only at the strong interface locations (i.e. for $j = 1, ..., n_p+n_a-1, n_p+n_a+1, ..., n_p+n_a+n_b-1$). For instance, at the crack front position ($x = L_u + L_s - a$), and for the layer assembly on the lower side of the interface crack, the matching force conditions are:

$$\begin{aligned} &\left[\!\left[\sum_{j=1}^{n_p+n_a} N_j \right]\!\right]_{L_u+L_s-a} = 0, \qquad \left[\!\left[\sum_{j=1}^{n_p+n_a} T_j \right]\!\right]_{L_u+L_s-a} = 0, \\ &\left[\!\left[M_1 + N_1 \frac{t_1}{2} \right]\!\right]_{L_u+L_s-a} = 0, \\ &\left[\!\left[M_i - \left(\sum_{j=1}^{i} N_j + \sum_{j=1}^{i-1} N_j \right) \frac{t_i}{2} \right]\!\right]_{L_u+L_s-a} = 0, \quad i = 2, ..., n_p + n_a - 1, \\ &\left[\!\left[M_{n_p+n_a} + \sum_{j=1}^{n_p+n_a-1} N_j \frac{t_j}{2} \right]\!\right]_{L_u+L_s-a} = 0 \end{aligned} \tag{2.4.18}$$

The concentrated forces at the i–th strong interface, arising from the discontinuities in membrane and shear stress resultants, similarly to Eq. (2.2.28) are characterized by the following expressions:

$$\begin{aligned} \Sigma_{zxi} &= \sum_{j=1}^{i} N_j^+ - \sum_{j=1}^{i} N_j^- \\ \Sigma_{zi} &= \sum_{j=1}^{i} T_j^+ - \sum_{j=1}^{i} T_j^- \\ & i = 1, ..., n_p + n_a - 1, n_p + n_a + 1, \\ & ..., n_p + n_a + n_b - 1 \end{aligned} \tag{2.4.19}$$

On the other hand, it must be evidenced that the boundary conditions at the cut off section ($x = L_u$) and at the end of the delaminated interface ($x = L_u + L_s$) for the lower layer assembly (i.e. $i = 1, ..., n_p + n_a$) are imposed in accordance with the requirement of free edge conditions. In particular, the free edge boundary conditions assume the same expressions of Eq. (2.4.17) where $L_u + L_s - a$ substituted by L_u, and where at $x = L_u$ it must be considered that

$$N_i^- = 0, \quad T_i^- = 0, \quad M_i^- = 0, \quad i = 1, ..., n_p + n_a \tag{2.4.20}$$

Assuming a weak formulation for the physical interface, and the corresponding interface stiffness parameters as finite, interface stress singularities at the interface crack tip are excluded since interfacial concentrated forces are not compatible with such interface formulation. On the contrary, when the stiffness parameters for the weak interface approach infinity, due to equivalence between the penalty formulation and the Lagrange multipliers method, stress singularities at the delamination front occur and turn out to be lumped into concentrated interfacial forces appearing as a consequence of the limit process. The interfacial concentrated forces, playing the role of the singular interlaminar stresses at the delamination tip caused by the interfacial crack in the context of the $2D$

elasticity, are fundamental in order to compute energy release rate during delamination growth since the in–plane and out–of–plane interfacial forces, directly correspond to the two mode of fracture, Mode II and Mode I, respectively. Moreover the use of a consistent approach rationally based on global parameters (crack tip interfacial forces) to compute ERR and its mode components, leads avoid the non–convergent behavior of mode partition arising when continuum FE methodologies are adopted, due to oscillatory stress singularities predicted by the $2D$ elasticity theory for an interface crack between two dissimilar materials (see [18, 44] for additional details).

Therefore, the major advantages of using the coupled multi–layer and interface elements models are related to the $ERRs$ evaluation. In fact, when a strong interface is used, it was proved by Greco et al. [18] that the total ERR does not decrease rapidly to zero for vanishing cracks, but has a smooth continuous behavior. On the other hand, when a weak interface is adopted, since interface stiffness and relative displacements have a finite value the stresses singularities are excluded, and the $ERRs$ may be computed also for a zero crack from these stresses, see Cornetti et al. [55].

In addition, also the individual model components of the ERR may be well defined, in both cases of strong or weak interface, in the former case from the vertical and horizontal interface concentrated forces, and in the latter by carrying out the penalty procedure. In fact, as proved by Bruno et al. [29], a good convergence of the individual $ERRs$ can be also obtained by refining the layer subdivision, which however may reflect the physical layer thicknesses.

However, although the numerical evaluation of $ERRs$ could be in theory easily obtained in terms of displacement variables calculated at the interface crack tip in the context of a weak interface, since the $ERRs$ must be computed in the limit as the interface stiffness parameters approach infinity, a very fine finite element mesh is required in proximity of the crack tip. Alternatively, it is possible to take advantage of the strong

interface formulation and to compute the energy release rate components as half the work of interfacial concentrated forces at the crack tip through corresponding displacement jumps occurring after the delamination is extended by an small (in theory infinitesimal) length da, according to the $VCCT$. For a sufficiently small da, the displacement jumps can be also evaluated at a distance da ahead the delamination tip, thus obtaining ERR and mode components by means of one stress analysis, see Section 2.3.2.3.

Consequently, the Mode I and Mode II ERR components at the interface crack tip can be expressed as:

$$\begin{aligned} G_I &= \lim_{k_{zx},k_z\to\infty} k_z \Delta w^2 = \frac{1}{2da}\Sigma_z \Delta w^+ \\ G_{II} &= \lim_{k_{zx},k_z\to\infty} k_{zx} \Delta u^2 \ = \frac{1}{2da}\Sigma_{zx} \Delta u^+ \end{aligned} \tag{2.4.21}$$

where in the first expression, valid for the weak interface formulation, Δw and Δu are the displacement jumps at the delamination tip, whereas in the second expression, applicable in the context of the strong interface formulation, Δw^+ and Δu^+ are the displacement jumps at a distance da ahead the delamination tip.

2.4.2 Analytic evaluation of the Energy Release Rates

In the present Section will be presented a closed form solution of the $ERRs$ components obtained in terms of force and moment resultants and generalized strains. In particular, the present formulation was proposed by Greco et al. [18] when the considered structural system (reinforced beam strengthened by FRP plate) is divided into two sub–laminates, and then extended to the case of general multi–layer assembly by Bruno et al. [29].

For a two layer assembly, where the FRP plate and the adhesive layer are coupled together, the relative displacements at interface (see

Eqs. (2.2.6) or (2.4.6)) reduce to:

$$\begin{cases} \Delta u = u_1 - \dfrac{t_1}{2}\psi_1 - u_2 - \dfrac{t_2}{2}\psi_2 \\ \Delta w = w_1 - w_2 \end{cases} \tag{2.4.22}$$

where the subscript 1 denotes the lower assembly, the vertical axis has positive values downward, and the positive side of the horizontal axis points to the right. The concentrated forces presented in Eq. (2.2.28) (or Eq. (2.4.19)) are given by

$$\begin{cases} \Sigma_z & = [\![T_1]\!]_d = -[\![T_2]\!]_d \\ \Sigma_{zx} & = [\![N_1]\!]_d = -[\![N_2]\!]_d \end{cases} \tag{2.4.23}$$

where the subscript d denotes the delamination tip, whereas the matching force conditions at the delamination tip can be obtained by adopting the same procedure carried out in Section 2.2.2, where a three layer assembly was studied, and are

$$\begin{aligned} &[\![N_1 + N_2]\!]_d = 0 \\ &[\![T_1 + T_2]\!]_d = 0 \\ &\left[\!\left[M_1 - N_2\frac{t_1}{2}\right]\!\right]_d = \left[\!\left[M_1 + N_1\frac{t_1}{2}\right]\!\right]_d \\ &\left[\!\left[M_2 - N_2\frac{t_2}{2}\right]\!\right]_d = \left[\!\left[M_2 + N_1\frac{t_2}{2}\right]\!\right]_d \end{aligned} \tag{2.4.24}$$

According to the $VCCT$, the Mode I component of the ERR is given by:

$$G_I = -\frac{1}{2da}\Sigma_z d\Delta w^+ \tag{2.4.25}$$

By virtue of Eqs. (2.4.3) and (2.4.22), the interface separation may be expressed as

$$d\Delta w^+ = -(w_1'^+ - w_2'^+)da = (\gamma_2^+ - \psi_2 - \gamma_1^+ + \psi_1)da \tag{2.4.26}$$

and, by considering Eq. (2.4.11) as

$$d\Delta w^{+} = \left(\frac{T_2^{+}}{H_2} - \frac{T_1^{+}}{H_1} - \psi_2 + \psi_1 \right) da \tag{2.4.27}$$

which takes into account the continuity of displacement variables across the crack tip (Eq. (2.2.39)). On the other hand, in the undelaminated region, the relative displacement vanishes, $d\Delta w^{-} = -(w_1'^{-} - w_2'^{-})da = 0$, and as a consequence:

$$\frac{T_2^{-}}{H_2} - \frac{T_1^{-}}{H_1} = \psi_2 - \psi_1 \tag{2.4.28}$$

Therefore, substitution of Eq. (2.4.28) into Eq. (2.4.27), together with Eq. (2.4.23), leads to express the Mode I ERR as:

$$G_I = -\frac{1}{2}[\![T_1]\!]_d \left(\frac{[\![T_2]\!]_d}{H_2} - \frac{[\![T_1]\!]_d}{H_1} \right) \tag{2.4.29}$$

which may rearranged as

$$G_I = -\frac{1}{2}[\![T_1]\!]_d [\![\gamma_2 - \gamma_1]\!]_d = \frac{1}{2}[\![T_1]\!]_d [\![\gamma_1 - \gamma_2]\!]_d \tag{2.4.30}$$

Since the shear stiffnesses are a material constant, namely $H_i^{+} = H_i^{-}$,

$$\frac{T_i^{+}}{\gamma_i^{+}} = \frac{T_i^{-}}{\gamma_i^{-}} \tag{2.4.31}$$

where $i = 1, 2$, and

$$T_i^{+}\gamma_i^{-} = T_i^{-}\gamma_i^{+} \tag{2.4.32}$$

Therefore, by developing the right hand side term of Eq. (2.4.30), and by using (2.4.32), the Mode I ERR becomes:

$$G_I = \frac{1}{2}\{[\![T_1\gamma_1 + T_2\gamma_2]\!]_d + 2[\![T_1]\!]_d(\gamma_2^{-} - \gamma_1^{-})\} \tag{2.4.33}$$

which, by considering Eq. (2.4.28) may be also expressed as

$$G_I = \frac{1}{2}\{[\![T_1\gamma_1 + T_2\gamma_2]\!]_d + 2[\![T_1]\!]_d(\psi_2 - \psi_1)\} \tag{2.4.34}$$

Therefore, by considering also Eq. (2.4.23), G_I can be set in the following form

$$G_I = \sum_{i=1}^{2}\left(\frac{1}{2}[\![T_i\gamma_i]\!]_d - [\![T_i]\!]_d\psi_i\right) \tag{2.4.35}$$

On the other hand, the Mode II ERR may be expressed, similarly to Eq. (2.4.24), as:

$$G_{II} = -\frac{1}{2da}\Sigma_{zx}d\Delta u^+ \tag{2.4.36}$$

where, owing to Eqs. (2.4.3) and (2.4.22),

$$d\Delta u^+ = -\left(u_1'^+ - \frac{t_1}{2}\psi_1'^+ - u_2'^+ - \frac{t_2}{2}\psi_2'^+\right) \tag{2.4.37}$$

and

$$d\Delta u^- = \left(u_1'^- - \frac{t_1}{2}\psi_1'^- - u_2'^- - \frac{t_2}{2}\psi_2'^-\right) = 0 \tag{2.4.38}$$

Therefore, the Mode II ERR may be rewritten by using Eqs. (2.4.3) and (2.4.23) in the following form:

$$G_{II} = \frac{1}{2}[\![N_1]\!]_d\left(\epsilon_1 - \epsilon_2 - \frac{t_1}{2}\kappa_1 - \frac{t_2}{2}\kappa_2\right)^+ \tag{2.4.39}$$

which is also equal to

$$G_{II} = \frac{1}{2}[\![N_1]\!]_d[\![\epsilon_1 - \epsilon_2 - \frac{t_1}{2}\kappa_1 - \frac{t_2}{2}\kappa_2]\!]_d \tag{2.4.40}$$

by virtue of Eq. (2.4.38).

By considering the matching conditions at the delamination tip, Eq. (2.4.24), one obtains:

$$G_{II} = \frac{1}{2}[\![N_1\epsilon_1 - N_1\epsilon_2 + M_1\kappa_1 + M_2\kappa_2]\!]_d \tag{2.4.41}$$

which is also equal to

$$G_{II} = \frac{1}{2}\left(\sum_{i=1}^{2}[\![N_i\epsilon_i + M_i\kappa_i]\!]_d - N_1^-\epsilon_1^+ - N_2^-\epsilon_2^+ - M_1^-\kappa_1^+ - M_2^-\kappa_2^+\right) \tag{2.4.42}$$

since $N_i^+\epsilon_i^- = N_i^-\epsilon_i^+$, similarly to Eq. (2.4.31).

In particular it is possible to demonstrate that:

$$\begin{aligned}&\frac{1}{2}(-N_1^-\epsilon_1^+ - N_2^-\epsilon_2^+ - M_1^-\kappa_1^+ - M_2^-\kappa_2^+) = \\ &= -\frac{1}{2}[\![N_1]\!]_d(\epsilon_1^- - \epsilon_2^-) - \frac{1}{2}[\![M_1]\!]_d\kappa_1^- - \frac{1}{2}[\![M_2]\!]_d\kappa_2^-\end{aligned} \tag{2.4.43}$$

However, these terms vanish since, due to Eqs. (2.4.24) and (2.4.38):

$$\begin{aligned}&\frac{1}{2}[\![N_1]\!]_d(\epsilon_1^- - \epsilon_2^-) = \frac{1}{2}[\![N_1]\!]_d\left(\kappa_1^-\frac{t_1}{2} + \kappa_2^-\frac{t_2}{2}\right) = \\ &= -\frac{1}{2}[\![M_1]\!]_d\kappa_1^- - \frac{1}{2}[\![M_2]\!]_d\kappa_2^-\end{aligned} \tag{2.4.44}$$

Therefore, the Mode II ERR is given by:

$$G_{II} = \frac{1}{2}\sum_{i=1}^{2}[\![N_i\epsilon_i + M_i\kappa_i]\!]_d \tag{2.4.45}$$

and the total ERR by

$$G = \sum_{i=1}^{2}\left(\frac{1}{2}[\![N_i\epsilon_i + M_i\kappa_i + T_i\gamma_i]\!]_d - [\![T_i]\!]_d\psi_i\right) \tag{2.4.46}$$

Then, Bruno et al. [29] proposed a generalized version of the $ERRs$

$$\begin{aligned}G_I &= \sum_{i=1}^{n_l+n_u}\left(\frac{1}{2}[\![T_i\gamma_i]\!]_d - [\![T_i]\!]_d\psi_i\right) \\ G_{II} &= \frac{1}{2}\sum_{i=1}^{n_l+n_u}[\![N_i\epsilon_i + M_i\kappa_i]\!]_d\end{aligned} \tag{2.4.47}$$

where n_l and n_u denote layers at the lower and upper side of the delaminated interface, respectively.

2.5 A coupled criterion for crack initiation

An important aspect which should be taken into account in order to obtain a realistic prediction of the actual debonding behavior of strengthened systems, is the crack initiation problem. This issue cannot be studied in the context of a classical Fracture Mechanics, and some of the several approaches developed in the literature will be reviewed in Section 2.5.1. Then, in Section 2.5.2, an innovative mixed mode coupled criterion able to predict debonding initiation accounting for both fracture energies and interfacial stresses, and valid within the $LEFM$, will be presented.

2.5.1 Literature review

The analysis of debonding phenomena at interfaces of strengthened systems requires the definition of a criterion able to predict, not only crack propagation, but also the crack initiation.

Several studies show that near the FRP free edges, similarly as near a notch, stresses are singular, and consequently a fulfillment of a stress condition leads to a null applied load for the crack onset. Moreover, the stress value obtained at the plate end in the FE analysis is high mesh dependent, therefore a simple stress criterion may not be able to represent properly the damage initiation. To overcome this issue, one way is to consider an average strength evaluated along a small length. However, the length choice is arbitrary, and it may depend on both material properties and structural sizes. Several stress criteria used to predicted crack initiation have been summarized by Borrelli [56] and are presented in Tab. 2.3, where $\sigma_{(c)t}$, $\sigma_{(c)c}$ and $\tau_{(c)}$ are the normal tensile and compressive strength and the shear strength in the different directions, which are denoted by subscripts 1, 2 and 3 (fiber direction,

its perpendicular within the ply plane, and outward direction), while σ_{eq} is an equivalent stress.

	$\sigma_3 \geq \sigma_{(c)3t},\ \tau_{31} \geq \tau_{(c)31},\ \tau_{32} \geq \tau_{(c)32}$
Hashin	$\left(\frac{\sigma_3}{\sigma_{(c)3t}}\right)^2 + \left(\frac{\tau_{23}}{\tau_{(c)23}}\right)^2 + \left(\frac{\tau_{31}}{\tau_{(c)31}}\right)^2 \geq 1$
Lee	$\sigma_3 \geq \sigma_{(c)3t}$ or $\sqrt{(\tau_{12}^2 + \tau_{13}^2)} \geq \tau_{(c)23}$
Ochoa	$\left(\frac{\sigma_3}{\sigma_{(c)3t}}\right)^2 + \frac{\tau_{23}^2 + \tau_{31}^2}{\tau_{(c)23}^2} \geq 1$
Brewer	$\left(\frac{\tau_{23}}{\tau_{(c)23}}\right)^2 + \left(\frac{\tau_{31}}{\tau_{(c)31}}\right)^2 + \left(\frac{\sigma_3^+}{\sigma_{(c)3t}}\right)^2 + \left(\frac{\sigma_3^-}{\sigma_{(c)3c}}\right)^2 \geq 1$
Tsai, 1997	$\frac{\sigma_1^2 - \sigma_1\sigma_3}{\sigma_{(c)1t}^2} + \left(\frac{\sigma_3}{\sigma_{(c)3t}}\right)^2 + \left(\frac{\tau_{23}}{\tau_{(c)23}}\right)^2 \geq 1$
Tong	$\frac{\sigma_1^2 - \sigma_1\sigma_3}{\sigma_{(c)1t}^2} + \frac{\sigma_3}{\sigma_{(c)3t}} + \left(\frac{\tau_{23}}{\tau_{(c)23}}\right)^2 \geq 1$
Degen	$\left(\frac{\sigma_1}{\sigma_{(c)1t}}\right)^2 + \left(\frac{\sigma_3}{\sigma_{(c)3t}}\right)^2 + \left(\frac{\tau_{23}}{\tau_{(c)23}}\right)^2 \geq 1$
Degen–Tong	$\left(\frac{\sigma_1}{\sigma_{(c)1t}}\right)^2 + \frac{\sigma_3}{\sigma_{(c)3t}} + \left(\frac{\tau_{23}}{\tau_{(c)23}}\right)^2 \geq 1$
Norris	$\frac{\sigma_1^2 - \sigma_1\sigma_3}{\sigma_{(c)1t}\sigma_{(c)1c}} + \left(\frac{\sigma_3}{\sigma_{(c)t}}\right)^2 + \left(\frac{\tau_{23}}{\tau_{(c)23}}\right)^2 \geq 1$
Tong–Norris	$\frac{\sigma_1^2 - \sigma_1\sigma_3}{\sigma_{(c)1t}\sigma_{(c)1c}} + \frac{\sigma_3}{\sigma_{(c)t}} + \left(\frac{\tau_{23}}{\tau_{(c)23}}\right)^2 \geq 1$
Wisnom	$2.6\sigma_{eq}^2 = (\sigma_1 - \sigma_2)^2 + (\sigma_2 - \sigma_3)^2 + (\sigma_3 - \sigma_1)^2 + 0.6\sigma_{eq}(\sigma_1 + \sigma_2 + \sigma_3)$

Table 2.3: Stress criteria for the crack onset prediction, [56]

On the other hand, also the classic Fracture Mechanics fails in predict debonding initiation since ERR vanishes when crack length approaches zero, and consequently an infinite load would be required for the crack initiation. For this reason, the fulfillment of a pure energetic requirements may be considered only in the analysis of crack propagation, i.e. when an initial defect is present and the ERR has a finite value. Therefore, total ERR or the individual components can be compared with

critical toughness values directly or according with a proper law. The propagation criteria summarized by Borrelli [56] are reported in Tab. 2.4.

	$G_I \geq G_{IC},\ G_{II} \geq G_{IIC},\ G_{III} \geq G_{IIIC}$
Hahn	$G_T \geq G_{IIC} - (G_{IIc} - G_{IC})\left(\frac{G_I}{G_{IC}}\right)^{1/2}$
Power Law	$\left(\frac{G_I}{G_{IC}}\right)^m + \left(\frac{G_{II}}{G_{IIC}}\right)^n + \left(\frac{G_{III}}{G_{IIIC}}\right)^p = 1$
White	$G_T \geq (G_{IIC} - G_{IC})e^{\eta\left(\frac{1}{G_{II}/G_I}\right)^{1/2}}$
Yan	$G_T \geq G_{IC} + \bar{\rho}\frac{G_{II}}{G_I} + \bar{\tau}\left(\frac{G_{II}}{G_I}\right)^2$
Benzeggagh–Kenane	$G_T \geq G_{IC} + (G_{IIC} - G_{IC})\left(\frac{G_{II}}{G_I + G_{II}}\right)^{\eta}$

Table 2.4: Energetic criteria for the crack propagation, [56]

where parameters $(m, n, p, \eta, \bar{\rho}, \bar{\tau})$ may be evaluated by correlation with experimental curves.

An energetic approach was also adopted by Martin et al. [57, 58], who focused on the competition between crack deflection or penetration at the fiber/matrix interface, by looking at the ERRs related to each crack path and the respective critical toughness. Another simplified method for the evaluation of a failure criterion for externally strengthened beams, and based on fracture mechanics, was developed by Rabinovitch [15]. The proposed criterion, adopting different analytic and numerical models ranging from the higher–order beam models to FE ones, is considered as an alternative to the classical allowable stress criteria, since the evaluated ERR is compared to the specific fracture of the bonded system. Then, Rabinovitch compared in [7] the $LEFM$ and the cohesive interface approaches for the debonding problems of strengthened beams, by pointing out both advantages and disadvantages.

However, a very innovative criterion for crack initiation were proposed also by Leguillon [59], who remarked that both energy and stress

criteria are necessary conditions for fracture, although neither one nor the other are sufficient. For this reason, a coupled stress/energy criterion was introduced, consisting in the simultaneous fulfillment of the two failure condition. A number of application of the *coupled criterion*, which has been adapted to specific loading conditions a damaged systems, may be found. For example, a variant of the coupled criterion was introduced in the framework of Finite Fracture Mechanics by Cornetti et al. [60] for quasi–brittle materials, by adopting an integral stress criterion in place of a point–wise one. Then, a theoretical study, based on a coupled point-wise stress criterion and an incremental energy criterion, has been developed by Mantič [61] for the prediction of the crack onset at the interface between a stiff circular cylindrical inclusion and a compliant unbounded matrix subjected to a remote uniaxial transverse tension. Recently, García and Leguillon [62] have extended the coupled criterion for brittle elastic materials under mixed mode loading, in order to consider the influence of the shear stresses and the mode–dependence of the fracture toughness. In [63, 64], the effects of micro–crack initiation and evolution under mixed mode loading conditions on the macroscopic response of elastic periodic composite materials, are investigated, analyzing both crack initiation by using a coupled stress and energy failure criterion and the subsequent propagation. Moreover, the influence of both material and geometrical nonlinearities on the homogenized response of composite solids containing microscopic defects, such as matrix cracking or interface debonding, has been investigated in [65, 66]. The coupled criterion was applied by Martin et al. [67] in order to predict edge debonding in composite laminates, pointing out as advantage, the possibility to overcome the arbitrary choice of a characteristic length necessary to employ an average stress criterion. Other applications are those of Hebel et al. [68], and of Müller et al. and Hell et al. [69, 70], who deal with the cracking initiation within adhesive joints.

2.5.2 Mixed mode coupled criterion

The coupled stress and energy failure criterion that will be below proposed is able to predict crack onset in case of mixed mode problems.

Basically, both a stress and an energy failure criterion must be satisfied simultaneously, leading to a system of two equations for two unknowns, which are the critical load level required for the crack onset β_c (intended as a multiplier of unit load) and the corresponding crack length a_c.

As far as the stress criterion is concerned, an integral or a point–wise form can be adopted (see Cornetti et al. and Andersons et al. [60, 71], for instance) and the non–linear equations system must be solved iteratively. In the next Chapter, both integral (Eq. (2.5.1)) and point–wise (Eq. (2.5.2)) form for the stress criterion will be adopted for the numerical evaluation of the edge debonding of reinforced concrete beams. In particular, the corresponding coupled failure criteria are respectively represented by the following equations:

$$\begin{cases} \dfrac{\beta^2 \int_0^a G_T(1,l)\ dl}{\int_0^a G_c\ dl} = 1 \\ \left(\dfrac{\beta \langle \int_0^a \sigma_y(1,l)\ dl \rangle}{\sigma_c\ a}\right)^2 + \left(\dfrac{\beta \langle \int_0^a \tau_x(1,l)\ dl \rangle}{\tau_c\ a}\right)^2 = 1 \end{cases} \tag{2.5.1}$$

$$\begin{cases} \dfrac{\beta^2 \int_0^a G_T(1,l)\ dl}{\int_0^a G_c\ dl} = 1 \\ \left(\dfrac{\beta \langle \sigma_y(1,l) \rangle}{\sigma_c\ a}\right)^2 + \left(\dfrac{\beta \langle \tau_x(1,l) \rangle}{\tau_c\ a}\right)^2 = 1 \end{cases} \tag{2.5.2}$$

where σ_c and τ_c denote the tensile and shear strengths, respectively, $G_T(1,l)$ is the total ERR for a unit load at the distance l from the plate end, $\sigma_y(1,l)$ and $\tau_x(1,l)$ are the normal and tangential interlaminar stresses for a unit load at a distance l behind the plate end, $<>$ are the Macaulay brackets and G_c is the fracture toughness. In particular, the proposed equations take into account that in linear elasticity stresses are directly proportional to load ($(\sigma_y, \tau_x) \sim \beta$), whereas ERR has a

quadratic proportionality ($G_T \sim \beta^2$) [70].

For a given a it is possible to calculate the load levels that guarantees the satisfaction of the stress and energy criterion. When the obtained load levels coincide, although within a small tolerance, the set of critical load and critical length is obtained (see [63, 64] for additional details).

Once the debonding onset length a_c is determined, the subsequent propagation starting from a_c may be modeled by using only the energetic criterion introduced in Eqs. (2.5.1) and (2.5.2), with the debonding length assumed to be a–priori known.

$$\beta^2 \frac{G_T}{G_c(\rho, \alpha)} = 1 \tag{2.5.3}$$

Bibliography

[1] B. Harris. *Engineering composite materials.* The Institute of Materials, London, 1999.

[2] L. Leonetti. *Multiscale approaches for failure anaylises of composite materials.* PhD thesis, Unversità della Calabria, 2014.

[3] N. A. Fleck. Compressive failure of fiber composites. *Advances in Applied Mechanics*, 33:43–117, 1997.

[4] B. Budiansky and N. A. Fleck. Compressive failure of fibre composites. *J. Mech. Phys. Solids*, 41(1):183–211, 1993.

[5] B. Budianksy and N. A. Fleck. Compressive kinking of fiber composites: a topical review. *Appl. Mech. Rev.*, 47(6):S246–S250, 1994.

[6] M. Achintha and C. Burgoyne. Fracture energy of the concrete–FRP interface in stregthened beams. *Engineering Fracture Mechanics*, 110:38–51, 2013.

[7] O. Rabinovitch. Debonding analysis of fiber–reinforced–polymer strengthened beams: Cohesive zone modeling versus a linear elastic fracture mechanics approach. *Engineering Fracture Mechanics*, 75:2842–2859, 2008.

[8] D. Bruno, F. Greco, S. Lo Feudo, and P. Nevone Blasi. Multi–layer modeling of edge debonding in strengthened beams using interface

stresses and fracture energies. *Engineering Structures*, Article in Press.

[9] O. Rabinovitch. An extended high order cohesive interface approach to the debonding analysis of FRP strengthened beams. *International Journal of Mechanical Sciences*, 81:1–16, 2014.

[10] P. Cornetti and A. Carpinteri. Modelling the FRP–concrete delamination by means of an exponential softening law. *Engineering Structures*, 33:1988–2001, 2011.

[11] J. G. Teng, H. Yuan, and J. F. Chen. FRP – to – concrete interfaces between two adjacent cracks: theoretical model for debonding failure. *Int. J. Solids Struct.*, 43:5750–5778, 2006.

[12] J. Teng, L. Zhang, and S. Smith. Interfacial stresses in reinforced concrete beams bonded with a soffit plate: a finite element study. *Construction and Building Materials*, 16:1–14, 2002.

[13] S. T. Smith and J. G. Teng. Interfacial stresses in plated beams. *Engineering Structures*, 23:857–871, 2001.

[14] O. Rabinovitch and Y. Frosting. Closed-form high–order analysis of RC beams strengthened with FRP strips. *Journal of Composites for Construction*, pages 65–74, 2000.

[15] O. Rabinovitch. Fracture–mechanics failure criteria for RC beams strengthened with FRP strips–a simplified approach. *Composite Structures*, pages 479–492, 2004.

[16] L. Zhang and J. Teng. Finite element prediction of interfacial stresses in structural members bonded with a thin plate. *Engineering Structures*, 32:459–471, 2010.

[17] C. P. Wu and H. C. Kuo. An interlaminar stress mixed finite element method for the analysis of thick laminated composite plates. *Composite Structures*, 24:29–42, 1993.

[18] F. Greco, P. Lonetti, and P. Nevone Blasi. An analytical investigation of debonding problems in beams strenghtened using composite plates. *Engineering Fracture Mechanics*, 74:346–372, 2007.

[19] Z. Zou, S. R. Reid, S. Li, and P. D. Soden. Application of a delamination model to laminated composite structures. *Composite Structures*, 56:375–389, 2002.

[20] Z. P. Bažant and J. Planas. *Fracture and Size Effect in Concrete and Other Quasibrittle Materials*. CRC Press, 1998.

[21] D. Broek. *Elementary Engineering Fracture Mechanics*. Klumer Academic Publishers, 4th edition, 1982.

[22] J. F. Knott. *Fundamental of Fracture Mechanics*. Butterworths, 1973.

[23] T. L. Anderson. *Fracture Mechanics. Fundamentals and Applications*. CRC Press. Taylor & Francis Group, 3th edition, 2005.

[24] W. L. Yin and J. T. S. Wang. The energy–release rate in the growth of a one–dimensional delamination. *Journal of Applied Mechanics*, 51(4):939–941, 1984.

[25] O. Park and B. V. Sankar. Crack–tip force method for computing energy release rate in delaminated plates. *Composite Structures*, 55:429–434, 2002.

[26] J. G. Williams. On the calculation of energy release rates for cracked laminates. *International Journal of Fracture*, 36(2):101–119, 1988.

[27] D. Bruno and F. Greco. Mixed mode delamination in plates: a refined approach. *International Journal of Solids and Structures*, 38:9149–9177, 2001.

[28] D. Bruno and F. Greco. Delamination in composite plates: influence of shear deformability on interfacial debonding. *Cement and Concrete Composites*, 23:33–45, 2001.

[29] D. Bruno, F. Greco, and P. Lonetti. A coupled interface–multilayer approach for mixed mode delamination and contact analysis in laminated composites. *International Journal of Solids and Structures*, 40:7245–7268, 2003.

[30] A. Diaz Diaz, J. F. Caron, and Ehrlacher A. Analytical determination of the modes I, II and III energy release rates in a delaminated laminate and validation of a delamination criterion. *Composite Structures*, 78:424–432, 2007.

[31] G. H. Quing, Y. H. Liu, and D. H. Li. A semi–analytical model for the energy release rate analyses of composite laminates with a delamination. *Finite Elements in Analysis and Design*, 47(9):1017–1024, 2011.

[32] S. Wang and L. Guan. On fracture mode partition theories. *Computational Materials Science*, 52:240–245, 2012.

[33] C. M. Harvey and S. Wang. Mixed–mode partition theories for one–dimensional delamination in laminated composite beams. *Engineering Fracture Mechanics*, 96:737–759, 2012.

[34] Z. Suo. Singularities interacting with interfaces and cracks. *International Journal of Solids and Structures*, 25(10):1133–1142, 1989.

[35] J. W. Hutchinson and Z. Suo. Mixed mode cracking in layered materials. *Advances in Applied Mechanics*, 29:63–191, 1992.

[36] M. Y. He and J. W. Hutchinson. Crack deflection at an interface between dissimilar elastic materials. *International Journal of Solids and Structures*, 25(9):1053–1067, 1989.

[37] O. Buyukozturk. Interface fracture and crack propagation in concrete composites. *Micromechanics of Concrete and Cementitious Composites*, pages 203–212, 1993.

[38] J. W. Eischen annd C. Chung and J. h. Kim. Realistic modeling of edge effect stresses in bimaterial elements. *Journal of Electronic Packaging*, 112:16–23, 1990.

[39] I. Sheinman and G. A. Kardomateas. Energy release rate and stress intensity factor for delaminated composite laminates. *International Journal of Solids and Structures*, 34(4):451–459, 1997.

[40] Q. Luo and L. Tong. Analytic formulas of energy release rates for delamination using a global-â€“local method. *International Journal of Solids and Structures*, 49:3335–3344, 2012.

[41] M. Toya. On mode I and mode II energy release rates of an interfacial crack. *International Journal of Fracture*, 56:345–352, 1992.

[42] R. Krueger. The virtual crack closure technique: history, approach and applications. *Appl Mech Rev*, 57(2):109–143, 2004.

[43] Z. Zou, S. R. Reid, P. D. Soden, and S. Li. Mode separation of energy release rate for delamination in composite laminates using sublaminates. *International Journal of Solids and Structures*, 38:2597–2613, 2001.

[44] D. Bruno, R. Carpino, and F. Greco. Modelling of mixed mode debonding in externally FRP reinforced beams. *Composite Science and Technology*, 67(7–8):1459–1474, 2007.

[45] Q. S. Yang, X. R. Peng, and A. K. H. Kwan. Strain energy release rate for interfacial cracks in hybrid beams. *Mechanics Research Communications*, 33:796–803, 2006.

[46] M. L. Benzeggagh and M. Kenane. Measurement of mixed–mode delamination fracture toughness of unidirectional glass/epoxy composites with mixed–mode bending apparatus. *Composite Science and Technology*, 56:439–449, 1996.

[47] M. Kenane and M. L. Benzeggagh. Mixed–mode delamination fracture toughness of unidirectional glass/epoxy composites under fatigue loading. *Composites Science and Technology*, 57:597–605, 1997.

[48] F. Ducept, D. Gamby, and P. Davies. A mixed–mode failure criterion derived from tests on symmetric and asymmetric specimens. *Composite Science and Technology*, 59:609–619, 1999.

[49] M. J. Mathews and S. R. Swanson. Characterization of the interlaminar fracture toughness of a laminated carbon/epoxy composite. *Composites Science and Technology*, 67:1489–1498, 2007.

[50] P. Prombut, L. Michel, F. Lachaud, and J. J. Barrau. Delamination of multidirectional composite laminates at $0°/\theta°$.

[51] J. H. Hwang, C. S. Lee, and W. Hwang. Effect of crack propagation directions on the interlaminar fracture toughness of carbon/epoxy composite materials. *Applied Composite Materials*, 8:411–433, 2001.

[52] J. Andersons and M. König. Dependence of fracture toughness of composite laminates on interface ply orientations and delamination growth direction. *Composites Science and Technology*, 64:2139–2152, 2004.

[53] D. A. Dillard, H. K. Singh, D. J. Pohlit, and J. M. Starbuck. Observations of decreased fracture toughness for mixed mode fracture testing of adhesively bonded joints. *Journal of Adhesion Science and Technology*, 23:1515–1530, 2009.

[54] D. Lau and Oral Büyüköztürk. Fracture characterization of concrete/epoxy interface affected by moisture. *Mechanics of Materials*, 42:1031–1042, 2010.

[55] P. Cornetti, V. Mantič, and A. Carpinteri. Finite fracture mechanics at elastic interfaces. *International Journal of Solids and Structures*, 49:1022–1032, 2012.

[56] R. Borrelli. *Sviluppo di procedure numeriche per la simulazione del danno in strutture in composito*. PhD thesis, Università degli Studi di Napoli "Federico II", 2011.

[57] E. Martin, P. W. M. Peters, D. Leguillon, and J. M. Quenisset. Conditions for matrix crack deflection at an interface in ceramic matrix composites. *Material Science and Engineering*, A250:291–302, 1998.

[58] E. Martin, D. Leguillon, and C. Lacroix. A revisited criterion for crack deflection at an interface in a brittle bimaterial. *Composites Science and Technology*, 61:1671–1679, 2001.

[59] D. Leguillon. Strength or toughness? a criterion for crack onset at a notch. *European Journal of Mechanics A/Solids*, 21:61–72, 2002.

[60] P. Cornetti, N. Pugno, A. Carpinteri, and D. Taylor. Finite fracture mechanics: A coupled stress and energy failure criterion. *Engineering Fracture Mechanics*, 73:2021–2033, 2006.

[61] V. Mantič. Interface crack onset at a circular cylindrical inclusion under a remote transverse tension. application of a coupled stress and energy criterion. *International Journal of Solids and Structures*, 46:1287–1304, 2009.

[62] I. Garcìa and D. Leguillon. Mixed–mode crack initiation at a v–notch in presence of an adhesive joint. *International Journal of Solids and Structures*, 49:2138–2419, 2012.

[63] F. Greco, L. Leonetti, and P. Nevone Blasi. Non–linear macroscopic response of fiber–reinforced composite materials due to initiation and propagation of interface cracks. *Engineering Fracture Mechanics*, 80:90–113, 2012.

[64] F. Greco, L. Leonetti, and P. Lonetti. A two–scale failure analysis of composite materials in presence of fiber/matrix crack initiation

and propagation. *International Journal of Solids and Structures*, 95:582–597, 2013.

[65] F. Greco and R. Luciano. A theoretical and numerical stability analysis for composite microstructures by using homogenization theory. *Composites: Part B*, 42(3):382–401, 2011.

[66] F. Greco. A study of stability and bifurcation in micro–cracked periodic elastic composites including self–contact. *International Journal of Solids and Structures*, 50:1646–1663, 2013.

[67] E. Martin, D. Leguillon, and N. Carrère. A twofold strength and toughness criterion for the onset of free–edge shear delamination in angle–ply laminates. *International Journal of Solids and Structures*, 47:1297–1305, 2010.

[68] J. Hebel, R. Dieringer, and W. Becker. Modelling brittle cracks formations at geometrical and material discontinuities using a finite fracture mechanics approach. *Engineering Fracture Mechanics*, 77:3558–3572, 2010.

[69] A. Müller, W. Becker, D. Stolten, and J. Hohe. A hybrid method to assess interface debonding by finite fracture mechanics. *Engineering Fracture Mechanics*, 73:994–1008, 2006.

[70] S. Hell, P. Weißgraeber, J. Felger, and W. Becker. A coupled stress and energy criterion for the assessment of crack initiation in single lap joints: A numerical approach. *Engineering Fracture Mechanics*, 117:112–126, 2014.

[71] J. Andersons, S. Tarasovs, and E. Spārņinš. Finite fracture mechanics analysis of crack onset at a stress concentrations in a UD glass/epoxy composite in off-axis tension. *Composites Science and Technology*, 70:1380–1385, 2010.

Chapter 3

Numerical computation of interfacial stresses and fracture energies

In this Chapter numerical calculations, carried out by means of the proposed multi–layer model, and by using the commercial finite element software Comsol Multiphysics 4.4 [1], are presented in order to evaluate interfacial stresses and fracture energy of a reinforced concrete beams strengthened with externally bonded fiber–reinforced composite plates. This multi–layer approach provides a refined methodology able to accurately predict the local quantities governing the debonding problem for reinforced beams and thus overcomes the inaccuracies of the beam based models already proposed in the literature. Specifically the proposed multi–layer model leads to an accurate evaluation of interface stresses in bimaterial interface systems, despite its reduced computational cost with respect to a continuum FE model, and provides well defined fracture energies for bimaterial interface systems, avoiding the non–convergent behavior of mode partition arising when continuum elasticity models are adopted.

Therefore, the accuracy of the multilayer formulation, implemented

by using a one–dimensional finite element model, is analyzed showing comparisons with results obtained by using the more computational demanding continuum FE model, which is presented in Sections 3.1.1 and 3.2.1.

In particular, in Section 3.1.2 a comparison between the $2D$ continuum model and the proposed FE multi–layer formulation in terms of interfacial stresses is carried out with reference to a simply supported beam strengthened by a steel plate and subjected to an uniformly distributed load. Then, in Section 3.1.3 a Three Point Bending (TPB) loading scheme is considered. Finally, in Section 3.2, fracture energies for the TPB scheme evaluated by using the $2D$ continuum model and the multi–layer models are compared.

3.1 Interfacial stress prediction

3.1.1 2D Finite Element model

The behavior of shear and normal interlaminar stresses in a simply supported beam reinforced with a bonded plate, at different section locations across the adhesive layer, are here investigated. Three section locations are studied, namely the adhesive/concrete and the adhesive/plate interfaces and the mid-adhesive section, which will be denoted hereafter as AC, AP and MA, respectively.

In order to accurately calibrate the $2D$ FE model solution (especially in terms of mesh organization), a comparison of interfacial stresses with the solution obtained by Teng et al. [2] is carried out with reference to a simply supported beam strengthened by a steel plate, as shown in Fig. 2.20, and subjected to a uniformly distributed load of 15 N/mm; geometrical and material properties for the analyzed scheme are the same of those used in [2] and are reported in the following Tab. 3.1. In particular, the calibration of the $2D$ FE model is essential not only to assess the accuracy of the proposed multi–layer formulation in terms of interfacial stresses, but also in view of its use for the second application

Component	Width [mm]	Thickness [mm]	Length [mm]	Young modulus [MPa]	Poisson's ratio
Concrete beam	100	150	2,400	20,000	0.17
Adhesive layer	100	4	1,800	2,000	0.25
Bonded plate	100	4	1,800	200,000	0.30

Table 3.1: Geometrical and material properties for the simply supported strengthened beam

which will be developed in Section 3.1.3, for which, contrarily to the present case, $2D$ FE solutions in terms of interfacial stresses are not available in the literature.

The modeling of an accurate $2D$ FE model constitutes a difficult task since very different thicknesses are involved by the physical components of the system, and due to the fact that stress singularities arise at the plate end. In fact, as a consequence of the stress singularities, the stresses near the plate end are high mesh dependent, generally rising by refining the mesh, and a very fine mesh is needed in order to obtain accurate results. Therefore, to properly calibrate the $2D$ FE model, a mapped mesh with a local refinement near the singularity points located at the plate end, for the AC and AP interfaces, is accounted in numerical simulations.

The analysis of the composite system is carried out with reference to a unit width, and a two–dimensional formulation is considered, assuming that the loads are constant in the width direction and, consequently, all the generalized displacements are independent on the correspondent coordinate. Since a strengthened beam geometry is here analyzed (with the width dimension comparable with the height one) plane stress conditions are adopted, whereas plane strain conditions can be assumed in the case of strengthened plates in cylindrical bending (with the width dimension comparable to the length one). Therefore, $2D$ plane stress four–noded quadrilateral elements are used, and results obtained by varying the smallest element size and the number of elements across the adhesive according to Tab. 3.2 are compared with those reported in [2].

Minimum element size [mm]	Number of elements
0.4	8
0.2	12
0.1	16

Table 3.2: Minimum element size and number of elements across the adhesive layer

As in [2], the smallest elements are placed near the AC and the AP interfaces, the adhesive is divided vertically by the other elements, and horizontally a graded mesh is used, by starting with an aspect ratio of 1 for the smallest element. A graded mesh is also used for the Reinforced Concrete (RC) beam and the FRP plate.

In order to guarantee displacement continuity, a strong interface formulation is accounted for the physical interfaces, by means of the "Form Union" option implemented in the Comsol Multiphysics software and, to best catch stresses at the MA, the adhesive is subdivided into two elements. For example, when the minimum element height is of 0.1 mm, the FE model involves $2,510,766$ degrees of freedom and $417,600$ mesh elements. The $2D$ FE model mesh near the plate end is shown in Fig. 3.1

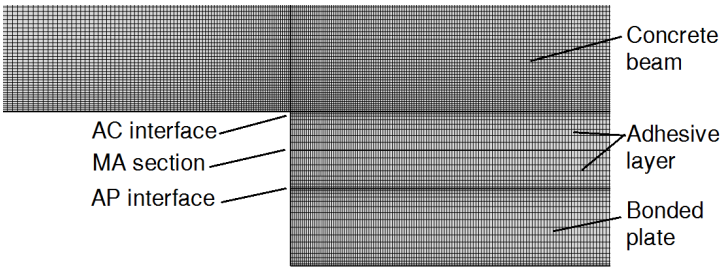

Figure 3.1: Finite element mesh in the case of the perfectly bonded 2D FE continuum model when the size of the smallest element is equal to 0.1 mm

Minimum element size [mm]	**AC interfacial stresses [MPa]**			**Relative error %**	
	Model	Normal	Shear	Normal	Shear
0,4	Teng et al.	17,00	-5,32	13,05%	2,85 %
	Present 2D FE	19,22	-5,47		
0,2	Teng et al.	21,60	-6,47	13,40 %	3,07 %
	Present 2D FE	24,49	-6,67		
0,1	Teng et al.	27,10	-7,97	12,56 %	1,21 %
	Present 2D FE	30,50	-8,07		

Table 3.3: Normal and shear stresses near the plate end at the AC interface: comparisons with results obtained in [2]

Minimum element size [mm]	**MA section stresses [MPa]**			**Relative error %**	
	Model	Normal	Shear	Normal	Shear
0,4	Teng et al.	2,63	-0,95	0,20 %	-11,07 %
	Present 2D FE	2,64	-0,84		
0,2	Teng et al.	2,60	-0,47	0,38 %	-9,33 %
	Present 2D FE	2,61	-0,43		
0,1	Teng et al.	2,59	-0,24	0,70 %	-3,68 %
	Present 2D FE	2,61	-0,23		

Table 3.4: Normal and shear stresses near the plate end at the MA section: comparisons with results obtained in [2]

Minimum element size [mm]	**AP interfacial stresses [MPa]**			**Relative error %**	
	Model	Normal	Shear	Normal	Shear
0,4	Teng et al.	-12,00	-1,39	-1,80 %	23,23 %
	Present 2D FE	-11,78	-1,71		
0,2	Teng et al.	-14,30	-1,35	-1,55 %	28,74 %
	Present 2D FE	-14,08	-1,74		
0,1	Teng et al.	-16,70	-1,42	-1,67 %	45,55 %
	Present 2D FE	-16,42	-2,07		

Table 3.5: Normal and shear stresses near the plate end at the AP interface: comparisons with results obtained in [2]

Therefore, interfacial shear and normal stresses near the plate end, obtained by means of the above described $2D\ FE$ models, are represented in the following Figures 3.2, 3.3 and 3.4, with reference to the AC interface, the MA section and the AP interface, respectively, by varying

the height of the smallest element. Moreover, in Tabs. 3.3, 3.4 and 3.5 the values of stresses obtained at the plate end by the present $2D$ FE model and by Teng et al. [2] are compared.

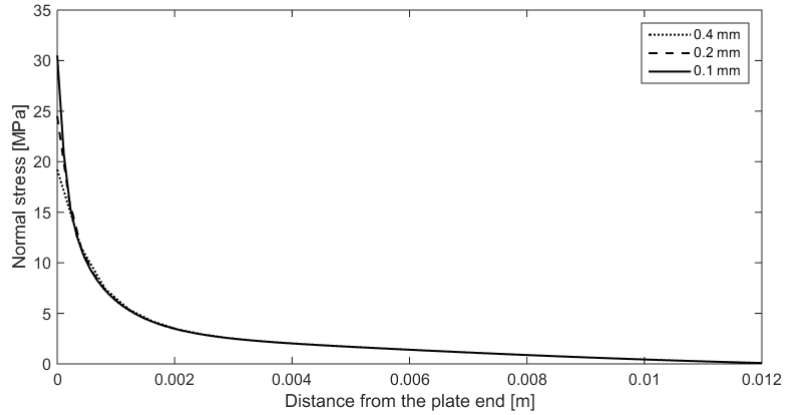

(a)

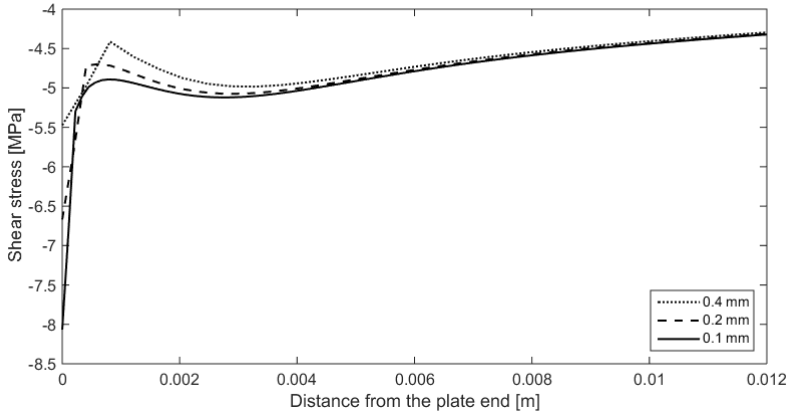

(b)

Figure 3.2: (a) Normal and (b) Shear stresses at the AC interface by varying the mesh size

From the aforementioned Figures it is possible to remark that, as expected, there is an high concentration of stresses near the plate end. Moreover, normal stresses pass to be tensile in AC to compressive in AP, which is one of the reason delamination generally occurs in AC,

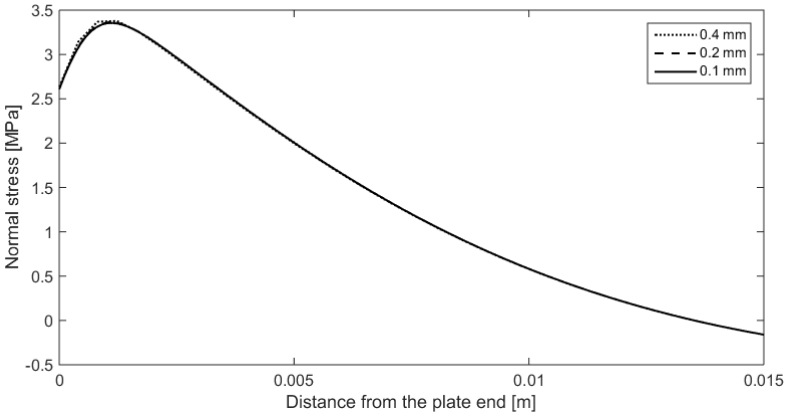

(a)

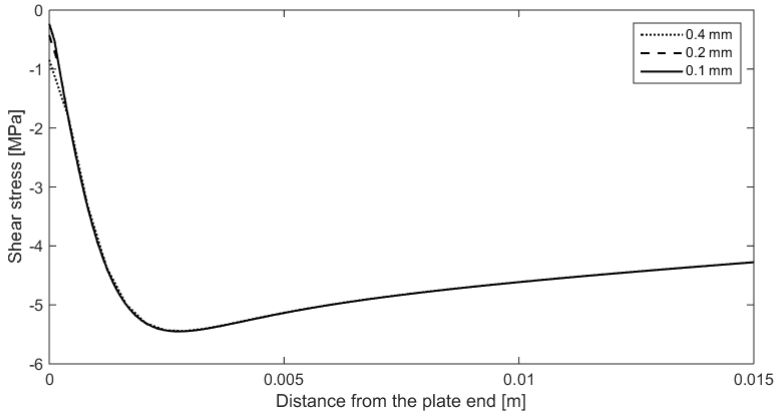

(b)

Figure 3.3: (a) Normal and (b) Shear stresses in the MA section by varying the mesh size

and shear stresses in the MA tend to vanish, which satisfies the condition of zero shear stress at a free surface. As far as the mesh size is concerned, generally the stresses are affected only within a small region near the plate end, and a refined mesh leads to higher maximum values. Consequently, by considering Tabs. 3.3 – 3.5, and according also to [2], only in MA, where no singularity occurs, stresses converge with the element size and, for this reason the most accurate mapped mesh is

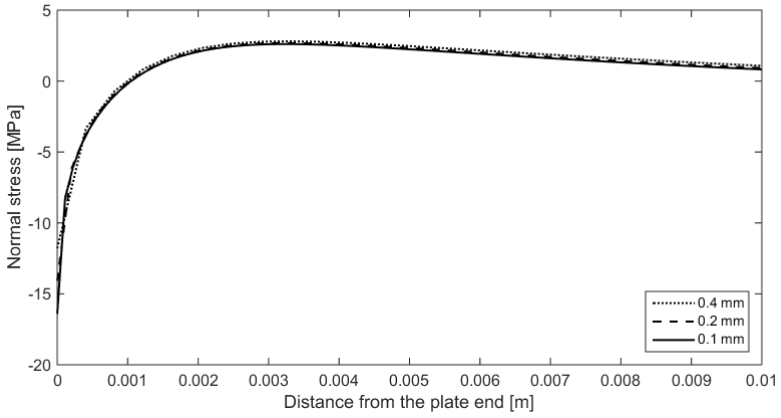

(a)

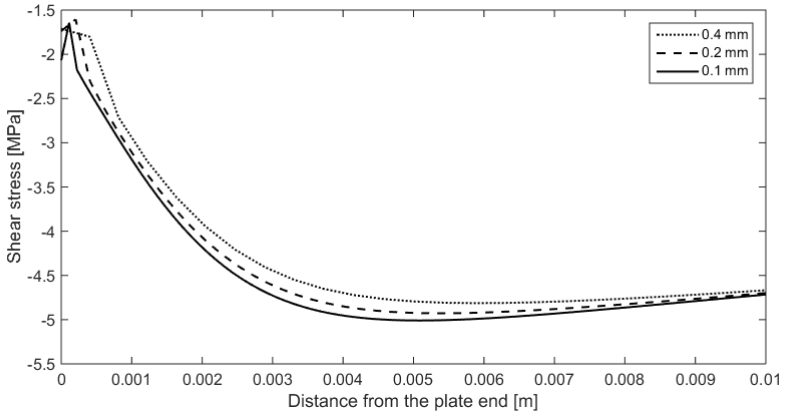

(b)

Figure 3.4: (a) Normal and (b) Shear stresses at the AP interface by varying the mesh size

considered that one with the minimum element height of 0.1 mm.

Figure 3.5, 3.6 and 3.7 show how results carried out by means of the proposed $2D$ model with the finest mesh are in good agreement with the solution developed by Teng et al. [2] for all the analyzed locations across the adhesive layer. Moreover, also the analytic solution of Smith and Teng [3], which is based on the assumption of constant normal and shear stresses across the adhesive thickness and it does not take into account

shear deformation, is presented. It can be seen that such a formulation gives reasonable approximation of stresses along the MA section.

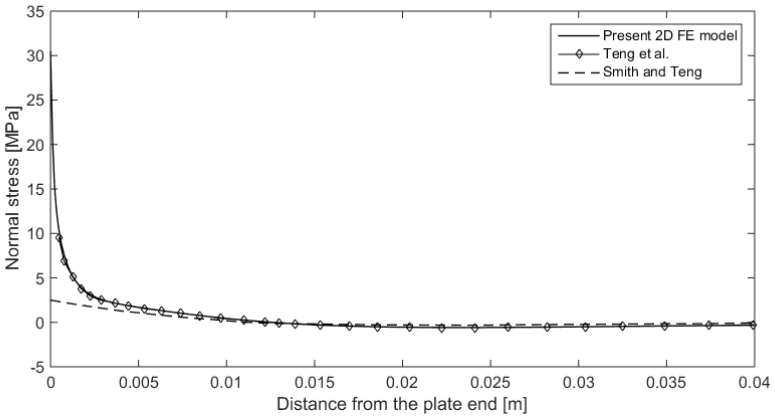

(a)

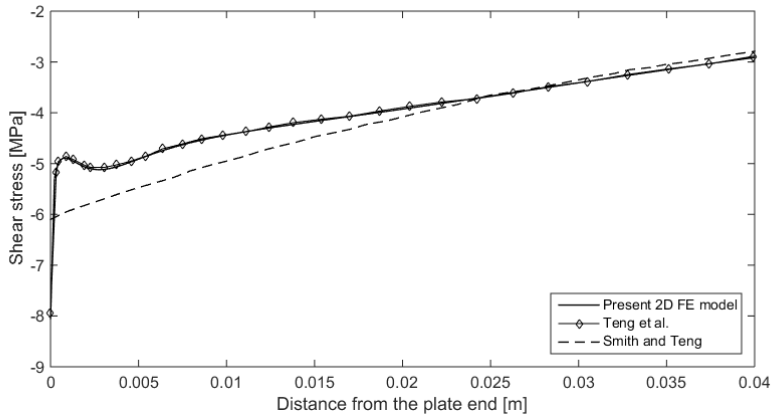

(b)

Figure 3.5: (a) Normal and (b) Shear stresses at the AC interface: comparisons with results obtained in [2, 3]

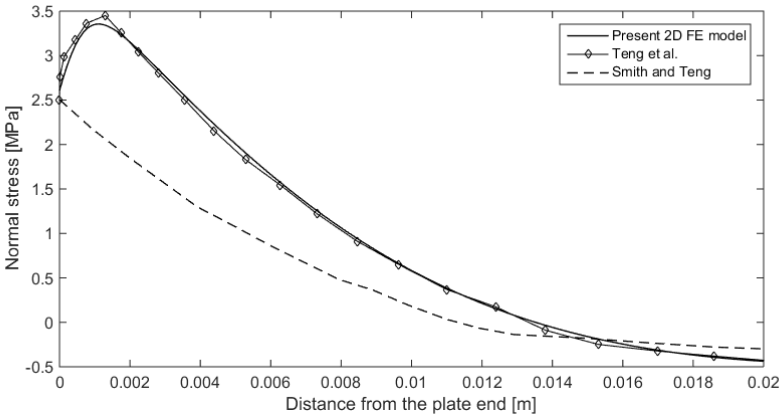

(a)

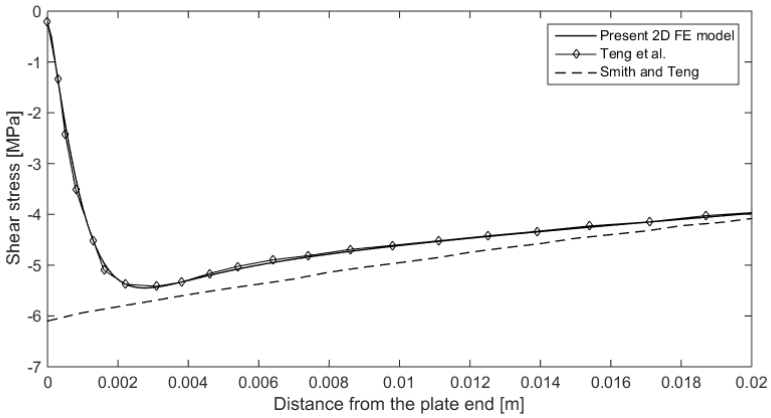

(b)

Figure 3.6: (a) Normal and (b) Shear stresses at the MA section: comparisons with results obtained in [2, 3]

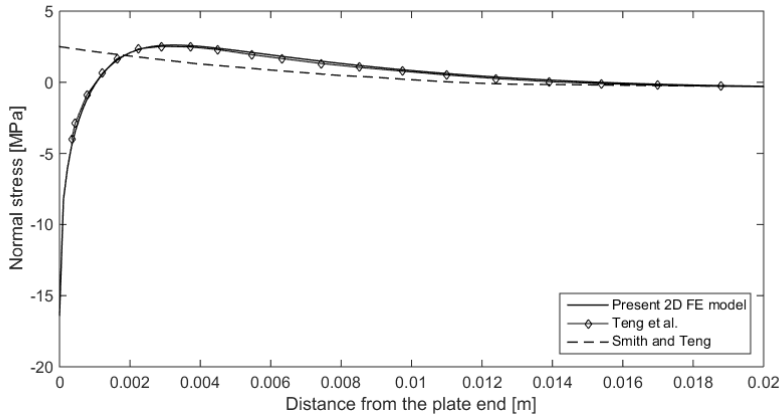

(a)

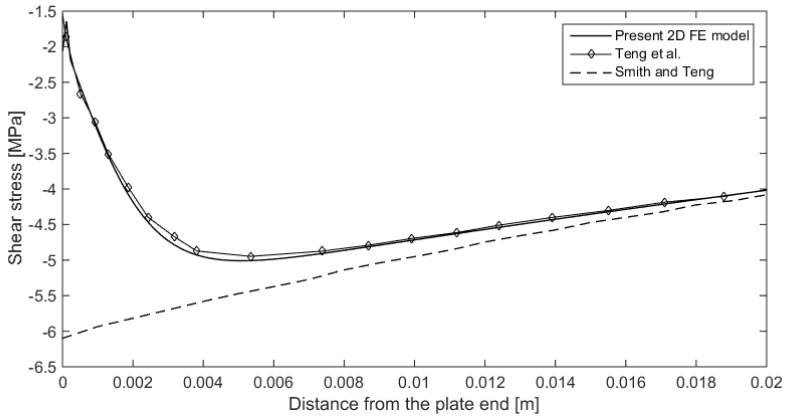

(b)

Figure 3.7: (a) Normal and (b) Shear stresses at the AP interface: comparisons with results obtained in [2, 3]

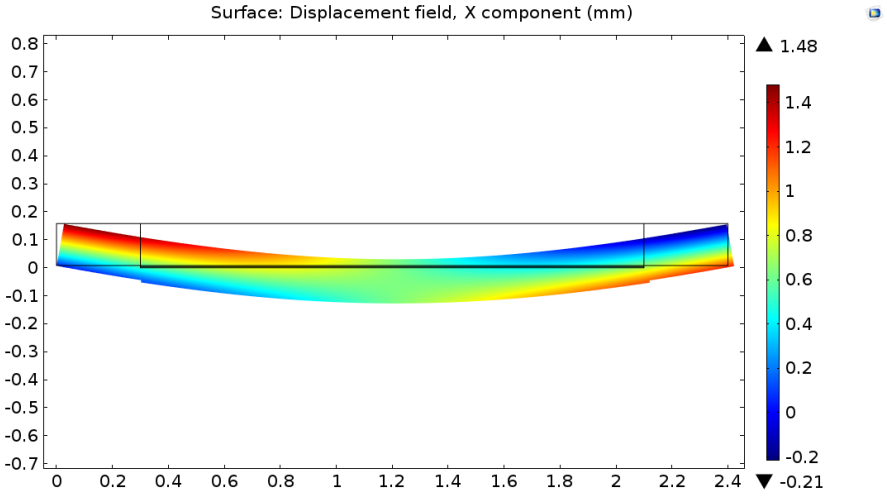

(a)

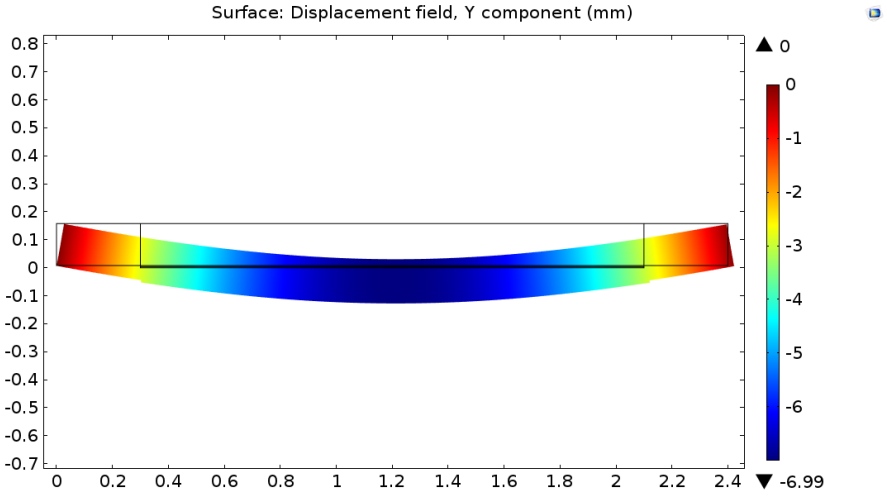

(b)

Figure 3.8: Displacement field in the (a) longitudinal and (b) transverse direction

In Fig. 3.8 the longitudinal and transverse displacements of the structural system are shown, and in Fig. 3.9 the displacement field is evaluated across the adhesive layer, at different distances from the plate end. It is possible to conclude that displacements are not linear at the cut–off section but, at a distance of about 10 mm from the plate end, the longitudinal displacement becomes linear, and the transverse nearly constant. Finally, in Fig. 3.10 the stress variation across the adhesive evaluated at

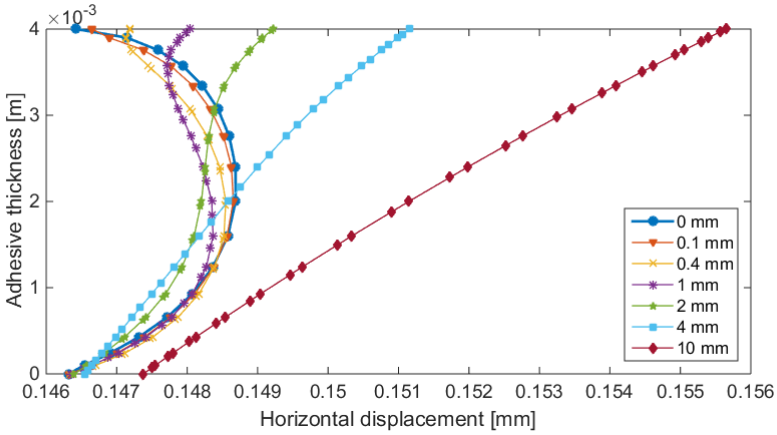

(a)

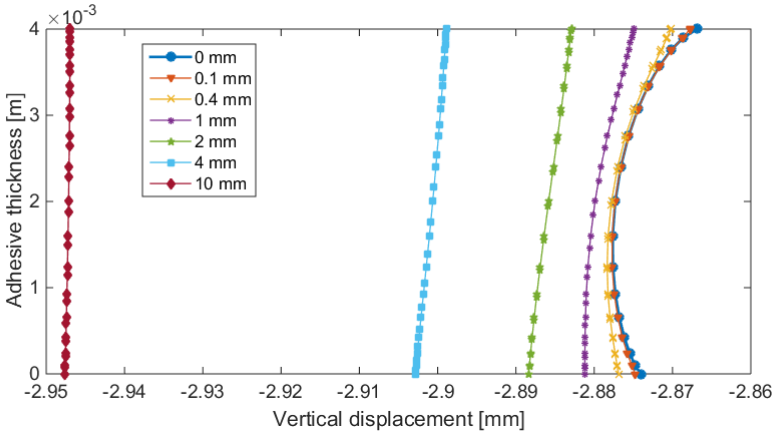

(b)

Figure 3.9: Displacement field in the (a) horizontal and (b) vertical direction across the adhesive thickness

different distances from the plate end is compared with results obtained in [2]. Stresses vary strongly within the adhesive, mostly at plate end. Then, at a distance of about 4 *mm* they can be considered as uniforms. Since stresses are high mesh dependent, the correspondence between the present and the [2] results is considered to be acceptable.

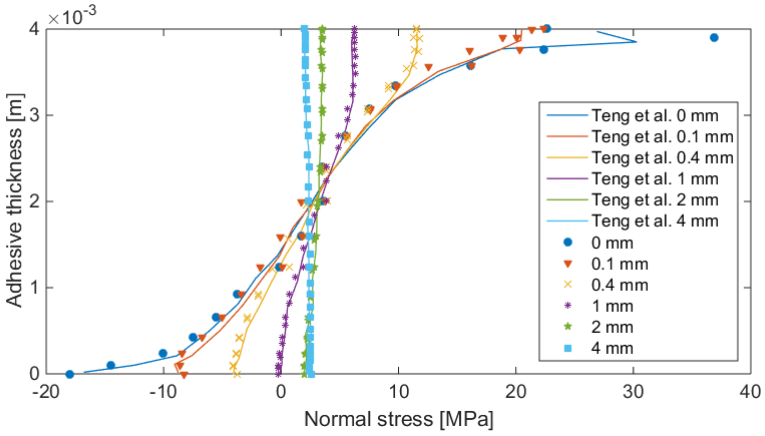

(a)

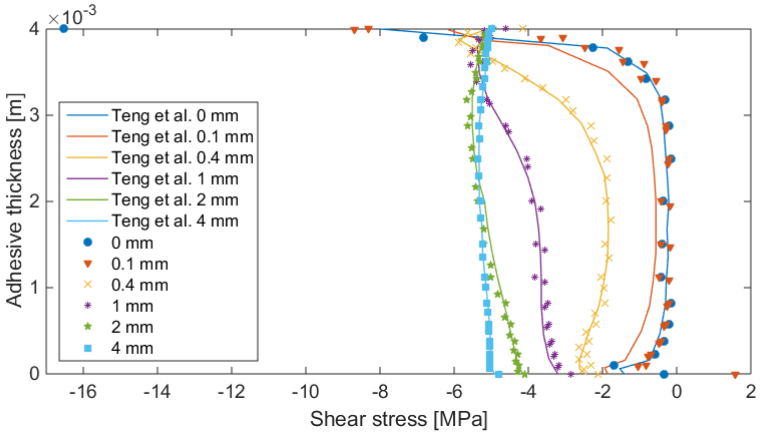

(b)

Figure 3.10: (a) Normal and (b) Shear stresses across the adhesive thickness: comparisons with results obtained in [2, 3]

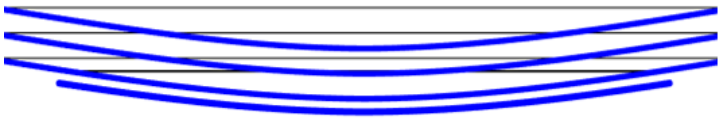

Figure 3.11: Multi–layer 3/2/1 model

3.1.2 Multi–layer models

In this Section the behavior of the interfacial stresses near the plate end is analyzed by means of the proposed multi–layer formulation.

The three physical components of the system, namely the beam, the adhesive layer and the bonded plate, are modeled by means of one or several first–order shear deformable layers (see Section 1.3.2) and, in order to model the two physical interfaces (i.e. AC and AP interfaces), both strong and weak interface constitutive relations are introduced, whereas a strong formulation is adopted to model the mathematical interfaces between layers inside each components.

In the developed FE models, a maximum size of the finite element equal to 0.5 mm is adopted, assuming a mesh refinement near the plate end. Two–noded straight elements with an Hermitian formulation are used for each layers, considering the Timoshenko beam formulation in order to take into account the shear deformations. In particular, in the FE formulation accurate cubic shape functions for bending, being an appropriate extension of the classical cubic Hermitian shape functions for the Euler–Bernoulli beam theory, are adopted depending on the ratio between bending and shear stiffness (see [1] for additional details).

Several multi–layer models, which essentially differ for the number of layers adopted to model the adhesive physical layer and the concrete beam, their thickness distribution, and for the type of interface formulation assumed to simulate the adhesion between components, are developed.

In particular 3, 4, 6 or 8 mathematical layers are accounted in the formulation, see for example Fig. 3.11, leading respectively to the 1/1/1,

the 1/2/1, the 3/2/1 and the 3/4/1 multi–layer models, for which the first number indicates the layers accounted for the concrete beam (n_b), the second one those for the adhesive physical layer (n_a) and the last one those for the bonded plate (n_p). The layers thickness (t_i for the i–th layer) varies depending on the chosen assembly and according to Tab. 3.6.

Model	*RC* beam	Adhesive	Bonded plate
1/1/1	H_b	H_a	H_p
1/2/1	H_b	$\frac{H_a}{2}$ $\frac{H_a}{2}$	H_p
3/2/1	H_b	$\frac{H_a}{2}$ $\frac{H_a}{2}$	H_p
$3/4/1_1$	$\frac{H_b}{3}$ $\frac{H_b}{3}$ $\frac{H_b}{3}$	$\alpha\frac{H_a}{2}$ $\left[(1-\alpha)\frac{H_a}{2}\right]$ $\left[(1-\alpha)\frac{H_a}{2}\right]$ $\alpha\frac{H_a}{2}$	H_p
$3/4/1_2$	$\frac{H_b}{3}$ $\frac{H_b}{3}$ $\frac{H_b}{3}$	$0.65\frac{H_a}{2}$ $0.35\frac{H_a}{2}$ $0.35\frac{H_a}{2}$ $0.65\frac{H_a}{2}$	H_p
$3/4/1_3$	$\frac{2H_b}{3}$ $\left(\frac{H_b}{3}-\alpha\frac{H_a}{2}\right)$ $\alpha\frac{H_a}{2}$	$\alpha\frac{H_a}{2}$ $\left[(1-\alpha)\frac{H_a}{2}\right]$ $\left[(1-\alpha)\frac{H_a}{2}\right]$ $\alpha\frac{H_a}{2}$	H_p

Table 3.6: Layers assembly and thickness distribution

where

$$\alpha = \begin{cases} [0.05\ 0.20\ 0.35\ 0.50\ 0.65\ 0.80\ 0.95] & \text{for the } 3/4/1_1 \text{ model} \\ [0.45\ 0.65\ 0.75\ 0.85\ 0.95] & \text{for the } 3/4/1_3 \text{ model} \end{cases} \tag{3.1.1}$$

In order to guarantee displacements continuity at the perfect (i.e. undelaminated) interfaces both strong and weak interface formulations for the *AC* and *AP* interfaces are accounted. In particular three different kinds of formulations are considered to model the physical interfaces (see Fig. 3.12):

- strong interface formulation (assuming appropriate Lagrange multipliers representing interfacial stresses) in both vertical and horizontal direction, referred to as the (a) model in the multi–layer

notation;

- weak interface formulation (assuming elastic springs whose stiffness represent the interface stiffness parameters) in vertical direction, and strong interface formulation in horizontal direction, referred to as the (b) model in the multi–layer notation;
- weak interface formulation in both vertical and horizontal direction, referred to as the (c) model in the multilayer notation.

In order to implement the above interface formulations, considered as constraint conditions in the FE models, in the case of a strong interface a prescribed displacement is assigned in the required direction on the lower of the two adjacent layers involved by the interface, after that the displacement variables of the upper one are extruded on the lower one. Specifically the constraint equations impose that the interface relative displacement (see Eq. (2.4.6)) vanishes, thus simulating the displacements continuity requirement.

On the other hand, the weak interface may be seen as a continuous distribution of linear normal and tangent springs (see Cornetti et al. [4]), and an edge load is assigned in the needed direction on both the adjacent layers but with opposite sign, being linearly related to the interface relative displacements through the interface stiffness parameters. Since the

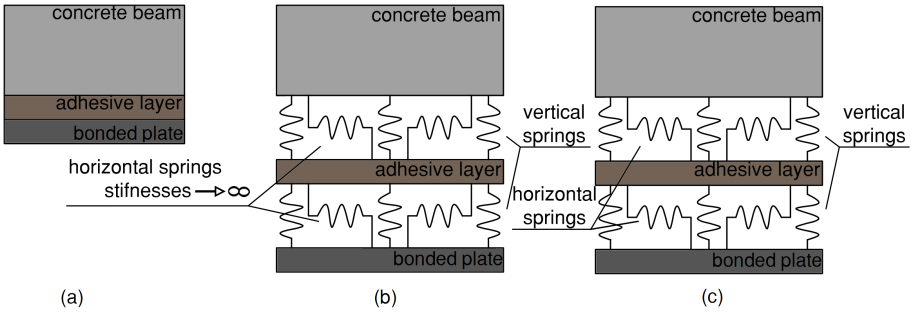

Figure 3.12: Adopted interface formulations: (a) strong interface formulation, (b) coupled strong/weak interface formulation and (c) weak interface formulation

edge load assigned in the x direction is applied on the central axis of the layer, an edge distributed moment is also considered. This load system is therefore equivalent to an edge load acting on the interface between layers as required. The corresponding constraint equations implemented in the finite element models are reported in the following Table 3.7.

Strong interface	Prescribed displacement **x direction**	Prescribed displacement **z direction**
i–th mathematical layer	$u_i = u_{i+1} + \frac{t_i}{2}\psi_i + \frac{t_{i+1}}{2}\psi_{i+1}$	$w_i = w_{i+1}$
Weak interface	Edge load **x direction**	Edge load **z direction**
$(i+1)$–th mathematical layer	$-K_{j,h}\left(u_{i+1} - u_i + \frac{t_i}{2}\psi_i + \frac{t_{i+1}}{2}\psi_{i+1}\right)$	$-K_{j,v}(w_{i+1} - w_i)$
i–th mathematical layer	$K_{j,h}\left(u_{i+1} - u_i + \frac{t_i}{2}\psi_i + \frac{t_{i+1}}{2}\psi_{i+1}\right)$	$K_{j,v}(w_{i+1} - w_i)$

Strong interface	Prescribed rotation
i–th mathematical layer	-
Weak interface	Edge distributed moment
$(i+1)$–th mathematical layer	$-K_{j,h}\left(u_{i+1} - u_i + \frac{t_i}{2}\psi_i + \frac{t_{i+1}}{2}\psi_{i+1}\right)\frac{t_{i+1}}{2}$
i–th mathematical layer	$-K_{j,h}\left(u_{i+1} - u_i + \frac{t_i}{2}\psi_i + \frac{t_{i+1}}{2}\psi_{i+1}\right)\frac{t_{i+1}}{2}$

Table 3.7: Constraint conditions implemented in the proposed multi-layer formulation

Details should be given about the stiffnesses coefficients of the vertical and horizontal springs ($K_{j,v}$ and $K_{j,v}$, respectively), introduced in Tab.

3.7 in order to define an equivalent distributed loading system able to model the weak interface formulation for the j–th interface of the finite element procedure here implemented.

In the Section 2.4.1, it is stated that the theoretical formulation is carried out with reference to a unit width for the structural system and, for the weak interface formulation, the stiffness parameters k_z and k_{zx} (whose dimensions are $[FL^{-3}]$), respectively, are introduced. It follows that energy functional Π, introduced in Eq. (2.4.1), must be considered for unit width, and that the actual energy functional of the structural system can be obtained by multiplying Π by the system width B. On the other hand, in the finite element implementation of the proposed multi–layer model, the interface stiffness coefficients $K_{j,l}$, with the first index denoting the location of the physical interface ($j = AC,\ AP$) and the second one the direction ($l = v, h$ for the vertical and horizontal direction, respectively), may be obtained by multiplying the interface stiffness parameters k_z and k_{zx} by the width B. These stiffness coefficients, having dimensions $[FL^{-2}]$, are introduced to define the equivalent distributed loading system able to model the weak interface formulation within the finite element procedure here implemented. Specifically, edge loads ($[FL^{-1}]$) and edge moments ($[F]$) for unit length are introduced according to the definitions given in Tab. 3.7, in order to implement the constraint conditions for the weak interface formulations; they are defined multiplying the stiffness coefficients $K_{j,l}$ by the relative displacement, in the case of the edge load, and by the relative displacement and half the layer thickness for the edge moment. It emerges that the interface stiffness parameters k_z and k_{zx} of the theoretical formulation correspond to distributed stiffness per unit of area, whereas the stiffness coefficients $K_{j,k}$ of the finite element formulation represent distributed stiffness for unit horizontal length.

In the present weak formulation, the interface stiffness parameter in the vertical direction is directly related to the layer thickness and to the elastic moduli E_a of the adhesive, since it is the most deformable layer.

In this way the vertical compliance of the adhesive layer, neglected when the strong interface is adopted, is recovered in the structural model.

In addition, the use of horizontal weak interfaces leads to a refined representation of the structural system shear deformability. As a matter of fact, the multi–layer $FSDT$ formulation incorporates in an approximate way shear deformability of the system, by accounting for the shear modulus G of each physical components (see Eq. (2.4.11)), and leading to a *Zig–Zag* distribution of horizontal displacements across the system vertical section. However, as confirmed by the subsequent numerical results, an accurate evaluation of interface shear stress distribution at the physical interfaces requires an enrichment of the above kinematic formulation by introducing additional compliance to the system by means of horizontal weak interfaces. Therefore, since shear deformability is already incorporated in the kinematic model of each mathematical layer, the stiffness parameter of the horizontal weak interface involves, in addition to the shear modulus of the adhesive layer G_a, only a fraction of its thickness. Consequently, in order to calibrate the stiffness for the horizontal springs, a parametric study has been carried out by means of a parameter β, which allows to vary the adhesive thickness taken into account. The interface stiffness parameters can be therefore expressed in the following form:

$$\begin{aligned} K_{j,v} &= \frac{E_a B_a}{H_a/2} \\ K_{j,h} &= \frac{G_a B_a}{\beta H_{ai}/2} \end{aligned} \tag{3.1.2}$$

where H_{ai} denotes the thickness of the sub–layer representing the adhesive and adjacent to the interface.

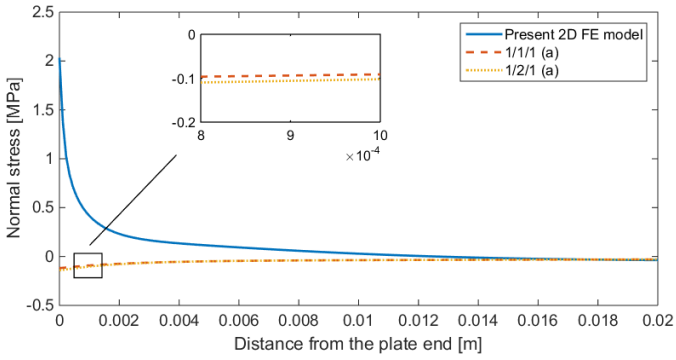

(a)

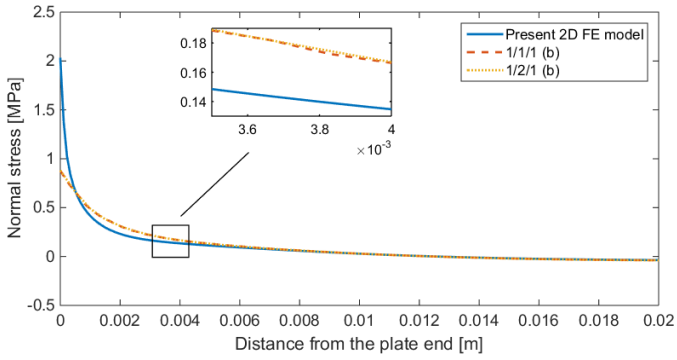

(b)

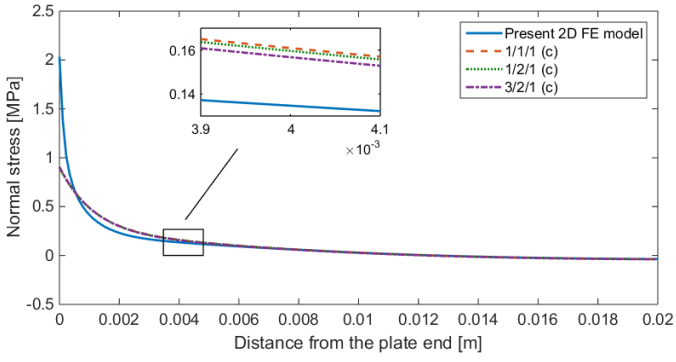

(c)

Figure 3.13: Interfacial normal stresses near the plate end in the AC interface: comparison between the 2D FE continuum model and the proposed multi–layer formulation

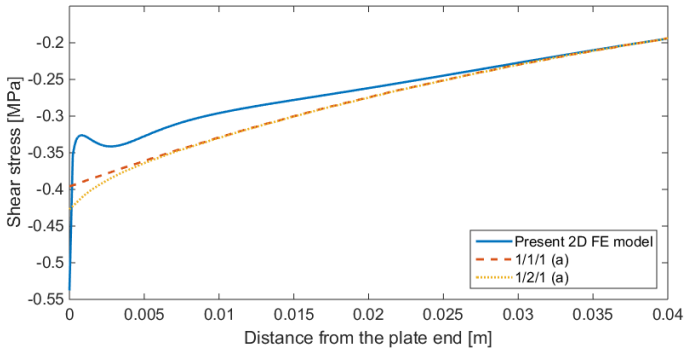

(a)

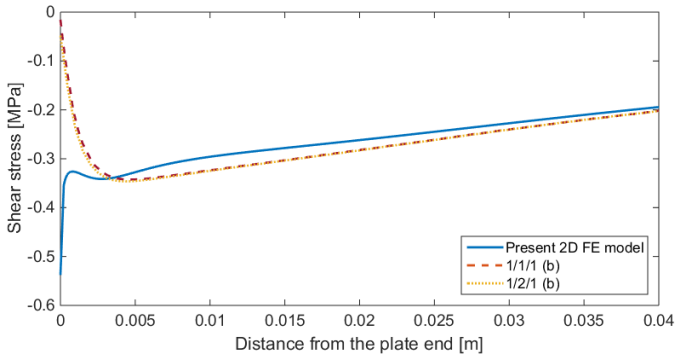

(b)

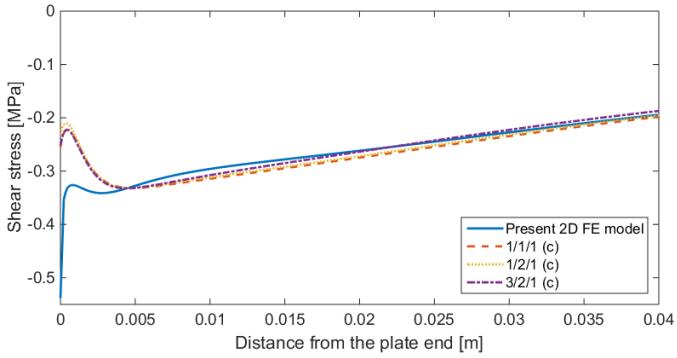

(c)

Figure 3.14: Interfacial shear stresses near the plate end in the AC interface: comparison between the 2D FE continuum model and the proposed multi–layer formulation

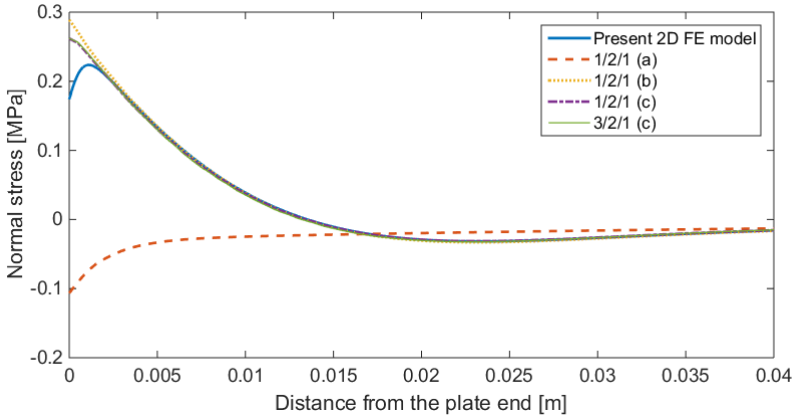

(a)

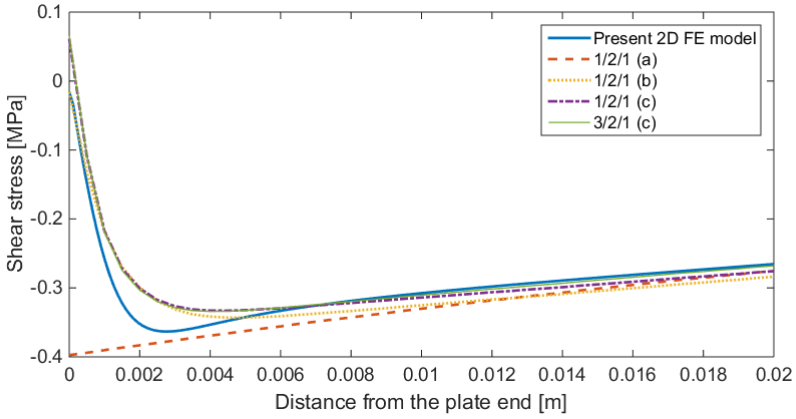

(b)

Figure 3.15: Interfacial stresses near the plate end in the MA section: comparison between the 2D FE continuum model and the proposed multi–layer formulation

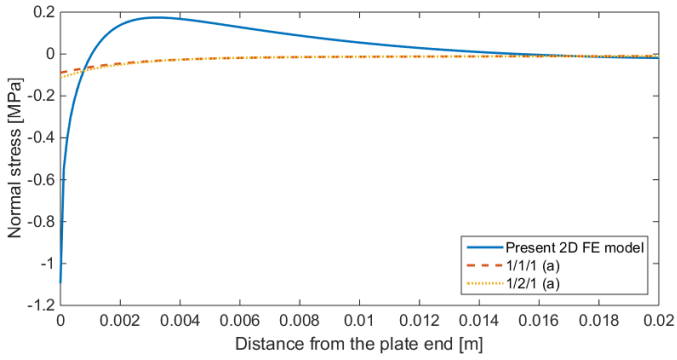

(a)

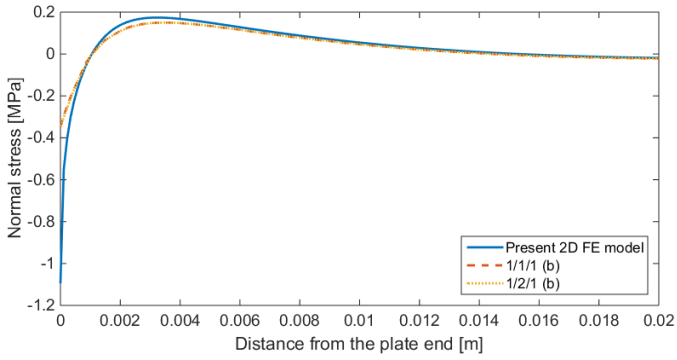

(b)

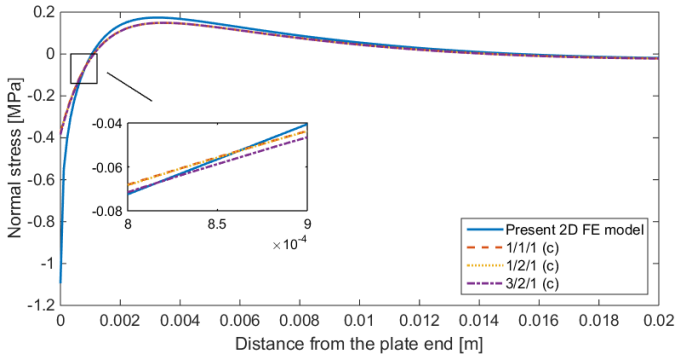

(c)

Figure 3.16: Interfacial normal stresses near the plate end in the AP interface: comparison between the 2D FE continuum model and the proposed multi–layer formulation

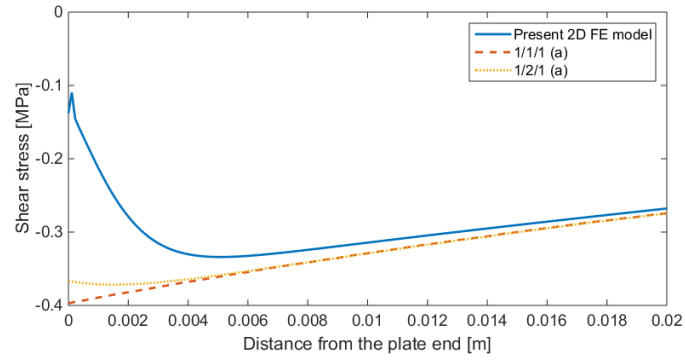

(a)

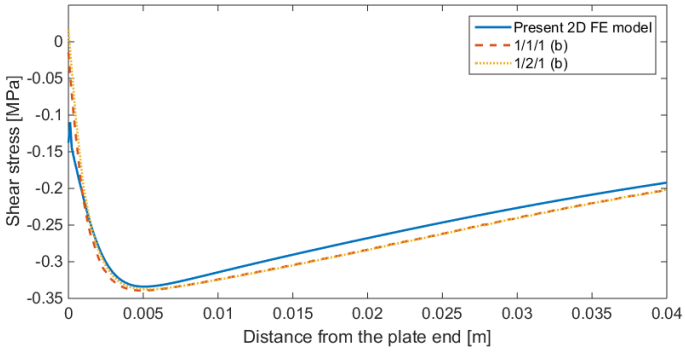

(b)

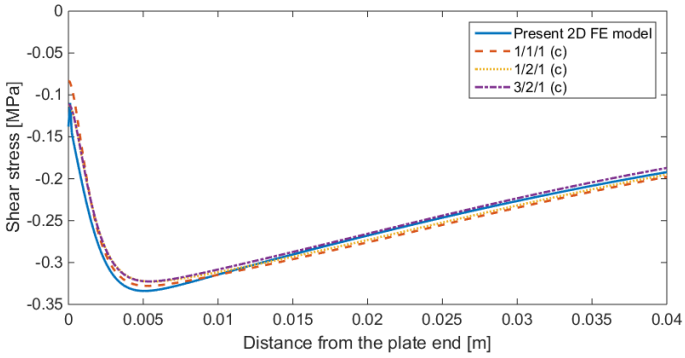

(c)

Figure 3.17: Interfacial shear stresses near the plate end in the AP interface: comparison between the 2D FE continuum model and the proposed multi–layer formulation

Comparisons, in terms of normal and shear interfacial stresses, between the $2D$ FE continuum model and the proposed multi–layer formulation are illustrated in Figs. 3.13–3.17, for all the developed models, assuming a unit uniformly distributed loading condition and adopting the same geometrical and material properties reported in Tab. 3.1. In particular, the horizontal stiffnesses adopted for the (c) models are $K_{j,h} = G_a B_a/(0.1H_a/2)$, $K_{j,h} = G_a B_a/(0.125H_a/2)$ and $K_{j,h} = G_a B_a/(0.125H_a/2)$ for the 1/1/1 (c), the 1/2/1 (c) and the 3/2/1 (c) assembly, respectively.

From the above Figures, it is possible to observe how the adopted interface formulation plays a stronger role in the interfacial stresses behavior with respect to the number of layers considered in the multi–layer model. For the multi–layer FE models in which a strong interface formulation is considered for both the physical interfaces (i.e. AC and AP interfaces), i.e. (a) models, the interfacial normal stress distribution, contrary to the $2D$ continuum model, is always compressive in all the analyzed locations, so that its contribution to crack initiation is ineffective, whereas the shear stress results overestimated. However, the inaccuracy introduced by the multi–layer models adopting the strong interface formulation, being confined in a relatively small zone near the plate end (about 10^{-2} L_s and 2×10^{-2} L_s for the normal and shear stresses, respectively), will have a scarce influence on debonding onset mechanisms, as will be shown in the next Chapter. On the other hand, when the weak formulation is considered by introducing the elastic springs in the vertical direction, i.e. (b) models, the normal stress distributions turn out to be in good agreement with the $2D$ FE continuum solution, and notable improvement in the prediction of the interface traction fields is obtained. In particular, results show how near the edge of the bonded plate the AC interface is subjected to tensile stresses, whereas the AP interface is subjected to compressive stresses. As far as the shear stress distribution is concerned, results have shown that in order to obtain a reasonable accuracy, a weak interface model must be introduced also

with respect to the horizontal direction, i.e. (c) models. In particular, the weak interface formulation is able to provide an improved interface stresses prediction since when a strong interface formulation is adopted stress singularities at the delamination tip of the AC and AP interfaces are substituted by concentrated forces, as shown in Section 2.4.1. Indeed, when the stiffness parameters for the weak interface approach infinity, thus reproducing the strong interface formulation, stress singularities at the delamination front occur turn out to be lumped into concentrated interfacial forces, appearing as a consequence of the limit process and corresponding to concentrated Lagrangian multipliers.

In addition, it is possible also to remark that, when the weak interface formulation is considered only in the vertical direction and a strong interface model is accounted in the horizontal one, the shear stress reduces to zero at the plate end in all the analyzed locations. This is in good agreement with results obtained by Rabinovitch and Frostig [5] by means of a high–order model, which provides a null shear stress through the adhesive thickness at the free edge. On the contrary, when the weak interface formulation is accounted in both vertical and horizontal direction, the obtained shear stress is not equal to zero and approaches result obtained by means of the used $2D$ FE model.

Rabinovitch and Frostig [5] have shown also that exists an high correlaction between the normal and the shear stress. Indeed, where shear stresses reach their maximum, so that the shear gradient is zero, the normal stresses in the AC and in the AP interface coincide. This issue was approximately verified also in the proposed multi–layer formulation by considering shear stresses at the MA location, which represent an average stress.

In the following Figs. 3.18 and 3.19, the interface stresses obtained from the $3/4/1_1$ (c) model by varying the adhesive thickness distribution are shown, while in Figs. 3.20 and 3.21 the interface stresses obtained from the $3/2/1$ (c) model by varying the horizontal stiffness are presented.

It has to be pointed out that when the multi–layer formulation is used together with a weak interface, interface stresses may be evaluated equivalently from derivative of the resultant forces (Eq. (2.4.16)), or by dividing the edge loads assigned at interfaces (Tab. 3.7) by the width B.

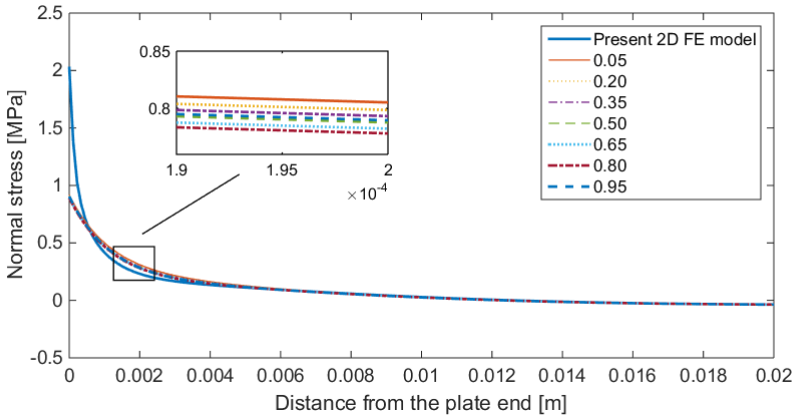

(a)

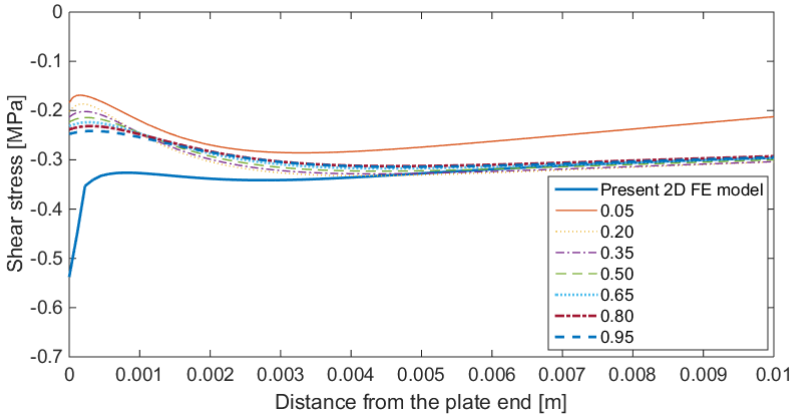

(b)

Figure 3.18: (a) Normal and (b) Shear stresses at the AC interface by varying α, i.e. the layer thickness distribution within the adhesive ($3/4/1_1$ (c) model)

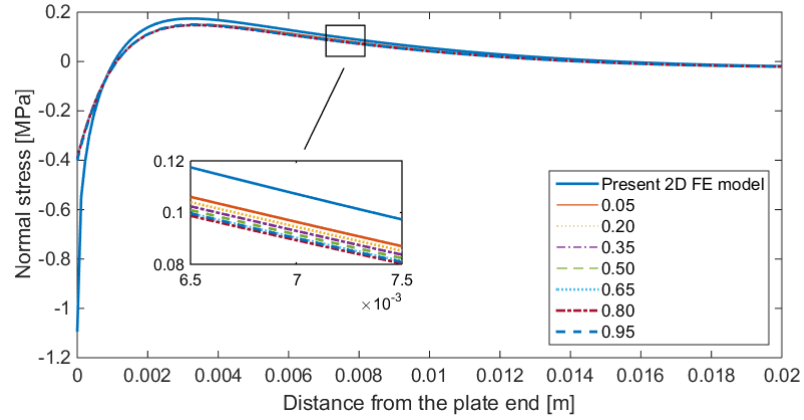

(a)

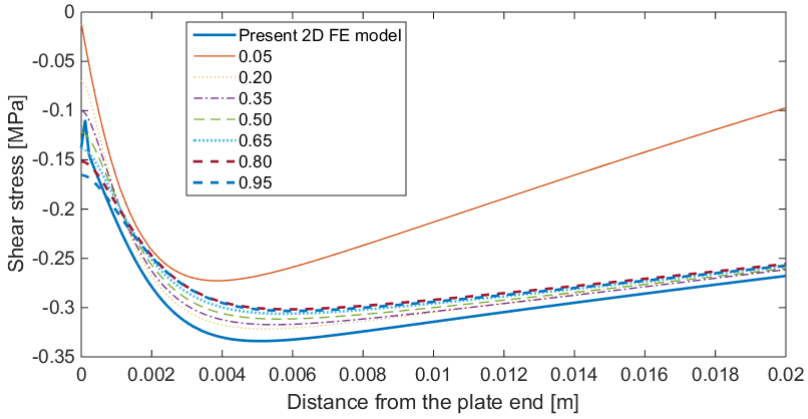

(b)

Figure 3.19: (a) Normal and (b) Shear stresses at the AP interface by varying α, i.e. the layer thickness distribution within the adhesive ($3/4/1_1$ (c) model)

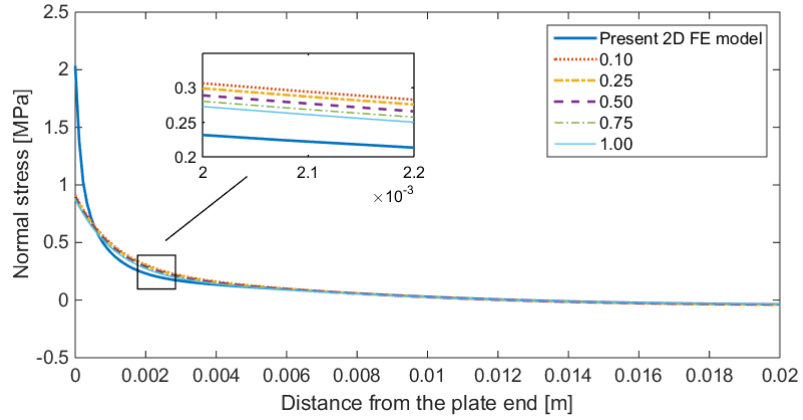

(a)

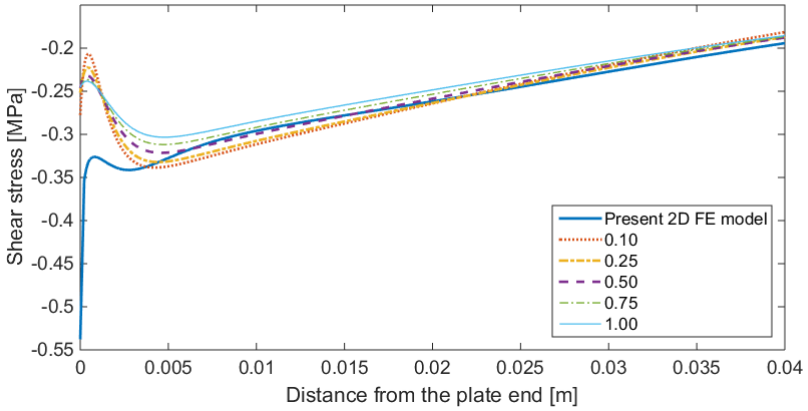

(b)

Figure 3.20: (a) Normal and (b) Shear stresses at the AC interface by varying β, i.e. the horizontal interface stiffness (3/2/1 (c) model)

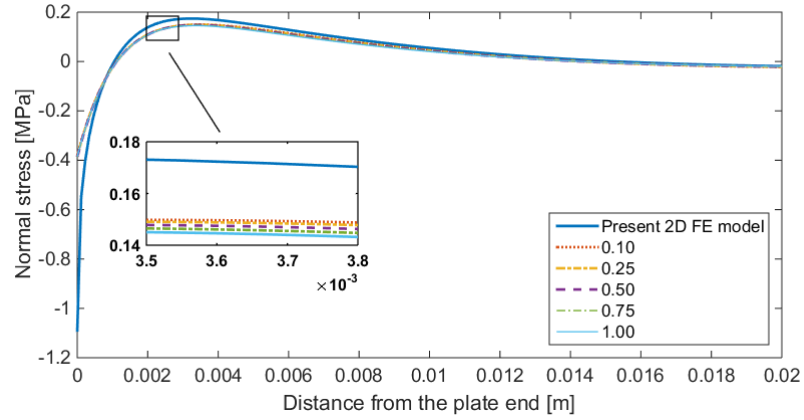

(a)

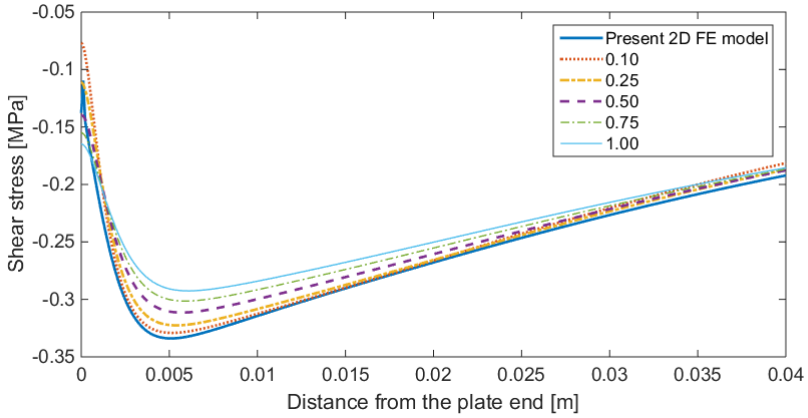

(b)

Figure 3.21: (a) Normal and (b) Shear stresses at the AP interface by varying β, i.e. the horizontal interface stiffness (3/2/1 (c) model)

In the following Figs. 3.22, 3.23 and 3.24, the percentage errors with respect to the $2D$ continuum solution for the different models are reported. In particular, the error is obtained by computing the integral of stresses evaluated from the cut–off section to a distance of 0.1 m to the plate end.

It emerges that (b) models improve estimation of normal stresses and, the above numerical calculations show that models adopting a weak interface formulation in both directions, i.e. the (c) models, lead to a reasonable prediction of interlaminar stresses distribution at all the analyzed section locations across the adhesive layer, with small improvements in accuracy as the number of layers increases, especially between the 1/2/1 (c), 3/2/1 (c), $3/4/1_1$ (c) and $3/4/1_3$ (c) models.

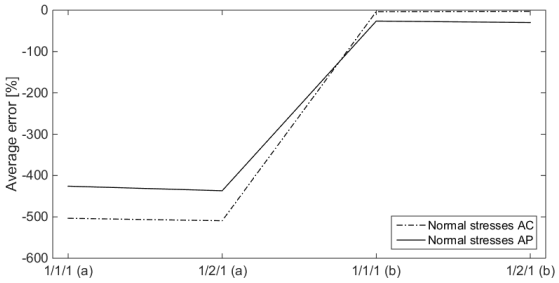

(a)

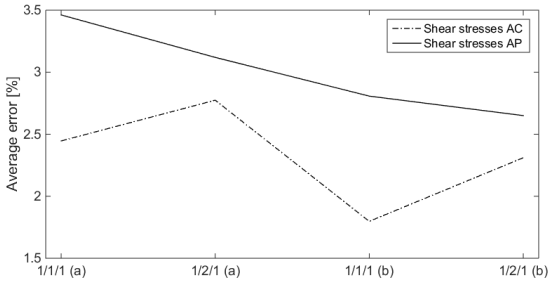

(b)

Figure 3.22: Percentage error with respect to the 2D FE solution in terms of integral of interface stresses evaluated near the plate end

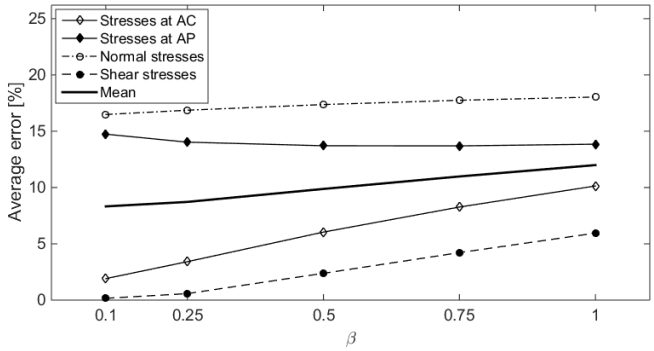

(a)

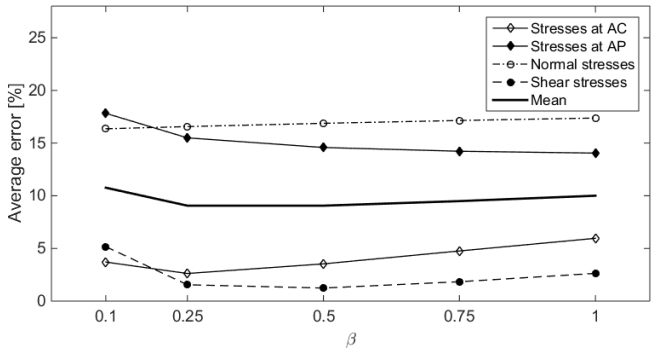

(b)

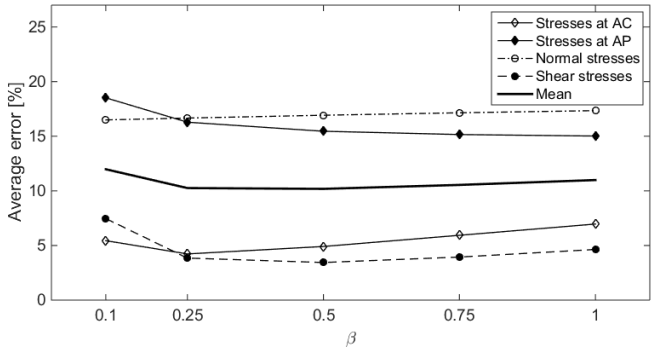

(c)

Figure 3.23: Average percentage error with respect to the 2D FE solution in terms of integral of interface stresses evaluated near the plate end (from the top: 1/1/1 (c), 1/2/1 (c) and 3/2/1 (c) models)

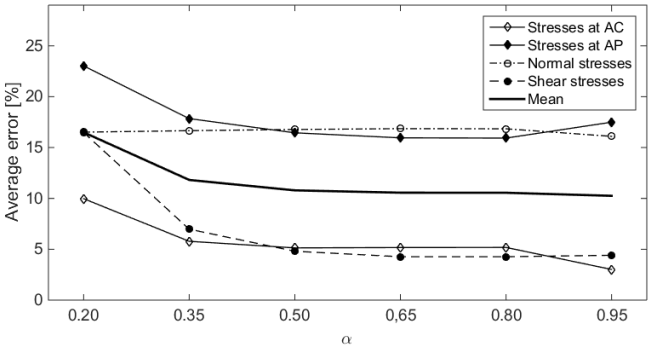

(a)

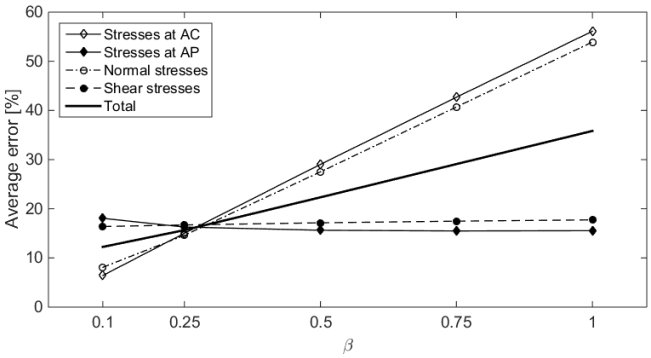

(b)

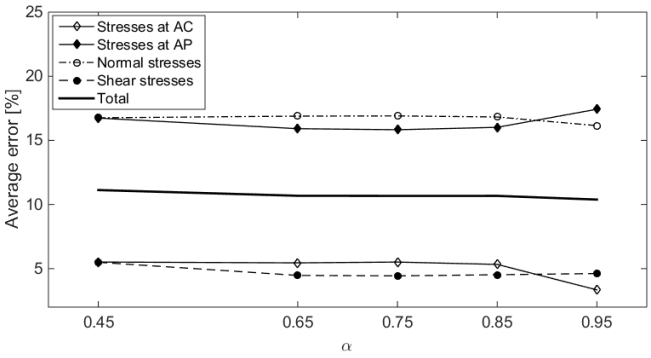

(c)

Figure 3.24: Average percentage error with respect to the 2D FE solution in terms of integral of interface stresses evaluated near the plate (from the top: $3/4/1_1$ (c), $3/4/1_2$ (c) and $3/4/1_3$ (c) models)

3.1.3 Application to a Three Point Bending specimen

In this Section, a simply supported reinforced beam subjected to a point load of 10 kN applied at the mid–span is considered. Geometrical and material properties for the analyzed three point bending sample are those used by Bruno et al. [6] and summarized in the following Tab. 3.8, where a Carbon FRP ($CFRP$) is considered as strengthening plate. In particular, an isotropic linear elastic material is considered for the concrete beam and the adhesive layer, whereas the composite plate is modeled as an orthotropic linear elastic material. A maximum size of the finite element equal to 0.1 mm is adopted, and a mesh refinement near the plate end is assumed. Two–noded straight elements with an Hermitian formulation are used for each layers and, in order to account shear deformations, the Timoshenko beam formulation is used.

In Figs. 3.25 and 3.26, the percentage errors with respect to the $2D$ continuum solution in terms of integral of stresses evaluated at 0.1 m from the plate end are shown. Similarly to the case of a simply supported reinforced beam subjected to a uniformly distributed load, (b) models lead to a better estimation of normal stresses and, in terms of shear stresses, models with one layer representing the adhesive give lower errors in AC. On the other hand, behavior of (c) models is slightly different from those obtained in Section 3.1.2. In fact, by increasing β, i.e. by decreasing the horizontal interface stiffness through Eq. (3.1.2), stress average error at both interfaces grows, mostly in terms of normal stresses. Moreover, by decreasing β, normal and shear stresses do not converge when the 1/1/1 (c) and 1/2/1 (c) models are used. However, by comparing results obtained for the TPB sample with those of the uniform distribute loading, it is possible to remark that in case of TPB, the multi–layer formulation leads to lower errors in terms of normal and shear stresses, of stresses at AP, and although slightly, also in AC.

Comparisons, in terms of normal and shear interfacial stresses, between the $2D$ FE continuum model and the proposed multi–layer formulation are illustrated in the following Figs. 3.27–3.29. In partic-

Component	Width [mm]	Thickness [mm]	Length [mm]	Young modulus [MPa]	Shear modulus [MPa]	Poisson's ratio
Concrete beam	1,000	300	3,000	30,000	12,820.5	0.17
Adhesive layer	1,000	2	1,800	2,000	740.74	0.35
CFRP laminate	1,000	4	2,400	$E_1 = E_2 =$ E_3 =160,000	$G_{12} = G_{23} =$ G_{13} =5,333.3	$\nu_{12} = \nu_{13}$ =0.3 ν_{23} =0.4

Table 3.8: Geometrical and material properties for the TPB sample

ular, when a weak interface formulation is accounted, Eq. (3.1.2) is assumed, and the horizontal stiffnesses adopted for the (c) models are $K_{j,h} = G_a B_a/(0.25H_a/2)$, $K_{j,h} = G_a B_a/(0.05H_a/2)$ and $K_{j,h} = G_a B_a/(0.05H_a/2)$ for the 1/1/1 (c), the 1/2/1 (c) and the 3/2/1 (c) assembly, respectively.

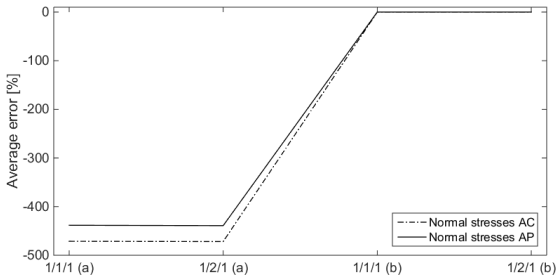

(a)

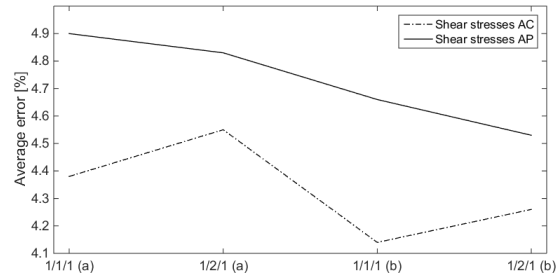

(b)

Figure 3.25: Percentage error with respect to the 2D FE solution in terms of integral of interface stresses evaluated near the plate end (TPB sample)

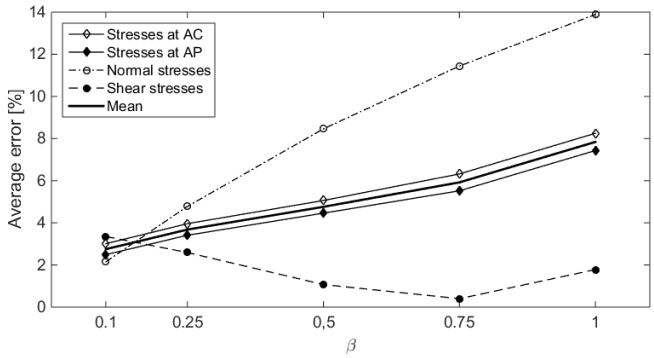

(a)

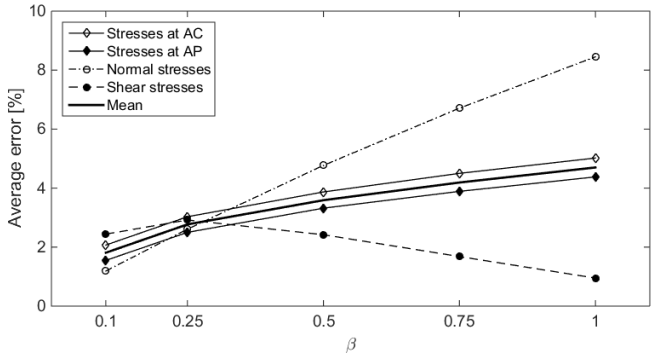

(b)

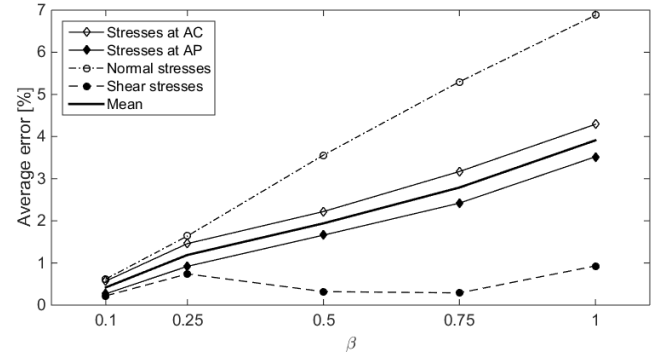

(c)

Figure 3.26: Average percentage error with respect to the 2D FE solution in terms of integral of interface stresses evaluated near the plate end (TPB sample) – from the top: 1/1/1 (c), 1/2/1 (c) and 3/2/1 (c) models

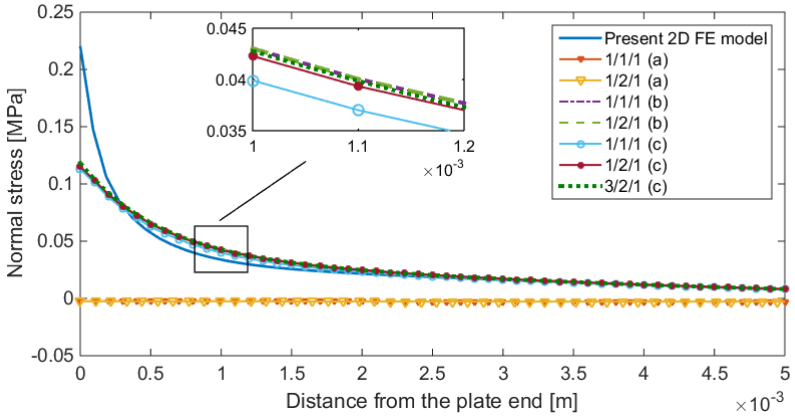

(a)

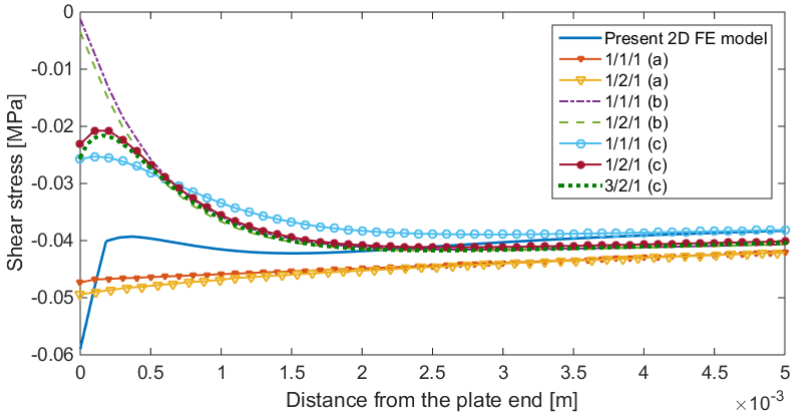

(b)

Figure 3.27: Interfacial stresses near the plate end at the AC interface: comparison between the 2D FE continuum model and the proposed multi–layer formulation (TPB sample)

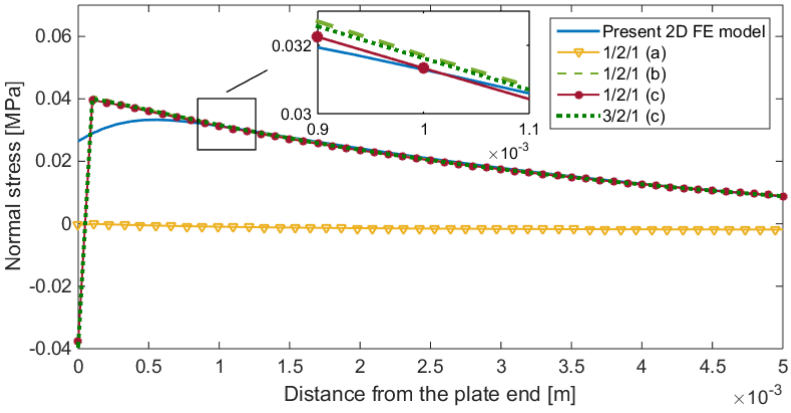

(a)

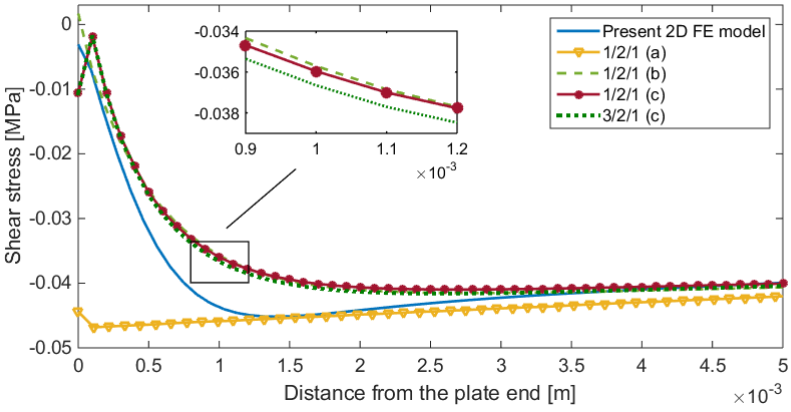

(b)

Figure 3.28: Interfacial stresses near the plate end in the MA section: comparison between the 2D FE continuum model and the proposed multi–layer formulation (TPB sample)

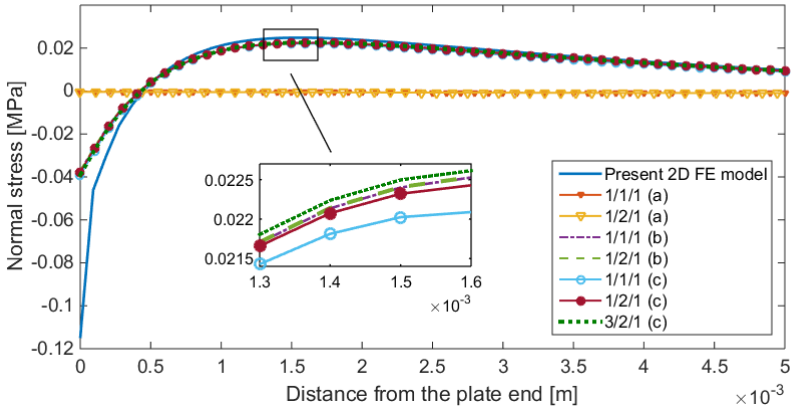

(a)

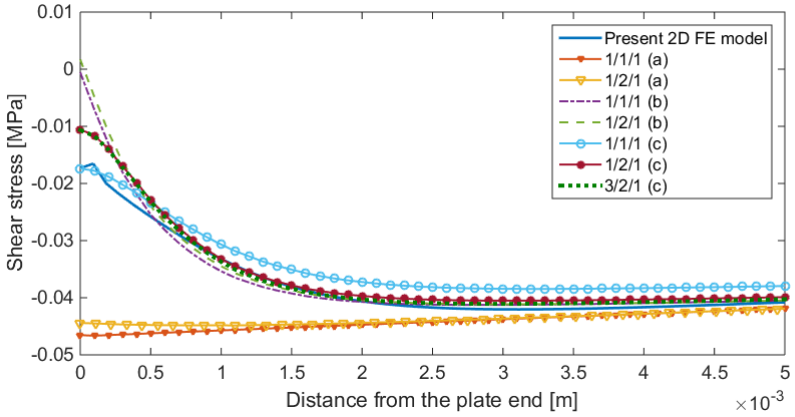

(b)

Figure 3.29: Interfacial stresses near the plate end at the AP interface: comparison between the 2D FE continuum model and the proposed multi–layer formulation (TPB sample)

It is possible to conclude that the trend for the analyzed TPB sample, in terms of interfacial stresses, is similar to those obtained in case of uniform loading condition, with the models involving the weak interface formulation giving the better predictions.

3.2 Fracture energies computation

In this Section, the energy release rate behavior for the different analyzed locations (i.e. AC, MA and AP), as a function of the debonded length a, is investigated. For both the $2D$ FE model and the proposed multi–layer models the $VCCT$ is adopted to obtain the total ERR and modal partition, assuming a strong interface formulation in both vertical and horizontal direction.

3.2.1 2D Finite Element model

Regarding the $2D$ FE model, two types of mesh are implemented. When the behavior of the total ERR and its mode partitions is analyzed for the AC and the AP interfaces, respectively, a mapped mesh, refined near the crack tip, with the minimum element size equal to 1 mm, is accounted. In particular, the refined strip, which is symmetric with respect to the crack tip, has a width of 20 mm and a height of 306 mm. Conversely, when energy release rates are investigated in the MA position, a free triangular mesh is adopted everywhere except around the crack tip, where a mapped mesh of four quadrilateral elements with a size of 0.1 mm is used, (see Tab. 3.9 and 3.30). Note that in Fig. 3.30 the debonded region extends at the right of the crack tip up to the cut–off section.

However, as pointed out by Greco et al. [7], for the $2D$ solution at the AC and AP interface, only results in terms of the total energy release rate can be considered as accurate, since the FE values of the individual mode components are not well defined due to the influence of the underlying oscillatory singularities predicted by the $2D$ elasticity theory. For example, in Fig. 3.31 the variation of the $ERRs$ obtained

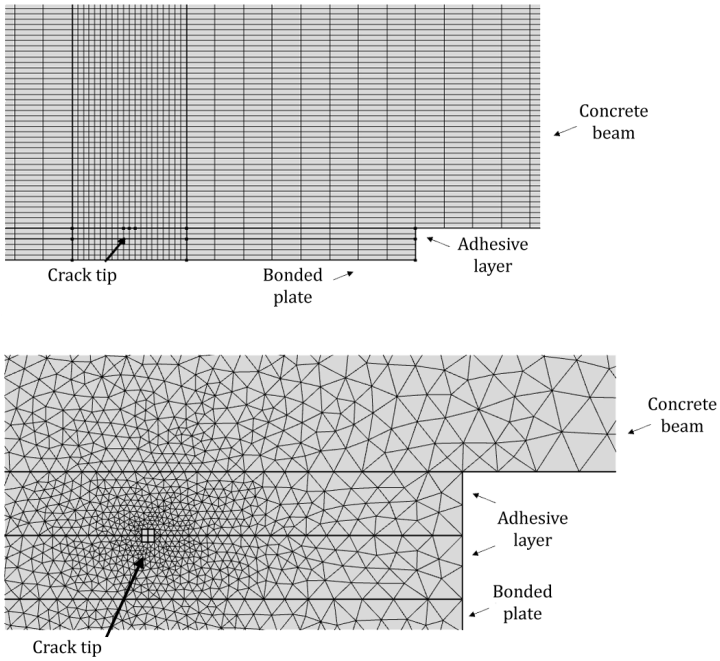

Figure 3.30: Mapped and free triangular mesh adopted in the case of edge debonding

for a fixed crack length and by decreasing the minimum element size of the mesh is shown. Note that $ERRs$ will be hereafter expressed in a dimensionless form (using the factor $E_b H_b/(F/B)^2$), and that Δa denotes the minimum element size when a mapped mesh is used in AC and AP, and the size of the quadrilateral elements placed around the crack tip when delamination occurs in the MA section.

Location	**AC**	**MA**	**AP**
Mesh types	Mapped mesh	Free triangular	Mapped mesh
Minimum element size	1 mm	0.06 mm	1 mm
Maximum element size	5 mm	30 mm	5 mm

Table 3.9: Details on the 2D Finite Element models near the delamination tip

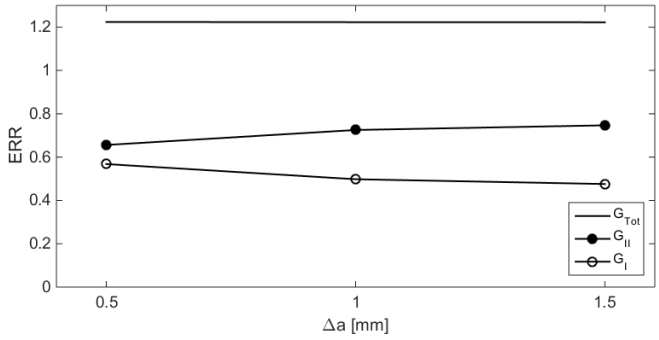

(a)

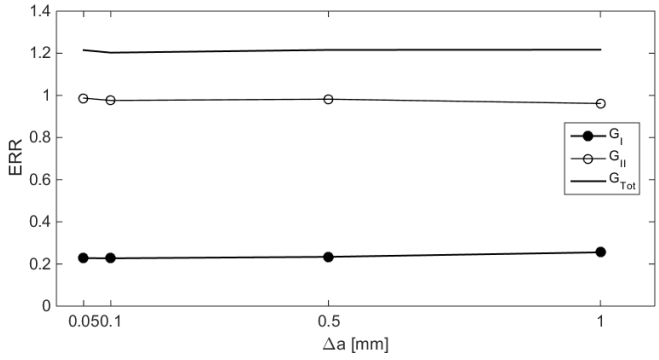

(b)

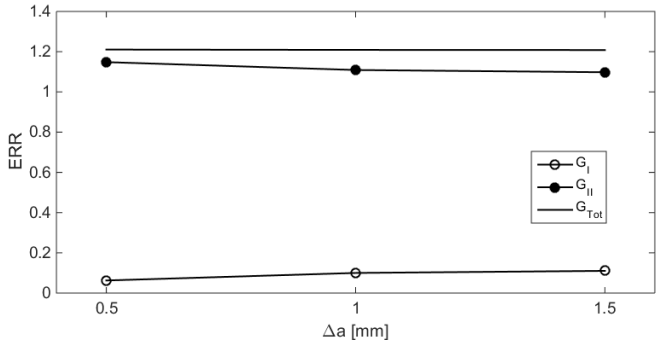

(c)

Figure 3.31: Normalized ERRs at (a) AC interface, (b) MA section and (c) AP interface by varying Δa for a fixed crack length (a=300 mm)

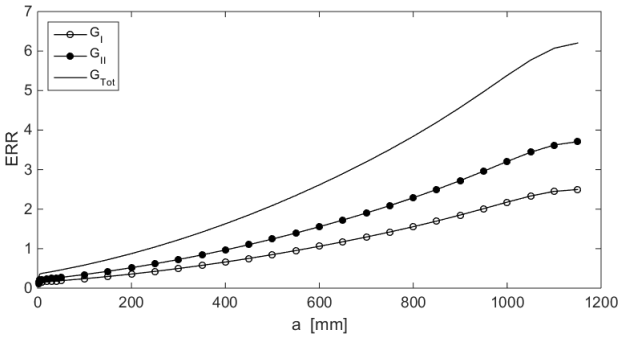

(a)

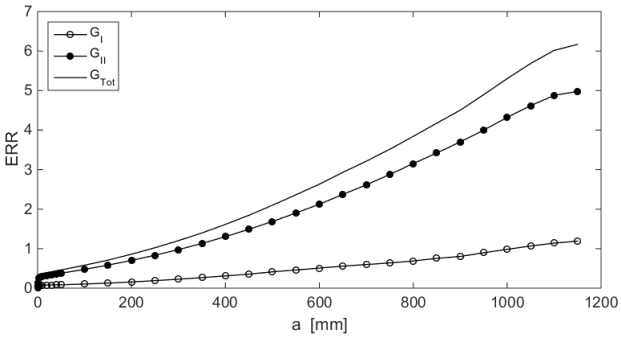

(b)

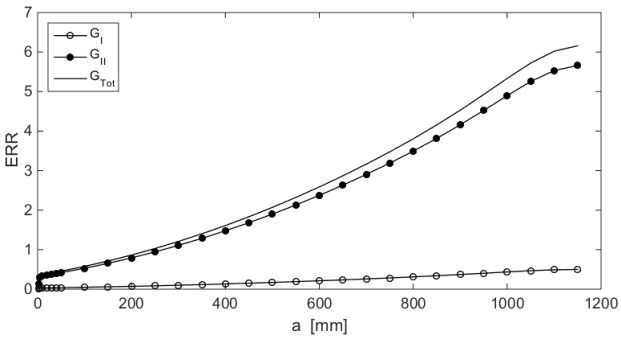

(c)

Figure 3.32: Normalized ERRs at (a) AC interface, (b) MA section and (c) AP interface as a function of the delamination length

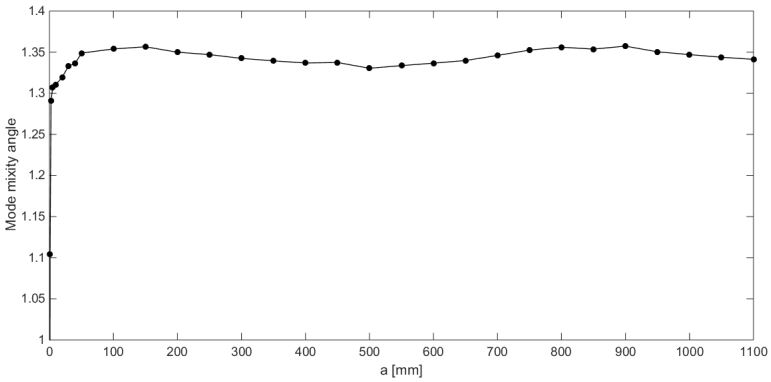

Figure 3.33: Mode mixity angle at the MA section

From Fig. 3.31b appears that, as expected, $ERRs$ at the MA section are nearly independent from the mesh size.

Therefore, in Figs. 3.32 the $ERRs$ evolution at all considered locations is shown and, in Fig. 3.33, the modal partition in MA in terms of mode mixity angle (see Eq. 2.3.39) is illustrated. Then, in Fig. 3.34 the variation of the total and of the individual $ERRs$ with the $CFRP$ plate properties is evaluated. Note that the 1 axis is parallel to the beam length, the 2 axis to the beam height and the 3 axis to the beam width. Therefore, it is possible to conclude that the total ERR is not affected by the $CFRP$ shear modulus, by E_2 and by ν_{12}, whereas modal components depend on these parameters except for Poisson's ratio.

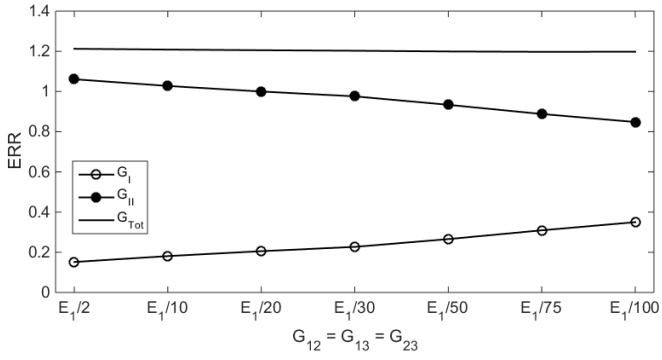

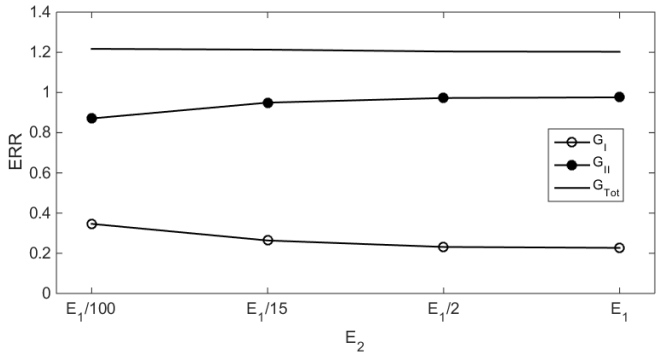

(b)

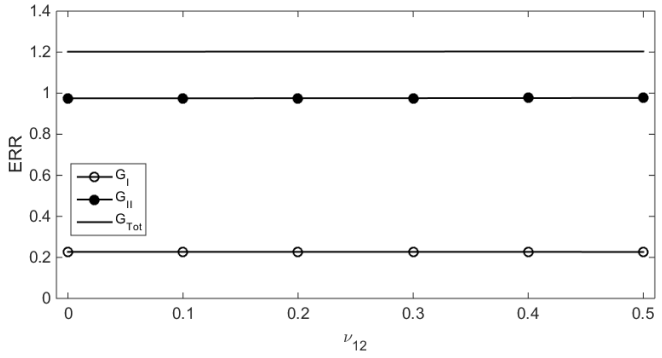

(c)

Figure 3.34: Normalized ERRs at the MA section by varying some properties of the CFRP plate

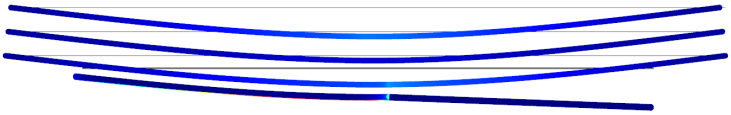

Figure 3.35: Delaminated multi–layer 3/2/1 model

3.2.2 Multi–layer models

In this Section it will be shown that an effective evaluation of both the total and individual $ERRs$ can be obtained by using the proposed multi–layer models. In addition, it will be demonstrated that the fracture energy accuracy strongly depends on the adopted layer assembly, which is in contrast to what occurs in the case of interface stresses, where the interface formulation as a major role. Again, two–noded straight elements with an Hermitian formulation are used for each layer in the FE models, and the Timoshenko beam formulation is considered.

The $ERRs$ evaluation is obtained by means of the modified version of the $VCCT$, which requires computation of nodal forces at the crack tip, and relative displacements at a distance Δa from the tip, see Section 2.3.2.3 for further details. However, $2D$ FE models give unreliable results in terms of ERR individual components, owing to the oscillatory singularity at the bi–material interface and, adopting multi–layer models is a way to overcome this issue. Indeed it's been proven by [6, 7, 8, 9, 10] that multi–layers lead to a direct and correct estimation of modal partition. In particular, when a strong interface is used, that is displacement continuity at interfaces is obtained by prescribed displacements,

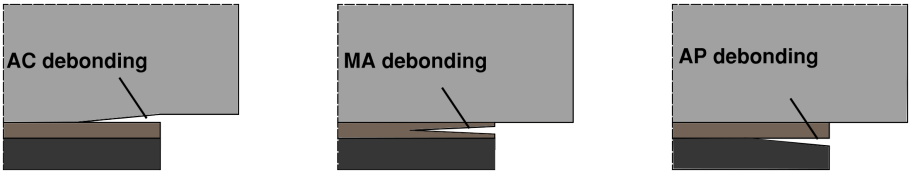

Figure 3.36: Debonding locations

the ERR components can be easily computed from concentrated forces at the crack tip, arising from the stress discontinuities and expressed in term of Lagrangian multipliers (see Section 2.4.2).

Therefore, in Figs. 3.35 and 3.36 a delaminated multi–layer FE model, and the considered delamination locations are shown, respectively. Then, with reference to the 1/2/1 (a) and 3/2/1 (a) assemblies, in Fig. 3.37 a convergence analysis of the ERR by refining the mesh size is presented. In particular, the parameter Δa represents the mesh element size and, consequently, also distance between nodes where concentrated forces and relative displacements are computed. It appears that the total ERR does not depend on the mesh size, whereas for the individual component Δa equal to 0.1 mm gives adequate results. Moreover, the 1/2/1 (a) and 3/2/1 (a) models lead to equal results in term of Mode I ERR, whereas the 1/2/1 (a) model slightly underestimates the Mode II ERR.

Results show a very good agreement between the $2D$ and the multi–layer models in terms of the total ERR, with errors within 2.17%, 1.82% and 2.08% for the 3/2/1 (a) model in the AC, MA and AP locations, respectively. On the contrary, especially when debonding occurs at the AC interface, due to the fact that $2D$ FE solution involves an intrinsic oscillatory behavior in the evaluation of individual ERR components for an interface crack between two dissimilar layers, it is possible to observe the strongly different behavior in terms of mode partitions between the two proposed FE models (for the $2D$ FE model the fixed mesh assembly shown in Fig. 3.30 is adopted). On the other hand, when the oscillatory singularities do not occur as in the case of the MA section, a reasonable agreement with the $2D$ FE results is obtained also in terms of individual ERR mode components, in spite of the small number of layers adopted in the multi–layer models (as shown in [6, 10] a better accuracy can be gained by increasing the number of mathematical layers inside each physical layer). For instance, in case of equal to 300 mm, the G_I component obtained from the 3/2/1 (a) multi–layers model show an un-

derestimation with respect to the $2D$ FE model of the 19.5%, whereas the G_{II} is characterized by an overestimation of the 5.4%.

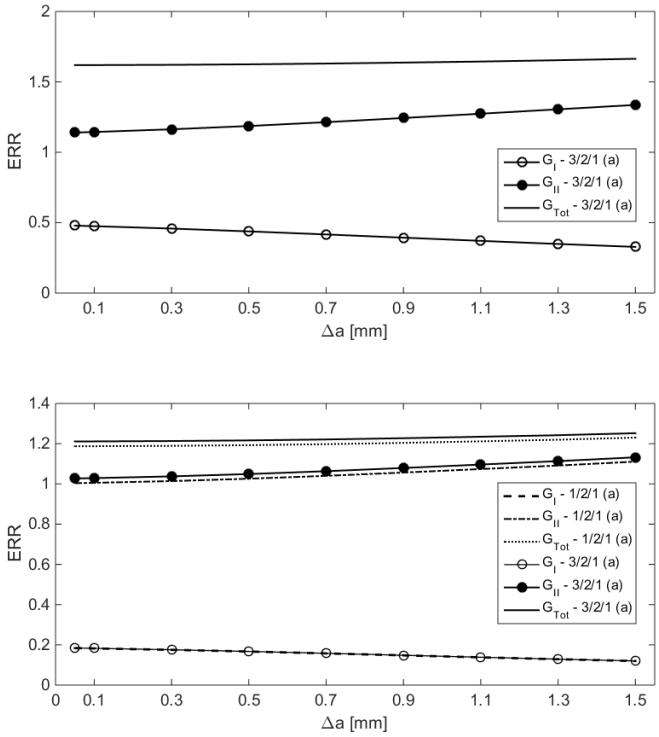

(b)

Figure 3.37: Normalized ERRs obtained with the multi–layer models by varying Δa for a fixed crack length at (a) AC ($a = 400\ mm$) and (b) MA ($a = 300\ mm$)

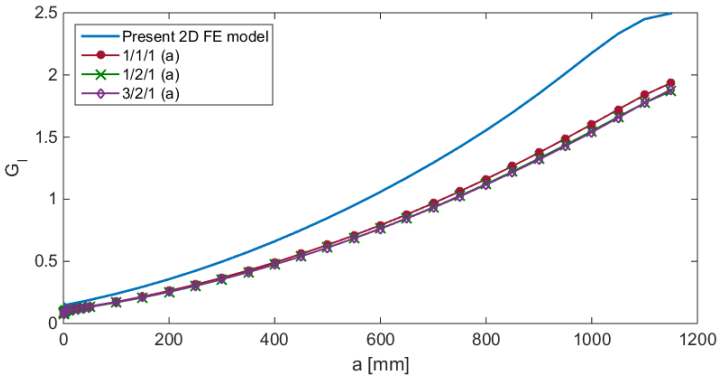

(a)

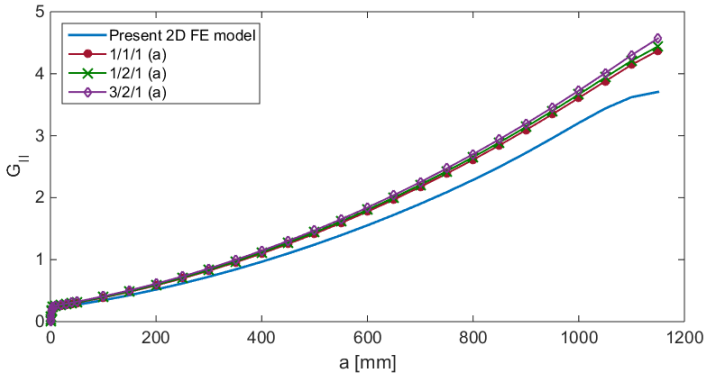

(b)

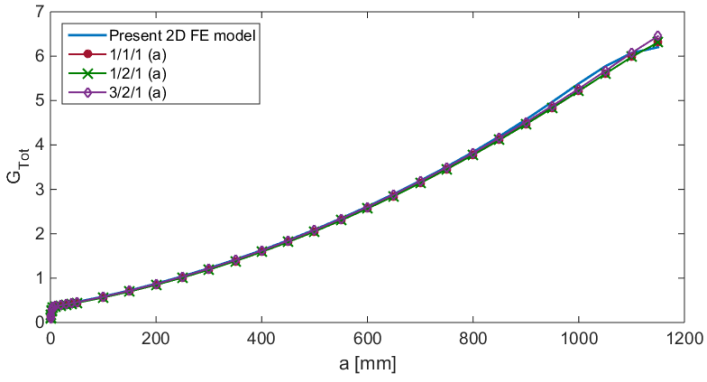

(c)

Figure 3.38: Normalized (a) G_I, (b) G_{II} and (c) G_{Tot} at the AC interface as a function of the delamination length

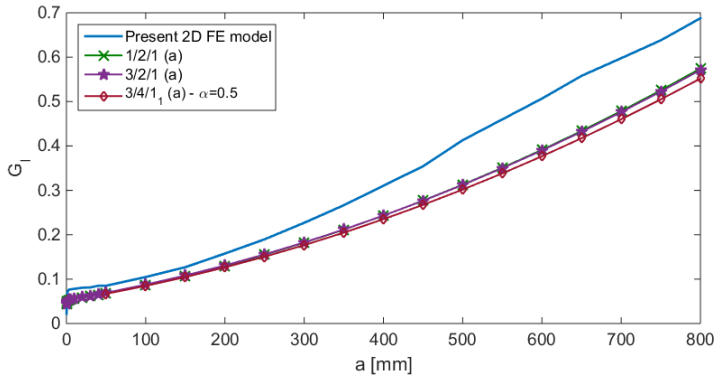

(a)

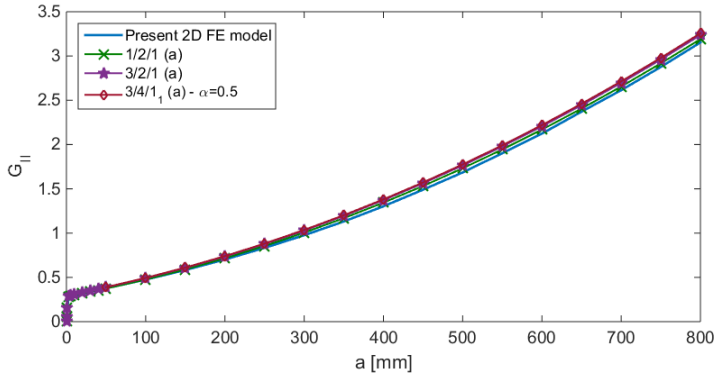

(b)

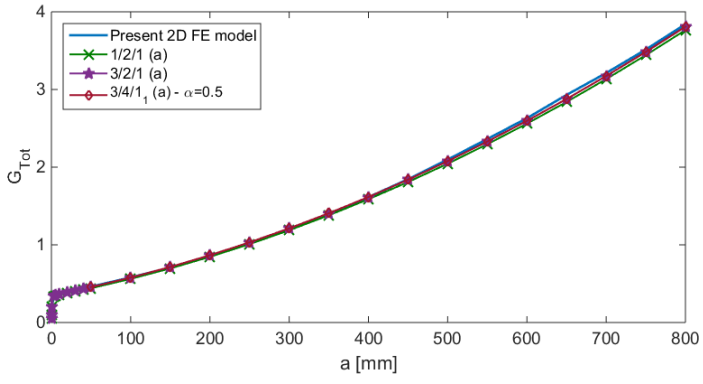

(c)

Figure 3.39: Normalized (a) G_I, (b) G_{II} and (c) G_{Tot} at the MA section as a function of the delamination length

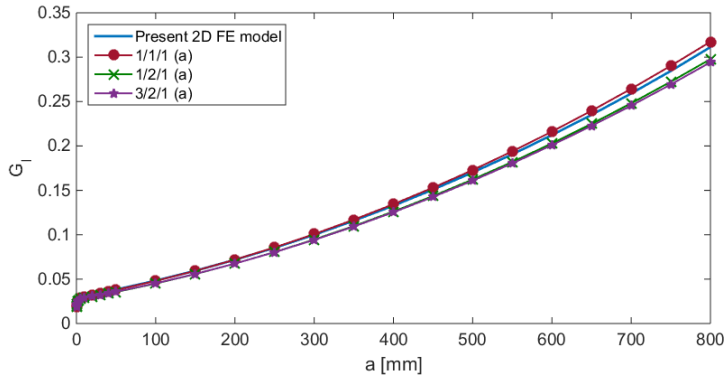

(a)

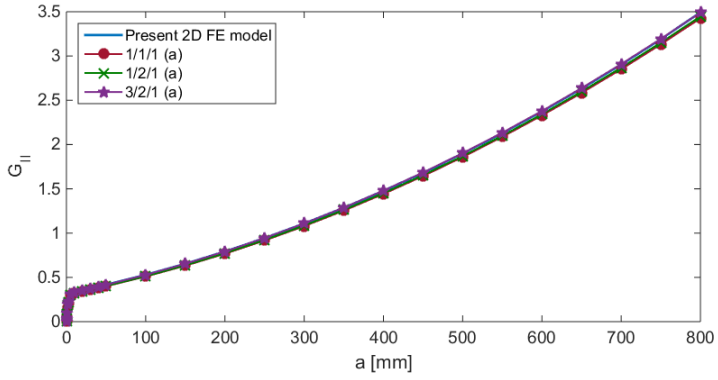

(b)

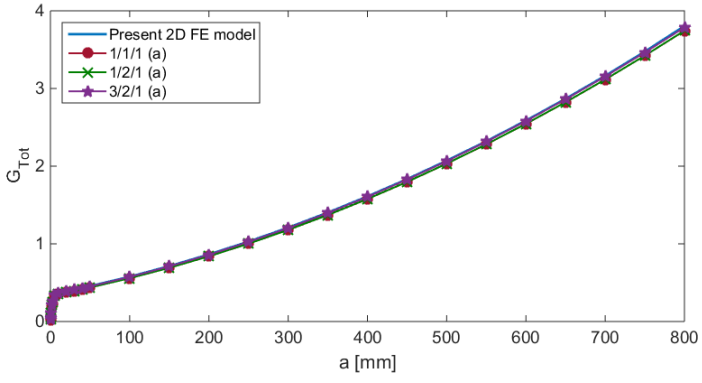

(c)

Figure 3.40: Normalized (a) G_I, (b) G_{II} and (c) G_{Tot} at the AP interface as a function of the delamination length

Bibliography

[1] *COMSOL–AB, COMSOL Multiphysics Reference Manual*, October 2014.

[2] J. Teng, L. Zhang, and S. Smith. Interfacial stresses in reinforced concrete beams bonded with a soffit plate: a finite element study. *Construction and Building Materials*, 16:1–14, 2002.

[3] S. T. Smith and J. G. Teng. Interfacial stresses in plated beams. *Engineering Structures*, 23:857–871, 2001.

[4] P. Cornetti, V. Mantič, and A. Carpinteri. Finite fracture mechanics at elastic interfaces. *International Journal of Solids and Structures*, 49(7–8):1022–1032, 2012.

[5] O. Rabinovitch. Closed–form high–order analysis of RC beams strengthened with FRP strips. *Journal of Composites for Construction*, pages 65–74, 2000.

[6] D. Bruno, R. Carpino, and F. Greco. Modelling of mixed mode debonding in externally FRP reinforced beams. *Composite Science and Technology*, 67:1459–1474, 2007.

[7] F. Greco, P. Lonetti, and P. Nevone Blasi. An analytical investigation of debonding problems in beams strenghtened using composite plates. *Engineering Fracture Mechanics*, 74:346–372, 2007.

[8] Z. Zou, S. R. Reid, P. D. Soden, and S. Li. Mode separation of energy release rate for delamination in composite laminates using sublaminates. *International Journal of Solids and Structures*, 38:2597–2613, 2001.

[9] Z. Zou, S. R. Reid, S. Li, and P. D. Soden. Application of a delamination model to laminated composite structures. *Composite Structures*, 56:375–389, 2002.

[10] D. Bruno, F. Greco, and P. Lonetti. A coupled interface–multilayer approach for mixed mode delamination and contact analysis in laminated composites. *International Journal of Solids and Structures*, 40:7245–7268, 2003.

Chapter 4

Crack initiation and propagation

In this Chapter the edge debonding onset and propagation of a reinforced concrete beam strengthened with externally bonded FRP composite plates is investigated numerically. A mixed mode coupled criterion, representing an original extension of those existing in the literature, is adopted. In particular, in Section 4.1 debonding onset for different locations across the adhesive layer is predicted, accounting also the influence of critical parameters, and by adopting the innovative multi–layer formulation presented in Chapter 3. Then, in Section 4.2 the subsequent damage propagation along the considered locations is analyzed.

4.1 Coupled failure criterion for crack onset in mixed mode problems

In order to predict crack initiation at interfaces of strengthened systems, the coupled criterion defined in Section 2.5.2, which accounts both interfacial stresses and fracture energies, is here adopted. In particular, such a criterion was introduced in order to overcome difficulties in the onset evaluation due to the singularity of the stress field at plate end, and to

the impossibility to apply the $LEFM$ for vanishing cracks. Indeed, the present criterion, which is here adapted to mixed mode cases, requires a simultaneous fulfillment of an energetic and a tensional (integral or pointwise) condition, and is given by (see Eqs. (2.5.1) and (2.5.2)):

$$\begin{cases} \dfrac{\beta^2 \int_0^a G_T(1,l)\ dl}{\int_0^a G_c\ dl} = 1 \\ \left(\dfrac{\beta \langle \int_0^a \sigma_y(1,l)\ dl \rangle}{\sigma_c\ a}\right)^2 + \left(\dfrac{\beta \langle \int_0^a \tau_x(1,l)\ dl \rangle}{\tau_c\ a}\right)^2 = 1 \end{cases} \tag{4.1.1}$$

$$\begin{cases} \dfrac{\beta^2 \int_0^a G_T(1,l)\ dl}{\int_0^a G_c\ dl} = 1 \\ \left(\dfrac{\beta \langle \sigma_y(1,l) \rangle}{\sigma_c\ a}\right)^2 + \left(\dfrac{\beta \langle \tau_x(1,l) \rangle}{\tau_c\ a}\right)^2 = 1 \end{cases} \tag{4.1.2}$$

where σ_c and τ_c are the tensile and shear strengths, respectively, $G_T(1,l)$ is the total ERR for a unit load at the distance l from the plate end, $\sigma_y(1,l)$ and $\tau_x(1,l)$ are the normal and shear interlaminar stresses for a unit load at a distance l behind the plate end, $<>$ are the Macaulay brackets and G_c is the fracture toughness. Therefore, the multiplier of unit load β, and the crack length a which satisfy the above two conditions represent the couple (β_c, a_c) of critical load and length at crack initiation.

In the present study, a TPB scheme (Tab. 3.8) is again considered. Debonding is predicted from the interlaminar stresses distribution estimated by using both strong and weak interface formulations (Section 3.1.3) and from total and individual $ERRs$ determined by using the multi–layer models endowed with strong interfaces (Section 3.2.2). At first, in Section 4.1.1 critical loads obtained from $2D$ FE and multi–layer models is compared considering only Mode I fracture toughness at the physical interfaces AC and AP, and accounting mode mixity in MA. Then, in Section 4.1.2 a mixed mode critical ERR is accounted in all locations. Finally, in Section 4.1.3 a parametric study aimed to evaluate influence of interface critical parameters on debonding is carried out. In particular, the critical parameters considered in the numerical

simulations are summarized in the Tab. 4.1 and are taken from [1, 2]:

	σ_c [MPa]	τ_c [MPa]	G_{Ic} [N/m]	α
AC	7.2	7.2	100	0.2/1
MA	7.2	7.2	500	0.2
AP	7.2	7.2	500	0.2/1

Table 4.1: Critical parameters assumed for the coupled stress–energy criterion

where σ_c and τ_c are the tensile and the shear strengths, respectively, G_{IC} is the Mode I interface toughness and α is a sensitivity parameter which takes into account mode mixity. In particular, when $\alpha = 1$ only the fracture Mode I toughness is considered according to the following mixed mode toughness function [3]:

$$\Gamma(\bar{\psi}) = G_{IC}\{1 + \tan^2[(1-\alpha)\bar{\psi}]\} \tag{4.1.3}$$

In the present numerical analysis, the shear strength value, $\tau_c = 7.2\ MPa$, is the same as the one adopted in Carpinteri et al. [2], and the tensile strength σ_c is assumed equal to τ_c. Moreover, the Mode I interface toughness at the AC interface is about equal to that of the concrete, since experimental evidences show that delamination often occurs within the reinforced concrete beam, between the steel bars and the AC interface [4, 5]. On the other hand, G_{IC} at MA and AP is driven by the FRP composite plate properties. However, in Section 4.1.3 influence of these parameters on crack initiation will be checked.

4.1.1 2D FE and multi–layer models debonding onset loads

The efficacy of the proposed multi–layer modelling technique is now verified in terms of predictions of debonding onset load (denoted as F_c) for both the coupled stress–energy criteria introduced in Eqs. (4.1.1) and (4.1.2). To this end, results are obtained by using both the $2D\ FE$ and

the multi–layer models, the former model being considered as a reference solution. However, in the case of crack onset at the AC or AP interface, in order to carry out comparisons with the $2D$ FE model, only the influence of the fracture Mode I toughness on the debonding initiation is considered, due the influence of oscillatory singularities on the $2D$ FE model. Conversely, in the MA section also the mode mixity is taken into account. In fact, individuals $ERRs$ obtained in the $2D$ case in MA are well defined owing to the absence of the oscillatory singularities.

Stress criterion	$F_{c,2D}$ **[kN]**	1/1/1 (a)	1/1/1 (b)	1/1/1 (c)	1/2/1 (a)	1/2/1 (b)	1/2/1 (c)	3/2/1 (c)
AC interface								
Integral	1,719.38	1.21%	2.21%	4.13%	0.57%	1.50%	1.83%	0.40%
Pointwise	1,875.35	-2.64%	-1.98%	1.57%	-3.23%	-2.53%	-1.83%	-2.78%
AP interface								
Integral	3,255.02	0.28%	0.77%	0.24%	0.34%	0.18%	0.32%	-0.52%
Pointwise	3,523.22	0.67%	0.44%	0.11%	0.40%	0.38%	0.12%	-0.97%
MA section								
Integral	3,805.76	/	/	/	1.55%	1.57%	1.62%	0.89%
Pointwise	4,148.79	/	/	/	2.87%	2.70%	2.65%	1.57%

Table 4.2: Relative percentage errors for the debonding onset loads with respect to the 2D results

Stress criterion	$a_{c,2D}$ **[mm]**	1/1/1 (a)	1/1/1 (b)	1/1/1 (c)	1/2/1 (a)	1/2/1 (b)	1/2/1 (c)	3/2/1 (c)
AC interface								
Integral	9.8	20.41%	10.20%	-6.12%	19.39%	9.18%	6.12%	2.04%
Pointwise	5.6	42.86%	37.50%	10.71%	39.29%	32.14%	25.00%	17.86%
AP interface								
Integral	81.8	11.98%	11.49%	7.95%	11.49%	11.00%	10.39%	3.91%
Pointwise	38.5	9.87%	13.25%	12.73%	9.35%	12.73%	12.73%	4.94%
MA section								
Integral	113.2	/	/	/	9.36%	9.19%	8.92%	3.80%
Pointwise	49.2	/	/	/	8.54%	11.38%	11.59%	4.88%

Table 4.3: Relative percentage errors for the debonding onset length with respect to the 2D results

Percentage errors between the critical loads obtained by using the multi–layer model ($F_{c,ML}$) and the $2D$ FE one ($F_{c,2D}$), evaluated as $(F_{c,ML} - F_{c,2D}/F_{c,2D})\%$, are reported in the above Tab. 4.2. Similarly, in Tab. 4.3 are reported the percentage errors between critical lengths obtained by using the multi–layer ($a_{c,ML}$) and the $2D$ FE ($a_{c,2D}$) models, evaluated as $(a_{c,ML} - a_{c,2D}/a_{c,2D})\%$. Then, in Figs. 4.1 – 4.3 actual values of critical load and length are illustrated, where

subscript ML denotes multi–layer models. The layer arrangements are referred to the multi–layer models adopted for the interface stresses predictions, since $ERRs$ are always calculated by using a strong interface formulation. In particular, when a weak interface formulation is accounted in both directions, i.e. (c) models, the horizontal stiffnesses adopted are $K_{j,h} = G_a B_a/(0.25H_a/2)$, $K_{j,h} = G_a B_a/(0.05H_a/2)$ and $K_{j,h} = G_a B_a/(0.05H_a/2)$ for the 1/1/1 (c), the 1/2/1 (c) and the 3/2/1 (c) assembly, respectively. Results can be summarized as follows

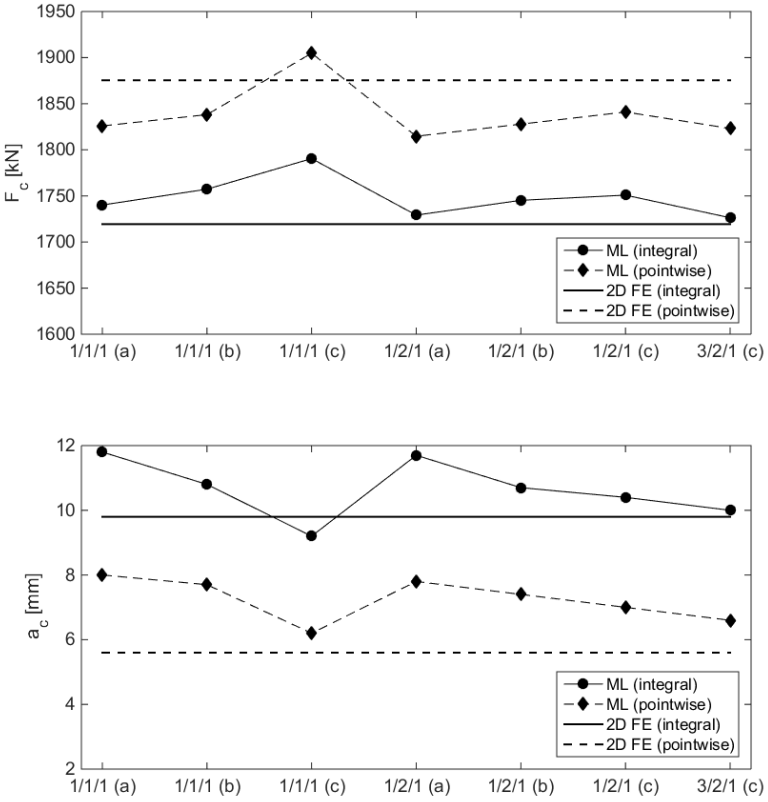

(b)

Figure 4.1: Critical (a) load and (b) length at the AC interface: comparison between 2D FE and multi–layer results

- **Pointwise criterion**: compared to the integral one, it leads to higher values for the critical load and, consequently, to lower critical lengths.
- **Onset load**: percentage errors between the multi–layer and $2D$ FE models are always of low magnitude and within 4.13%, with the maximum error obtained by the 1/1/1 (c) model in AC.
- **Onset length**: larger errors are obtained, with a maximum absolute percentage error equal to 42.86% obtained for the 1/1/1 (a)

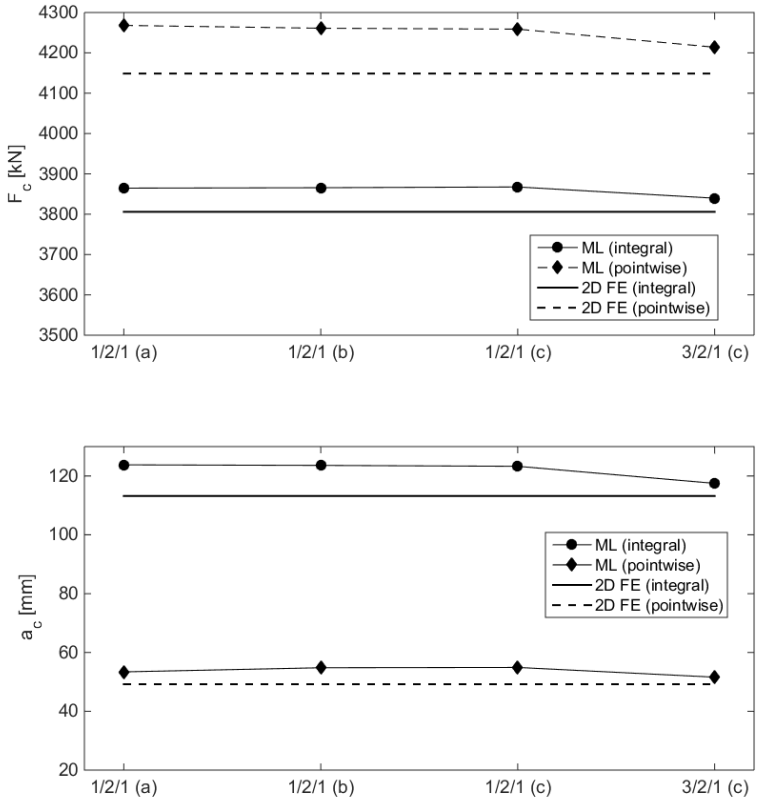

(b)

Figure 4.2: Critical (a) load and (b) length at the MA section: comparison between 2D FE and multi–layer results

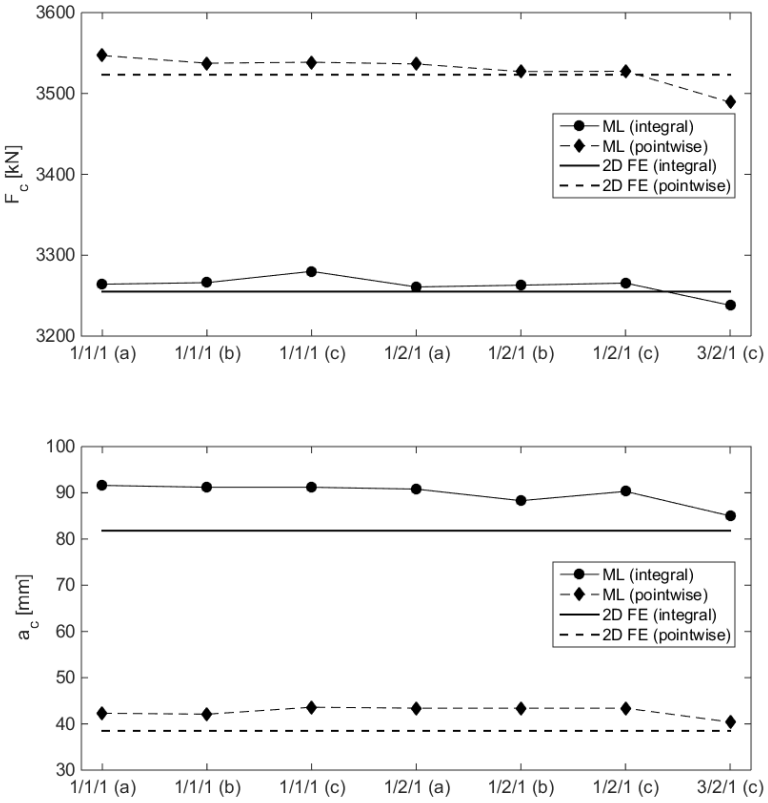

(b)

Figure 4.3: Critical (a) load and (b) length at the AP interface: comparison between 2D FE and multi–layer results

layer assembly. However, the onset length is small compared to the $CFRP$ plate size.

- **AC interface**: when an integral stress criterion is adopted, the lower absolute percentage errors are obtained by using the 3/2/1 (c) arrangement in terms of both critical load and length; conversely, in case of pointwise stress criterion the 1/1/1 (c) assembly gives the lower absolute errors.

- **AP interface**: percentage errors are of low magnitude. In partic-

ular, when an integral stress criterion is adopted, the lower absolute percentage errors are obtained by using the 1/2/1 (b) and the 3/2/1 (c) arrangement for onset load and length, respectively; on the other hand, in case of pointwise stress criterion, lower absolute errors are given by the 1/1/1 (c) and 1/2/1 (a) assemblies.

- **MA section**: in this case, where the 1/1/1 assembly is not able to study debonding, the 3/2/1 (c) assembly gives better approximations of delamination onset for both stress criteria types.

Although generally speaking, more enriched multi–layer models provide better accuracy, it transpires that reasonably accurate results in terms of debonding onset loads at AC and AP interfaces can be obtained by considering only one mathematical layer within each physical layer. This is true also when a strong interface formulation is adopted, and interfacial normal stresses are inaccurately predicted near the plate end. Indeed, the error in interfacial normal stresses is confined within a small zone near the plate end, and interfacial shear stresses, which are overestimated by the (a) models, play a more significant role in the fulfillment of the crack onset coupled criterion.

In addition, from results given in Tabs. 4.2 and 4.3, a general trend can be observed, pointing out that for both the integral and pointwise stress criteria, the 3/2/1 (c) assembly gives on average the lowest absolute relative percentage error with respect to the $2D$ FE solution, as reported in Tab. 4.4.

	1/1/1 (a)	1/1/1 (b)	1/1/1 (c)	1/2/1 (a)	1/2/1 (b)	1/2/1 (c)	3/2/1 (c)
Onset load	1.20%	1.35%	1.51%	1.49%	1.48%	1.40%	1.19%
Onset length	21.28%	18.11%	9.38%	16.24%	14.27%	12.46%	6.24%

Table 4.4: Average absolute relative percentage error on crack initiation prediction at all location between multi–layer and $2D$ FE models

4.1.2 Critical load and critical length for multi–layer models by considering mode mixity

With references to the 1/2/1 and 3/2/1 multi–layer assemblies, and assuming the critical parameters introduced in the previous Table 4.1 (with α fixed to 0.2 everywhere), numerical simulations show how the most favorable location for crack initiation is the AC interface (see Fig. 4.4). In fact, a lowest load is required, and this is true independently of the interface formulation adopted to capture interfacial stresses. Therefore, in Fig. 4.5 load–delamination length curves satisfying the energetic and the stress (pointwise and integral) criteria are reported, respectively, for all considered debonding locations. The critical pair of crack onset load and length values can be obtained at the intersection between the two curves associated to the energetic and stress criteria.

Fig. 4.5 show that the stress criterion satisfied in the pointwise form, leads to higher loads for crack onset. Moreover, at MA and AP, for very small crack lengths the stress criterion is fulfilled for high values of applied load. This result is presumably due to the fact that at these locations shear stresses tend to vanish at the cut–off section.

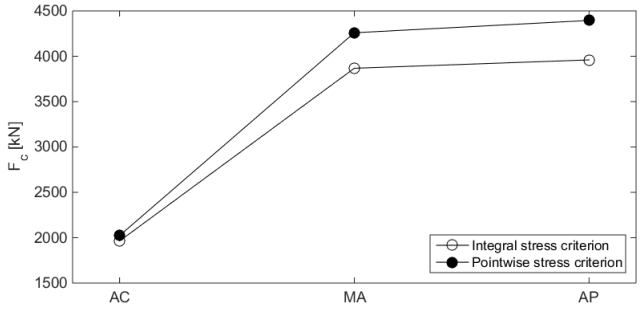

Figure 4.4: Critical onset load for the 3/2/1 layer assembly (the 3/2/1 (c) model is adopted for interfacial stresses)

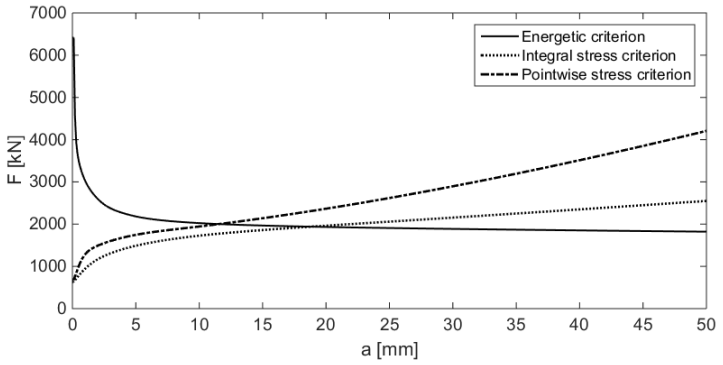

(a)

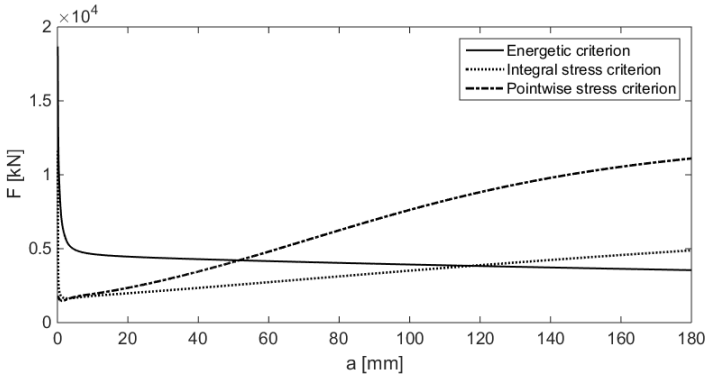

(b)

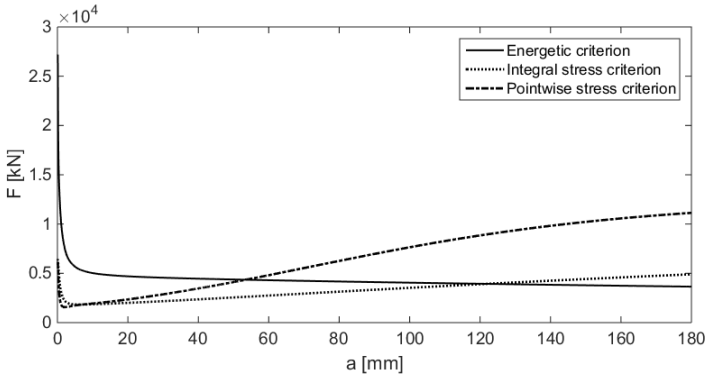

(c)

Figure 4.5: Critical load and critical length according to the mixed mode coupled criterion at (a) AC, (b) MA and (c) AP for the 3/2/1 layer assembly (the 3/2/1 (c) model is adopted for interfacial stresses)

Then, results given in Fig. 4.6 point out that the delamination prediction obtained by the different multi–layer models are in a reasonable agreement in terms of load and delamination length at the crack onset, whatever interface formulation is adopted for the stress distribution evaluation.

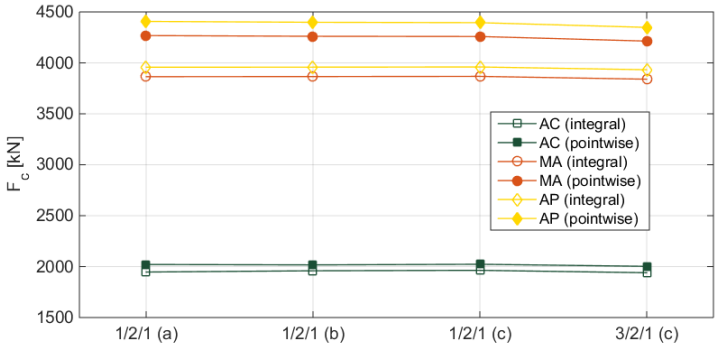

(a)

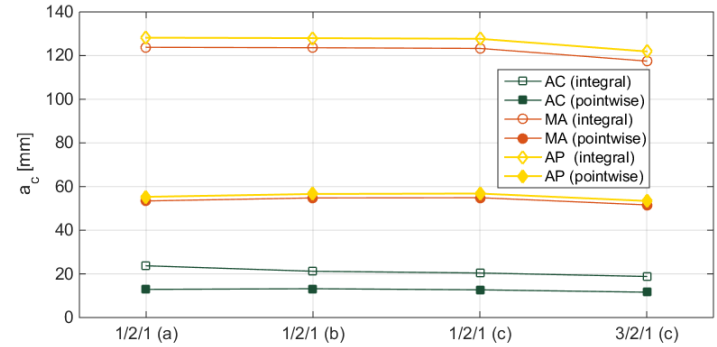

(b)

Figure 4.6: Debonding onset load (F_c) and critical length (a_c) for various multi–layer assemblies and different debonding locations across the adhesive layer

4.1.3 Influence of critical parameters

In this Section, the influence on debonding initiation of the Mode I fracture toughness (G_{Ic}), the shear (τ_c) and tensile (σ_c) strengths is evaluated.

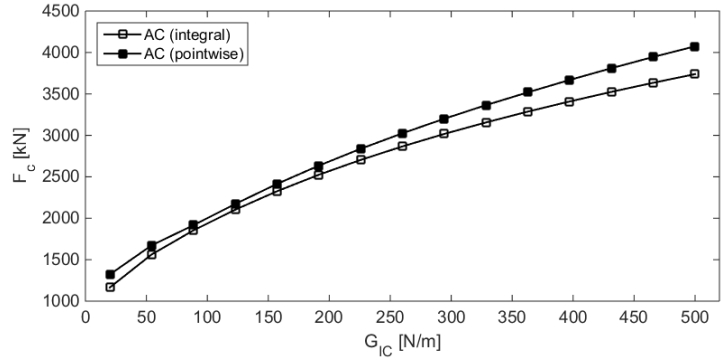

(a)

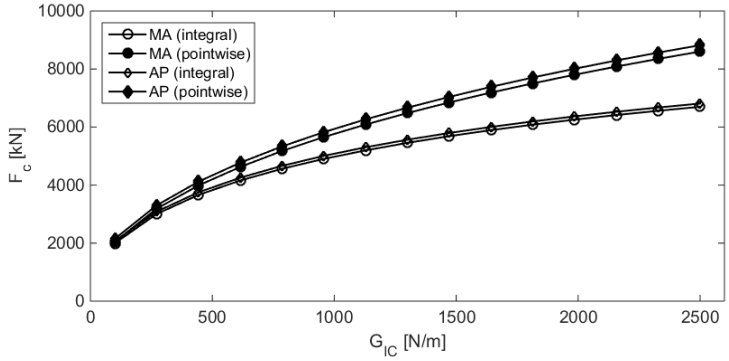

(b)

Figure 4.7: Influence of G_{Ic} on the critical load for crack onset for the 3/2/1 layer assembly (the 3/2/1 (c) model is adopted for interfacial stresses)

Results are illustrated in Figs. 4.7 – 4.11, leading to the following conclusions:

- **Mode I fracture toughness**: increasing G_{Ic} leads to increase the critical crack onset load (Fig. 4.7) and length (Fig. 4.8).

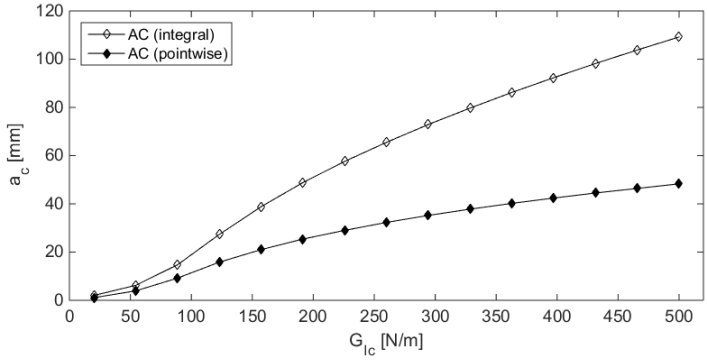

(a)

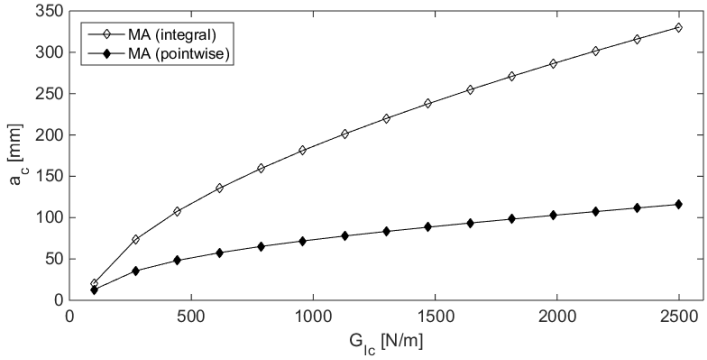

(b)

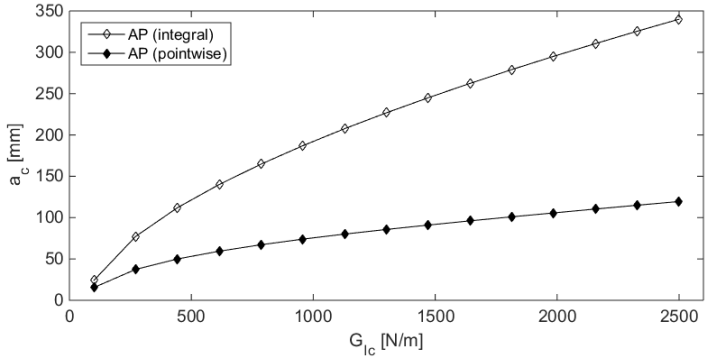

(c)

Figure 4.8: Influence of G_{Ic} on the critical crack onset length at (a) AC, (b) MA and (c) AP for the 3/2/1 layer assembly (the 3/2/1 (c) model is adopted for interfacial stresses)

- **critical strengths**: for G_{Ic} fixed, and by increasing the shear and tensile strengths assumed equals, the applied load at debonding onset rises (4.9). Conversely, for high values of interface strengths, onset lengths become very small (4.10). Moreover, in Fig. 4.9 appears that the onset load at AP obtained by increasing shear and tensile strengths has a non smooth behavior. This issue is probably due to the fact that debonding takes place at small lengths. Indeed, it can be seen in Fig. 4.5 that near the plate end the energy criterion behaves in a singular manner and, consequently, the intersection point between stress and energetic criterion strongly depends on the discretization adopted in the numerical procedure (0.1 mm in the present case).

- **tensile strength**: when the shear strength and the critical value of the Mode I fracture toughness are fixed, the critical load and length and scarcely affected by the tensile strength σ_c (Fig. 4.11). However, in case of low tensile strength, and when the integral stress criterion is used, the onset load slight decreases while the onset length increases.

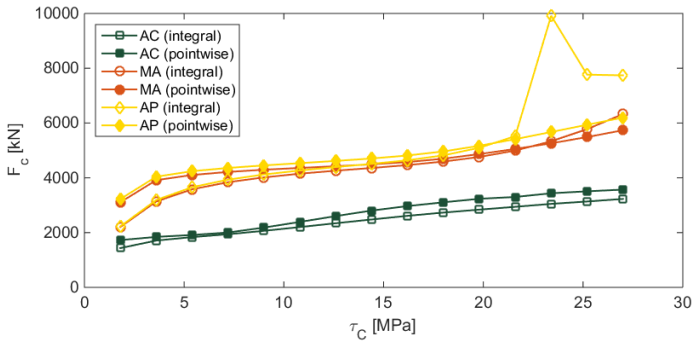

Figure 4.9: Influence of the critical shear strength on the critical crack onset load for the 3/2/1 layer assembly (the 3/2/1 (c) model is adopted for interfacial stresses)

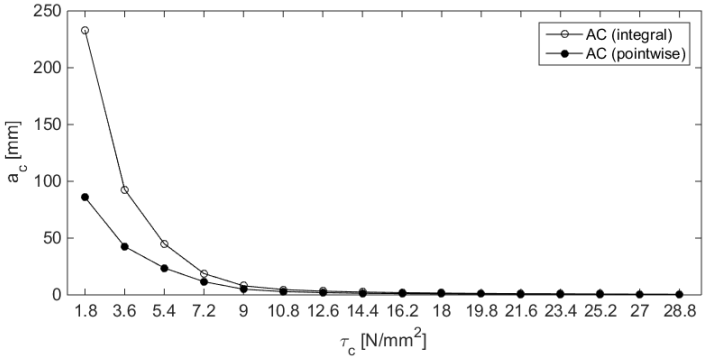

(a)

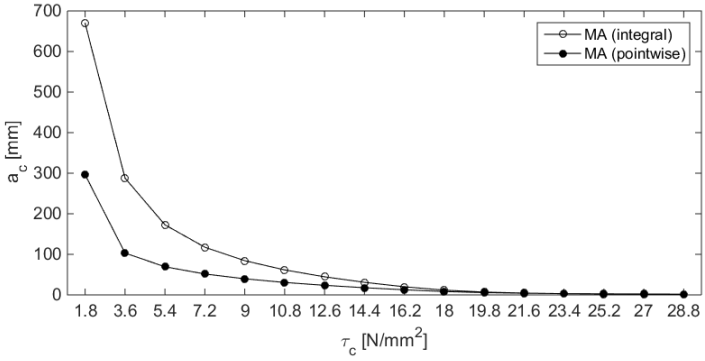

(b)

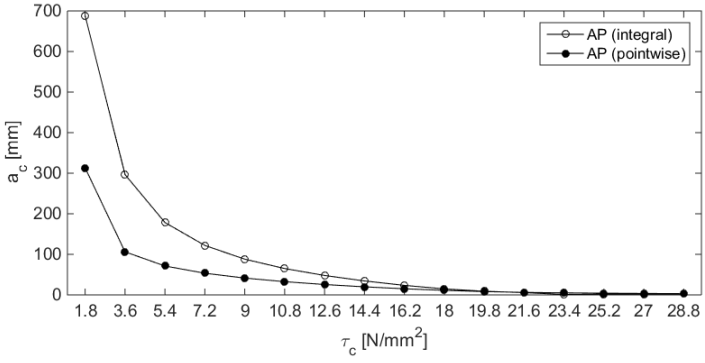

(c)

Figure 4.10: Influence of the critical shear strength on the critical crack onset length at (a) AC, (b) MA and (c) AP for the 3/2/1 layer assembly (the 3/2/1 (c) model is adopted for interfacial stresses)

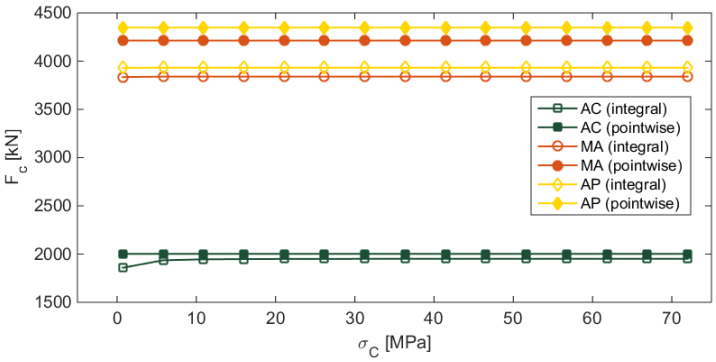

(a)

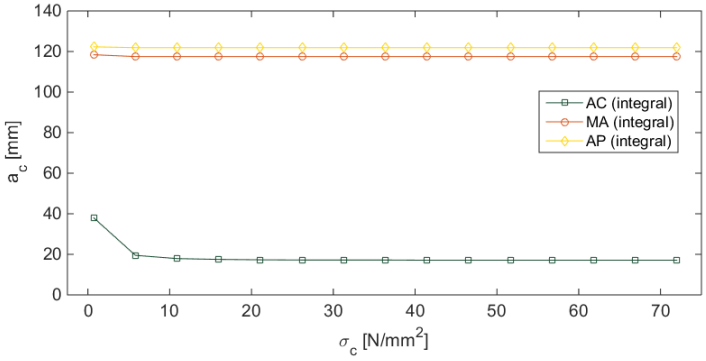

(b)

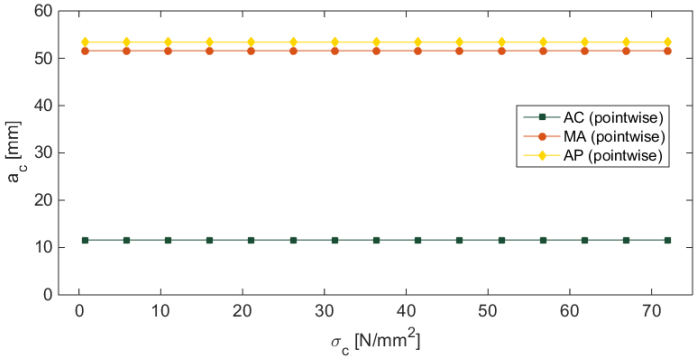

(c)

Figure 4.11: Influence of the critical tensile strength on the critical crack onset (a) load and (b)–(c) length for the 3/2/1 layer assembly (the 3/2/1 (c) model is adopted for interfacial stresses)

4.2 Crack propagation

.

Once that edge debonding initiation of FRP in strengthened systems is predicted, the damage propagation can be studied with the aid of the mixed–mode fracture energy criterion introduced in Section 2.5.2:

$$\beta^2 \frac{G_T}{G_c(\rho, \alpha)} = 1 \tag{4.2.1}$$

Therefore, in Fig. 4.12 debonding propagation is illustrated for the three analyzed locations across the adhesive layers, by evaluating for each value of the debonding length a the associated load satisfying the mixed mode crack propagation criterion. In particular, the point at $a = 0$ corresponds to the critical load at the crack onset, which is attributed to a zero debonding length and evaluated with the proposed coupled criterion, while the onset length corresponds to the first point of the curves. Also during propagation, debonding at the AC interface takes place at lower loads than those required at MA and AP.

In this context, Carpinteri et al. [2] computed the post–peak re-

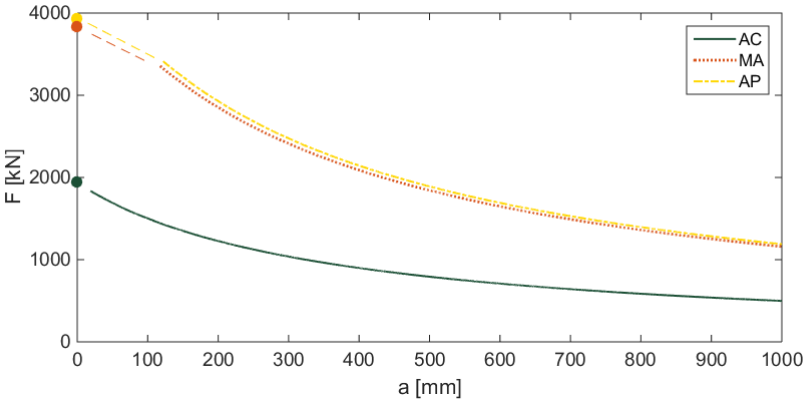

Figure 4.12: Crack propagation for the 3/2/1 multi–layer assembly (the 3/2/1 (c) model is adopted for interfacial stresses)

sponse in case of FRP debonding, by evaluating the load–displacement curve (corresponding to the mid–span deflection of a TPB scheme) for an undamaged and a damaged configuration. In particular, by assuming a linear elastic interface, when no reinforcement is used, load and displacement are related by a straight line. Then, by adding the FRP plate, a slope increase is obtained until delamination and, at crack onset, the load drops in an unstable manner through a softening curve. Finally, load increases again by tending to the original line (when no FRP is used). A typical post–peak response is shown in Fig. 4.13, where symbols B and L_s denote the plate width and the bonded region length when half structure is considered, respectively.

Such behavior is confirmed in the present case, as shown in Fig. 4.14, where the mid–span deflection is measured at the lower beam sub–layer, being the axis origin taken at the AC interface. Delamination lengths associated to the points marked on the Figure are reported in Tab. 4.5.

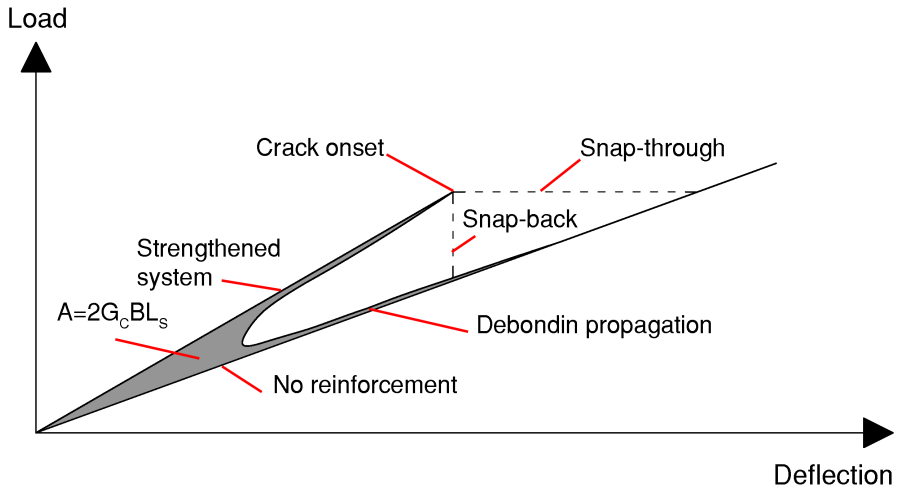

Figure 4.13: Load–deflection curve for a reinforced TPB beam

Point	a [m]	F [kN]
1	0.000	1.00
2	0.000	100.00
3	0.000	1000.00
4	0.000	1800.00
5	0.019	1835.41
6	0.020	1829.95
7	0.050	1691.67
8	0.100	1502.44
9	0.200	1227.79
10	0.400	899.07
11	0.600	709.20
12	0.800	585.57
13	1.000	498.67
14	1.120	458.69
15	1.140	453.25
16	1.300	502.18
17	1.400	543.74
18	1.500	591.78
19	1.600	648.95
20	1.700	718.32
21	1.800	804.32
22	1.900	913.87
23	2.000	1058.85

Table 4.5: Crack propagation at the AC interface

In particular,

- **From point 1 to point 4**: the FRP is perfectly bonded to the reinforced concrete beam, and the load–displacement relationship is linear.
- **Point 5**: debonding starts at the AC interface.
- **From point 6 to point 15**: debonding propagates along the interface until the mid–span, corresponding to a softening behavior of the load–displacement curve.

- **From point 16 to point 23**: debonding is beyond the mid–span, and the whole system loses stiffness returning to that of the unstrengthened system.

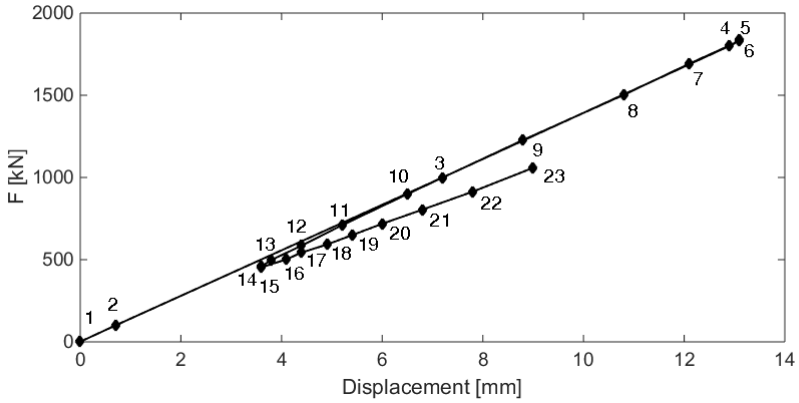

Figure 4.14: Load – displacement curve for the 3/2/1 multi–layer assembly (the 3/2/1 (*c*) model is adopted for interfacial stresses) when debonding occurs at the *AC* interface

Bibliography

[1] D. Bruno, R. Carpino, and F. Greco. Modelling of mixed mode debonding in externally FRP reinforced beams. *Composite Science and Technology*, 67:1459–1474, 2007.

[2] A. Carpinteri, P. Cornetti, and N. Pugno. Edge debonding in FRP strengthened beams: Stress versus energy failure criteria. *Engineering Structures*, 31:2436–2447, 2009.

[3] J. W. Hutchinson and Z. Suo. Mixed mode cracking in layered materials. *Advances in Applied Mechanics*, 29:63–191, 1992.

[4] O. Rabinovitch and Y. Frostig. Experiments and analytical comparison of RC beams strengthened with CFRP composites. *Composites: Part B*, 34:663–677, 2003.

[5] M. Achintha and C. Burgoyne. Fracture energy of the concrete–FRP interface in stregthened beams. *Engineering Fracture Mechanics*, 110:38–51, 2013.

Conclusions

In the present research work, edge debonding of FRP plates bonded to reinforced concrete beams is studied. First, the mechanical behavior at both micro and macro scales is described, then the use of FRP in strengthened systems is discussed. Several studies concerning evaluation of interfacial stresses and fracture energies are reviewed, and a multi–layer formulation, with both strong or weak interfaces, able to overcome shortcomings of the commonly used method is developed. In the strong formulation the interface element imposes a perfect adhesion constraint between adjacent layers and the interfacial stresses are recovered as Lagrange multipliers, whereas in the weak one a linear interface constitutive law with finite stiffness parameters simulates the connection between the adjacent layers and directly defines interfacial stresses. The accuracy of the proposed multi–layer model can be improved by means of an appropriate calibration of the stiffness parameters of the weak interface model as a function of the geometrical and mechanical parameters of the adjacent physical components (the adhesive layer, particularly) and by increasing the layer number within the mathematical assembly. The calibration of the stiffness parameters in the weak interface formulation leads to recover the effects of deformability neglected in the context of beam theory (especially the transverse one). It is worth noting that while the transverse deformability is completely neglected by the kinematical model adopted for each mathematical layer, the shear deformability of the system is already incorporated, although in a simplified way, within

the multi–layer first–order shear deformable formulation. As a consequence, the horizontal stiffness parameter involves, in addition to the shear modulus of the adhesive layer, only a fraction of its thickness. This is in contrast to the case of the vertical stiffness parameter, which are defined in terms of the adhesive layer Young modulus and of its whole thickness.

The proposed multi–layer model, implemented by using a finite element formulation of the multivariable one–dimensional equations, involves a considerably reduced computational cost with respect to a continuum FE model, while providing a reasonably accurate evaluation of both interlaminar stresses and fracture energies. On the other hand, the proposed formulation overcomes the inaccuracies of the beam based models proposed in the literature in the prediction of the quantities governing the debonding behavior of strengthened beams. At the same time it leads to well defined fracture energies for bi–material interface system, where the $2D$ elasticity solution causes a non–convergent behavior of ERR mode components.

Within the proposed multi–layer model, ERR and its mode components are determined by using the strong interface formulation, whereas the interlaminar stresses distribution, useful to predict delamination initiation, are calculated by using both the strong and weak interface formulation. As a matter of fact, interlaminar stresses predicted by means of the strong interface formulation are not effective in that significant information are lost as a consequence of crack tip interfacial concentrated forces arising owing to crack tip stress singularities. On the contrary, when the interface stiffness parameters are appropriately calibrated in order to take into account for transverse deformability of layers, an effective prediction of interlaminar stresses distribution can be obtained by using the weak interface formulation. Moreover, the above interfacial concentrated forces provides a consistent approach rationally based on global parameters (crack tip interfacial forces) to compute ERR and its mode components, since in–plane and out–of–plane interfacial con-

centrated forces correspond to the two mode of fracture, Mode II and Mode I, respectively.

Numerical examples are devoted to the case of a simply supported beam scheme strengthened by a bonded plate subjected to both a uniformly distributed load and a point load in the mid–span. The accuracy of a multi–layer formulation is thus analyzed showing comparisons with results obtained by using a $2D$ continuum FE model of the strengthened system. With reference to the uniform loading condition, a comparison between results obtained by using the proposed multi–layer formulation and the $2D$ continuum FE model is carried out in terms of interfacial stresses. Three section locations are studied, namely the AC and AP interfaces and the MA section, respectively. Several multi–layer models, which essentially differ for the number of layers adopted to model the adhesive physical layer and the concrete beam, and for the type of interface formulation assumed to simulate the adhesion between components, are developed. Results show how the adopted interface formulation plays a stronger role in the interfacial stresses behavior with respect to the number of layers considered in the multi-layer model. In the case of multi–layer FE models in which a strong interface formulation is considered for both the physical interfaces (i.e. AC and AP interfaces) the interfacial normal stress distribution, contrary to the $2D$ continuum model, is always compressive in all the analyzed locations, whereas the shear stress results overestimated. However, the inaccuracy introduced by the multi–layer models adopting the strong interface formulation turns out to have a scarce influence on the debonding onset mechanism, the inaccuracy being confined in a relatively small zone near the plate end. On the other hand, when the weak formulation is adopted to simulate connections in the transverse direction to the layers, normal stress obtained by means of the multi–layer model becomes in good agreement with the $2D$ FE continuum, the normal stresses being tensile or compressive near the bonded plate edge at the AC and the AP interface, respectively.

Finally, numerical calculations show that enhanced prediction of

interlaminar stresses distribution at all the analyzed section locations across the adhesive layer can be obtained by means of the models adopting a weak interface formulation in both transverse and longitudinal directions, with small improvements in accuracy as the number of layers increases with respect to a 1/2/1 assembly.

In the case of the mid–span point load, debonding onset and propagation are investigated by using the proposed innovative mixed mode coupled failure criterion, by also analyzing the influence of the main parameters governing debonding behavior, such as interfacial fracture toughness and strength. The energy release rate behavior for the different analyzed locations (i.e. AC, MA and AP), as a function of the debonded length a, is investigated by using a strong interface formulation.

The efficacy of the proposed multilayer modelling technique is then verified in terms of predictions of debonding onset load. Results show how the percentage errors in terms of onset loads between the multi–layer and FE models are always of low magnitude. It emerges that the AC interface is the most favorable location for the debonding onset, since it requires a lower load to initiate, and that the pointwise stress criterion leads to higher values of critical load. Moreover the analyzed multi–layer models lead to results in terms of debonding onset load and length in reasonable agreement with the FE solution and with error always low in magnitude, especially in terms of the debonding onset load. As expected, for both the integral and pointwise stress criteria, the more enriched layer assembly 3/2/1 gives, on average, the lowest absolute relative percentage error.

Therefore, for the study of debonding at an arbitrary location across the adhesive thickness, the 3/2/1 assembly can be considered as an optimal one, since it is expected that further increasing of the layers number do not lead to appreciable improvements.

Finally, the influence of the critical stress and fracture parameters is studied with reference to the case of 3/2/1 multi–layer assembly. It

can be noted that both fracture toughness and shear strength plays a significant role on debonding onset, while the effect of tensile strength can be considered negligible. The above results and considerations point out that the proposed model appears to be sufficiently general to be adopted for the analysis of more general debonding mechanisms, such as that promoted by an intermediate flexural or shear crack in the base beam.

Appendix A

The coefficients introduced in the expressions of the axial displacement of the lower layer (Eq. (2.2.35)),

$$u_1(x) = -\frac{b\psi_1(x) + c\psi_2(x) + gx + \dfrac{hx^2}{2}}{a}$$

are

$$a = \frac{1}{2}\,\frac{\left(\left(A_1 + A_2\right)t_3^2 + \left(\left(2t_2 + t_1\right)A_1 + A_2 t_2\right)t_3 + 4D_3\right)A_3 + 4D_3\left(A_1 + A_2\right)}{A_3 t_3}$$

$$b = \frac{1}{4}\,\frac{\left(\left(-A_2 t_2 t_3 - A_2 t_3^2 - 4D_3\right)t_1 + 4D_1 t_3\right)A_3 - 4D_3 t_1 A_2}{A_3 t_3}$$

$$c = \frac{1}{4}\,\frac{\left(-A_2 t_2^2 t_3 + \left(-A_2 t_3^2 - 8D_3\right)t_2 + 4D_2 t_3\right)A_3 - 4D_3 t_2 A_2}{A_3 t_3}$$

$$g = -\left(\bar{F}L + \bar{M}\right)$$

$$h = \bar{F}$$

The coefficients introduced in the system of second order ODE governing the problem (Eq. (2.2.36)),

$$\begin{cases} \psi_1''(x) + \lambda_1\psi_1(x) + \lambda_2\psi_2''(x) + \lambda_3\psi_2(x) + c_1x^2 + c_2x + c_3 = 0 \\ \psi_1''(x) + \lambda_4\psi_1(x) + \lambda_5\psi_2''(x) + \lambda_6\psi_2(x) + c_4x^2 + c_5x + c_6 = 0 \end{cases}$$

are

$$\lambda_1 = \left(2H_2\left(\left(\frac{1}{4}\left(t_1+2t_2+t_3\right)\left(-H_1t_3+H_3t_1\right)A_1-\frac{1}{4}t_3H_1\left(t_2+t_3\right)A_2+H_3D_1\right.\right.\right.$$
$$\left.\left.\left.-D_3H_1\right)A_3+\left(\frac{1}{4}H_3t_1\left(t_1+t_2\right)A_2+H_3D_1-D_3H_1\right)A_1+A_2\left(-H_1D_3+H_3D_1\right)\right)\right)$$
$$\Big/\left(H_Tt_2\left(\left(\left(\frac{1}{8}t_1t_3\left(t_1-t_3\right)A_2+D_1t_3-D_3t_1\right)A_1+\frac{1}{2}D_1t_3A_2\right)A_3\right.\right.$$
$$\left.\left.-\frac{1}{2}D_3t_1A_1A_2\right)\right)$$

$$\lambda_2 = \frac{1}{8}\left(-16\left(\left(-\frac{1}{16}t_2^2t_3\left(t_1-t_3\right)A_2+\frac{1}{4}D_2t_1t_3+\frac{1}{4}D_2t_3^2+D_3t_2^2\right)A_1+\left(\frac{1}{4}D_2t_3^2\right.\right.\right.$$
$$\left.\left.\left.+\frac{1}{4}D_3t_2^2\right)A_2+D_2D_3\right)A_3-16D_3\left(\left(\frac{1}{4}A_2t_2^2+D_2\right)A_1+D_2A_2\right)\right)\Big/$$
$$\left(t_2\left(\left(\left(\frac{1}{8}t_1t_3\left(t_1-t_3\right)A_2+D_1t_3-D_3t_1\right)A_1+\frac{1}{2}D_1t_3A_2\right)A_3-\frac{1}{2}D_3t_1A_1A_2\right)\right)$$

$$\lambda_3 = \left(2\left(\left(\frac{1}{2}\left(\left(\frac{1}{2}H_3+\frac{1}{2}H_1\right)t_3+H_3t_2\right)\left(t_1+2t_2+t_3\right)A_1+\frac{1}{4}\left(t_2+t_3\right)\left(\left(H_1\right.\right.\right.\right.$$
$$\left.\left.\left.+H_3\right)t_3+H_3t_2\right)A_2+\left(D_2+D_3\right)H_3+D_3H_1\right)A_3+\left(\frac{1}{4}H_3t_2\left(t_1+t_2\right)A_2+\left(D_2\right.\right.$$
$$\left.\left.+D_3\right)H_3+D_3H_1\right)A_1+\left(\left(D_2+D_3\right)H_3+D_3H_1\right)A_2\right)H_2\Big)\Big/\left(H_Tt_2\left(\left(\left(\frac{1}{8}t_1t_3\left(t_1\right.\right.\right.\right.$$
$$\left.\left.\left.-t_3\right)A_2+D_1t_3-D_3t_1\right)A_1+\frac{1}{2}D_1t_3A_2\right)A_3-\frac{1}{2}D_3t_1A_1A_2\right)\right)$$

$$c_1 = \frac{8\overline{F}H_3H_2\left(A_1+A_2+A_3\right)}{t_2\left(\left(\left(t_1t_3\left(t_1-t_3\right)A_2-8D_3t_1+8t_3D_1\right)A_3-4D_3t_1A_2\right)A_1+4A_3t_3A_2D_1\right)H_T}$$

$$c_2 = -\frac{16\left(\overline{F}L+\overline{M}\right)H_3H_2\left(A_3+A_1+A_2\right)}{H_Tt_2\left(\left(\left(t_1t_3\left(t_1-t_3\right)A_2-8D_3t_1+8D_1t_3\right)A_3-4t_1A_2D_3\right)A_1+4t_3A_2A_3D_1\right)}$$

$$c_3 = \left(4\overline{F}\left(2A_1A_3H_1t_2t_3-A_1A_3H_2t_1t_3-A_1A_3H_2t_3^2+2A_1A_3H_3t_2t_3+A_2A_3H_1t_2t_3\right.\right.$$
$$\left.\left.-A_2A_3H_2t_3^2+A_2A_3H_3t_2t_3-4A_1H_2D_3-4A_2H_2D_3-4A_3H_2D_3\right)\right)\Big/\left(\left(A_1A_2A_3\right.\right.$$
$$\left.\left.t_1^2t_3-A_1A_2A_3t_1t_3^2-4A_1A_2D_3t_1+8A_1A_3D_1t_3-8A_1A_3D_3t_1+4A_2A_3D_1t_3\right)H_Tt_2\right)$$

$$\lambda_4 = -\left(\left(\left(\frac{1}{4}\left(\left(t_1+t_3\right)H_1+t_1H_2\right)\left(t_1+2t_2+t_3\right)A_3+\frac{1}{4}t_1\left(H_1+H_2\right)\left(t_1+t_2\right)A_2 + \left(D_1+D_3\right)H_1+D_1H_2\right)A_1+\left(\frac{1}{4}t_3H_1\left(t_2+t_3\right)A_2+\left(D_1+D_3\right)H_1+D_1H_2\right)A_3 + A_2\left(\left(D_1+D_3\right)H_1+D_1H_2\right)\right)H_3\right)\Big/\left(H_T\left(\left(\left(\frac{1}{16}t_1t_3^2\left(t_1+t_2\right)A_2+\frac{1}{4}D_1t_3^2 + \frac{1}{4}D_3t_1^2+\frac{1}{2}D_3t_1t_2\right)A_3+\left(\frac{1}{4}t_1\left(t_1+t_2\right)A_2+D_1\right)D_3\right)A_1+\left(\left(\frac{1}{4}t_3^2A_2 + D_3\right)A_3+D_3A_2\right)D_1\right)\right)$$

$$\lambda_5 = \frac{1}{16}\left(16\left(\left(\frac{1}{16}t_2t_3^2\left(t_1+t_2\right)A_2+\frac{1}{4}D_2t_3^2+\frac{1}{2}D_3t_1t_2+D_3t_2^2\right)A_3+\left(\frac{1}{4}t_2\left(t_1 + t_2\right)A_2+D_2\right)D_3\right)A_1+16\left(\left(\frac{1}{4}D_2t_3^2+\frac{1}{4}D_3t_2^2\right)A_2+D_2D_3\right)A_3+16D_2D_3A_2\right) \Big/\left(\left(\left(\left(\frac{1}{16}t_1t_3^2\left(t_1+t_2\right)A_2+\frac{1}{4}D_1t_3^2+\frac{1}{4}D_3t_1^2+\frac{1}{2}D_3t_1t_2\right)A_3+\left(\frac{1}{4}t_1\left(t_1 + t_2\right)A_2+D_1\right)D_3\right)A_1+\left(\left(\frac{1}{4}t_3^2A_2+D_3\right)A_3+D_3A_2\right)D_1\right)$$

$$\lambda_6 = -\left(\left(\left(\frac{1}{2}\left(t_2H_1+H_2\left(t_2+\frac{1}{2}t_3\right)\right)\left(t_1+2t_2+t_3\right)A_3+\frac{1}{4}t_2\left(H_1+H_2\right)\left(t_1+t_2\right)A_2 + D_2H_1+H_2\left(D_2+D_3\right)\right)A_1+\left(\frac{1}{4}\left(t_2H_1+H_2\left(t_2+t_3\right)\right)\left(t_2+t_3\right)A_2+D_2H_1 + H_2\left(D_2+D_3\right)\right)A_3+\left(D_2H_1+H_2\left(D_2+D_3\right)\right)A_2\right)H_3\right)\Big/\left(H_T\left(\left(\left(\frac{1}{16}t_1t_3^2\left(t_1 + t_2\right)A_2+\frac{1}{4}D_1t_3^2+\frac{1}{4}D_3t_1^2+\frac{1}{2}D_3t_1t_2\right)A_3+\left(\frac{1}{4}t_1\left(t_1+t_2\right)A_2+D_1\right)D_3\right)A_1 + \left(\left(\frac{1}{4}t_3^2A_2+D_3\right)A_3+D_3A_2\right)D_1\right)\right)$$

$$c_4 = \left(8\left(H_1+H_2\right)\overline{F}\left(A_1+A_2+A_3\right)H_3\right)\Big/\left(H_T\left(\left(\left(4t_1\left(2t_2+t_1\right)D_3+\left(t_1\left(t_1+t_2\right)A_2 + 4D_1\right)t_3^2\right)A_3+4\left(t_1\left(t_1+t_2\right)A_2+4D_1\right)D_3\right)A_1+4D_1\left(\left(A_2t_3^2+4D_3\right)A_3 + 4D_3A_2\right)\right)\right)$$

$$c_5 = \left(16\left(\overline{F}L+\overline{M}\right)\left(H_1+H_2\right)\left(A_1+A_3+A_2\right)H_3\right)\Big/\left(\left(\left(\left(4t_1\left(t_1+2t_2\right)D_3+\left(t_1\left(t_1 + t_2\right)A_2+4D_1\right)t_3^2\right)A_3+4\left(t_1\left(t_1+t_2\right)A_2+4D_1\right)D_3\right)A_1+4D_1\left(\left(A_2t_3^2+4D_3\right)A_3 + 4D_3A_2\right)\right)H_T\right)$$

$$c_6 = \left(4\overline{F}\left(A_1A_3H_1t_3^2 + A_1A_3H_2t_3^2 - A_1A_3H_3t_1t_3 - 2A_1A_3H_3t_2t_3 + A_2A_3H_1t_3^2 + A_2A_3H_2t_3^2 - A_2A_3H_3t_2t_3 + 4A_1D_3H_1 + 4A_1D_3H_2 + 4A_2D_3H_1 + 4A_2D_3H_2 + 4A_3D_3H_1 + 4A_3D_3H_2\right)\right) \Big/ \left(H_T\left(A_1A_2A_3t_1^2t_3^2 + A_1A_2A_3t_1t_2t_3^2 + 4A_1A_2D_3t_1^2 + 4A_1A_2D_3t_1t_2 + 4A_1A_3D_1t_3^2 + 4A_1A_3D_3t_1^2 + 8A_1A_3D_3t_1t_2 + 4A_2A_3D_1t_3^2 + 16A_1D_1D_3 + 16A_2D_1D_3 + 16A_3D_1D_3\right)\right)$$

Finally, the coefficients appearing in the boundary conditions (Eq. (2.2.37)),

$$\begin{cases} \psi_1'(L_d) = -c_7\bar{M}_{tot} \\ \psi_2'(L_d) = c_8\bar{M}_{tot} \end{cases}$$

are

$$c_7 = \left(\left(A_2t_2^2 - 4D_2\right)A_3t_3t_1\bar{M}_{tot}A_1\right) \Big/ \left(\left(\left(\left(\left(D_2t_3^2 + D_3t_2^2\right)t_1^2 + t_2^2t_3^2D_1\right)A_2 + 4t_1^2D_2D_3 + 16t_2^2D_1D_3 + 4t_3^2D_1D_2\right)A_3 + 4D_3\left(\left(D_1t_2^2 + D_2t_1^2\right)A_2 + 4D_1D_2\right)\right)A_1 + 4\left(\left(\left(D_2t_3^2 + D_3t_2^2\right)A_2 + 4D_2D_3\right)A_3 + 4D_2D_3A_2\right)D_1\right)$$

$$c_8 = \left(\left(\left(A_2t_1^2 + 8D_1\right)A_1 + 4A_2D_1\right)t_2A_3t_3\bar{M}_{tot}\right) \Big/ \left(\left(\left(t_2^2\left(A_3t_3^2 + 4D_3\right)A_2 + \left(4D_2t_3^2 + 16D_3t_2^2\right)A_3 + 16D_2D_3\right)D_1 + \left(\left(\left(D_2t_3^2 + D_3t_2^2\right)A_3 + 4D_2D_3\right)A_2 + 4A_3D_2D_3\right)t_1^2\right)A_1 + 4\left(\left(\left(D_2t_3^2 + D_3t_2^2\right)A_3 + 4D_2D_3\right)A_2 + 4A_3D_2D_3\right)D_1\right)$$

Ringraziamenti

Desidero ringraziare il Prof. Domenico Bruno per avermi sapientemente guidato, motivato, consigliato ed ascoltato. Ringrazio il Prof. Fabrizio Greco, che ha seguito questo lavoro con grande pazienza e disponibilità, e l'Ing. Paolo Nevone Blasi per il suo valido aiuto. Ringrazio il Prof. Pierre Argoul, che mi ha accolto nella sua équipe fin dal primo giorno senza riserve e come se ne avessi da sempre fatto parte. Ringrazio l'Università della Calabria, che ancora una volta mi ha dato la possibilità di studiare e di imparare.

Ringrazio le persone incontrate lungo questo percorso, con cui ho condiviso momenti di nervosismo, stanchezza, incertezze, ma anche risate, aspirazioni e piccoli successi. Ringrazio inoltre chi ha capito l'importanza di questa fase della mia vita, supportandomi e spingendomi a credere nelle mie capacità.

Ringrazio la mia famiglia, una presenza costante e fondamentale in ogni istante della mia vita.